HAL
open science

Optomechanical transduction applied to M/NEMS devices

Luca Leoncino

To cite this version:

Luca Leoncino. Optomechanical transduction applied to M/NEMS devices. Optics [physics.optics]. Université Grenoble Alpes, 2017. English. NNT : 2017GREAY067 . tel-01757058

HAL Id: tel-01757058

https://theses.hal.science/tel-01757058v1

Submitted on 3 Apr 2018

HAL is a multi-disciplinary open access archive for the deposit and dissemination of scientific research documents, whether they are published or not. The documents may come from teaching and research institutions in France or abroad, or from public or private research centers.

L'archive ouverte pluridisciplinaire **HAL**, est destinée au dépôt et à la diffusion de documents scientifiques de niveau recherche, publiés ou non, émanant des établissements d'enseignement et de recherche français ou étrangers, des laboratoires publics ou privés.

Communauté UNIVERSITÉ Grenoble Alpes

THÈSE

Pour obtenir le grade de

DOCTEUR DE LA COMMUNAUTÉ UNIVERSITÉ GRENOBLE ALPES

Spécialité : **Nanophysique**

Arrêté ministériel : 7 août 2006

Présentée par

Luca LEONCINO

Thèse dirigée par **Laurent DURAFFOURG** et
codirigée par **Guillaume JOURDAN**

préparée au sein du **CEA - LETI / DCOS / SCMS / LCMS**
dans **l'École Doctorale de Physique**

Optomechanical transduction applied to M/NEMS devices

Thèse soutenue publiquement le **11/10/2017**
devant le jury composé de :

M. Ahmad BSIESY
Professeur UJF, Grenoble, Président
M. Bernard LEGRAND
Directeur de recherche LAAS-CNRS, Toulouse, Rapporteur
M. Ivan FAVERO
Directeur de recherche CNRS, Paris, , Rapporteur
M. Laurent VIVIEN
Directeur de recherche CNRS, Paris, Membre
M. Sébastien HENTZ
Ingénieur Chercheur CEA, Grenoble, Membre
M. Guillaume JOURDAN
Ingénieur Chercheur CEA, Grenoble, Encadrant de thèse
M. Laurent DURAFFOURG
Ingénieur Chercheur CEA, Grenoble, Directeur de thèse

Avvertendo e riconoscendo la nuvola, voi potete, cari miei, pensare anche alla vicenda dell'acqua (e perché no?) che divien nuvola per divenir poi acqua di nuovo. Bella cosa, sí. E basta a spiegarvi questa vicenda un povero professoruccio di fisica. Ma a spiegarvi il perché del perché?

Luigi Pirandello, Uno nessuno centomila.

Abstract

Over the past few years years, technological advances in the field of silicon micromachining have initiated the industrial growth of *Micro/Nano Electro Mechanical Systems* (*M/NEMS*) for fabricating sensors or actuators.
In the field of *NEMS* with sub-micron sizes, the properties allow targeting applications in biomedical or biochemical analyses. It has been demonstrated that these nano mass (or force) sensors achieve resolutions of the order of zeptogram ($10^{-21}\,g$) or picoNewton, hence allowing early diagnosis of certain cancers.
Transduction schemes of these systems are currently based on electrical principles: many teams have nevertheless shown that photonics operates and detects tiny displacement in the order of femtometer. This hybrid technology, photonic circuit associated with *M/NEMS*, potentially offers a significant improvement compared to electrical transduction.
The purpose of the thesis consists in developing the optomechanical transduction for *NEMS* resonators displacement. A simple analytical model is presented together with a numerical simulation. The performance of optical detection is compared to electrical detection features. The comparison is based on objective criteria (sensitivity, noise, crowding) for designing original optomechanical structures. A dedicated bench has been developed for the optical and mechanical characterizations of the samples placed in a controlled environment. Measurements on fabricated devices allow a better understanding of the design constrains and, more in general, of the optomechanical detection applied to *NEMS*.

Résumé

Au cours de ces dernières années, les progrès technologiques dans le domaine du micro-usinage sur silicium ont permis le développement de *Micro/Nano Systèmes Électro Mécaniques* (*M/NEMS*) pour réaliser des capteurs ou des actionneurs.
Dans le domaine des *NEMS*, dont les dimensions sont par définition submicroniques, les propriétés obtenues permettent de viser des applications en analyse biochimique ou biomédicale. Il a été démontré que ces nano capteurs de masse (ou de force) atteignent des résolutions de l'ordre du zeptogramme ($10^{-21}\,g$) ou du picoNewton ce qui permet d'envisager des diagnostics précoces de certains cancers.
Tous ces systèmes utilisent à l'heure actuelle des moyens d'actionnement et de détection électriques: de nombreuses équipes ont néanmoins démontré que la photonique actionne et détecte des mouvements de très faibles amplitudes, de l'ordre du femtomètre. Cette technologie hybride, circuit photonique associé au *M/NEMS*, offre potentiellement un gain de performance important par rapport aux moyens de transduction électromécanique.
L'objectif de la thèse est le développement de la transduction optomécanique afin de détecter le déplacement de résonateurs *NEMS*. Un simple modèle analytique est proposé avec le support d'un simulation numérique. Les performances de transduction optique sont comparées aux caractéristiques de la transduction électrique. La comparaison se base sur des critères objectifs (sensibilité, bruit, encombrement) puis de proposer des structures optomécaniques originales. Un banc de caractérisation optique et mécanique est développé pour la caractérisation des échantillons dans un environnement contrôlé. Des mesures sur des composants fabriqués permettent de mieux appréhender les contraintes de dimensionnement et, de façon plus générale, la transduction optomécanique appliquée aux dispositifs *NEMS*.

Contents

Thesis presentation **1**
Goal of the thesis . . . 2
Outline of the manuscript . . . 3

1 Introduction **5**
1.1 *M/NEMS* sensors . . . 5
1.2 Silicon photonics and optical cavities . . . 7
1.3 Optomechanical detection . . . 8

2 Mechanical resonator as mass transducer **11**
2.1 Cantilever theory . . . 12
2.2 Driven harmonic oscillator . . . 15
2.3 Neutral mass sensing . . . 17
2.3.1 Uniform mass deposition . . . 17
2.3.2 Punctual mass addition and multimode operation . . . 18
2.4 Scaling down effects . . . 20
2.5 Conclusions . . . 21

3 Optical ring resonator **23**
3.1 All pass resonator . . . 24
3.2 Add-drop resonator . . . 27
3.3 Spectral characteristics . . . 31
3.3.1 The Free Spectral Range . . . 31
3.3.2 The Finesse . . . 32
3.3.3 The quality factor . . . 33
3.3.4 The contrast . . . 33
3.3.5 Small ring losses and weak symmetrical coupling . . . 34
3.4 $C \cdot Q$ improvement . . . 35
3.5 Conclusions . . . 36

4 Optomechanical theory **37**
4.1 Optomechanical coupling . . . 38
4.2 Optomechanical factor simulation . . . 40
4.3 Optomechanical transduction . . . 42
4.4 Optical gradient force . . . 47
4.5 Conclusions . . . 48

5 The devices **49**
5.1 Waveguides . . . 50
5.2 Ring resonator . . . 51
5.3 Grating coupler . . . 52
5.4 Mechanical resonator . . . 56
5.4.1 In-plane cantilever resonator . . . 56
5.4.2 Membrane resonator . . . 58
5.5 Piezoresistive gauges . . . 60
5.6 Drive electrode . . . 60
5.7 Fabrication process . . . 62
5.7.1 On-chip photonics . . . 63
5.7.2 Optical Q-factor improvement . . . 65
5.7.3 In-plane cantilever fabrication . . . 67
5.7.4 Membrane fabrication . . . 71
5.7.5 Fabrication problems . . . 73
5.8 Conclusions . . . 75

6 Design and setup of test bench **77**
6.1 Specifications and solutions . . . 77
6.2 Vacuum chamber, stages and fiber alignment . . . 80
6.3 Measurement equipments . . . 81
6.3.1 Laser . . . 81
6.3.2 Photodetectors . . . 82
6.3.3 Lock-In Amplifier . . . 82
6.4 The complete setup . . . 83
6.5 Test bench noise evaluation . . . 85
6.5.1 Laser noise . . . 85
6.5.2 Mechanical resonator noise . . . 87
6.5.3 Instrumentation noise . . . 88
6.5.4 Light injection . . . 92
6.6 Test bench noise measurements . . . 94
6.6.1 Noise investigation for the optomechanical detection . . . 94
6.6.2 Noise investigation for the optical characterisation . . . 97
6.7 Conclusions . . . 99

7 Experimental characterization of the device **101**
7.1 Piezoresistive detection . . . 103
7.1.1 Cut-off frequency of the system . . . 103
7.1.2 The piezoresistive downmixing . . . 105
7.1.3 Optimisation of the downmixing frequency . . . 107
7.2 Optical spectrum . . . 110
7.2.1 Continuous wavelength scanning . . . 110
7.2.2 Step by step wavelength scanning . . . 112
7.3 Optomechanical direct detection . . . 116
7.3.1 Transduction scheme . . . 116
7.3.2 Thermomechanical noise and dynamic range . . . 121
7.3.3 Allan deviation . . . 123
7.3.4 Readout calibration . . . 125
7.3.5 Optomechanical factor evaluation . . . 128
7.3.6 Comparison with piezoresistive detection . . . 129
7.3.7 Transduction for different wavelengths . . . 135
7.4 Optomechanical downmixing . . . 140
7.4.1 Transduction scheme . . . 140
7.4.2 Comparison with direct transduction . . . 142
7.4.3 Higher-order modes . . . 144
7.5 Optical actuation . . . 146
7.6 Conclusions . . . 151

8 Conclusion **153**

A Ring Resonators **155**
A.1 All pass resonator . . . 155
A.2 Add-Drop resonator . . . 157

Bibliography **168**

Thesis presentation

This thesis has been realised within the *Laboratoire Composants Micro-Capteurs*[1] (*LCMC*) of *CEA-Leti* in Grenoble. The core expertise of the laboratory consists in the full realisation of *M/NEMS* sensors comprising the conception, the fabrication and the characterisation. For 30 years, the efforts of this group have produced mass sensors, accelerometers, gyroscopes, magnetometers, pressure sensors, hygrometer and microphones based on *M/NEMS* technology.
Given the topics of this thesis, a collaboration was established with the *Département d'optoélectronique*[2] (*DOPT*) which is present in the same institute. This allowed to benefit from their expertise on simulation and fabrication of photonic elements, furthermore they provided some preliminary characterisations and an endorsed test bench as reference.

This work has been supervised by Laurent Duraffourg, currently chief of the *Optical Sensors & Nanophotonics laboratory*, and by Guillaume Jourdan, staff scientist of *LCMC* involved in the *OLYMPIA* project. Sébastien Hentz collaborated daily and funded the experimental setup thanks to the *European Research Grant ENLIGHTENED*. Although I was the first on this activity, the presence of Geoffroy Scherrer and Marc Sansa Perna greatly contributed to the setup development and to sample characterisation. The fabrication of the devices was possible thanks to the professionalism of Jean Marc Fedeli and Marc Gely. Philippe Grosse and Karen Ribaud provide equipments and preliminary optical characterisations. Numerical simulations were performed by Daivid Fowler, Geoffroy Scherrer and Taurel Boris.

[1] *MEMS sensors laboratory*
[2] *Optics and photonics department*

Goal of the thesis

This work aims at developing a new transduction method for measuring the displacement of *NEMS* devices. Whereas traditional readout methods do not tolerate the downscaling and struggle in the GHz domain, the optomechanical detection is the perfect candidate for a high responsivity and high bandwidth transduction of *M/NEMS* displacement.
Although the optomechanical detection has a wide range of applications, we focused on the neutral mass sensing based on nanomechanical resonators [1]. The recent demonstration of neutral mass spectrometry [2] and high-resolution inertial imagers [3] opens up new avenues for portable analytical instruments. These applications however, require the resonator to be operated on several modes simultaneously. Even today, the combination of very high frequencies, small readout signals and multi-mode operation remains a challenge for most electrical transduction techniques. New transduction schemes with high bandwidth and high displacement sensitivity are required.
Nano-optomechanics exhibits these features, and the progress made in the last decade now allows simple on-chip integration [4]. Extremely high displacement sensitivities are attained with devices that are both optically and mechanically resonating [5] in which case the optomechanical coupling is exquisite. Mass sensing applications however, require low-mass mechanical resonators such as 1D devices; in this case, the optomechanical coupling is less impressive, and integrated realizations are scarce, in particular for force [6], or mass sensing applications [7]. Multi-mode operation required for mass sensing implies high-frequency readout signals of low amplitude, which remain delicate to handle in the GHz range.
The optomechanical detection benefits from the virtues of the photonics such as a large bandwidth, the wavelength division multiplexing and the immunity to electromagnetic interferences, providing a near-field detection which is limited theoretically by the *shot noise* of the light.

Leti approaches the optomechanical readout by merging two technologies on the same substrate: the *M/NEMS* technology together with the *silicon on-chip photonics* (fig. 1). The fabrication of new devices went together with a dedicated test bench: different requirements have to be fulfilled in order to test hybrid devices which cover optical, mechanical and electrical domains.
This thesis faced many aspects: the design of *NEMS* and photonic elements, the fabrication of the devices, the instrumentation and the test bench assembly which all together allowed to perform experimental measurements on optomechanical devices. The optomechanical transduction developed in this thesis will be a powerful tool in the *LCMC* laboratory. It may be the basis of new generations of optomechanical accelerometers, gyroscopes or gas sensors with enhanced performances.

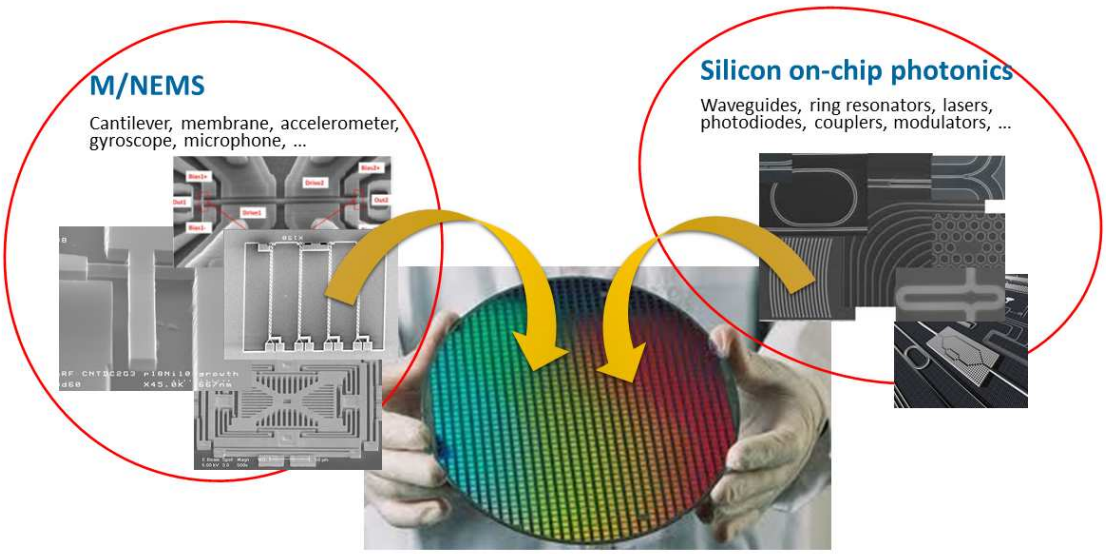

Figure 1: This thesis addresses the challenge of merging of two technologies on the same substrate: the *M/NEMS* together with the *silicon on-chip photonics*.

Outline of the manuscript

Chapter 1 introduces the state-of-the-art of integrated photonics and *M/NEMS* sensors. The merging of these two technologies improves the transduction performance in terms of bandwidth and resolution.

Chapter 2 introduces the challenge of neutral mass sensing with nanoresonators. The downscaling of the cantilever and the multimode operation require a transduction at very high frequency preserving a good signal-to-noise ratio and stability. Furthermore the simplified multiplexing offered by the photonics improves the surface of detection via a network of *NEMS*.

Chapter 3 introduces the theory of the ring resonators which forms the basis of optomechanical transduction. It aims to introduce the correct glossary and the right tools to the reader.

Chapter 4 gives an overview of the optomechanical theory. More concretely, the interaction between the ring resonator and an oscillating cantilever is studied for the purpose of developing the nanoresonator readout.

Chapter 5 shows the design of the optomechanical devices and their fabrication process. Once the photonic elements have been endorsed, we coupled the ring to a

NEMS resonator such as a cantilever or a membrane. A well-studied piezoresistive detection is also available for a smooth technology transition and for *in-situ* comparison between different transductions. A fair comparison between piezoresistive and optomechanical transduction will be done establishing similarities and differences and limits of these techniques.

Chapter 6 describes the design of the experimental setup: the sample, placed inside a vacuum chamber, has to be connected to external instrumentation. The test bench description is followed by the noise characterisation of the setup and of the equipments.

Chapter 7 concerns the experimental characterisation of the device: preliminary experiments test the mechanical and photonic parts separately, then, the optomechanical transduction is investigated deeply.
The mechanical response, the *thermomechanical noise* and the *Allan deviation* of the cantilever are obtained by the means of the optomechanical detection and compared *in-situ* thanks to a parallel piezoresistive detection. The optomechanical coupling factor and the transduction responsivity are evaluated experimentally. The optomechanical downmixing technique, presented here, removes some limits of the optomechanical transduction. The optical actuation is performed as well on the cantilever by the means of the optical gradient force.

Chapter 1

Introduction

NanoElectroMechanical Systems (*NEMS*) are mechanical systems at the nanoscale which suit well as sensors. By virtue of their small dimensions, the are extremely sensitive and reactive to the external stimulus which we want to measure. They can be considered as the natural evolution of *MEMS*: with the progresses of microelectronics, one or more dimensions are reduced to the sub-micron range (see fig. 1.1).

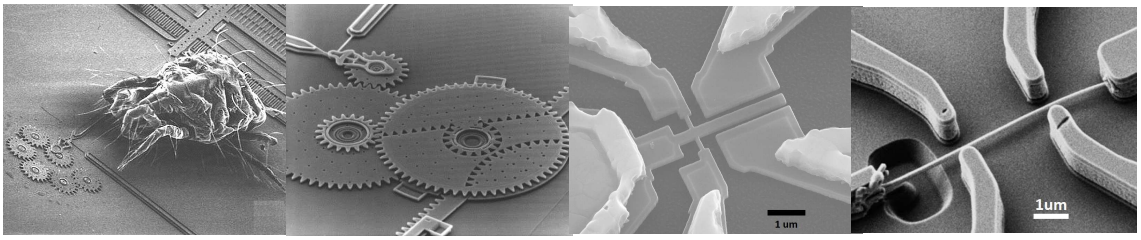

(a) A mite. (b) MEMS. (c) M/NEMS. (d) NEMS.

Figure 1.1: Evolution of mechanical system: from micrometric to nanometric scale. (a)(b) Courtesy of Sandia National Laboratories, (c) from [8] and (d) from [9].

From their appearance in the early 2000, *M/NEMS* are applied in different fields: gas detection, atomic force microscopy, inertial sensing, magnetometry, pressure detection, biological sensing and mass spectrometry.
M/NEMS are tools also for more fundamental investigation, they can be considered like a sort of gym for testing phenomena at the nano and mesoscopic scales.

1.1 *M/NEMS* sensors

The mechanical system is formed by a mobile element which is subject to the external perturbations. The mobile part is a mechanical oscillator such as a cantilever, a

membrane or more in general a suspended proof mass for inertial sensors.
The *M/NEMS* operate mainly in resonance mode in order to realize mechanical oscillators which act as force or mass sensor. The underlying principle of detection of resonant sensors is based on the *gravimetric effect*: the system is driven to resonance and the resonance frequency is monitored in real time. The presence of an additional mass or an acceleration shifts the resonance frequency and, as consequence, the amplitude and the phase response of the oscillator are modified (see fig. 1.2). The mass addition could be the consequence of a gas abortion or caused by a particle landed on the cantilever, whereas an inertial force originates from an acceleration or from a sample-tip interaction.
It is easy to understand that in the former case, we obtain a gas or mass sensor whereas the second situation deals with acceleration or force sensing.

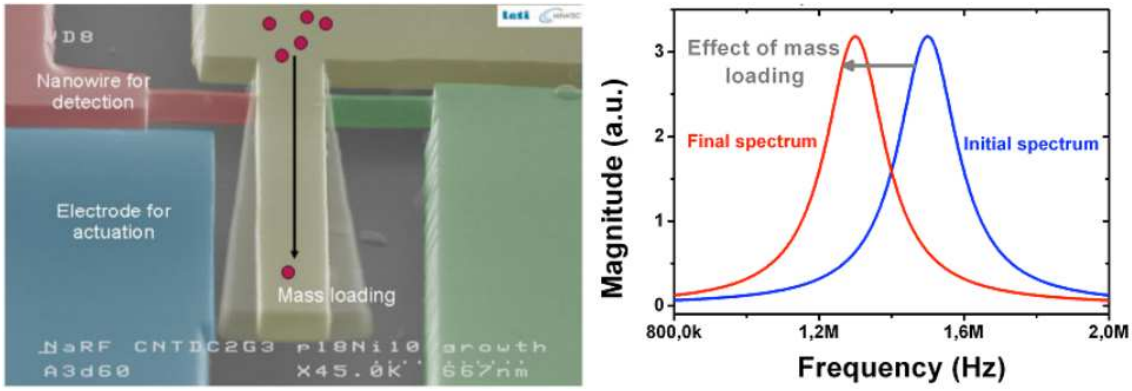

Figure 1.2: The principle of the gravimetric effect: an additional mass shifts the mechanical resonance frequency of the *NEMS*. Extracted from [10]

.

To track the resonance frequency, we have to readout the displacement of the *NEMS*. Traditionally the transduction and the excitation are performed electrically, that explains the name *electromechanical system*.
In the search for better transduction performances, the *NEMS* sizes are scaled down by applying an homothetic reduction: in this way the responsivity to the external perturbation is extremely enhanced. However, some drawbacks show up: the resonance frequency increases and the *NEMS* displacement becomes smaller. In the frame of mass sensing, the detection of single particle requires the detection of higher modes (at higher frequencies) in addition to the fundamental resonance. Capacitive, piezoresistive and magnetomotive detections are well established techniques but they became inefficient or difficult to integrate as the device scales down. The combination of very high frequencies, small readout signal and multimode operation still remains a challenge for most electrical transduction techniques.
Optomechanical transduction instead, overcomes naturally all these limits thanks

to the virtues of photonics. Unlike the electrical signals, the optical signals do not suffer from parasitic capacitances which limit the transduction bandwidth. The detection of *NEMS* displacement at very high frequency and the access to higher order modes is easily available with the optomechanical detection.
Tiny displacements of downscaled *NEMS* are not an issue for the optomechanical detection: the absence of electromagnetic interferences does not require any signal amplification in the proximity of the device, furthermore the weak optical signals are transmitted over long distances by the means of waveguides which have negligible losses.
The downscaling presents a further problem: the *NEMS* offers a smaller surface to the flux of particles decreasing, as consequence, the number of detectable events. The *Very Large Scale Integration* (*VLSI*) offers a solution by deploying a matrix of devices. However, piezoresistive technique requires up to three electric contacts for the transduction and one for the electrostatic actuation, so the matrix size is soon limited for design reasons. The electrical paths of several devices would be hard to manage on the wafer. By using the *wavelength division multiplexing*, several wavelengths coexist into the same waveguide and each of them addresses a single NEMS device. In this way, the matrix of *NEMS* is not limited any more and the capture surface is easily enhanced by a factor from 20 to 100.

1.2 Silicon photonics and optical cavities

The optical fibers already replaced the electrical cables in the telecommunication lines over long distances, similarly, the silicon photonics aims to substitute the microelectronics in the signal processing or in the inter-chip communication. Unlike electrical signals, optical signals do not suffer from the parasitic capacitances or the electromagnetic interferences, this means that photonic devices have a larger signal bandwidth and a reduced power consumption compared to electronic devices.
The silicon photonics integrates the industry of microelectronics which already offers an endorsed *CMOS* technology and the possibility of a *VLSI*. In the last decade, the progress made in fabrication allow a simple on-chip integration of photonic elements [11]. Nowadays the light is coupled and managed along the wafer by using couplers, waveguides, filters, splitters and multiplexers. The photonics becomes complete with the emerging of active elements like lasers, modulators [12] and photodetectors which are integrated on the wafer.

The light can be confined in optical cavities which play an important role in the success of photonics because they are already employed for on-chip lasers or wavelength demultiplexers. The simplest optical cavity is the *Fabry-Perot* cavity but more practical on-chip realisations consist in the whispering gallery resonators: a

looped waveguide, a disk or a sphere is coupled evanescently to the external world via a bus waveguide. Similarly to a *Fabry-Perot* cavity, a whispering gallery hosts only wavelengths which are submultiples of the circular optical path. Photonic crystals are a third solution to confine the light into a cavity. The most common optical cavities are gathered in fig. 1.3:

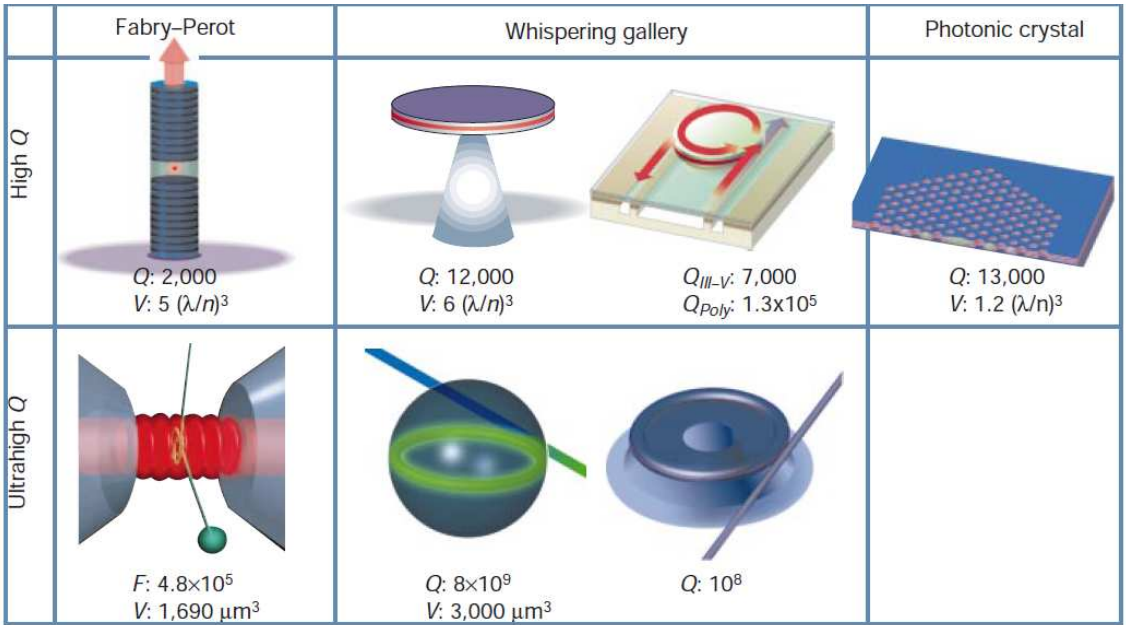

Figure 1.3: Different optical cavities geometry according to the confinement method: *Fabry-Perot*, whispering gallery and photonic crystal. Q is the optical quality factor and V the volume of the cavity. Extracted from [13]

The standard tools of the *CMOS technology* provide on-chip whispering galleries with interesting quality factors, and stable monomode bus waveguides which are prealigned with the cavity (see section 5.7). Furthermore the light coupling is easily implemented using the grating couplers (see section 5.3).
Since the fabrication technology enables the wafer integration of photonics and *NEMS* devices, we employ one of this photonic resonators to perform the optomechanical transduction of the *NEMS* displacement.

1.3 Optomechanical detection

In this work, photonics is a tool to ameliorate the state of the art of *NEMS* sensors: the improved readout displacement of a *NEMS* is obtained coupling the mechanical resonator to the optical cavity. Since the light circulates several times inside the cavity before leaving it, any perturbation of the cavity impacts the light several

times and the effect of this perturbation cumulates. Compared to a single reflection technique, the optical cavity detection has a responsivity improved by the cavity *finesse*. In this way, also a weak cavity perturbation is easily detectable.
Furthermore, the light stocked inside the cavity achieves enough power to actuate the *NEMS* by the means of the radiation pressure or optical gradient force.

The most intuitive example is a *Fabry-Perot* resonator whose one of the two mirrors is free to move: any displacement of the mobile mirror modifies the wavelength (or the frequency) of the standing lightwave which resonates in between (see fig. 1.4).

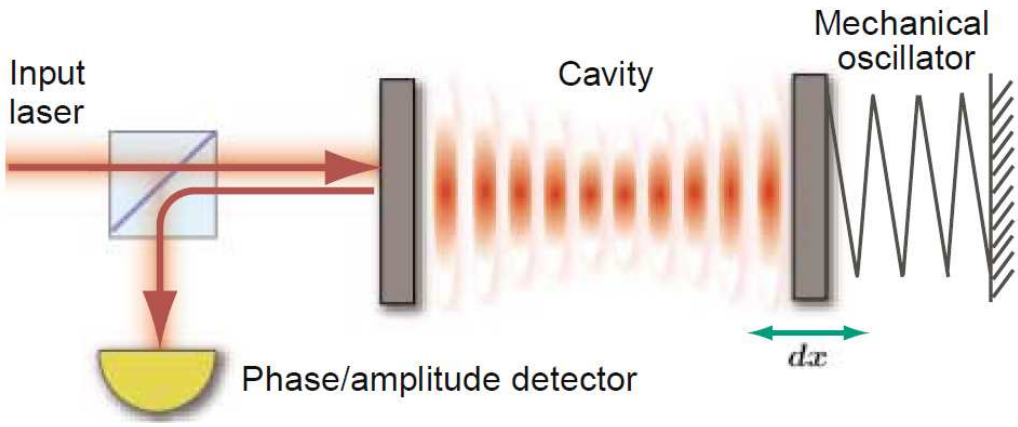

Figure 1.4: A *Fabry-Perot* resonator having a mobile mirror. Extracted from [14]

By analogy, the optical properties of the whispering gallery are perturbed by the presence of a *NEMS* which is placed within the evanescent tail of the intra-cavity propagating wave. If a whispering gallery or a photonic crystal is free to oscillate, it acts as mechanical and optical resonator simultaneously.
Fig. 1.5 offers a short-list of experimental achievements: a cantilever close to a cleaved optical fiber (fig. 1.5a) forms a *Fabry-Perot* resonator very similar to schema in fig. 1.4. A whispering gallery is perturbed by a in-plane cantilever (fig. 1.5b) or by a torsional oscillator (fig. 1.5c) but it can also oscillate when it is released from the substrate being an optical and a mechanical resonator at the same time (fig. 1.5d and fig. 1.5e). In a similar way, a released photonic crystal serves as an optomechanical resonator (fig. 1.5f).
Best optomechanical couplings are attained with devices which are both optically and mechanically resonating (see fig. 1.5d, 1.5e and 1.5f). However, the mass sensing applications require low-mass mechanical resonators such as a cantilever or thin membrane (see fig. 1.5a, 1.5b and 1.5c).

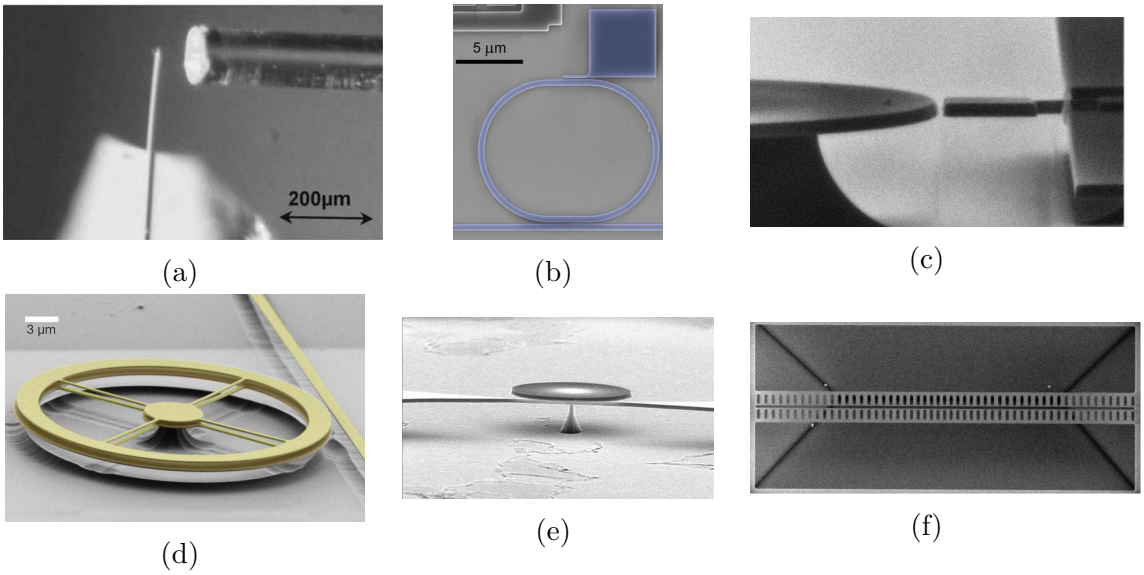

Figure 1.5: A short-list of experimental optomechanical system: (a) a *Fabry-Perot* realised between a cantilever and an optical fiber from [15], (b) an in-plane cantilever coupled to ring resonator from [7], (c) a torsional oscillator into coupled to a disk from [16], (d) a suspended double disk resonator from [17], (e) breath mode detection of a disk from [5], (f) a photonic crystal released from the substrate from [18].

For this work, we choose an optical ring resonator for the optomechanical transduction of an *in-plane* cantilever (see section 5.4.1). The fabricated device reminds the system in fig. 1.5b.
Aiming at mass sensing applications, a more original design was attempted in order to improve the capture surface: a membrane, which vibrates out of plane, is placed over the ring resonator (see section 5.4.2).

Chapter 2

Mechanical resonator as mass transducer

Without being exhaustive, this chapter shows the theory of a cantilever in the regime of small oscillation. We investigate the in-plane displacement $u(x,t)$ along the beam in the time domain finding the resonance frequency and the shape for each flexural mode.
The goal is to show the cantilever performances for mass sensing applications and to evaluate the pros and cons of cantilever downscaling. As we will see, the optomechanical detection solves some problems for *NEMS* displacement readout, particularly within the frame of *neutral mass spectrometry* [1][2].

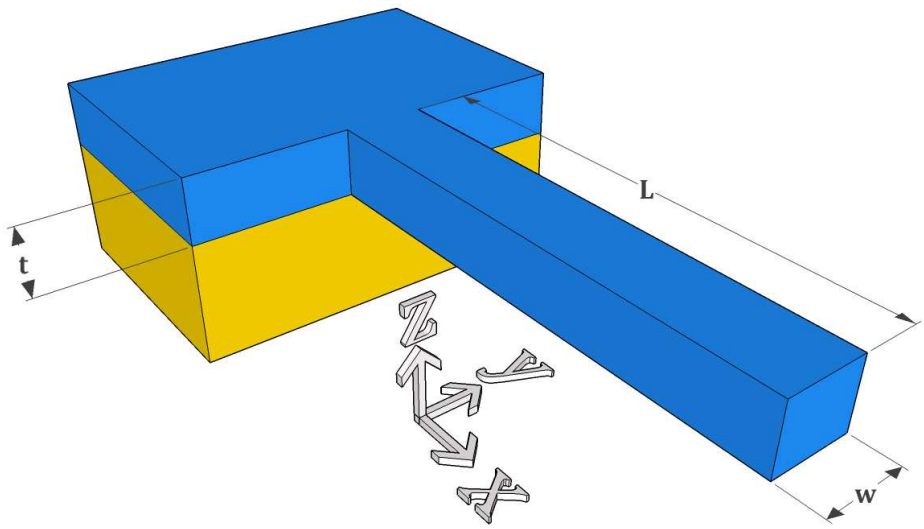

Figure 2.1: Single clamped cantilever having thickness t, width w and length L.

2.1 Cantilever theory

For small deflection along the y-axis ($u \ll w$), the motion of a thin homogeneous cantilever ($t \ll L$) is described by the equation of *Euler-Bernoulli* [19]

$$EI\frac{\partial^4 u(x,t)}{\partial x^4} + \rho S\frac{\partial^2 u(x,t)}{\partial t^2} = 0 \tag{2.1}$$

where E is the young modulus, $I = t \cdot w^3/12$ the momentum of inertia, ρ is the density and $S = w \cdot t$ the cross section area.
Following the *Galerkin* procedure, we separate the spatial and temporal dependency of the displacement

$$u(x,t) = \sum_{n=1}^{\infty} u_n(t) \cdot \psi_n(x) \tag{2.2}$$

so the beam deformation is given by the contribution of infinite modes having a shape $\psi_n(x)$ and a temporal oscillation $u_n(t)$.
The mode shapes $\psi_n(x)$ form a orthogonal base satisfying

$$\int_0^L \psi_n(x)\psi_m(x)\,dx = 0 \quad if \;\; n \neq m \tag{2.3}$$

and they are normalised to the maximum amplitude

$$max[\psi_n(x)] = 1 \tag{2.4}$$

The resonance frequencies are obtained inserting the equation 2.2 in equation 2.1,

$$EIu_n(t)\frac{\partial^4 \psi_n(x)}{\partial x^4} + \rho S\psi_n(x)\frac{\partial^2 u_n(t)}{\partial t^2} = 0 \tag{2.5}$$

for each mode n we have

$$\frac{EI}{\rho S}\frac{1}{\psi_n(x)}\frac{\partial^4 \psi_n(x)}{\partial x^4} = -\frac{1}{u_n(t)}\frac{\partial^2 u_n(t)}{\partial t^2} \tag{2.6}$$

and, looking for solution of type $u_n(t) = U_n e^{-i\omega_n t}$, we find

$$\frac{EI}{\rho S}\frac{1}{\psi_n(x)}\frac{\partial^4 \psi_n(x)}{\partial x^4} = -\frac{1}{u_n(t)}\frac{\partial^2 u_n(t)}{\partial t^2} \equiv \omega_n^2 \tag{2.7}$$

so, $\psi_n(x)$ are eigensolutions of equation 2.1 satisfying

$$\frac{\partial^4 \psi_n(x)}{\partial x^4} = \lambda_n^4 \psi_n(x) \tag{2.8}$$

The resonance frequencies $f_n = \omega_n/2\pi$ for all the modes are

$$\boxed{\Rightarrow f_n = \frac{\lambda_n^2}{2\pi}\sqrt{\frac{EI}{\rho S}} = \frac{(\lambda_n L)^2 w}{4\pi L^2}\sqrt{\frac{E}{3\rho}}} \tag{2.9}$$

The eigenvalues λ_n are obtained by solving the equation 2.8 with the help of the boundary conditions. The general solution for the mode shape is

$$\psi_n(x) = A_n \sinh(\lambda_n x) + B_n \cosh(\lambda_n x) + C_n \sin(\lambda_n x) + D_n \cos(\lambda_n x) \tag{2.10}$$

and the boundary condition for a single-clamped cantilever are

$$\psi_n(0) = 0 \tag{2.11a}$$
$$\psi_n'(0) = 0 \tag{2.11b}$$
$$\psi_n''(L) = 0 \tag{2.11c}$$
$$\psi_n'''(L) = 0 \tag{2.11d}$$

This leads to the system

$$\begin{cases} B_n + D_n = 0 & (2.12a) \\ A_n + C_n = 0 & (2.12b) \\ A_n \sinh(\lambda_n L) + B_n \cosh(\lambda_n L) - C_n \sin(\lambda_n L) - D_n \cos(\lambda_n L) = 0 & (2.12c) \\ A_n \cosh(\lambda_n L) + B_n \sinh(\lambda_n L) - C_n \cos(\lambda_n L) + D_n \sin(\lambda_n L) = 0 & (2.12d) \end{cases}$$

which accepts non-null solutions only if $\lambda_n L$ verifies the following condition

$$\cosh(\lambda_n L)\cos(\lambda_n L) + 1 = 0 \tag{2.13}$$

We can find the values of $\lambda_n L$ via a graphic solution combined with the numerical bisection method as shown in fig. 2.2.

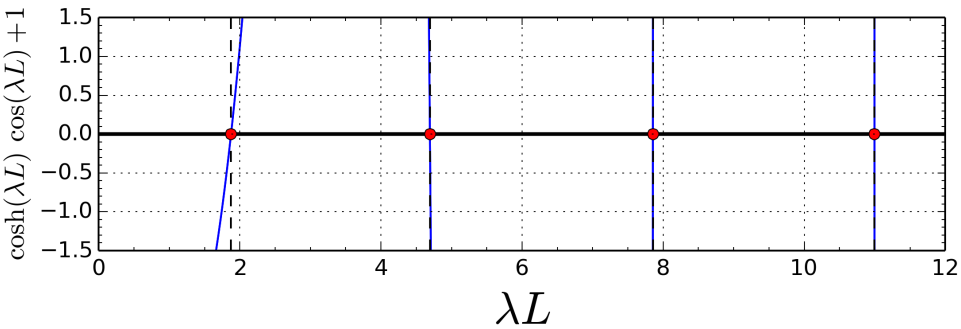

Figure 2.2: Graphic solution for transcendental equation in (2.13)

The eigenvalues $\lambda_n L$ are listed up to the 4-th mode in the table 2.1. The values for the doubly-clamped cantilever are obtained solving the system with different boundary conditions so that $\psi_n(0) = \psi_n'(0) = \psi_n(L) = \psi_n'(L) = 0$.

	$\boldsymbol{\lambda_1 L}$	$\boldsymbol{\lambda_2 L}$	$\boldsymbol{\lambda_3 L}$	$\boldsymbol{\lambda_4 L}$
Cantilever	1.875	4.694	7.854	10.995
Doubly clamped	4.73	7.853	10.995	14.14

Table 2.1: Eigenvalues of $\psi_n(x)$ up to the 4-th mode.

A further effort is required to find the analytic expression of the mode shape $\psi_n(x)$ and the parameter A_n. From eq. (2.10) and (2.12d), we obtain

$$\psi_n(x) = A_n \left\{ [\sinh(\lambda_n x) - \sin(\lambda_n x)] - \frac{[\sinh(\lambda_n x) + \sin(\lambda_n x)]\,[\cosh(\lambda_n x) - \cos(\lambda_n x)]}{\cosh(\lambda_n x) + \cos(\lambda_n x)} \right\} \tag{2.14}$$

where A_n is fixed by the mode normalisation condition in eq. (2.4)

$$A_n = \frac{\cosh(\lambda_n L) + \cos(\lambda_n L)}{[\sinh(\lambda_n L) - \sin(\lambda_n L)]\,[\cosh(\lambda_n L) + \cos(\lambda_n L)] - [\sinh(\lambda_n L) + \sin(\lambda_n L)]\,[\cosh(\lambda_n L) - \cos(\lambda_n L)]} \tag{2.15}$$

$\boldsymbol{A_1}$	$\boldsymbol{A_2}$	$\boldsymbol{A_3}$	$\boldsymbol{A_4}$
-0.367047756802	0.509233659366	-0.499612248377	0.500016779064

Table 2.2: Values for A_n up to the 4-th mode.

We can finally plot the mode shapes $\psi_n(x)$ in fig. 2.3 introducing the scaled variable $\xi = x/L$ along the beam length.

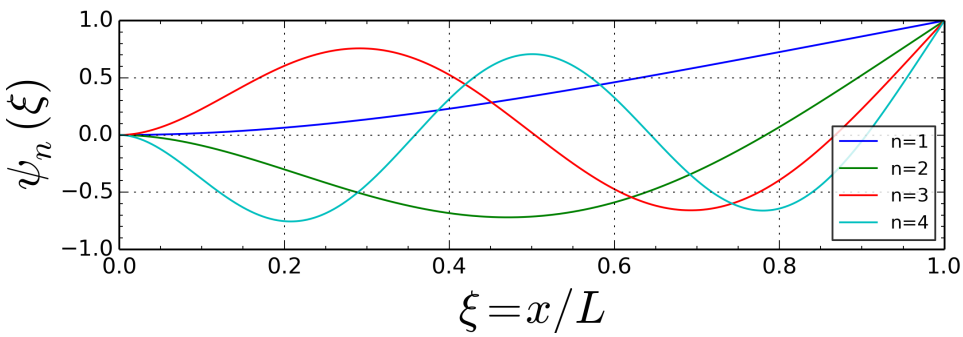

Figure 2.3: Mode shapes for a free end cantilever. The x-axis is normalised to the beam length.

2.2 Driven harmonic oscillator

We are going to describe the cantilever displacement by the means of a unidimensional harmonic oscillator model.
Differently from the previous section, the cantilever is now subject to a damping b caused by a viscous environment. If we drive the cantilever with an arbitrary force per unit length $f(x,t)$, the *Euler-Bernoulli* equation in eq. (2.1) results as

$$EI\frac{\partial^4 u(x,t)}{\partial x^4} + \rho S\frac{\partial^2 u(x,t)}{\partial t^2} + b\frac{\partial u(x,t)}{\partial t} = f(x,t) \tag{2.16}$$

Projecting the equation on the n-mode, we find

$$\begin{aligned} EI\int_0^L \sum_{m=1}^{\infty} \psi_n(x)\lambda_n^4\psi_m(x)u_m(t)\,dx + \rho S\int_0^L \sum_{m=1}^{\infty} \psi_n(x)\psi_m(x)\frac{\partial^2 u_m(t)}{\partial t^2}\,dx \\ + b\int_0^L \sum_{m=1}^{\infty} \psi_n(x)\psi_m(x)\frac{\partial u_m(t)}{\partial t}\,dx = \int_0^L \psi_n(x)f(x,t)\,dx \end{aligned} \tag{2.17}$$

$$\begin{aligned} u_n(t)\lambda_n^4 EI\int_0^L \psi_n^2(x)\,dx + \frac{\partial^2 u_n(t)}{\partial t^2}\rho S\int_0^L \psi_n^2(x)\,dx \\ + \frac{\partial u_n(t)}{\partial t} b\int_0^L \psi_n^2(x)\,dx = \int_0^L \psi_n(x)f(x,t)\,dx \end{aligned} \tag{2.18}$$

Rearranging the above equation in a more compact form, we obtain the equation of a harmonic oscillator

$$M_n\ddot{u}_n(t) + \gamma\dot{u}_n(t) + k_n u_n(t) = F_n(t) \tag{2.19}$$

where the modal mass is

$$\boxed{M_n = M\int_0^1 \psi_n^2(\xi)\,d\xi = \alpha_n M} \tag{2.20}$$

the modal stiffness is

$$\boxed{k_n = (\lambda_n L)^4\frac{EI}{L^3}\int_0^1 \psi_n^2(\xi)\,d\xi = \alpha_n(\lambda_n L)^4\frac{EI}{L^3}} \tag{2.21}$$

and the damping coefficient is equal to

$$\boxed{\gamma = bL\int_0^1 \psi_n^2(\xi)\,d\xi = \alpha_n bL} \tag{2.22}$$

To simplify the equations, we introduced the scaled variable $\xi = x/L$ along the beam length. Numerical calculation provides the values for the factors $\alpha_n = \int_0^1 \psi_n^2(\xi)\, d\xi$ shown in table 2.3.

$\boldsymbol{\alpha_1}$	$\boldsymbol{\alpha_2}$	$\boldsymbol{\alpha_3}$	$\boldsymbol{\alpha_4}$
0.25	0.25	0.25	0.25

Table 2.3: Values for α_n up to the 4-th mode for a cantilever.

The force $F_n(t)$ driving the oscillator has to be calculated depending on the actuation force in the following way

$$\boxed{F_n(t) = \int_0^L \psi_n(x) f(x,t)\, dx} \tag{2.23}$$

For a sinusoidal drive force $F_n(t) = F_n e^{-i\omega t}$, the harmonic oscillator which describes the n-th mode has a magnitude and a phase (fig. 2.4)

$$R_n(\omega) = \frac{F_n}{M_n \sqrt{\left(\omega_n^2 - \omega^2\right)^2 + \omega^2 \gamma^2}} \tag{2.24}$$

$$\phi_n(\omega) = \arctan\left(\frac{\gamma\omega}{\omega_n^2 - \omega^2}\right) \tag{2.25}$$

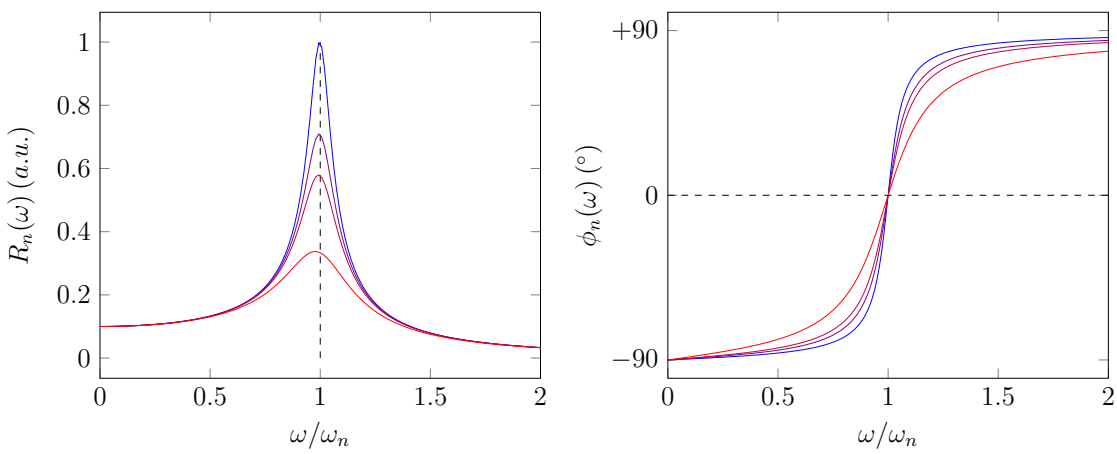

Figure 2.4: Magnitude and phase of the harmonic oscillator with the change in damping $\gamma_1 < \gamma_2 < \gamma_3 < \gamma_4$.

When the cantilever is under vacuum, the damping is negligible ($\gamma/\omega_n \ll 1$), so the resonance frequency of the damped oscillator is almost unchanged

$$\omega_r = \omega_n \sqrt{1 - \gamma/\omega_n} \simeq \omega_n \tag{2.26}$$

and the mechanical quality factor of the resonator is

$$\boxed{Q_{mech} = \frac{\omega_n}{\gamma} = \frac{energy\ stored}{energy\ lost\ per\ cycle}} \tag{2.27}$$

The cantilever displacement at the generic point x will be

$$u(x,t) = \sum_{n=1}^{\infty} \psi_n(x) R_n(\omega) e^{-i(\omega t + \phi_n(\omega))} = \sum_{n=1}^{\infty} \psi_n(x) \frac{F_n e^{-i(\omega t + \phi_n(\omega))}}{M_n \sqrt{(\omega_n^2 - \omega^2)^2 + \omega^2 \gamma^2}} \tag{2.28}$$

thus the cantilever displacement in x is the result of infinite harmonic oscillators, one for each mode, having different amplitudes and phases.

2.3 Neutral mass sensing

Modelling the cantilever mode as a damped harmonic oscillator of mass M_n and stiffness k_n (see section 2.2), the resonance frequency for the n-mode results

$$f_n = \frac{1}{2\pi} \sqrt{\frac{k_n}{M_n}} \tag{2.29}$$

If now a mass Δm is added to the cantilever, it applies on the cantilever an additional force [20]. We have to update the harmonic oscillator equation in eq. (2.19) adding a term $F_n^{\Delta m}(t)$ due to the supplementary mass Δm on the cantilever.
In the following subsections, we will deal with two typical mass sensing scenarios: the uniform mass deposition and the particle stick on the cantilever.

2.3.1 Uniform mass deposition

For a uniform mass deposition, the cantilever is subject to a force per unit length

$$f_{uniform}(x,t) = -\frac{\Delta m}{L} \ddot{u}_n(t)\, \psi_n(x) \Rightarrow F_n^{\Delta m}(t) = -\alpha_n\, \Delta m\, \ddot{u}_n(t) \tag{2.30}$$

as a result, the equation of the harmonic oscillator for the n-mode in eq. (2.19) becomes

$$M_n \ddot{u}_n(t) + \gamma \dot{u}_n(t) + k_n u_n(t) = F_n(t) - \alpha_n\, \Delta m\, \ddot{u}_n(t) \tag{2.31}$$

so the resonance frequency shifts down from f_n to f_n^* where

$$f_n^* = \frac{1}{2\pi} \sqrt{\frac{k_n}{M_n + \alpha_n \Delta m}} \tag{2.32}$$

In the hypothesis that the mass addiction does not modify the stiffness and the additional mass is minute ($\Delta m \ll M_n$), it is possible to develop the previous formula at the first order in Δm

$$f_n^* - f_n = \Delta f_n \simeq -\frac{1}{2\pi}\sqrt{\frac{k_n}{M_n}}\frac{\Delta m}{2M} \tag{2.33}$$

we obtain in this way the *responsivity* for the mass sensing

$$\boxed{\mathfrak{R}_n \equiv \frac{\Delta f_n}{\Delta m} = -\frac{f_n}{2M}} \tag{2.34}$$

Within the *NEMS* mass sensing context, the deposited mass Δm is obtained measuring the shift of the cantilever resonance frequency Δf_n.
The smallest mass detectable by the cantilever is directly linked to its frequency stability which is estimated by the *Allan deviation* [21][22][23]. The mass resolution δm results as

$$\boxed{\delta m = 2M\frac{\delta f_n}{f_n} = 2M\,\sigma_{f_n}(\tau)} \tag{2.35}$$

where $\sigma_{f_n}(\tau)$ is the *Allan deviation* of the resonance frequency signal calculated for an integration time of the measurement τ.
The *Allan deviation* is a statistical tool which evaluates the frequency fluctuations of a resonator over a given interval of time τ. For a generic signal $y(t)$, the *Allan deviation* is calculated as follows

$$\sigma_y(\tau) = \sqrt{\frac{1}{2(N-1)}\sum_{i=1}^{N-1}\left(\overline{y}_{i+1} - \overline{y}_i\right)^2} \tag{2.36}$$

where $\overline{y}_i$ is a generic sample of the signal $y(t)$ averaged over a time τ. N is the number of independent samples large enough for a correct statistics.

This principle opens the way for mass sensing of neutral particles [2][24][25]. Classical mass spectroscopy demands ionized particles measuring only the m/q ratio; it fails for mass values bigger than few *kDalton* [26] and the presence of multiples ionisation levels complicates the data interpretation. Furthermore, the mass of biological species which cannot be ionized (unless destroy them) is now accessible [27][28].

2.3.2 Punctual mass addition and multimode operation

In the case of single particle detection, the frequency shift strongly depends on the landing position. Intuitively, the deposited point-mass Δm affects more the

cantilever dynamics if it lands where the mode shape has a wider amplitude. We have to modify the eq. (2.34) taking into account that the mass addition is localised in a position x_1.
For a punctual mass addiction in x_1, the cantilever is subject to a force per unit length

$$f_{particle}(x,t) = -\delta(x - x_1)\,\Delta m\,\ddot{u}_n(t)\,\psi_n(x_1) \Rightarrow F_n(t) = -\Delta m\,\ddot{u}_n(t)\,\psi_n^2(x_1) \quad (2.37)$$

as a result, the equation of the harmonic oscillator for the n-mode in eq. (2.19) becomes

$$M_n\ddot{u}_n(t) + \gamma\dot{u}_n(t) + k_n u_n(t) = F_n(t) - \Delta m\,\ddot{u}_n(t)\,\psi_n^2(x_1) \quad (2.38)$$

and consequently, the new resonance frequency is

$$f_n^* = \frac{1}{2\pi}\sqrt{\frac{k_n}{M_n + \Delta m\psi_n^2(x_1)}} \quad (2.39)$$

Developing to the first order, as done before in eq. (2.33), we find the resonance frequency shift due to a localised mass addition

$$\Delta f_n \simeq -\frac{f_n}{2M_n}\Delta m\psi_n^2(x_1) \quad (2.40)$$

The above equation is consistent with the intuition, if the particle lands in a node of the mode shape, the resulting frequency shift will be null.
We also note that two different particles give rise to the same frequency shift if the following condition is fulfilled

$$\frac{\Delta m_1}{\Delta m_2} = \frac{\psi_n^2(x_2)}{\psi_n^2(x_1)} \quad (2.41)$$

To decorrelate the mechanical frequency shift from the landing position, we have to simultaneously track three modes for a free-end cantilever [29][30] and only two modes for a doubly clamped beam [3].
The cantilever transduction bandwidth must be large enough to detect not only the fundamental mode but higher modes. It results that for a cantilever at 60 MHz, the third resonance frequency achieves the GHz domain, being almost 17 times higher than the fundamental one. Since piezoresistive transduction struggles as the signal frequencies exceed 200-300 MHz, the optomechanical readout is a valid alternative for this application.

2.4 Scaling down effects

The most important advantage of the downscaling is the mass responsivity improvement. For the sake of simplicity, we limit ourselves to the case of uniform mass deposition.
Applying a homothetic reduction to the cantilever, we find from eq. (2.34) that the mass responsivity scales as l^{-4}

$$\mathfrak{R}_n \equiv \frac{\Delta f_n}{\Delta m} = -\frac{f_n}{2M} = \frac{(\lambda_n L)^2}{8\pi t L^3}\sqrt{\frac{E}{3\rho^3}} \propto \frac{1}{l^4} \tag{2.42}$$

this means that a modest size reduction of the devices causes a huge improvement of the mass responsivity $\mathfrak{R}_n$ for the all modes.
On the other hand, from eq. (2.9), the resonance frequencies scale as

$$f_n = \frac{(\lambda_n L)^2 w}{4\pi L^2}\sqrt{\frac{E}{3\rho}} \propto \frac{1}{l} \tag{2.43}$$

thus the transduction technique must be fast enough to detect the cantilever displacement at higher and higher frequencies. If we add the fact that we need to track up to the third mode, the transduction bandwidth is a key for the mass sensing. As stated above, classical transduction methods (e.g. piezoresistive one) become tricky for frequencies above 200-300 MHz.
But that is not all, compared to the fundamental mode, the cantilever stiffness increases for the higher modes

$$k_n = k_1 \frac{\alpha_n}{\alpha_1}\left(\frac{\lambda_n}{\lambda_1}\right)^4 \tag{2.44}$$

This means that the readout technique must have a good responsivity in order to detect smaller and smaller displacement of higher modes which are stiffer than the fundamental one.
The last inconvenience of the downscaling is the reduced surface of capture ($L \cdot w$): less landing area is offered to the flux of particles, fewer events are detected. A solution is to deploy a matrix of *NEMS* much closer as possible to each other. (See fig. 2.5)

A successful attempt was already done with *NEMS* having a piezoresistive readout, but the requirement of three electrical contacts for each device limits the matrix dimension and complicates the fabrication (see fig. 2.5a). In that case, the multiplexing was done in the frequency domain tuning the cantilever resonance via the beam length.
By the means of photonics, instead, we can address many optomechanical devices on the same bus waveguide tuning the resonance wavelengths of the optical rings (see fig. 2.5b).

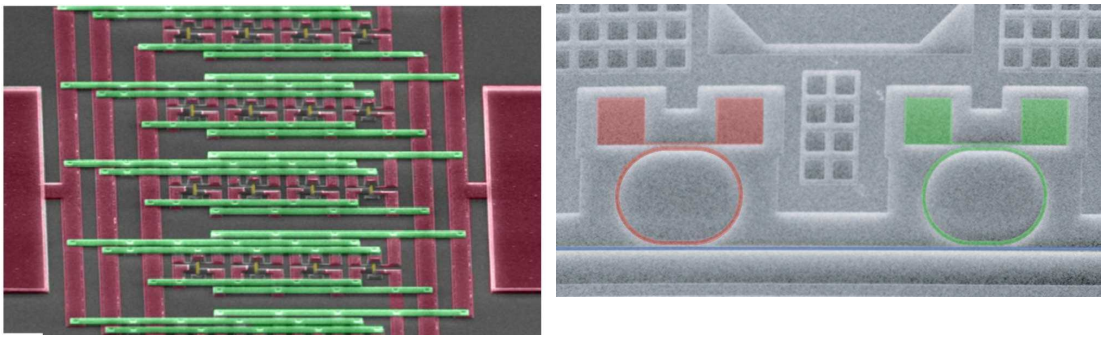

(a) Matrix of piezo *NEMS* from [31] (b) Wavelength multiplexing from [32]

Figure 2.5: *NEMS* multiplexing complexity: comparison between the two readout techniques.

2.5 Conclusions

Along the chapter, we have defined all the useful properties of a cantilever in the context of mass sensing application (resonance frequency, effective mass, mass responsivity...). Simple consideration about dimensional relations leads to clear conclusions summed up in table 2.4: scaling down the sizes improves the mass responsivity but it increases as well the cantilever resonance frequency and reduces the landing area.

Parameters	**Law scale**	**Typical values**
Mass	$\propto l^3$	$1\,pg - 10\,fg$
Resonance frequency	$\propto l^{-1}$	$10\,MHz - 1\,GHz$
Mass responsivity	$\propto l^{-4}$	$10^{19} - 10^{23}\,Hz/g$
Stiffness	$\propto l$	$0.1 - 100\,N/m$
Surface of capture	$\propto l^2$	$0.5 - 5\,\mu m^2$

Table 2.4: Resuming the downscale effects for a homotethic miniaturisation of the cantilever.

All these disadvantages (higher mechanical frequencies, small displacement and limited multiplexing) are neutralised by an appropriate transduction technique: the optomechanical transduction has an improved displacement responsivity, a larger bandwidth and a simplified possibility of multiplexing.

Chapter 3

Optical ring resonator

As we will see in chapter 4, the optomechanical transduction results from the sensitivity of the photonic circuit faced to the external perturbations. For example, the evanescent wave of the light travelling through a waveguide is sensitive to scattering: as a result, the light transmission is modified when an object approaches the waveguide [33][34]. This makes the readout of the relative displacement possible.
Similarly, the phase velocity of the light is modified by the presence of the external object such as a cantilever. Measuring the phase delay via an interferometric technique, we obtain an image of the cantilever displacement [35].
By using a optical resonator instead of a simple waveguide, we obtain an amplifying effect: on average, a photon travels across the cavity $\mathcal{F}$ times before to leave it; we call *finesse* this cavity parameter described in section 3.3.2. This means that the action of the perturbation on each photon is multiplied by $\mathcal{F}$: for example, the phase delay of the photon into the ring cumulates each round-trip making its detection easier [7]. That is why it is possible to achieve the best performances in terms of displacement readout only by using an optical cavity.
The optical cavity fits also for the actuation of the *NEMS*, the light power is stocked in a small volume enhancing the optical actuation on the cantilever (see section 4.4).

For this work, we chose a cavity made up with an optical ring: by the virtue of easy on-chip integration and interesting quality factors, the ring resonator is a good tool for the *NEMS* displacement readout.
This chapter aims to recall the characteristics of the optical ring resonator, especially those which have a particular relevance for optomechanical applications. The model described here provides the optical spectrum of the ring on the basis of the geometry and the material optical properties.

3.1 All pass resonator

A generic ring resonator consists of an optic waveguide which is looped back on itself, such that a resonance occurs when the optical path length of the resonator is exactly a whole number of wavelengths [36]

$$n_{eff} \cdot L = m \cdot \lambda_r \Rightarrow \lambda_r = \frac{n_{eff} \cdot L}{m} \qquad with \quad m = 1, 2, 3 \ldots \tag{3.1}$$

where L is the circumference of the ring, n_{eff} is the effective index of the ring and λ_r the resonance wavelength.
A ring resonator as stand alone device only becomes useful when it is coupled to the outside world. The most common coupling mechanism is the codirectional evanescent coupling between the ring and an adjacent bus waveguide [36].
The simplest configuration is a ring coupled with a single waveguide (fig. 3.1):

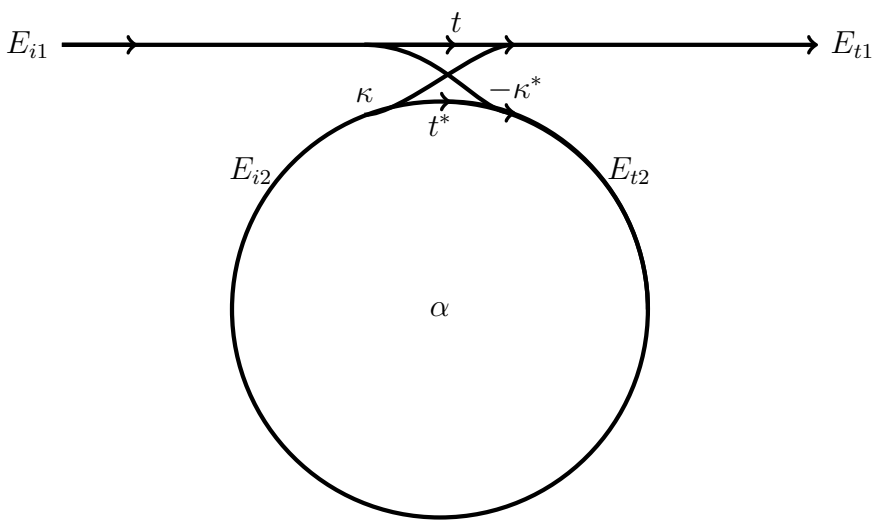

Figure 3.1: Model of a all pass ring resonator

If the evanescent coupling between the guide and the ring is lossless and only single polarization is considered, the interaction can be described by the matrix relation [37]:

$$\begin{pmatrix} E_{t1} \\ E_{t2} \end{pmatrix} = \begin{pmatrix} t & \kappa \\ -\kappa^* & t^* \end{pmatrix} \begin{pmatrix} E_{i1} \\ E_{i2} \end{pmatrix} \tag{3.2}$$

E_{t1}, E_{t2}, E_{i1}, E_{i2} are the complex mode amplitudes in the different parts of the system; since they are normalized, their squared magnitude corresponds to the modal power. The coupler parameters t and κ are unit-less and represent the amount of light transmitted or coupled into the ring.

For a lossless coupler the matrix is unitary, so

$$|\kappa|^2 + |t|^2 = 1 \tag{3.3}$$

In order to simplify the model, we will choose E_{i1} equal to 1 so all the field amplitudes will be normalised to the input wave.
Equation (3.2) and (3.3) are supplemented by the circulation condition of the ring

$$E_{i2} = \alpha \cdot e^{i\theta} E_{t2} \tag{3.4}$$

where α is the loss coefficient of the ring (zero loss means $\alpha = 1$) and $\theta = 2\pi\nu L/v_{ph}$ is the phase shift of the light due to a round trip.
For the sake of clarity:

- $L = 2\pi r$ is the circumference of the ring with r the radius of the ring
- $\alpha = 10^{-\mathcal{A}L/20}$ is the round-trip loss coefficient ($\mathcal{A}$ is the attenuation in dB/m)
- c is the speed of the light in vacuum
- $v_{ph} = c/n_{eff}$ is the phase velocity of the ring mode
- $k = 2\pi/\lambda$ is the vacuum wavenumber
- $\nu = k\,c/2\pi$ is the light frequency
- $\beta = k \cdot n_{eff} = \frac{2\pi \cdot n_{eff}}{\lambda}$ is the propagation constant

With simple steps, it is possible to introduce the effective index n_{eff} into the ring coupling relations by

$$\theta = \frac{2\pi\nu\, L}{v_{ph}} = \frac{k\,c\,L}{v_{ph}} = k \cdot n_{eff} \cdot L = \frac{2\pi\, n_{eff} \cdot L}{\lambda} \tag{3.5}$$

From eq. (3.2) and (3.4), we obtain:

$$\begin{cases} E_{t1} = \dfrac{-\alpha + te^{-i\theta}}{-\alpha t^* + e^{-i\theta}} & (3.6a) \\ E_{i2} = \dfrac{-\alpha\kappa^*}{-\alpha t^* + e^{-i\theta}} & (3.6b) \\ E_{t2} = \dfrac{-\kappa^*}{1 - \alpha t^* e^{i\theta}} & (3.6c) \end{cases}$$

this leads to the output power which is reflected from the ring $\mathcal{R}$

$$\boxed{\mathcal{R} = |E_{t1}|^2 = 1 - \frac{(1-\alpha^2)(1-|t|^2)}{1 + \alpha^2|t|^2 - 2\alpha|t|\cos(\theta - \phi_t)}} \tag{3.7}$$

where $t = |t|e^{i\phi_t}$. (Details in eq. (A.1))
$|t|$ represents the portion of light which is not coupled into the ring and ϕ_t the phase shift of the coupler.
The circulating power $\mathcal{P}$ inside the ring is given by (see eq. (A.2))

$$\boxed{\mathcal{P} = |E_{i2}|^2 = \frac{\alpha^2(1-|t|^2)}{1+\alpha^2|t|^2 - 2\alpha|t|\cos(\theta-\phi_t)}} \tag{3.8}$$

On resonance, $(\theta - \phi_t) = 2\pi m$, where m is an integer, the *through* and the internal ring power result as

$$\mathcal{R}|_{resonance} = \frac{\alpha^2 + |t|^2 - 2\alpha|t|}{1+\alpha^2|t|^2 - 2\alpha|t|} = \frac{(\alpha - |t|)^2}{(1-\alpha|t|)^2} \tag{3.9}$$

$$\mathcal{P}|_{resonance} = \frac{\alpha^2|\kappa|^2}{1+\alpha^2|t|^2 - 2\alpha|t|} = \frac{\alpha^2(1-|t|^2)}{(1-\alpha|t|)^2} \tag{3.10}$$

A special case happens when the internal losses are equal to the coupling efficiency, this means $\alpha = |t|$ which forces to zero the *through* power $\mathcal{R}$. This is known as the critical coupling, which is due to destructive interference between the wave transmitted directly and the wave which had a round trip and is coupled again

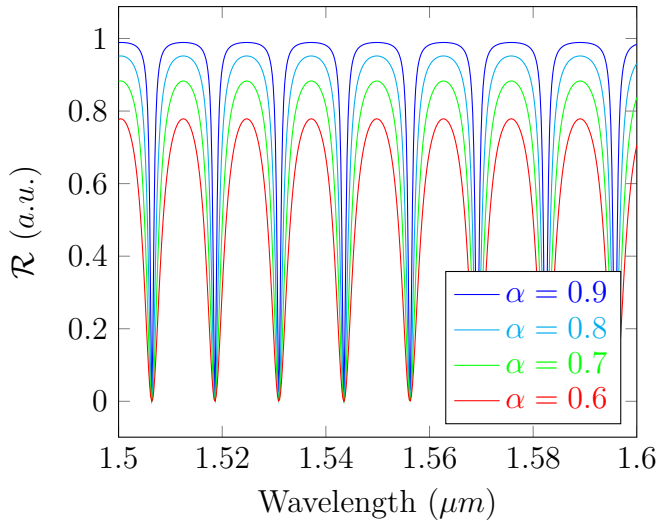

Figure 3.2: Wavelength response of the all pass resonator at critical coupling with $r = 10\,\mu m$ and $n_{eff} = 3$.

From eq. (3.9) and (3.10), we notice that $\mathcal{R}|_{resonance} \ll 1$ and $\mathcal{P}|_{resonance} \gg 1$ when α and $|t|$ tend towards the unity. As we will see better in section 3.3.5, the light power stocked into the ring is proportional to the *finesse* of the optical ring resonator.

3.2 Add-drop resonator

In this configuration, a second waveguide is coupled on the other side of the ring. The four ports of the ring are referred to in the following as *input* port, *through* port, *drop* port and *add* port, as shown in the fig. 3.3:

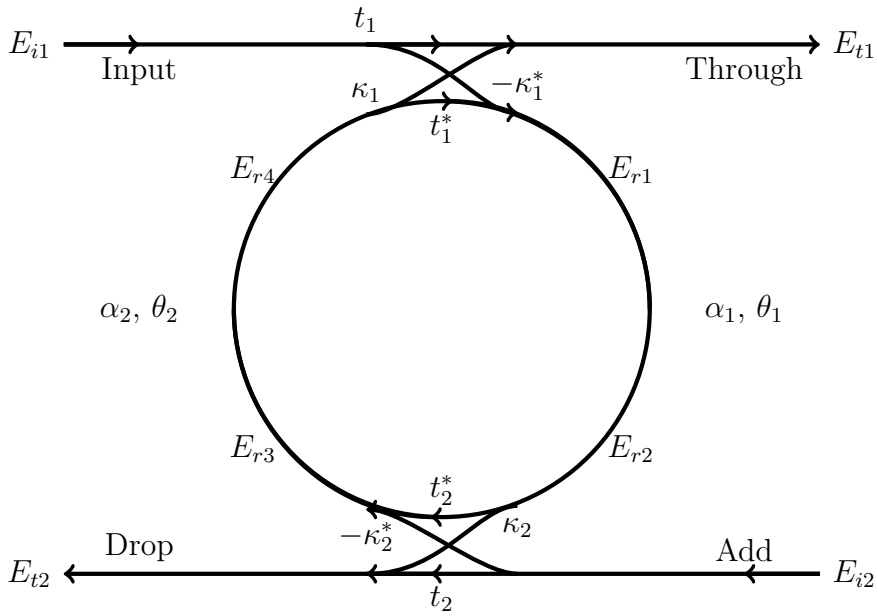

Figure 3.3: Model of a basic add-drop ring resonator

As before, we describe the system by matrix relations

$$\begin{pmatrix} E_{t1} \\ E_{r1} \end{pmatrix} = \begin{pmatrix} t_1 & \kappa_1 \\ -\kappa_1^* & t_1^* \end{pmatrix} \begin{pmatrix} E_{i1} \\ E_{r4} \end{pmatrix} \tag{3.11a}$$

$$\begin{pmatrix} E_{t2} \\ E_{r3} \end{pmatrix} = \begin{pmatrix} t_2 & \kappa_2 \\ -\kappa_2^* & t_2^* \end{pmatrix} \begin{pmatrix} E_{i2} \\ E_{r2} \end{pmatrix} \tag{3.11b}$$

together with the condition of looseless couplers

$$|\kappa_1|^2 + |t_1|^2 = 1 \tag{3.12a}$$

$$|\kappa_2|^2 + |t_2|^2 = 1 \tag{3.12b}$$

and circulation phase shift

$$E_{r2} = \alpha_1 \cdot e^{i\theta_1} E_{r1} \tag{3.13a}$$

$$E_{r4} = \alpha_2 \cdot e^{i\theta_2} E_{r3} \tag{3.13b}$$

$$\alpha = \alpha_1 \cdot \alpha_2 \tag{3.13c}$$

$$\theta = \theta_1 + \theta_2 \tag{3.13d}$$

For the sake of simplicity, E_{i1} is normalised to the unity, and E_{i2} is equal to zero. So we rewrite the two matrix relations in eq. (3.11) in the following system:

$$\begin{cases} E_{t1} = t_1 + \kappa_1 E_{r4} & (3.14a) \\ E_{r1} = -\kappa_1^* + t_1^* E_{r4} & (3.14b) \\ E_{t2} = \kappa_2 E_{r2} & (3.14c) \\ E_{r3} = t_2^* E_{r2} & (3.14d) \end{cases}$$

Applying the conditions eq. (3.13a) and (3.13b), the system evolves in

$$\begin{cases} E_{t1} = \dfrac{t_1 - t_2^* \alpha e^{i\theta}}{1 - t_1^* t_2^* \alpha e^{i\theta}} & (3.15a) \\ E_{r1} = \dfrac{-\kappa_1^*}{1 - t_1^* t_2^* \alpha e^{i\theta}} & (3.15b) \\ E_{t2} = \dfrac{-\kappa_1^* \kappa_2 \alpha_1 e^{i\theta_1}}{1 - t_1^* t_2^* \alpha e^{i\theta}} & (3.15c) \\ E_{r3} = \dfrac{-\kappa_1^* t_2^* \alpha_1 e^{i\theta_1}}{1 - t_1^* t_2^* \alpha e^{i\theta}} & (3.15d) \end{cases}$$

Details of calculation are in appendix A.2.
We obtain the mode amplitude at the *through* and *drop* ports respectively from equations (3.15a) and (3.15c).

Let is now calculate the normalised output power at the *through*:

$$\mathcal{R} = |E_{t1}|^2 = 1 - \frac{(1 - |t_1|^2)(1 - \alpha^2 |t_2|^2)}{1 + \alpha^2 |t_1|^2 |t_2|^2 - 2\alpha |t_1||t_2| \cos(\theta - \phi_{t_1} - \phi_{t_2})} \tag{3.16}$$

where $t_1 = |t_1| e^{i\phi_{t_1}}$ and $t_2 = |t_2| e^{i\phi_{t_2}}$.
Similar steps for $\mathcal{T}$, the normalised power at the *drop* port:

$$\mathcal{T} = |E_{t2}|^2 = \frac{\alpha_1^2 (1 - |t_1|^2)(1 - |t_2|^2)}{1 + \alpha^2 |t_1|^2 |t_2|^2 - 2\alpha |t_1||t_2| \cos(\theta - \phi_{t_1} - \phi_{t_2})} \tag{3.17}$$

From eq. (3.15), we calculate the normalised power stocked into the ring:

$$\mathcal{P} = |E_{r1}|^2 = \frac{|\kappa_1|^2}{1 + \alpha^2 |t_1|^2 |t_2|^2 - 2\alpha |t_1||t_2| \cos(\theta - \phi_{t_1} - \phi_{t_2})} \tag{3.18}$$

For the following chapters, it is more convenient to write $\mathcal{R}$, $\mathcal{T}$ and $\mathcal{P}$ in a better form introducing the power transmission coefficients

$$K_i = |\kappa_i|^2 = 1 - |t_i|^2 \tag{3.19a}$$
$$\Gamma = \alpha^2 \tag{3.19b}$$

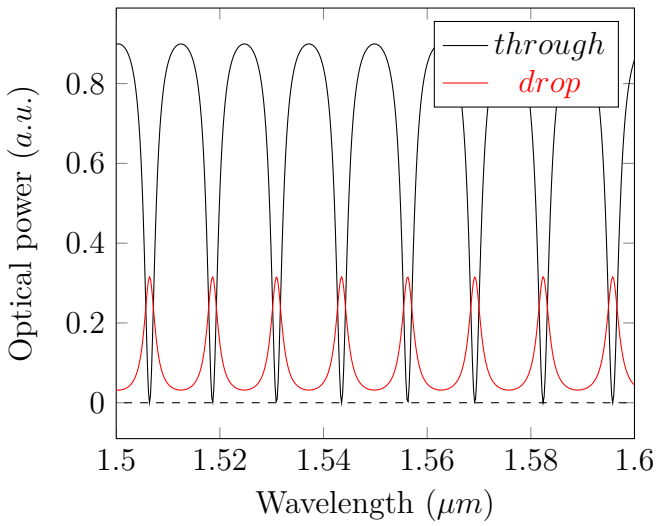

Figure 3.4: Wavelength response of the add-drop resonator at critical coupling with $r = 10\,\mu m$, $n_{eff} = 3$, $\alpha = 0.8$, $t_1 = 0.72$ and $t_2 = 0.9$

the total power amplitude attenuation coefficient

$$Z = \sqrt{(1 - K_1)(1 - K_2)\Gamma} = \alpha |t_1||t_2| \tag{3.20}$$

and the total cavity detuning

$$\varphi = \theta - \phi_{t_1} - \phi_{t_2} \tag{3.21}$$

Rewriting the equations (3.16), (3.17) and (3.18), the normalised powers result

$$\mathcal{R} = 1 - \frac{K_1[1 - (1 - K_2)\Gamma]}{1 + Z^2 - 2Z\cos(\varphi)} \tag{3.22a}$$

$$\mathcal{T} = \frac{K_1 K_2 \sqrt{\Gamma}}{1 + Z^2 - 2Z\cos(\varphi)} \tag{3.22b}$$

$$\mathcal{P} = \frac{K_1}{1 + Z^2 - 2Z\cos(\varphi)} \propto \mathcal{T} \tag{3.22c}$$

The power circulating inside the ring will be proportional to the power at the *drop* port. From here a practical convenience to use the drop port as a probe for the optical power inside the ring.
A small last effort for writing the two output powers in a form similar to the *Airy*

functions (fig. 3.5), remembering that $\cos(\varphi) = 1 - 2\sin^2(\varphi/2)$:

$$\boxed{\begin{aligned} \mathcal{R} &= 1 - \frac{\mathcal{R}_0}{1 + \mathcal{M}\sin^2(\varphi/2)} && (3.23a) \\ \mathcal{T} &= \frac{\mathcal{T}_0}{1 + \mathcal{M}\sin^2(\varphi/2)} && (3.23b) \\ \mathcal{P} &= \frac{\mathcal{P}_0}{1 + \mathcal{M}\sin^2(\varphi/2)} && (3.23c) \end{aligned}}$$

with $\mathcal{R}_0$, $\mathcal{T}_0$, $\mathcal{P}_0$ and $\mathcal{M}$ defined as

$$\begin{cases} \mathcal{R}_0 = \dfrac{K_1[1 - (1 - K_2)\Gamma]}{(1 - Z)^2} & (3.24a) \\ \mathcal{T}_0 = \dfrac{K_1 K_2 \sqrt{\Gamma}}{(1 - Z)^2} & (3.24b) \\ \mathcal{P}_0 = \dfrac{K_1}{(1 - Z)^2} & (3.24c) \\ \mathcal{M} = \dfrac{4Z}{(1 - Z)^2} & (3.24d) \end{cases}$$

On resonance ($\varphi = 2m\pi$), the *drop* output power achieves the maximum whereas the through output power is minimum

$$\mathcal{R}_{min} = 1 - \mathcal{R}_0 \tag{3.25a}$$
$$\mathcal{T}_{max} = \mathcal{T}_0 \tag{3.25b}$$
$$\mathcal{P}_{max} = \mathcal{P}_0 \tag{3.25c}$$

from eq. (3.25a), in a lossless ring ($\Gamma = 1$) the *through* port will be zero only for symmetrical coupling $K_1 = K_2$. For a realistic ring ($\Gamma < 1$), the possibility to achieve complete filtering ($\mathcal{R}_{min} = 0$) is obtained only adjusting the coupling parameters as follows

$$\Gamma = \frac{1 - K_1}{1 - K_2} \tag{3.26}$$

Conversely, on the anti-resonance $\varphi = (2m + 1)\pi$, we have

$$\mathcal{R}_{max} = 1 - \frac{\mathcal{R}_0}{1 + \mathcal{M}} \tag{3.27a}$$
$$\mathcal{T}_{min} = \frac{\mathcal{T}_0}{1 + \mathcal{M}} \tag{3.27b}$$
$$\mathcal{P}_{min} = \frac{\mathcal{P}_0}{1 + \mathcal{M}} \tag{3.27c}$$

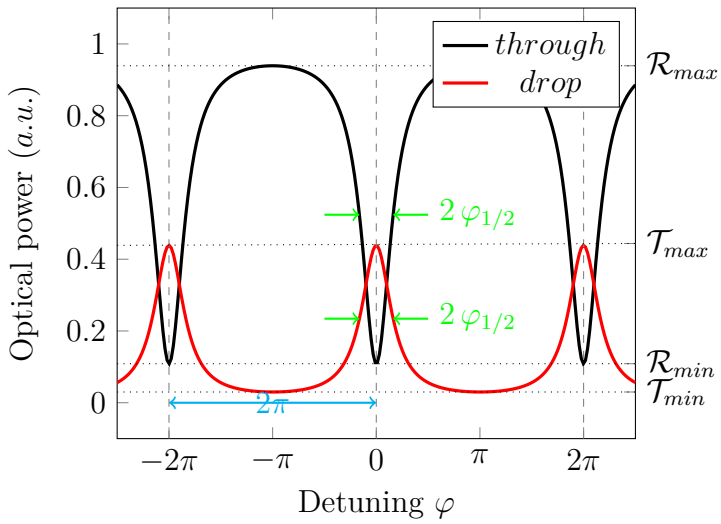

Figure 3.5: Response of the add drop resonator with $\Gamma = 0.7$, $K_1 = K_2 = 0.3$

3.3 Spectral characteristics

In this section we link the parameters K_1, K_2 and Γ to some spectral properties like the optical quality factor Q, the free spectral range FSR, the finesse $\mathcal{F}$ and the contrast C. These are much more intuitive and more accessible from the experimental curves.

3.3.1 The Free Spectral Range

The distance between two subsequent resonance peaks is called the *free spectral range* (FSR). Bearing in mind the resonance condition in eq. (3.1),

$$\varphi_m = \frac{2\pi}{\lambda_m} n_{eff} L = \beta_m L = 2\pi m \tag{3.28}$$

a simple evaluation of FSR can be obtained approximating β at the first order:

$$\beta_{m-1} = \frac{2(m-1)\pi}{L} = \beta_m - \frac{2\pi}{L} \approx \beta_m + \left.\frac{\partial \beta}{\partial \lambda}\right|_m \Delta\lambda \tag{3.29}$$

$$\Rightarrow FSR_\lambda = \Delta\lambda = -\frac{2\pi}{L}\left(\left.\frac{\partial \beta}{\partial \lambda}\right|_m\right)^{-1} \tag{3.30}$$

If now we calculate $\dfrac{\partial \beta}{\partial \lambda}$ as follows,

$$\frac{\partial \beta}{\partial \lambda} = -\frac{2\pi\, n_{eff}}{\lambda^2} + \frac{2\pi}{\lambda}\frac{\partial n_{eff}}{\partial \lambda} = -\frac{\beta}{\lambda} + k\frac{\partial n_{eff}}{\partial \lambda} \tag{3.31}$$

$$\frac{\partial \beta}{\partial \lambda} = -\frac{k}{\lambda}\left(\frac{\beta}{k} - \lambda\frac{\partial n_{eff}}{\partial \lambda}\right) = -\frac{k}{\lambda}\left(n_{eff} - \lambda\frac{\partial n_{eff}}{\partial \lambda}\right) = -\frac{k}{\lambda}n_g \tag{3.32}$$

the *free spectral range* results as:

$$\boxed{\begin{aligned} FSR_\lambda &= \frac{\lambda^2}{n_g L} \qquad (3.33a) \\ FSR_\nu &= \frac{c}{n_g L} \qquad (3.33b) \end{aligned}}$$

where n_g is the group refractive index.

3.3.2 The Finesse

An important parameter is the *finesse* $\mathcal{F}$ which identifies how much the cavity is selective. The finesse is defined as the separation of two consecutive peaks (FSR) over the full width at half maximum of the peak ($\delta\lambda$):

$$\mathcal{F} = \frac{FSR_\lambda}{\delta\lambda} = \frac{FSR}{FWHM} \tag{3.34}$$

Equivalently, in the phase domain, the *finesse* is

$$\mathcal{F} = \frac{2\pi}{2\,\varphi_{1/2}} = \frac{\pi}{\varphi_{1/2}} \tag{3.35}$$

Using the expressions (3.23b), (3.25b) and (3.27b) for the *drop* port, we impose:

$$\mathcal{T}(\varphi_{1/2}) = \frac{\mathcal{T}_{max} + \mathcal{T}_{min}}{2} \tag{3.36}$$

and we obtain

$$\frac{1}{1 + \mathcal{M}\sin^2\left(\frac{\varphi_{1/2}}{2}\right)} = \frac{2 + \mathcal{M}}{2(1 + \mathcal{M})} \tag{3.37}$$

$$\sin^2\left(\frac{\varphi_{1/2}}{2}\right) = \frac{1}{2 + \mathcal{M}} \tag{3.38}$$

thanks to the trigonometric relation $\tan^2 x = \sin^2 x/(1 - \sin^2 x)$

$$\tan^2\left(\frac{\varphi_{1/2}}{2}\right) = \frac{\sin^2\left(\frac{\varphi_{1/2}}{2}\right)}{1 - \sin^2\left(\frac{\varphi_{1/2}}{2}\right)} = \frac{1}{1 + \mathcal{M}} \tag{3.39}$$

from equation (3.24d) it is also true that

$$\frac{1}{1+\mathcal{M}} = \left(\frac{1-Z}{1+Z}\right)^2 \tag{3.40}$$

so finally

$$\boxed{\mathcal{F} = \frac{\pi}{2\arctan\left(\frac{1-Z}{1+Z}\right)}} \tag{3.41}$$

3.3.3 The quality factor

As in other fields of physics, the optical *quality factor* is defined as the ratio between the resonance frequency and the full width at half maximum:

$$Q_{opt} = \frac{\nu_r}{\delta\nu} = \frac{\lambda_r}{\delta\lambda} \tag{3.42}$$

From equation (3.33a), (3.34) and (3.41), we obtain

$$\Rightarrow \boxed{Q_{opt} = \frac{\lambda_r}{FSR_\lambda}\mathcal{F} = \frac{n_g L}{\lambda_r}\frac{\pi}{2\arctan\left(\frac{1-Z}{1+Z}\right)}} \tag{3.43}$$

3.3.4 The contrast

Differently from the *finesse*, the *contrast* may differ for the *drop* and *through* ports. It is defined as

$$C_{\mathcal{R}} = \frac{\mathcal{R}_{max} - \mathcal{R}_{min}}{\mathcal{R}_{max}} \tag{3.44a}$$

$$C_{\mathcal{T}} = \frac{\mathcal{T}_{max} - \mathcal{T}_{min}}{\mathcal{R}_{max}} \tag{3.44b}$$

and, thanks to the equations (3.25) and (3.27), it becomes

$$C_{\mathcal{R}} = \frac{\mathcal{M}\mathcal{R}_0}{1+\mathcal{M}-\mathcal{R}_0} \tag{3.45a}$$

$$C_{\mathcal{T}} = \frac{\mathcal{M}\mathcal{T}_0}{1+\mathcal{M}-\mathcal{R}_0} \tag{3.45b}$$

3.3.5 Small ring losses and weak symmetrical coupling

In the very practical case of small ring looses ($\Gamma \simeq 1$) and symmetrical weak coupling ($K_1 = K_2 \ll 1$), $\mathcal{R}_{max}$ and $\mathcal{T}_{min}$ can be approximated as

$$\mathcal{R}_{max} \simeq 1 - \frac{K^2}{4} \simeq 1 \tag{3.46}$$

$$\mathcal{T}_{min} \simeq \frac{K^2}{4} \ll 1 \tag{3.47}$$

so, out of resonance, the *through* power is almost equal to the *input* power, while almost no light comes out from the *drop* port.
On resonance instead:

$$\mathcal{R}_{min} \simeq 0 \tag{3.48}$$

$$\mathcal{T}_{max} \simeq 1 \tag{3.49}$$

This means that the contrast is 100% for both output.
Under these conditions, the finesse is well approximated by

$$\mathcal{F} \simeq \pi/K \tag{3.50}$$

whereas on resonance the normalised power inside the ring is

$$\mathcal{P}_0 \simeq 1/K = \frac{\mathcal{F}}{\pi} \tag{3.51}$$

on resonance, the power circulating around the ring is proportional to the *finesse*.
Injecting a *input* power equal to P_{laser}, the power into the ring will results

$$P_{ring} = P_{laser} \cdot \mathcal{P}_0 \simeq P_{laser} \cdot \frac{\mathcal{F}}{\pi} \tag{3.52}$$

where P_{laser} is easily accessible from a measurement of the *through* port when the laser is out of resonance since $\mathcal{R}_{max} \simeq 1$.
The plot in fig. 3.6 shows the trend for *through* and *drop* power. As expected, the peaks are very thin and the contrast is almost 100%.

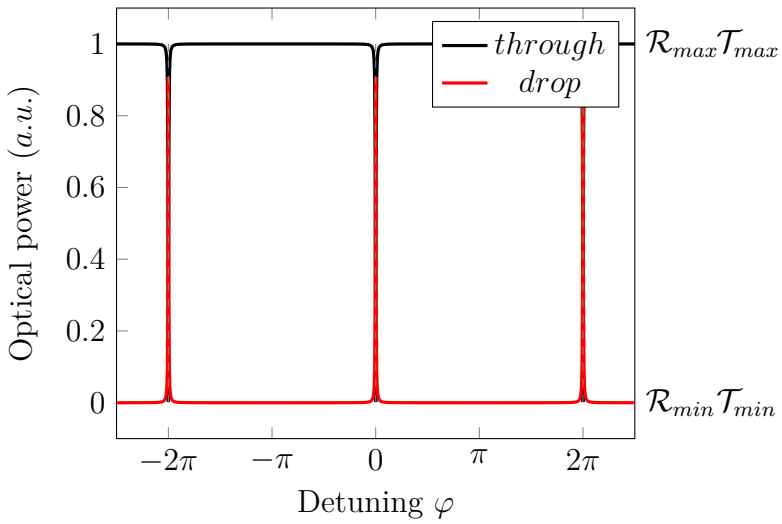

Figure 3.6: Response of the add-drop resonator for weak symmetrical coupling and small losses. (Here $\Gamma = 0.999$ and $K_1 = K_2 = 0.01$)

3.4 $C \cdot Q$ improvement

As we will see in chapter 4, the optomechanical transduction responsivity is proportional to the slope of the optical resonance peak. To improve it, we will look for a set of K and Γ parameters which maximize the $C \cdot Q$ value.
Considering an *add-drop* resonator with symmetrical coupling ($K = K_1 = K_2$), we generate in fig. 3.7 the cartography for $C \cdot Q$ values from equations (3.43) and (3.45). At first sight, the best choice is a coupling efficiency weaker than 0.2% together with ring losses lower than $2\,dB/cm$. The darker spot in fig. 3.7 shows the performances of the experimental devices in section 5.2: there is a good room for improvement with a correct tuning of the parameters K and Γ. In particularly, having a ring with linear losses smaller than $3\,dB/cm$, a modest reduction of the coupling efficiency impacts remarkably the $C \cdot Q$ value.
The tuning of the coupling efficiency is obtained by the waveguide-ring gap and by the coupling area. The optical indexes of the ring, of the gap medium and of the waveguide play as well an important role. Regarding the losses, the fabrication has to guarantee low ring losses reducing the light absorption and the light scattering. To do that, we have to play on the purity of the material and on the roughness side of the ring (see section 5.7.2). The curvature losses are often negligible for ring radius bigger than $5\,\mu m$ but the curvature tends to increase the losses due to the diffusion [38].
This evaluation fixes the upper limit for the $C \cdot Q$: the coupling of a mechanical element (e.g. *NEMS* cantilever) may cause a significant degradation of the optical

Q-factor.

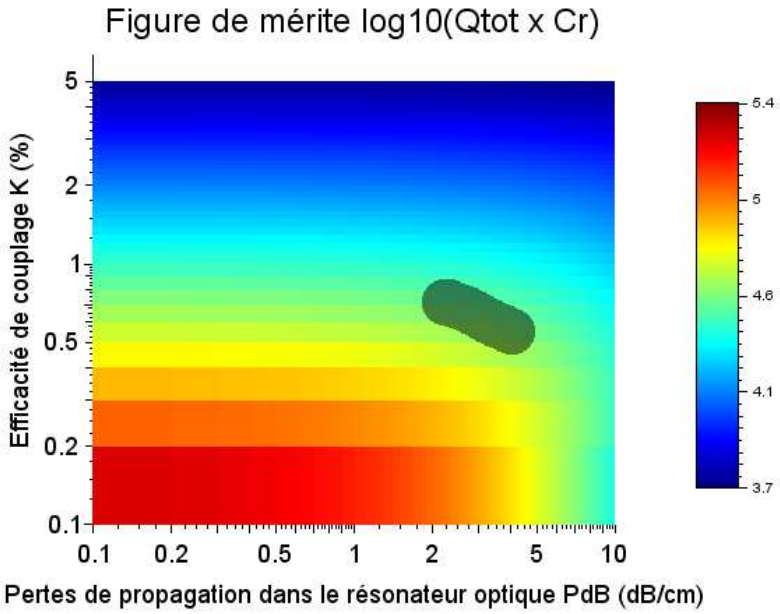

Figure 3.7: Cartography for $C \cdot Q$ values as function of coupling $K = K_1 = K_2$ and linear ring losses. The darker spot shows the performances of the experimental devices in section 5.2. Courtesy of Geoffroy Scherrer.

3.5 Conclusions

From this chapter, we have to retain that the ring resonator is a wavelength filter whose spectrum is a series of peaks. The peaks shape (spacing, width, amplitude) depends on the ring geometry (radius, optic gap, waveguides) and on the optical properties (n_{eff}, Γ). In the near future, all these parameters have to be optimised to get the best peak slope.

The optical resonator concentrates the optical energy inside the cavity in which the injected power is amplified by the *finesse* factor. Since, on average, a photon travels around the ring $\mathcal{F}$ times, the effect of an external perturbation is multiplied as well by the same factor. That is why, compared to simple a waveguide, the optical resonator is extremely sensitive to a light phase shift which is caused, for example, by the presence of an external object.
In the following chapter, we observe how the ring spectrum is modified by external perturbations, focusing on *NEMS* readout application.

Chapter 4

Optomechanical theory

The propagation of the light in a waveguide is affected by the perturbations from the external environment. The light path changes for a waveguide bending whereas the phase velocity and the optical losses of the light change with the evanescent coupling of an external object such as a second waveguide, a cantilever or a sticking particle.
We call *dispersive* a coupling mechanism which introduces only a phase delay of the light and does not affect the light power transmission. This phase delay arises from a local perturbation of the light phase velocity or from a light path modification due, for example, to a mechanical bending of the waveguide. A *dissipative* coupling, instead, impacts also the transmission of the light introducing supplementary waveguide losses.
As already discussed, the optical resonator amplifies the effects of the external perturbations because the phase delay and the absorption of the light accumulate for each roundtrip of the light into the ring.

From the resonance condition of the optical ring in eq. (3.1), the resonance position is modified by varying L, the circumference of the resonator, or varying n_{eff}, the average effective index of the ring.
The circumference of the resonator is simply perturbed by a mechanical deformation of the ring, such as the breath mode vibration of a released disk [5][39].
The effective index of the ring, instead, changes for different reasons: when the resonator is subject to a temperature variation [40] or when the intrinsic carrier concentration is altered [41]. Moreover, an object coupled to the evanescent wave of the ring modifies the effective index of the ring within the coupling area. Functionalised ring changes locally its effective index due to an interaction with biological particles like virus [42] or proteins [43].
Another perturbation mechanism origins from the bus waveguides: if the coupling waveguide moves away or close to the ring resonator, the coupler parameters t and

κ in eq. (3.2) or (3.11) change together with the coupling gap. In the hypothesis of dispersive coupling, the parameter t conserves the modulus $|t| \simeq |t'|$ whereas the coupler phase shift is modified from $\phi_t \to \phi'_t$. The hypothesis of dispersive coupling is reasonable for a small waveguide displacement.

The influence of above-listed perturbations is resumed by the parameter φ, the total detuning of the ring (see eq. (3.21))

$$\varphi = \theta - \phi_{t_1} - \phi_{t_2} = \frac{2\pi\, n_{eff}\, L}{\lambda} - \phi_{t_1} - \phi_{t_2} \tag{4.1}$$

Being φ the variable of the *Airy* equations in eq. (3.23), the spectral response of the ring is simply shifted proportionally to any variation of L, n_{eff}, ϕ_{t_i} or a combination of them.

4.1 Optomechanical coupling

Given the topics of this thesis, we applied the above considerations to a *NEMS* which interacts with a ring resonator by the means of dispersive coupling. In our case, the on-chip waveguides are fixed to the substrate which means that L and ϕ_{t_i} are constant. Placing a *NEMS* within the evanescent field of the ring, we modify locally its effective index and, as consequence, the light phase velocity is perturbed. The phase shift of the light per round trip now depends on the *NEMS* position x:

$$\theta(x) = \int_0^L \beta\, dl = \frac{2\pi\,\nu}{c} \int_0^L [n_{eff} + \Delta n_{eff}(x,l)]\, dl = \theta + \frac{2\pi\,\nu}{c} \int_0^L \Delta n_{eff}(x,l)\, dl \tag{4.2}$$

where Δn_{eff} is the local variation of the effective index at position l which is the variable along the ring circumference L. For the specific case of a cantilever displacement detection, the integral will be non-null only inside the coupling area.
The variation of the effective index induces a supplementary phase delay due to the optomechanical coupling

$$\boxed{\phi_{om}(x) = -\frac{2\pi\,\nu}{c} \int_0^L \Delta n_{eff}(x,l)\, dl} \tag{4.3}$$

so, the total detuning of the ring φ which is the argument of the sinus inside the *Airy* functions becomes

$$\varphi(x) = \frac{2\pi\, n_{eff}\, L}{c}\nu - \phi_{t_1} - \phi_{t_2} - \phi_{om}(x) \tag{4.4}$$

As final consequence of the ring detuning due to *NEMS* displacement, the optical spectrum of the ring, which is described by the *Airy* functions, shifts proportionally to ϕ_{om} (see fig. 4.1).

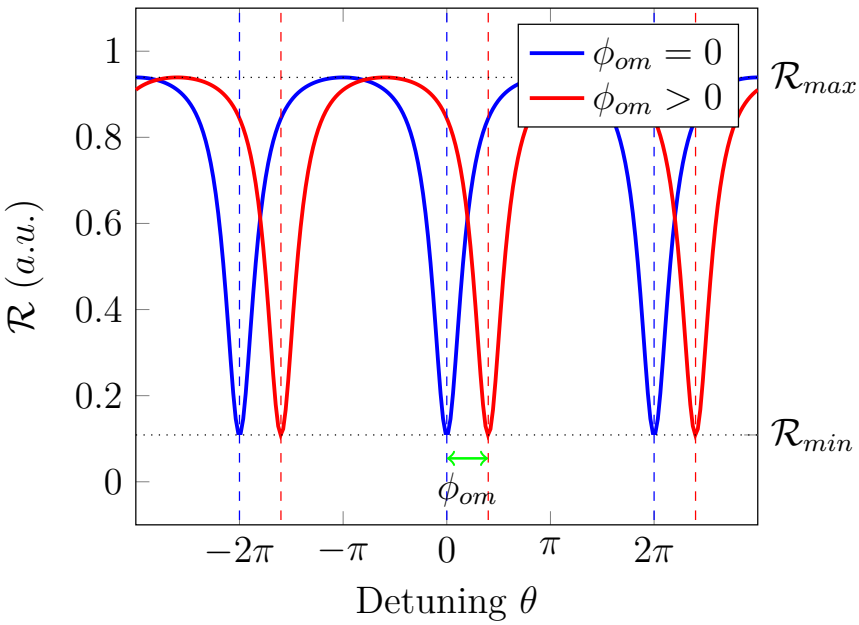

Figure 4.1: Shift of the *through* response to an additional phase delay due to a *NEMS* displacement. For graphical reason, the value of ϕ_{om} is over boosted. ($\Gamma = 0.7$, $K_1 = K_2 = 0.3$)

Making the differential of equation (4.4) for a small cantilever displacement, we find:

$$\frac{d\phi_{om}}{dx} = \frac{2\pi\, n_{eff}\, L}{c}\frac{d\nu}{dx} = \frac{n_{eff}\, L}{c} g_{om} \tag{4.5}$$

where g_{om} is named as the **optomechanical coupling factor**

$$\boxed{g_{om} = 2\pi \frac{d\nu}{dx}} \tag{4.6}$$

which defines the light angular frequency shift of the spectrum for a unity of cantilever displacement. Over large cantilever displacement, g_{om} is not linear at all since the phase shift ϕ_{om} depends strongly on superposition of the evanescent wave tails.

In the specific case of the in-plane cantilever coupled to the ring resonator, we can model the optomechanical coupling in a more intuitive way: the cantilever acts exactly like a third bus waveguide which has a weak coupling modulus $|t_{om}| \simeq 1$ and coupler phase shift $\phi_{om}(x)$ which depends on the beam position x.

For the sake of more intuitive approaches, we represent the optomechanical coupling in the frequency domain. From fig. 4.2, we see that the unperturbed ring

spectrum (in blue) is shifted to a new spectrum (in red) by the effect of cantilever approach. This shift is proportional to the optomechanical coupling factor g_{om}, and the new resonance frequency is

$$\nu_r^\star = \nu_r + d\nu = \nu + \frac{g_{om}}{2\pi}\, dx \tag{4.7}$$

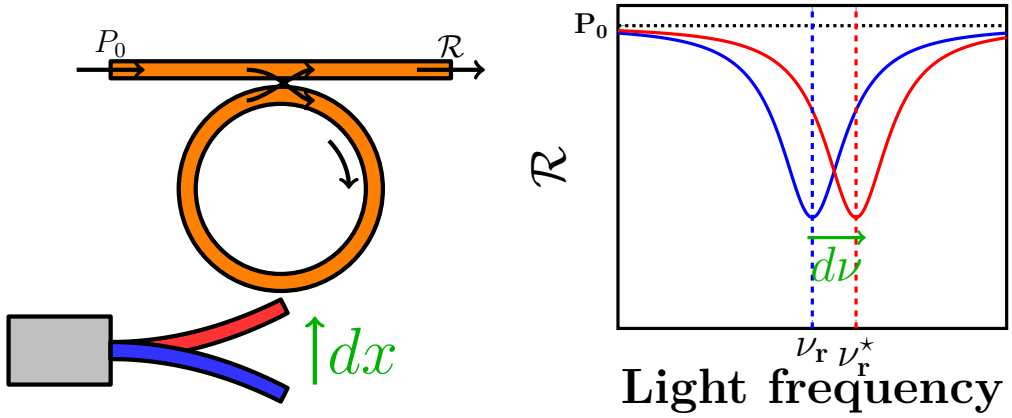

Figure 4.2: The in-plane cantilever oscillates in the evanescent field of the ring. The spectrum shifts from blue to red curve because of the cantilever displacement.

For a membrane placed over the optical resonator, the model has to be modified: as before, the membrane acts as a layer having a different optical index which modifies the effective index of the ring and induces a ring detuning. With a membrane covering the entire ring, the coupling surface is important, so the portion of the light coupled into the membrane could not be negligible anymore. As results of a dissipative coupling, the *Airy* function does not shift rigidly, but the peaks width and the contrast are modified as well. A more complicated interpretation is demanded.

4.2 Optomechanical factor simulation

We roughly evaluate the optomechanical coupling factor g_{om} by the means of a two-dimensional numerical simulation. Thanks to the software *RSOFT-Fullwave*, we can simulate the optical spectrum of a *add-drop* ring resonator.
The geometry of the simulation is identical to the devices which will be described in section 5.4.1 and successively characterised in chapter 7: a ring resonator with radius $R = 5\,\mu m$ is coupled to the *add* and *drop* waveguides with a optical gap of $200\,nm$. Close to the ring, we also added a cantilever having a optomechanical gap of $200\,nm$. The 2D-approximation is based on effective indexes calculated formerly

taking into account the silicon substrate and air superstrate.
Afterwards, we run different simulations tuning the optomechanical gap from 195 nm to 205 nm. The results are resumed in fig. 4.3.

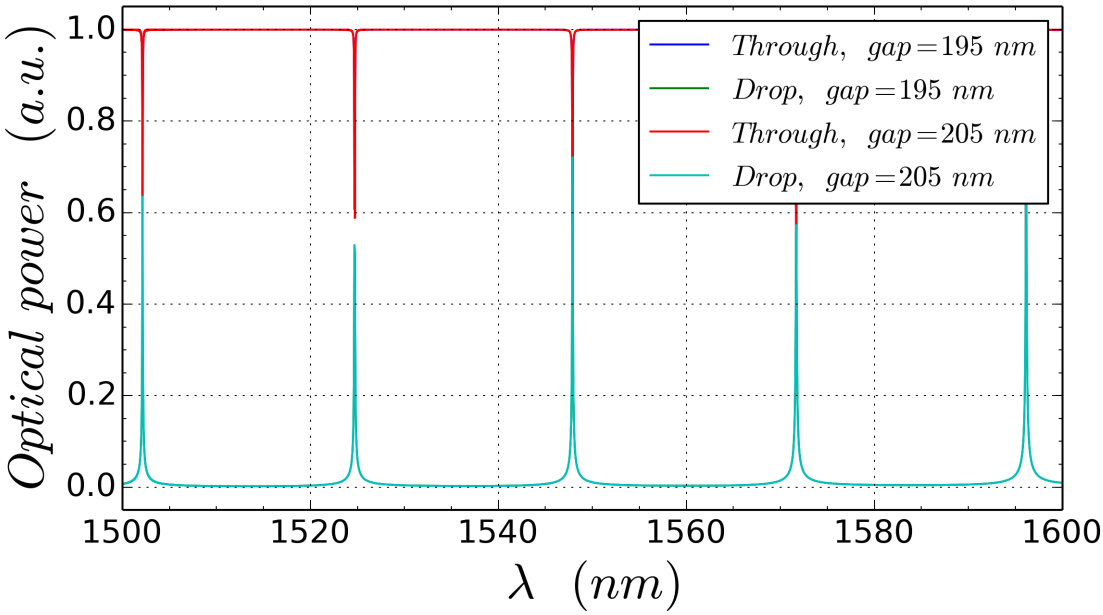

Figure 4.3: Optical spectra of the ring obtained from *RSOFT* simulation. Two simulations are performed: the gap between the cantilever passes from 195 nm to 205 nm.

Zooming on a single resonance peak (fig. 4.4), we clearly observe the wavelength shift that we described in section 4.1: for the *through* spectrum, the resonance wavelength passes from $\lambda_1 = 1547.8845$ to $\lambda_2 = 1547.8810\,nm$.
Neglecting for the moment the weak spectrum deformation, the frequency shift is equal to

$$\Delta\nu = \frac{c}{\lambda_2} - \frac{c}{\lambda_1} = \frac{2.99792458 \cdot 10^8\, m/s}{1547.8810 \cdot 10^{-9}\, m} - \frac{2.99792458 \cdot 10^8\, m/s}{1547.8845 \cdot 10^{-9}\, m} \simeq 0.43794\, GHz \tag{4.8}$$

Being the cantilever displacement equal to 10 nm, we estimate the optomechanical coupling factor as follows

$$\boxed{g_{om} = 2\pi \frac{\Delta\nu}{\Delta x} = 2\pi \frac{0.43794\, GHz}{10\, nm} \simeq 0.2752\, \frac{\text{Grad}}{s \cdot nm}} \tag{4.9}$$

Although the 2D-simulation has intrinsic limits, we find a value for g_{om} which is compatible with the experimental evaluation shown in section 7.3.5.

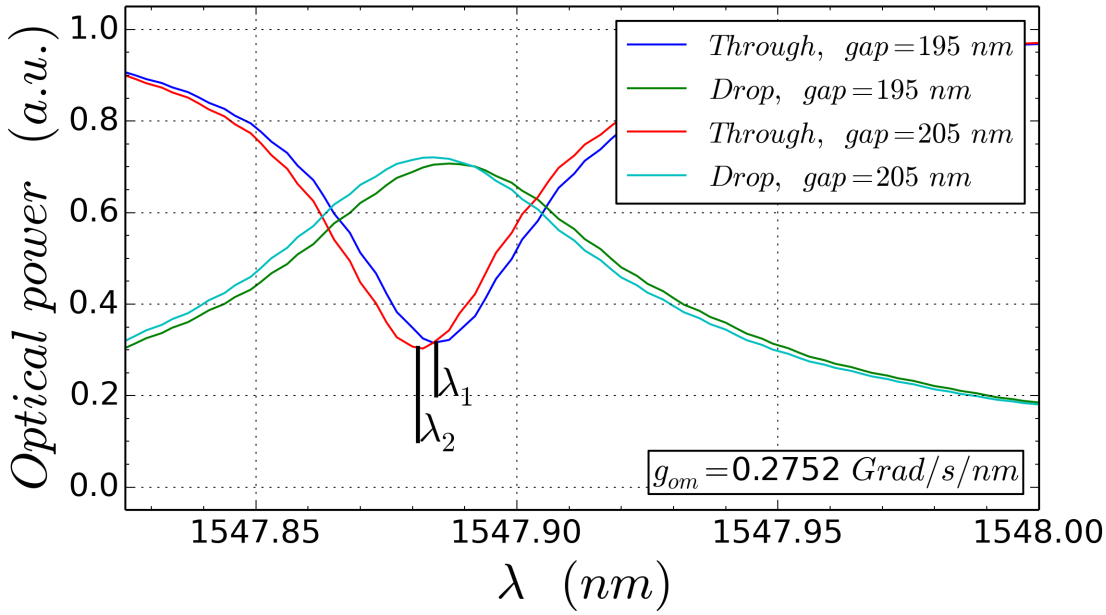

Figure 4.4: Zoom on a resonance peak of fig. 4.3: the optical spectrum shifts because of cantilever movement. The shift is not completely rigid already for a cantilever oscillation amplitude of $10\,nm$.

With a oscillation amplitude of only $5\,nm$, the cantilever approach shifts the two spectra together with a weak deformation: we are already at the limit of the hypothesis of small cantilever displacement. The cantilever modifies not only the phase of the light into the ring but also the amplitude. Although the peak amplitude changes slightly, here the optomechanical coupling is not completely dispersive but partially dissipative. This is a source of non-linearity in the transduction which is investigated in section 7.3.6 and 7.3.7.

This section is the result of a close collaboration with Geoffroy Scherrer and Boris Taurel who respectively wrote the code and ran the simulations. Further details in [44].

4.3 Optomechanical transduction

Once being known that the ring optical spectrum shifts proportionally to the cantilever displacement, we make use of this phenomenon to perform the optomechanichal transduction.
Tuning a laser on a resonance peak side, the output power is modulated by the cantilever oscillation. The mechanical displacement will be amplified by the local slope

of the optical peak (see fig. 4.5). The output optical signal will have an alternating component at the cantilever oscillation frequency over a continuous component.

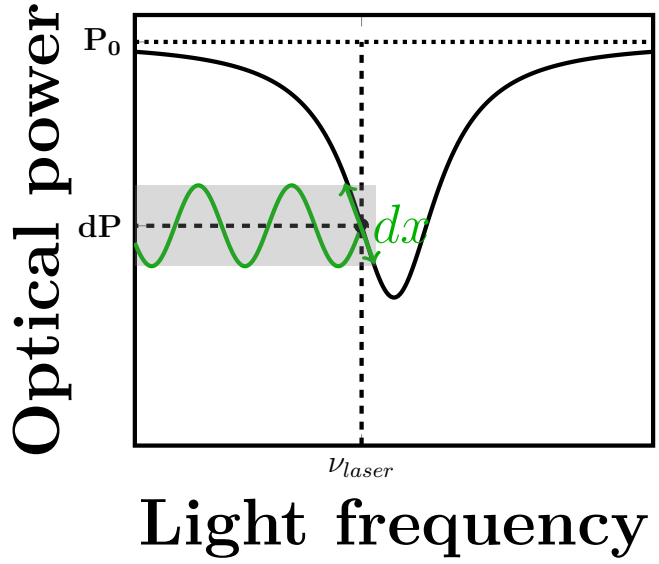

Figure 4.5: The optomechanical transduction concept: the laser which is tuned on the peak side is modulated by the cavity shift. If the shift is proportional to the cantilever displacement, the light modulation is a image of the cantilever oscillation.

Although the optical spectrum is described by the *Airy* function in eq. (3.23), we can approximate locally a single optical resonance peak with a *Lorentzian* function. Doing that, it is easier to estimate the order of magnitude of the signal that we expect from the optomechanical transduction.
We therefore model the optical response of the device as negative *Lorentzian* peak centred at ν_r and having a $FWHM = 2\gamma = \nu_r/Q_{opt}$ (see fig. 4.6). Let $C_{\mathcal{R}}$ be contrast and P_0 be the out-of-resonance light power, the peak amplitude is equal to $P_0\, C_{\mathcal{R}}$:

$$\mathcal{L}(\nu) = P_0 \left(1 - \frac{C_{\mathcal{R}}\gamma^2}{(\nu - \nu_r)^2 + \gamma^2}\right) \tag{4.10}$$

with the derivation at first and second order, we find for which frequency the response has the maximum slope and the best linearity:

$$\mathcal{L}'(\nu) = 2P_0 C_{\mathcal{R}}\gamma^2 \frac{(\nu - \nu_r)}{[(\nu - \nu_r)^2 + \gamma^2]^2} \tag{4.11}$$

$$\mathcal{L}''(\nu) = -2P_0 C_{\mathcal{R}}\gamma^2 \frac{3(\nu - \nu_r)^2 - \gamma^2}{[(\nu - \nu_r)^2 + \gamma^2]^3} \tag{4.12}$$

Since $\mathcal{L}''(\nu) = 0$ at $\nu^\star = \nu_r \pm \frac{\sqrt{3}}{3}\gamma$, we evaluate $\mathcal{L}$ and $\mathcal{L}'$ at this point:

$$\mathcal{L}'(\nu = \nu_r \pm \frac{\sqrt{3}}{3}\gamma) = \pm\frac{3\sqrt{3}}{8}\frac{P_0 C_\mathcal{R}}{\gamma} \tag{4.13}$$

$$\mathcal{L}(\nu = \nu_r \pm \frac{\sqrt{3}}{3}\gamma) = P_0\left(1 - \frac{3}{4}C_\mathcal{R}\right) \tag{4.14}$$

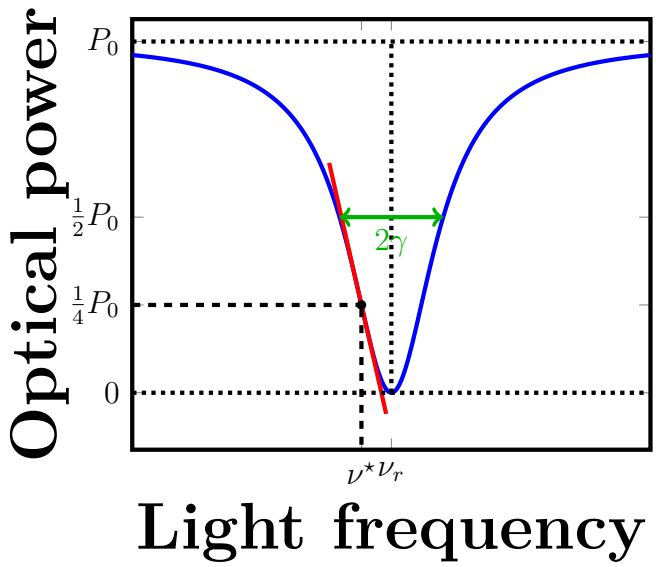

Figure 4.6: Lorentzian peak approximation for the optical resonator. The red line is a linear approximation for the peak slope around $\nu^\star = \nu_r - \frac{\sqrt{3}}{3}\gamma$. (For the sake of simplicity, $C_\mathcal{R} = 1$.)

For a small frequency shift $\Delta\nu \ll \gamma$ due to the mechanical coupling, it is possible to apply a linear approximation around $\nu^\star$. According to eq. (4.13), the output light power is modulated at the mechanical frequency of the cantilever with an amplitude

$$\Delta P = \mathcal{L}'(\nu^\star) \cdot \Delta\nu = \frac{3\sqrt{3}}{8}\frac{P_0 C_\mathcal{R}}{\gamma} \cdot \Delta\nu \tag{4.15}$$

If the system has a optomechanical coupling factor $g_{om} = \frac{d\omega}{dx} = 2\pi\frac{d\nu}{dx}$, we write the output power modulation as function of the cantilever displacement Δx

$$\boxed{\Delta P = \frac{3\sqrt{3}}{4}\frac{P_0 C_\mathcal{R} Q_{opt}}{\nu_r} \cdot \Delta\nu = \frac{3\sqrt{3}}{4}\frac{P_0 C_\mathcal{R} Q_{opt}}{\nu_r} \cdot \frac{g_{om}}{2\pi} \cdot \Delta x} \tag{4.16}$$

This formula is valid for small cantilever displacement $\Delta x \ll \gamma / g_{om}$.
A graphical representation for the light power modulation in the time domain is provided in fig. 4.7: the output signal at the *through* port has a continuous component plus a modulation which occurs at frequency ω_m, the mechanical oscillation frequency of the cantilever. The amplitude of this modulation is ΔP from eq. (4.16).

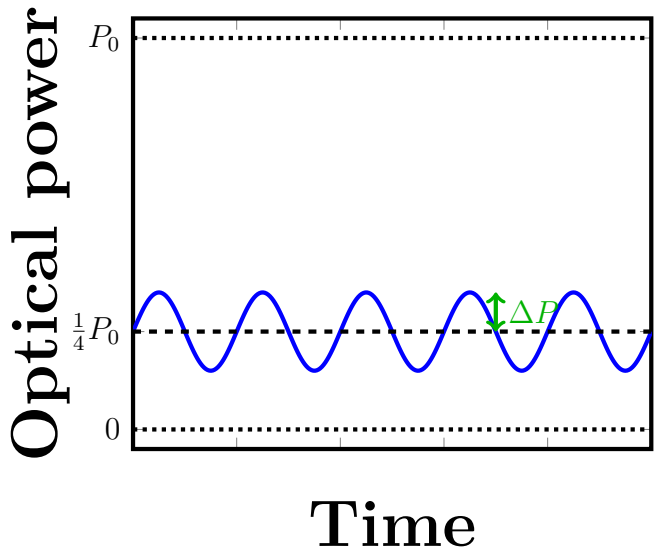

Figure 4.7: Output signal from the device: displacement signal at ω_m over a continuous component. $P_{out} = 1/4P_0 + \Delta P \cos(\omega_m t)$ (For the sake of simplicity, $C_{\mathcal{R}} = 1$.)

It is evident from eq. (4.16), that the transduction responsivity is proportional to the input power P_0 and to the product $Q_{opt} \cdot C_{\mathcal{R}}$. Maybe less intuitive, it is the dynamic range of transduction which is proportional Q_{opt}. In fact, for a very narrow optical peak, the linear approximation around ν^* is not valid any more as the cantilever moves at wide amplitudes.
By the virtue of photonic signals, the optomechanical transduction is not affected by electromagnetic interferences or parasitic capacitances which limit the transduction bandwidth. However the *Airy* functions properly describe the optical spectrum only if the ring resonator is in the steady state, therefore the bandwidth of the transduction is limited by the inverse of the time response of the optical resonator. This detection scheme remains valid for mechanical frequencies $\omega_m \ll \frac{\nu_r}{Q_{opt}}$. In this work, the transduction bandwidth is limited experimentally by photodetector bandwidth.

To give an idea of the orders of magnitude, we introduce some numbers from the experience:

- with a $P_{laser} = 1mW$, we obtain usually a $P_0 C_{\mathcal{R}} \simeq 15\,\mu W$
- $Q_{opt} \simeq 10000$
- $Q_m \simeq 8000$
- $\lambda_r = 1550\,nm \Rightarrow \nu_r = 192\,THz$ optical resonance frequency ($\nu = c/\lambda$)
- $\gamma_{opt} = \nu_r/2Q_{opt} = 9.6 \cdot 10^9 Hz$ is the HWHM
- $\dfrac{g_{om}}{2\pi} = \dfrac{d\nu}{dx} = 0.1\,GHz/nm$ is the optomechanical coupling factor. [45][7][4]
- $X(\omega) = 0.1 fm/\sqrt{Hz}$ is the sensitivity that we want to achieve
- $M_n = \alpha_n \cdot M \simeq 0.25 \cdot 1\,pg = 0.25 \cdot 10^{-15}\,kg$ is the modal mass of the cantilever
- $f_m = \omega_m/2\pi \sim$ 1-100 MHz is the mechanical resonance frequency of the cantilever
- $X_{th}(\omega) = \sqrt{\frac{4k_b T Q_m}{M_n \omega_m^3}} = \sqrt{\frac{4 \cdot 4.11 \cdot 10^{-21} \cdot 8000}{0.25 \cdot 10^{-15} \cdot (2\pi \cdot 10^8)^3}} \simeq 46\,fm/\sqrt{Hz}$ is the thermomechanical motion of the cantilever tip at room temperature (see section 6.5.2)

We then compute the light power variation induced by the signal and by the thermomechanical noise: according to the above values, the light power variation at the *through* port for a cantilever displacement $X(\omega)$ is equal to

$$\delta P(\omega) = \frac{3\sqrt{3}}{8} \frac{P_0 C_{\mathcal{R}}}{\gamma_{opt}} \cdot \frac{g_{om}}{2\pi} \cdot X(\omega) = \\ = \frac{3\sqrt{3}}{8} \frac{15 \cdot 10^{-6}}{9.6 \cdot 10^9} \cdot 10^{17} \cdot 10^{-16} \simeq 10^{-14}\,W/\sqrt{Hz} \quad (4.17)$$

Thanks to the same formula in eq. (4.15), we calculate also the noise power due to the thermomechanical noise of the cantilever:

$$\delta P_{th}(\omega) = \frac{3\sqrt{3}}{8} \frac{P_0 C_{\mathcal{R}}}{\gamma_{opt}} \cdot \frac{g_{om}}{2\pi} \cdot X_{th}(\omega) = \\ = \frac{3\sqrt{3}}{8} \frac{15 \cdot 10^{-6}}{9.6 \cdot 10^9} \cdot 10^{17} \cdot 4.6 \cdot 10^{-14} \simeq 4.7 \cdot 10^{-12}\,W/\sqrt{Hz} \quad (4.18)$$

In other words, the thermomechanical noise of the cantilever is detectable only if the photodetector at the *through* output has a *noise equivalent power* lower than $4.7\,pW/\sqrt{Hz}$. Even in the case of ideal photodetector, the *shot noise* of the light sets the ultimate limit for the displacement resolution. Further details are in section 6.5.3 confirmed by experimental characterisation in section 6.6.1.

4.4 Optical gradient force

The photonics applied to *M/NEMS* is not limited only to detection. Despite the optical forces being weak in the macroscopic world, they fit for the actuation of objects at the micro/nanoscale [45].
The most popular application of optical gradient force is the optical tweezers [46]: a particle is confined inside a laser beam having an inhomogeneous intensity profile. The optical gradient force is applied to an object which is placed in a electromagnetic field having a non-zero gradient. The high confinement of the light into a waveguide combined with the the exponential decay of the evanescent wave ensure a significant gradient of the electromagnetic field [47]. Moreover, for resonance wavelengths, the amount of light power stored into the ring is enhanced by the *finesse*, that gives rise to an improved optical force.
The optical gradient force is not at all intuitive like the light pressure force which could be understood actually via a simple wind-on-sail model. However, Pernice offers the analogy of the mirror charge in electrostatics [48].
Two parallel waveguides are subject to transverse optical forces as light travels through them (see fig. 4.8a). This force depends strongly on the gap, since the evanescent fields decrease exponentially with the distance. The optical gradient force can be attractive or repulsive depending on the modes symmetry, it increases with the light power and it is proportional to the optomechanical coupling factor (see fig. 4.8b).

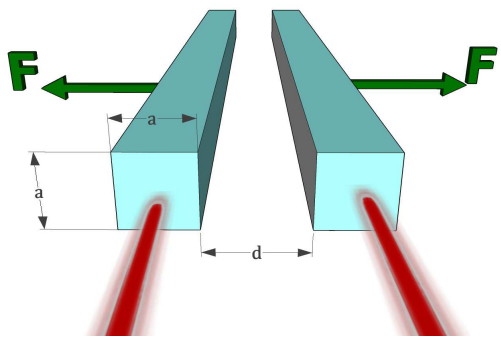

(a) Light travelling through two parallel waveguides ($\lambda = 1.5\,\mu m$, $P = 100\,mW$).

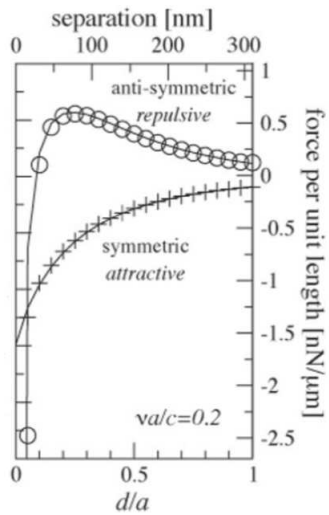

(b) Force trend according to the gap and symmetry modes. Extracted from [49].

Figure 4.8: The optical gradient force between two parallel waveguides.

We can see fig. 4.8b that the optical gradient force has an order of magnitude of $pN/\mu m/mW$ [49], large enough to actuate nanoscales devices.

While analytical models [50] and simulations [49][51][52] are well developed, only few articles show experimental observation of the optical gradient force applied to microsystem [53][54][55][56]. In the section 7.5 of this work, we propose a readout scheme suitable for a more comprehensive study of the phenomenon. The optical gradient force is used to excite an in-plane cantilever placed in the evanescent field of the ring resonator. The piezoresistive readout of the cantilever offers an uncorrelated and reliable detection which is appropriate for a quantitative investigation of the optical gradient force.

4.5 Conclusions

The optical spectrum of the ring resonator is modified by several perturbations such as temperature, mechanical deformation, carrier concentration and *NEMS* approaching. All of them can be described by an effective index variation, a deformed light path or a different coupling phase shift.
Under the condition of dispersive coupling, the ring spectrum shifts rigidly and proportionally to the optomechanical coupling factor g_{om}.
The optomechanical detection makes use of this phenomenon: a laser tuned on the resonance peak will be modulated by the cantilever oscillation. For small cantilever oscillations, the amplitude of the light power modulation is amplified by a factor which is proportional to the local slope of the peak.
High Q-factor for the ring not only assures a huge optical peak slope, but stocks high light power into a small volume. Under these circumstances, the optical gradient force is large enough to actuate objects at the microscale such as the cantilever.

At this point of the manuscript, we have now all the elements to understand the experimental part of this work: the fabrication of the device (chapter 5), the test bench setup (chapter 6) and the characterisation of the sample (chapter 7).

Chapter 5

The devices

As we saw in section 2.5, the *M/NEMS* mass sensing evolves with the optomechanical transduction: the basic idea behind our devices is a *NEMS* whose transduction and actuation is performed by the means of photonics as just described in chapter 4. The device fabrication has to provide a *M/NEMS* whose displacement readout is optomechanical by the virtue of a coupling with a photonic resonator.
To smoothly carry out this transition, we preserve the geometry of previous *NEMS* mechanics and we couple it to a separate ring resonator. In the next future, we envisage a device formed by a mechanical resonator which is simultaneously an optical resonator (e.g. whispering disk).

The design of the photonic elements was based on the wide experience about integrated photonics of *CEA* optical department. We took advantage of waveguides, ring resonators and grating couplers which are already reliable and well tested [57][58][59]. From our side, *M/NEMS* based sensors are the main activity of the *LCMC* laboratory.

Though this work focuses on the mass sensing application [2][60], the optomechanical transduction could be easily applied to every displacement readout.
We started from the simplest *M/NEMS* ever: an in-plane single clamped cantilever. The cantilever mechanics is already fully investigated and we chose layout dimensions similar to a successful project [61][60] in order to minimize the risk and focus on the optomechanical transduction.
Since we were new to optomechanics, we kept the piezoresistive readout of the cantilever via a single nanogauge. It turned out to be a practical debugging tool during the devices fabrication. Moreover, the parallel detection provides an independent displacement readout for *in-situ* comparison and linearity investigation.
Always for reasons of prudence, a drive electrode provides a electrostatic actuation of the cantilever. Anyway an optical actuation is possible for these devices.

A device with a suspended membrane over the ring was designed as well, it aims to improve the capture surface and the optomechanical coupling at the same time. Unluckily some errors in the fabrication process made a correct release of the membrane impossible.

All the elements which form the devices such as couplers, waveguides, cantilever (and related release) are described in the following pages. The presence of these endorsed bricks minimizes the risk letting us focusing on the real topic of the thesis: the development of the optomechanical transduction.

5.1 Waveguides

The crystalline silicon is transparent for telecommunication wavelengths around $1550\,nm$, in addition, the silicon oxide and the air have a lower optical index. This makes possible the realisation of on-chip waveguides with a strong confinement of the light and weak losses. The significant index difference ensures also acceptable waveguide bend radius down to some μm.

n_{Si}	n_{SiO_2}	n_{Air}
3.476	1.444	1.00026825

Table 5.1: Optical indexes of silicon, silicon oxide and air for $\lambda = 1550\,nm$.

For this work, we chose waveguides with a rectangular section, $500\,nm$ wide and $220\,nm$ thick in order to have a single mode waveguide with a TE polarisation. The presence of multiple modes would have complicated the interpretation of the spectrum of the optical resonator.

Figure 5.1: Waveguides section geometry.

The waveguide material is crystalline silicon $< 100 >$ of the top layer of the SOI wafer. However, the optical propagation properties of the silicon are anisotropic. From some tests, the losses are estimated around $3\,dB/cm$ but variations can occur from different wafers. Most of the time, the losses are dominated by other parameters like the roughness of the waveguide (see section 5.7.2).

5.2 Ring resonator

For the optical resonator, we opted for a ring resonator having a *add-drop* geometry (see section 3.2). The fabrication of the ring is done together with the waveguides and, thanks to the wafer integration, we obtain a resonator which is robust and it does not require any alignment. The easier realisation of the ring compared to disk or photonic crystal explains its large utilisation for telecommunication purposes. Despite other materials offer higher Q-factors, the silicon is more than adequate for our optomechanical transduction purposes. Moreover choosing the silicon as material, we can benefit from all the tools which are typical of CMOS technology.

The ring resonator waveguide has the same section of the coupling waveguides ($220 \times 500\,nm$). The high purity of crystalline silicon assures low losses (Γ) and a consequent high optical Q-factors.
Many variants were designed to investigate the properties of the system like the FSR and the optical Q-factor according to the theoretical evaluation made in chapter 3. Three different ring radius (R) are chosen: 5, 10 and $25\,\mu m$. The optical gap between the rings and waveguides (g_{opt}) is tuned between 140 and $200\,nm$ and some racetracks are present as well with straight parts (h,v) up to to $6\,\mu m$. (See fig. 5.2)

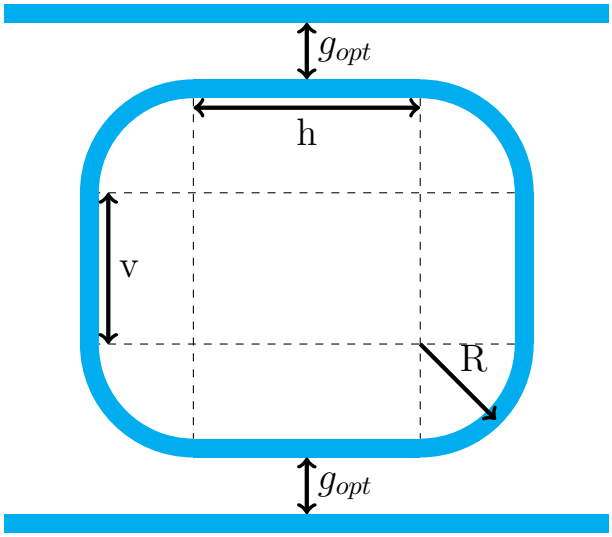

Figure 5.2: Ring resonator parameters

For the optomechanical devices, we set the dimensions of the optical resonator and we tuned other parameters like the optomechanical gap and the cantilever (or membrane) sizes. This avoids a countless number of variants, given that the target

of the run is the validation of the optomechanical transduction although not perfectly optimised.

The ring resonator used for the mechanical transduction has always a radius of $5\,um$ and coupling gaps of $200\,nm$ for the *through* and for the *add* waveguides.
In some cases, the *add* waveguide is moved to the right side of the ring to leave room for the mechanical resonator.

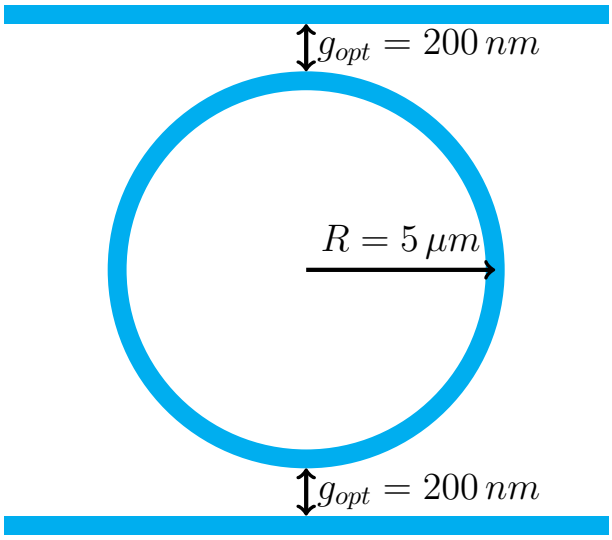

Figure 5.3: Ring resonator geometry chosen for the optomechanical devices.

The presence of the *add* output is a matter of debate: it introduces external losses ($K_2 \neq 0$) which degrade the optical Q-factor. At the same time, coupling the *add* waveguide with a proper gap improves the contrast of the ring spectrum especially when internal losses are non-negligible (see eq. (3.26)). Moreover, collecting the light at the *add* is trickier since during the alignment, the laser has to be tuned exactly at the resonance. For these reasons, all the optomechanical experiments are performed using the *in* and *through* ports only. During the phase of mask design, we did not remove the *add* port because we wanted to have a supplementary monitor to probe the system.

5.3 Grating coupler

The injection of light into the device is performed using a grating coupler etched on the substrate [62][63][64].
A grating coupler is a periodic pattern on the substrate with two different optical indexes: due to constructive interference, the light coming from a fiber is forced

to enter in the planar waveguide (see fig. 5.4). This grating coupler replaces other coupling techniques like prism-based or edge coupling technique which oblige to cut the wafer.

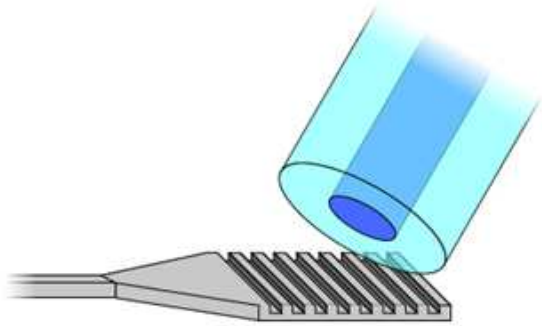

Figure 5.4: Optical fiber aligned to a grating coupler.

The main advantage of this technique is the possibility to perform tests *under probe* over a large number of devices across the wafer similarly to an electrical prober. Differently from an electric test, where the simple contact between the probe and the pad is sufficient, there are some requirements to fulfil in term of alignment: for the coupler integrated in our devices, the optical fiber has a coupling angle between 8° and 12° with respect to the normal and an alignment accuracy of $1\,\mu m$ on the three axes.
In addition, the grating coupler is sensitive to light polarisation: in our case, it is optimised for TE polarisation whereas it acts as a filter for any different polarisation. As shown in section 5.7, the couplers are obtained from a partial etching ($70\,nm$) of the top silicon layer of the waveguides with a pitch of $310\,nm$. The index pattern is obtained from the index difference between silicon and air (or silicon oxide when the device is wrapped).
The grating coupler allows many inputs and outputs, an easier alignment compared to edge coupling since the coupling angle is fixed. This is convenient for vacuum and cryogenic application or for automatic alignment. However the coupling efficiency is not exquisite, it is bandwidth limited (usually $100\,nm$) and the transmission depends on the light wavelength and polarisation.

In fig. 5.5, we observe a simulated spectrum of the transmitted light power for a grating coupler. The blue curve is obtained for a coupler in vacuum and the red curve for a grating wrapped into silicon oxide: the coupling losses are estimated 1.5 and $1.8\,dB$ (for $\lambda = 1550\,nm$). In both cases, the coupling efficiency depends on the light wavelength and this coupler is optimized for $1550\,nm$ with a *Gaussian* window of 80-100 nm.
A real coupler, instead, has a typical loss value of $6.2\,dB$ at the end of the fabrication process (for $\lambda = 1550\,nm$). This estimation is obtained from the experimental

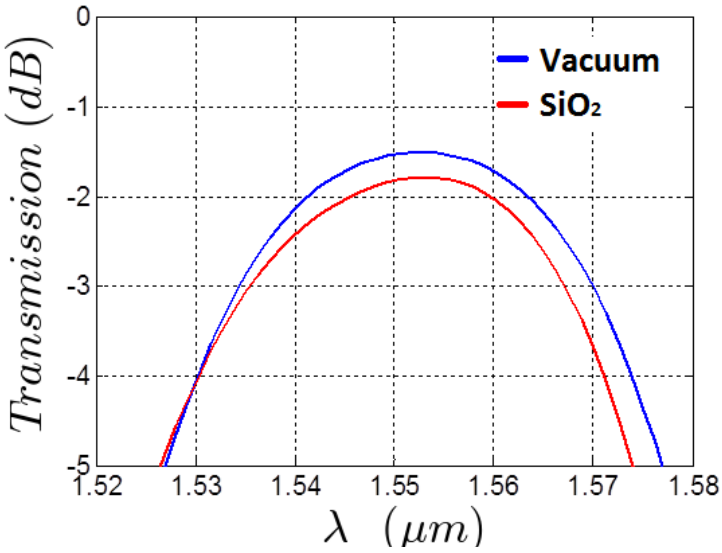

Figure 5.5: RSOFT simulation of the grating coupler efficiency for a fiber at 11.5° under vacuum or under a SiO_2 layer. Courtesy of Daivid Fowler (*CEA/LETI/DOPT*).

transmission spectrum of two couplers (input and output) shown in fig. 5.6: we have to subtract from $14.5\,dB$ all the losses due to the setup ($2.1\,dB$) and then divide by 2, the number of couplers. The setup losses, measured experimentally, are compatible with the values of manufacturers (see table 5.2).

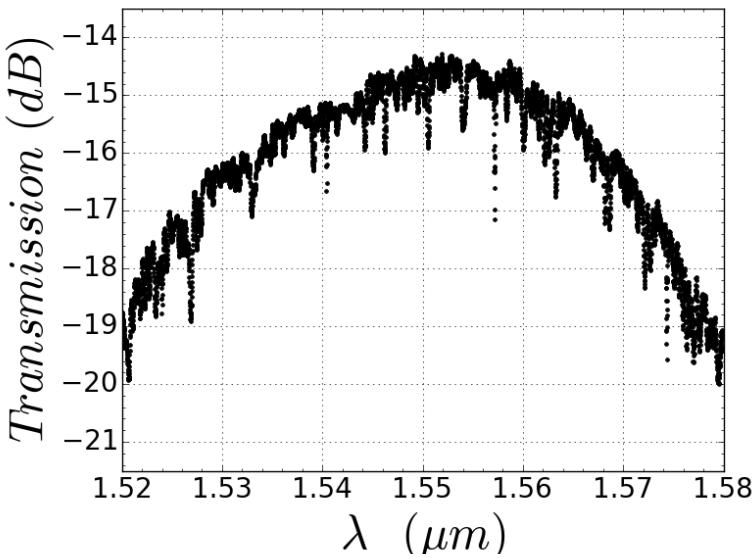

Figure 5.6: Experimental spectrum of two grating couplers. Here the optical resonance peaks are superposed to the couplers response.

Optical configuration	**Losses** $[dB]$
1-m fiber	0.0005
1-m polarisation maintaining (PM) fiber	< 0.5
APC connector or feedthrough	0.3
PM fiber - polarization controller - APC feedtrough - vacuum fiber - APC feedtrough - fiber	2.1
PM fiber - polarization controller - APC feedtrough - vacuum fiber - device - vacuum fiber - APC feedtrough - fiber	14.5

Table 5.2: Optical losses for different configuration. ($P_{laser} = 1\,mW$, $\lambda = 1550\,nm$)

It is obvious that the main losses come from the grating couplers of the device. The degradation of transmission coefficient is probably due to residues generated by the fabrication steps which follow the photonics (see section 5.7). Metal deposition and *M/NEMS* release are the main suspects but further investigations are required for matching the envisaged performances with the simulations.

5.4 Mechanical resonator

LCMC laboratory has been working on mechanical resonators for years. Previous projects already investigated the cantilever mechanics for gas and mass sensing applications [61][65][31][60]. From these experiences, we bequeath an endorsed layout for a single clamped cantilever equipped with a piezoresistive detection and a electrostatic actuation (see fig. 5.7).

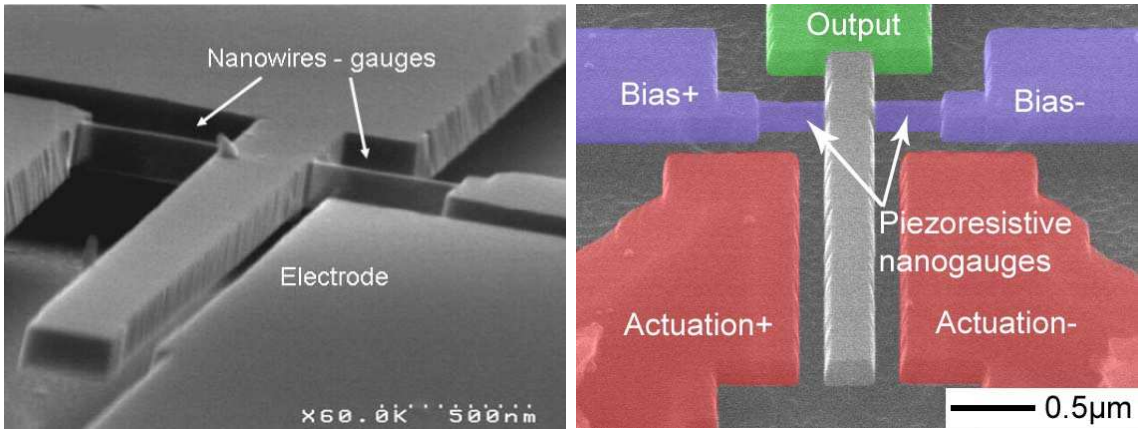

(a) from [61] (b) from [31]

Figure 5.7: SEM picture of the in-plane cantilever: both devices have drive electrodes and two gauges for a differential detection of the cantilever displacement.

From chapter 4, we know that a mechanical resonator placed in the evanescent field of the ring shifts the resonance wavelength as a result of its movement. That is why we fabricate a *M/NEMS* in proximity of the optical ring to perform the optomechanical transduction. Thanks to the innovative readout, the *M/NEMS* benefits from the advantages of photonics and circumvents the constraints described in sections 2.3.2 and 2.4.
The layout of two mechanical resonators is shown in the following pages.

5.4.1 In-plane cantilever resonator

The device is a crystalline silicon cantilever which interacts with the evanescent field of the light propagating in the ring resonator (fig. 5.8). The in-plane mechanical oscillation can be forced by an electrode placed next to the cantilever end. The cantilever readout is performed also via the piezoresistive nanogauge which is suspended close to the beam base. With the advantage of two completely independent readout, the device enables in-situ comparison between piezoresistive and optomechanical transduction. On the other hand, the fabrication complicates because of

local doping which is mandatory to obtain piezoresistive nanogauges and ohmic contacts but lethal for photonic elements.

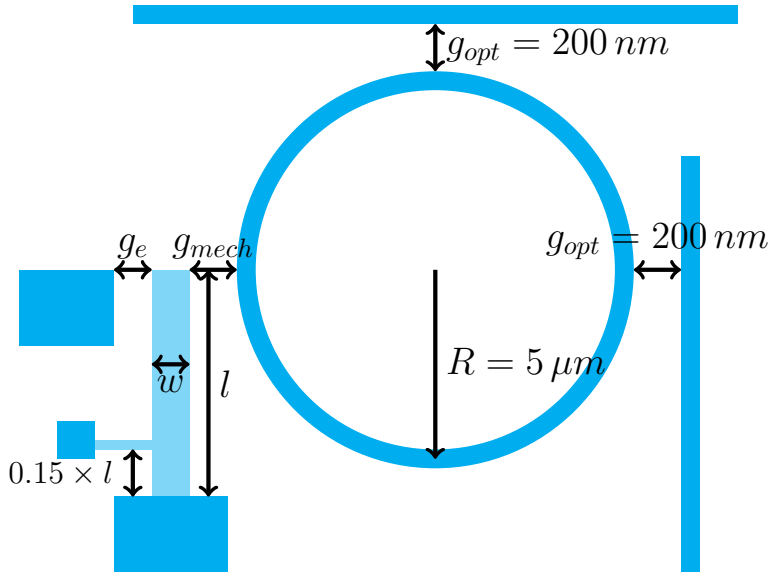

Figure 5.8: Cantilever devices: all the elements are patterned on the top silicon layer. The released parts are marked by the transparency.

The geometrical variations for the in-plane cantilever are collected in table 5.3 while the gauge and the electrode are described more in details in the following sections 5.5 and 5.6. To limit the number of variations, the electric gap g_e is fixed at $200\,nm$, the gauge length is always $400\,nm$ and the gauge width is $120\,nm$.

Device	**Length** (l) [μm]	**Width** (w) [nm]	**Thickness** (t) [nm]	**Optomechanical gap** (g_{mech}) [nm]	**1st resonance frequency** (f_r) [MHz]
# 1	5	150	220	200	$\simeq 8$
# 2	5	300	220	140	$\simeq 16$
# 3	5	300	220	200	$\simeq 16$
# 4	5	300	220	300	$\simeq 16$
# 5	10	150	220	200	$\simeq 2$
# 6	10	300	220	200	$\simeq 4$

Table 5.3: Parameters for cantilever devices.

A preview of the sample is offered by the SEM picture in fig. 5.9: the challenge of this device is the selective release and doping applied only to the cantilever. The

electrical contacts between the device and the pads are provided by the means of three metal paths and some via (see section 5.7.3).

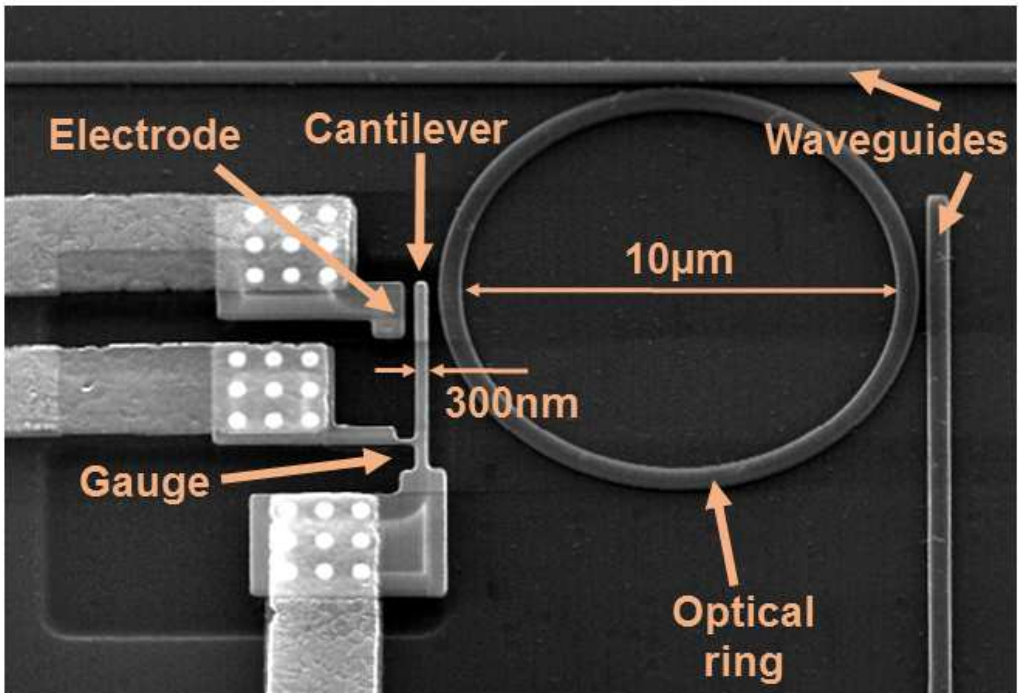

Figure 5.9: SEM picture of the in-plane cantilever device # 3.

5.4.2 Membrane resonator

This is an out-of-plane resonator made up of a membrane suspended over the ring resonator (see fig. 5.10). With a view to mass sensing application, this device is conceived to maximise the capture surface where the particles can land. At the same time, the interaction between the membrane and the ring occurs over a larger area compared to the cantilever device.
Piezoresistive transduction is omitted and the electrostatic actuation is proposed by the means of a metal electrode below the membrane.
The membrane release requires the presence of holes even though it reduces the capture surface.

The first resonance frequency is evaluated via the analytical formula for a four point supported membrane [66]. A more exhaustive description would take into account the holes and the real size of the anchors point. All the membranes have a hole side of $0.5\,um$, a hole pitch of $0.8\,um$ and a membrane support of $2 \times 2\,um$
The geometrical variants are collected in table 5.4:

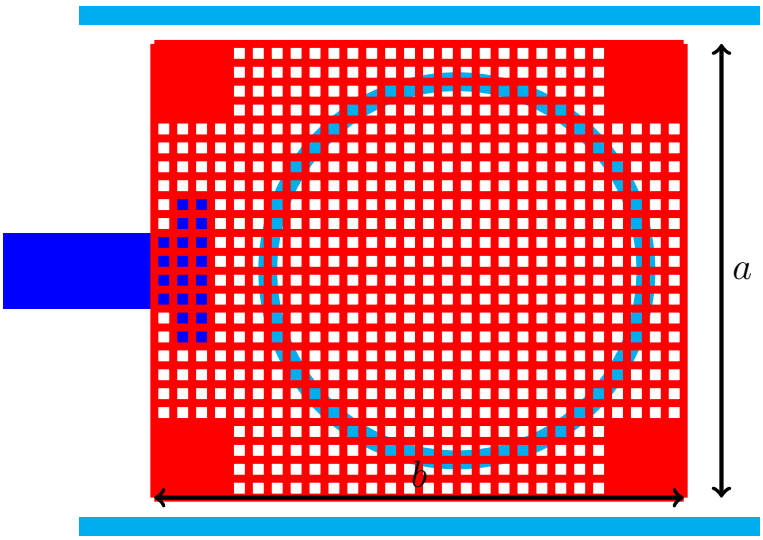

Figure 5.10: Membrane devices: the membrane (in red) is suspended over the ring resonator (cyan). The electrode (in blue) provides the actuation.

Device	**Length** (a) [μm]	**Width** (b) [μm]	**Thickness** [nm]	**1st resonance frequency** (f_r) [MHz]
# 1	11.5	20.3	200	$\simeq$ 1.7
# 2	8.3	8.3	200	$\simeq$ 8.3
# 3	4.3	9.8	200	$\simeq$ 7.9
# 4	20.3	20.3	200	$\simeq$ 1.4
# 5	0.5	5.0	200	$\simeq$ 69
# 6	1.0	5.0	200	$\simeq$ 69
# 7	1.0	10.0	200	$\simeq$ 17
# 8	2.0	10.0	200	$\simeq$ 17
# 9	4.0	10.0	200	$\simeq$ 17
# 10	3.0	15.0	200	$\simeq$ 8

Table 5.4: Parameters for membrane devices.

5.5 Piezoresistive gauges

The crystalline silicon acquires piezoresistive properties as it is rightly doped [67]. Piezoresistive transduction is a standard technique to read out the *NEMS* displacement [68]. It shows good performances in terms of signal-to-background ratio (SBR) and dynamic range (DR) [69][70][65][61]. The displacement of the proof mass stretches the piezoresistive gauges which are suspended between the resonator and an anchor point. By virtue of piezoresistive property, the resistance of these gauges varies proportionally to the stress, so a detection of the resistance provides an image of the cantilever displacement.

A piezoresistive transduction, in parallel to the optomechanical one, enables measurement of the cantilever displacement via an unrelated electrical channel which is perfectly mastered. From a practical point of view, it was very useful especially for testing the devices in an endorsed electrical setup: the localisation of devices which work properly helps to debug the critical fabrication step of the release.
With these devices, the transduction properties (linearity, dynamic range, etc.) can be compared on the same cantilever, simultaneously and for identical actuation. Moreover, the possibility of a double detection opens the way to innovative experiments like the *in-situ* comparison of *Allan deviation* (section 7.3.6) and the detection of optical gradient force (section 7.5).

5.6 Drive electrode

As seen in section 4.4, the optical actuation is awesome because it opens up the possibility of making a completely photonic device. However, the efficacy of the optical actuation could be scarce compared to electrostatic actuation, especially for non-optimised devices. Another consequence is that the setup gets more complicated with the addition of a second laser, a light modulator, a 50:50 coupler and a wavelength filter [7].
For these reasons, an electrode is patterned on the top silicon layer and doped like the gauges. Some Via, a metal path and a pad provide the electrical continuity (see fig. 5.9). The actuation is performed electrostatically applying a potential V_a between the electrode and the cantilever.

We can model the cantilever and the electrode as a capacitance $C = \frac{\epsilon_0 \epsilon_r A}{d}$, created by two surfaces A separated by a gap d having a relative permittivity ϵ_r. Being the energy stored in the capacitance equal to $E = \frac{1}{2} C V_a^2$, the force applied

on the mechanical beam is the derivative of this energy along the position:

$$F = -\frac{dE}{dy}\bigg|_Q = \frac{1}{2}\frac{dC}{dy}V_a^2 = \frac{1}{2}\frac{\epsilon_0\epsilon_r A}{(d-y)^2}V_a^2 = \frac{1}{2}\frac{\epsilon_0\epsilon_r A}{d^2\left(1-\frac{y}{d}\right)^2}V_a^2 \tag{5.1}$$

In the small displacement approximation ($y << d$), we simplify the previous formula obtaining

$$F \simeq \frac{1}{2}\frac{\epsilon_0\epsilon_r A}{d^2}V_a^2 \tag{5.2}$$

If we consider the general case of $V_a(t) = V_{DC} + V_d\cos(\omega t)$, the force results as

$$F(t) = \frac{1}{2}\frac{\epsilon_0\epsilon_r A}{d^2}\left(V_{DC}^2 + \frac{V_d^2}{2} + 2V_{DC}V_d\cos(\omega t) + \frac{V_d^2}{2}\cos(2\omega t)\right) \tag{5.3}$$

Unless otherwise specified, we used only the component at 2ω for all the experiments. Compared to actuation at ω, the actuation at 2ω has a lower background signal since the cross-talk with gauges polarisation is quasi absent. For the sake of simplicity, we eliminated also a variable parameter, fixing V_{DC} to zero.

When the drive voltage is important and the gap is small, the approximation made before is not any more valid. We have to develop the force up to the first order

$$F \simeq \frac{1}{2}\frac{\epsilon_0\epsilon_r A}{d^2}V_a^2\left(1+2\frac{y}{d}\right) \tag{5.4}$$

Inserting this force in the motion equation of the oscillator in eq. (2.19), we can rearrange a term of negative stiffness. This effect is observed experimentally in fig. 7.14, the resonance frequency of the cantilever shifts for higher drive voltages.

5.7 Fabrication process

The fabrication of the devices is performed with the modern CMOS tools widely applied in microelectronics.
During this thesis, different runs were made in the clean room of *Leti* except some steps at *STMicroelectronics* of Crolles. The run AD790 aims at the improvement of the optical Q-factor of the ring resonator, whereas the run AD607 is dedicated to the optomechanichal devices.

The first goal was the fabrication of the photonic elements with good performances in terms of light coupling, light losses and optical Q-factor. Then the efforts were focused on the fabrication of a mechanical resonator closed to the ring resonator avoiding any damaging of the photonic elements. The doping is mandatory for the *NEMS* operations but it has to be localised. Otherwise bore implantation would increase irremediably the light absorption in the waveguides. Similarly, the etching for the *NEMS* release has to be tuned in order to release only the cantilever and not the waveguides.

The starting point of the design was an existing process used for brokerage *ePIXfab*[1]. This process was created for the resonance tuning of ring resonators: a metal heater is placed over the ring resonator to modify the effective index via the temperature. In this way, it is possible to compensate the technological dispersion and tune a large number of resonator exactly on the same resonance wavelength. For this work, we kept the same photonics part and we used the metal layer as membrane or as pad. Some fabrication steps were added for the release of the mechanical resonator and for the doping of piezoresistive gauges.
The device is fabricated from *silicon-on-insulator* (SOI) wafers ($200\,mm$): the top silicon layer is etched with reactive ion etching to pattern the geometry of the device. The waveguides, the ring, the cantilever and the electrode are on the same layer. Then, a partial etching of the *buried oxide layer* (BOX) releases the mechanical resonator. Since the waveguide and the ring section are wider than the cantilever, the photonic elements remain anchored to the substrate via a pedestal. Knowing with accuracy the etching rate of the BOX (here 8 nm/min), the etching process is stopped as the mechanical resonator is released. The lateral etching is visible through the silicon layer by means of *SEM* images. The etching rate is calculated thanks to a preliminary partial etching lasting a fixed amount of time.

The process for photonic elements (couplers, waveguides and rings) is identical for all devices. A split of run AD607 made possible the fabrication of two optomechanichal devices: the in-plane cantilever and the membrane.

In the following pages we detailed technological process for each variation.

[1] http://www.epixfab.eu/

5.7.1 On-chip photonics

Here is the description of the technological process for the fabrication of photonic elements:

1. SOI substrate $220\,nm/2\,\mu m$ (fig. 5.11a)
2. Alignment mark fabrication
3. Grating coupler realisation (fig. 5.11b):
   - 3.1. BARC deposition
   - 3.2. Resist deposition
   - 3.3. DUV ($193\,nm$) photolithography of resist
   - 3.4. Stripping resist
   - 3.5. BARC etching
   - 3.6. Partial etching of Si ($70\,nm$)
   - 3.7. Stripping resist and BARC
4. Waveguides realisation (fig. 5.11c):
   - 4.1. Hard mask deposition SiO_2 ($80\,nm$)
   - 4.2. BARC deposition
   - 4.3. Resist deposition
   - 4.4. DUV ($193\,nm$) photolithography of resist
   - 4.5. BARC and hard mask etching
   - 4.6. Stripping resist and BARC
   - 4.7. Silicon etching down to the box ($220\,nm$)
   - 4.8. Polymer removal
   - 4.9. Thermal oxidation ($\simeq 5\,nm$) (fig. 5.11d)

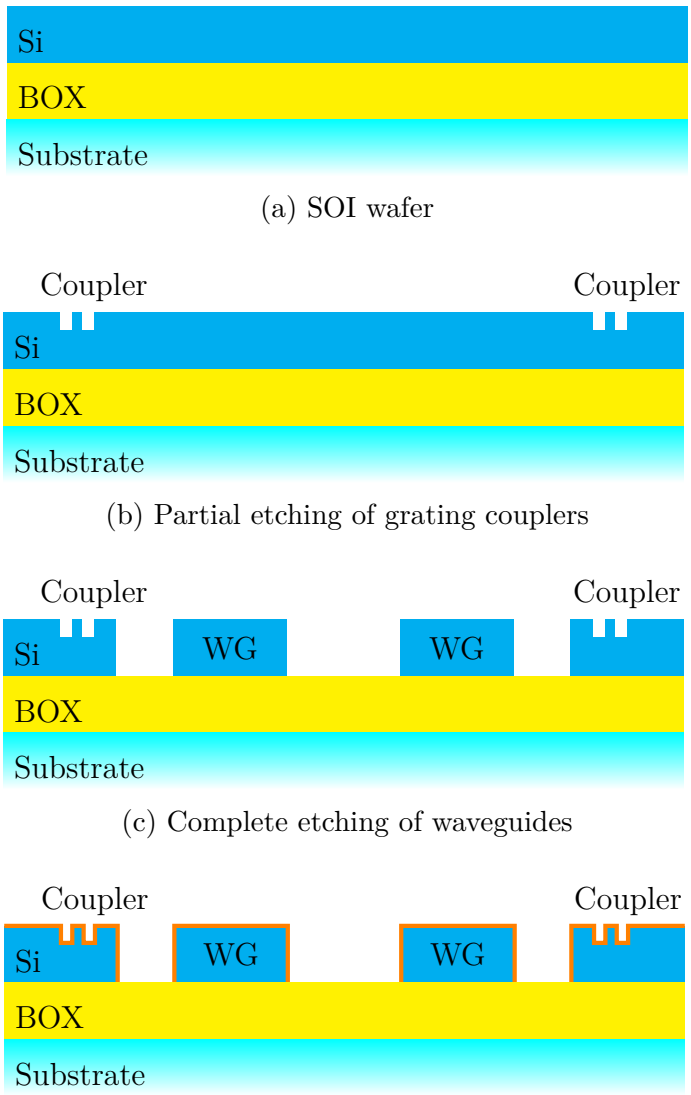

(a) SOI wafer

(b) Partial etching of grating couplers

(c) Complete etching of waveguides

(d) Thermal oxidation

Figure 5.11: Fabrication process for on-chip waveguides.

5.7.2 Optical Q-factor improvement

Fourteen wafers of run AD790 were dedicated to the improvement of the optical Q-factor via minimizing the losses Γ in the ring resonator.
The parameter Γ sums up different contributions: the light absorption, the surface/volume diffraction and the radiation. The light absorption is fixed by the silicon properties and the radiation losses depend on the radius of curvature. Once the geometry and the material are chosen, we can still minimize the surface diffraction losses reducing the roughness of the waveguides.
After the waveguide patterning described in section 5.7.1, the wafer underwent to additional steps of *creeping*, *deoxidation-reoxidation* and partial *etching* of the BOX. Thanks to the *creeping* or the *deoxidation-reoxidation* of the waveguide, the roughness of the ring surface should decrease reducing the scattering losses. The aim of the under-*etching*, instead, is to isolate the ring from the BOX, reducing in this way the losses due to the coupling with the substrate. The coupling efficiency K_1 and K_2 change as well due to the presence of air between the ring and the waveguides.
Some results are shown in the following images: the Q-factor values are averaged over different peaks on the same device or over different dies on the same wafer.

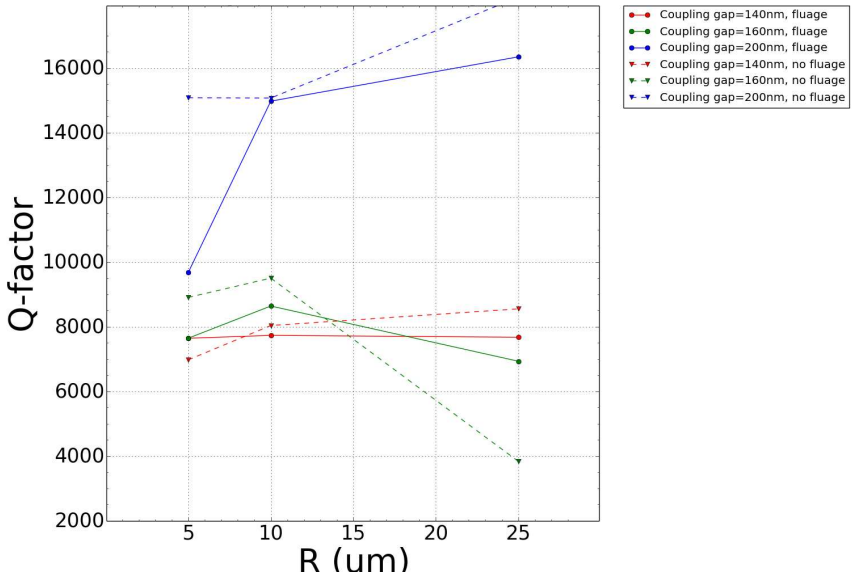

Figure 5.12: The effect of *creeping* on the optical Q-factor for different devices.

As we can see from fig. 5.12 and 5.13, the *creeping* turns out to be counterproductive whereas the process of *deoxidation-reoxidation* provides only modest optical quality factors around 15 000. Indeed, we saw from fig. 3.7 that the Q-factor weakly depends on the losses when the ring is overcoupled to bus waveguides. A variation of the ring internal losses (Γ) impacts the optical Q-factor only in the

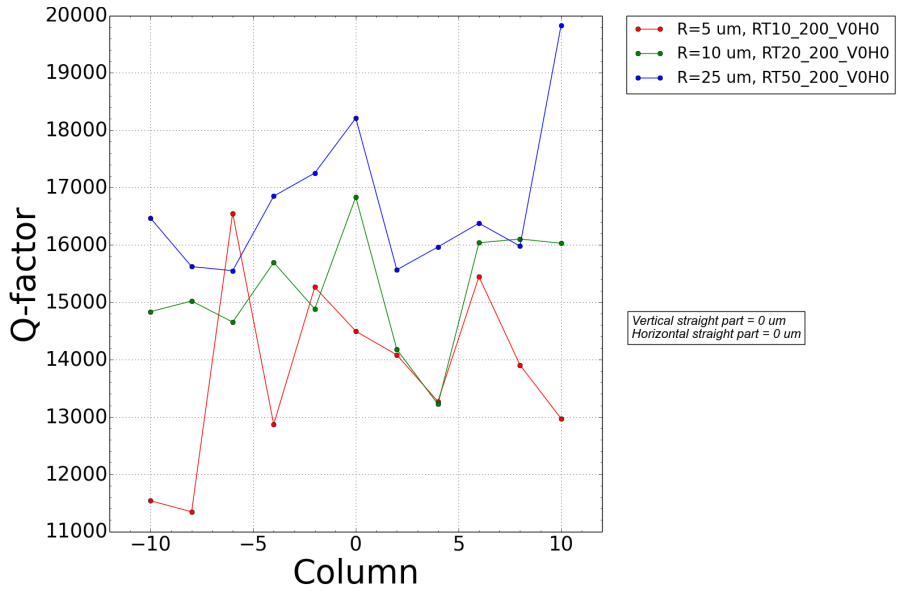

Figure 5.13: The effect of *deoxidation-reoxidation* on the optical Q-factor for different devices along the wafer columns.

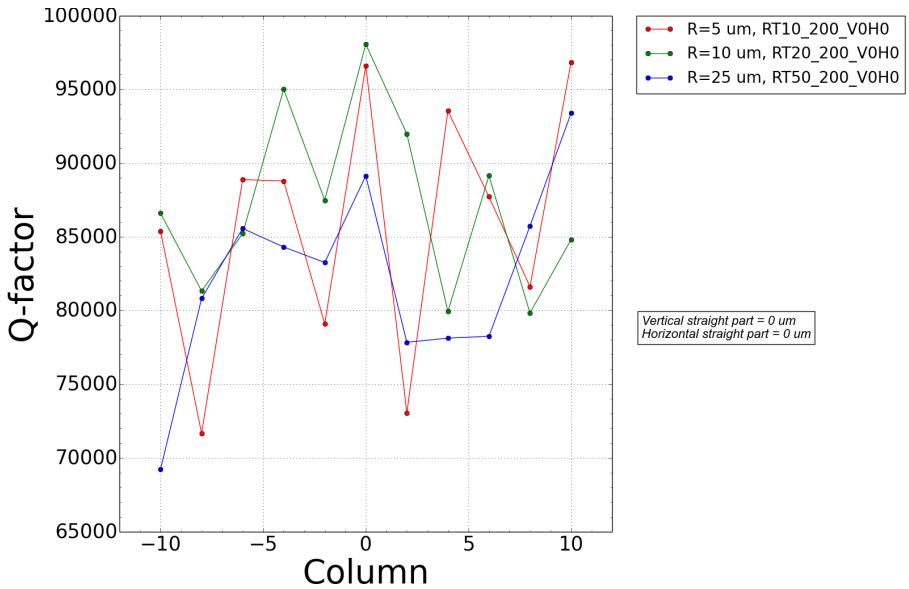

Figure 5.14: The effect of BOX *etching* (150 nm) on the optical Q-factor for different devices along the wafer columns.

undercoupled regime.
With under-*etching* (fig. 5.14), we obtained a significant improvement of the optical Q-factor achieving values between 75000 and 95000. This means that the BOX

etching, not only releases the mechanical resonator, but increases the quality factor of the ring resonator. The higher difference between air and silicon optical indexes confines the light better and reduces the coupling factors K_1 and K_2. As we can see from fig. 3.7, when the ring is overcoupled, the optical Q-factor strongly depends on the waveguide coupling factors K_1 and K_2 via the formula in eq. (3.43).

5.7.3 In-plane cantilever fabrication

Once the parameters for the photonic part were optimised, the run AD607 was dedicated to optomechanical devices: the split AD607A concerns the membrane suspended over the ring whereas the split AD607B is dedicated to the in-plane cantilever placed near the optical ring. We will start from it.
The cantilever, the ring, the electrode and the gauges are made of crystalline silicon and patterned together on the same layer [61]. The originality of this device is the piezoresistive detection of the cantilever: this added some difficulties to the fabrication process.
The doping implantation has to be localized only to the cantilever, nano-gauges and electrode; any doping of the ring increases the absorption degrading irreparably the optical Q-factor. The mask alignment for this step was tricky because the border of the doping area has to fall in the middle of the optomechanical gap g_{mech} (see fig. 5.8).
We must provide as well an electric path from three metal pads up to the device. The electrical contacts are mandatory to polarise the actuation electrode and for the nano-gauges biasing.
These efforts brought to the fabrication of hybrid devices where the mechanical, electrical and optical requirements have to be fulfilled.

Here is the enumeration of the technological steps:

1. Patterning of couplers, waveguides, ring, cantilever, gauges and electrode (fig. 5.15a). (Details in section 5.7.1 and fig. 5.11)
2. Local doping of the gauges (fig. 5.15b):
   - 2.1. Resist deposition ($820\,nm$) and DUV photolitography
   - 2.2. Implant Bore ($5 \cdot 10^{19}\,at/cm^3$)
   - 2.3. Stripping of photoresist
   - 2.4. Annealing for doping activation
3. HDP deposition of silane oxide ($700\,nm$)
4. CMP to reach 200 nm of oxide on the top of waveguide (fig. 5.15c).

5. Creation of VIA (fig. 5.15d):
   5.1. Photolithography of VIA
   5.2. Etching VIA down to electrode, cantilever and gauges
   5.3. Filling with Ti ($30\,nm$), TiN ($60\,nm$) and W ($600\,nm$)
   5.4. CMP for top metal removal
6. Creation of pads and electric paths (fig. 5.15e):
   6.1. Deposition of AlSi for the pads and electrical paths ($200\,nm$)
   6.2. DUV lithography of pads and electrical paths
   6.3. Etching AlSi ($200\,nm$)
7. Cantilever release:
   7.1. Photoresist for ring protection
   7.2. Dry etching RIE of oxide 400nm (fig. 5.15f)
   7.3. Desoxidation back side
   7.4. Stripping resist
   7.5. HF vapour etching for gauge and cantilever release (fig. 5.15g)

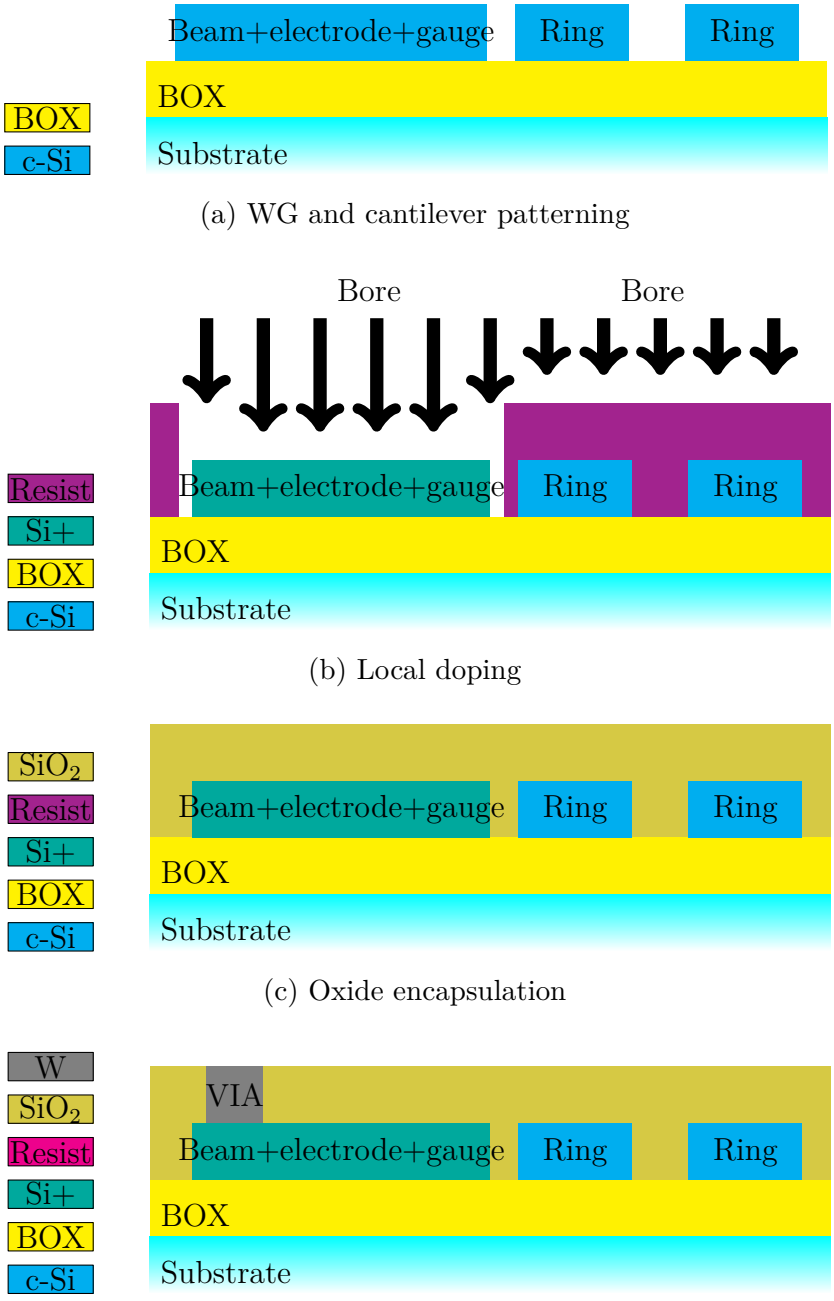

(a) WG and cantilever patterning

(b) Local doping

(c) Oxide encapsulation

(d) VIA

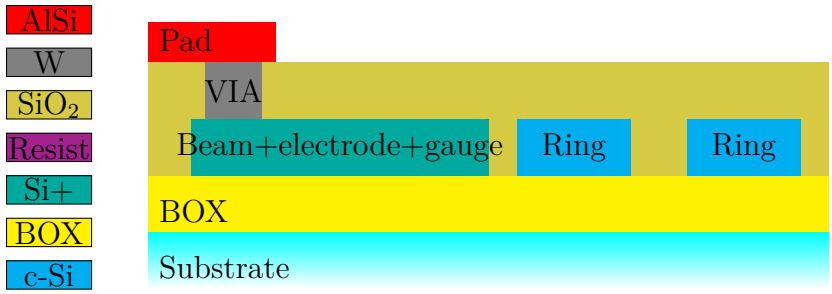

(e) Pad

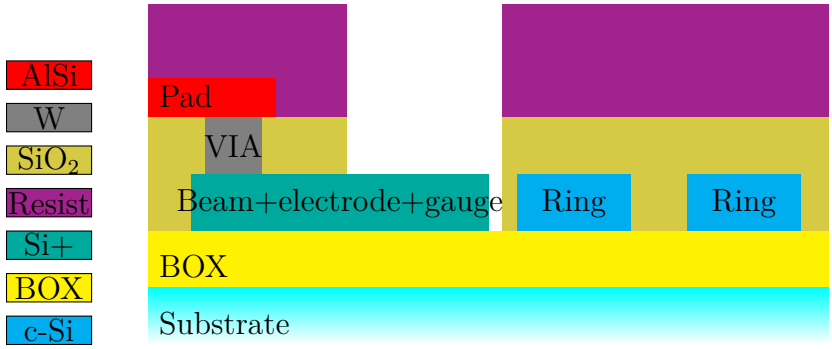

(f) Dry etching

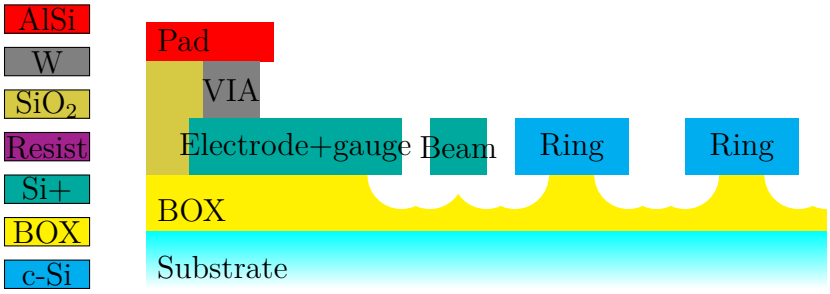

(g) HF releasing

Figure 5.15: Fabrication of cantilever device

5.7.4 Membrane fabrication

These devices come from a split of run AD607: a membrane is suspended above the ring and vibrates out of planes. This geometry has two advantages: the wide membrane surface provides a large surface of capture and an improved optomechanical coupling.

Here is the technological steps:

1. Patterning of couplers, waveguides, and ring. (See sec.5.7.1 and fig. 5.11)
2. Deposition of 40 nm of TEOS oxide
3. Actuation electrode fabrication (fig. 5.16a):
   - 3.1. Deposition of an adhesion layer: Ti (10 nm) and TiN (30 nm)
   - 3.2. Deposition of actuation electrode in AlCu (180 nm)
   - 3.3. Opening of the global mark (litho, etching, stripping)
   - 3.4. Photolitography of the electrode
   - 3.5. Etching 180nm of AlCu with stop on TEOS oxide
   - 3.6. Stripping
4. HDP deposition of 700 nm silane oxide
5. CMP to reach 100-200 nm of oxide on top of waveguide (fig. 5.16b)
6. VIA fabrication (fig. 5.16c):
   - 6.1. Lithography of VIA:
   - 6.2. Etching VIA down to electrode or down to substrate
   - 6.3. Filling with Ti (30 nm), TiN (60 nm) and W (600 nm)
   - 6.4. CMP for top metal removal
7. Membrane fabrication (fig. 5.16d):
   - 7.1. Deposition of AlSi membrane 200 nm
   - 7.2. Lithography
   - 7.3. Etching 200 nm of AlSi
8. Membrane releasing with HF etching (100-200 nm) (fig. 5.16e)
9. Remaining oxide measurement

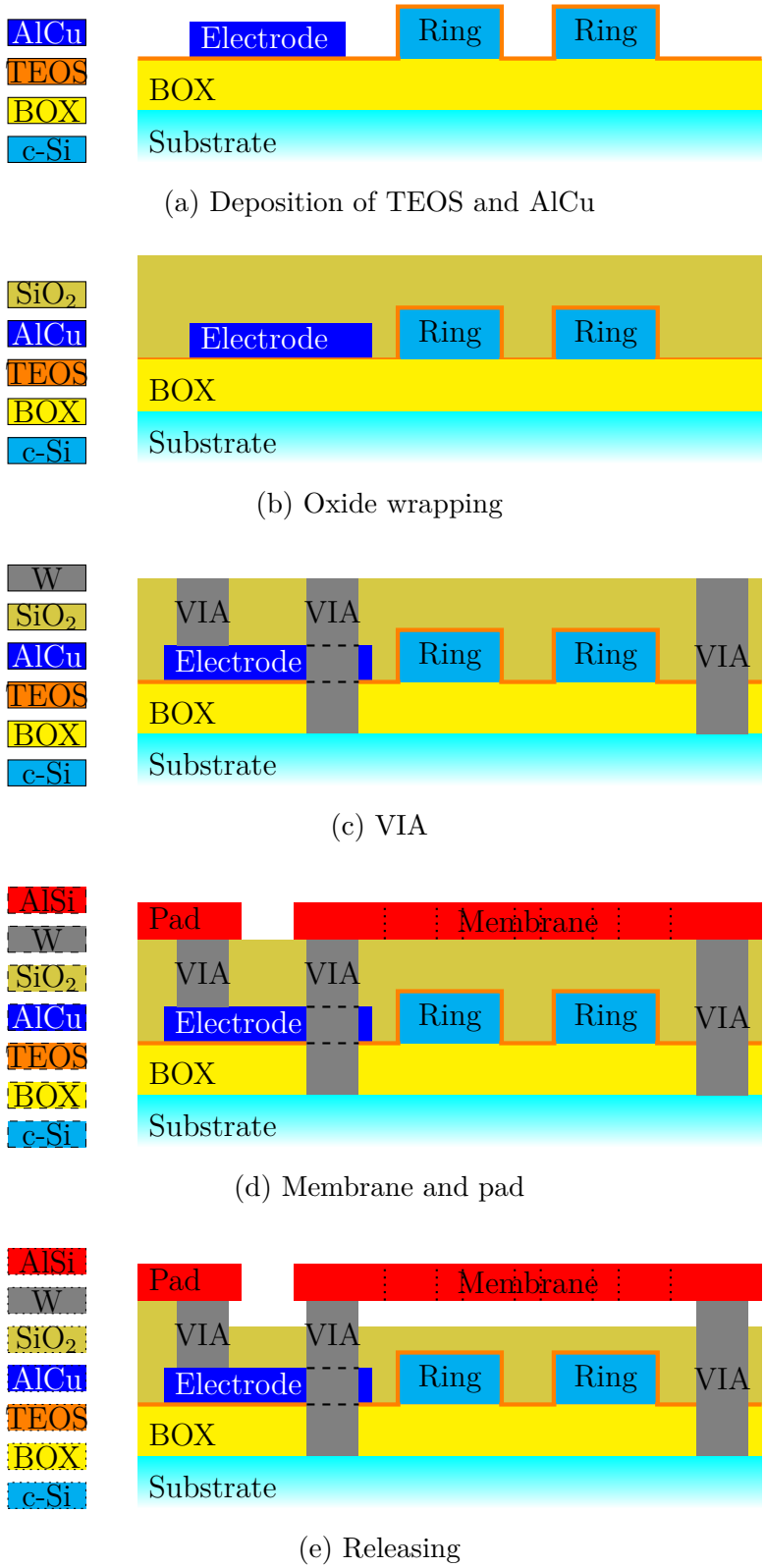

(a) Deposition of TEOS and AlCu

(b) Oxide wrapping

(c) VIA

(d) Membrane and pad

(e) Releasing

Figure 5.16: Fabrication process for the membrane

5.7.5 Fabrication problems

In-plane cantilever issues

Since the cantilever is less wide than the photonics, the anisotropic etching in fig. 5.15g releases the *NEMS* structure before the ring and the waveguides. If the etching rate or the etching time is not well known, it occurs a complete release of the photonic elements (fig. 5.17a).
Upon the occurrence of a correct release, the BOX under the ring is partially removed letting the photonic structure on a pedestal. Moreover, as seen in section 5.7.2, a partial BOX etching under the ring improves the optical Q-factor. Since the ring is overcoupled to the bus waveguides, decreasing the coupling factors K_1 and K_2 affects positively the optical Q-factor more than attenuating ring losses Γ.
The silane oxide is etched 2-3 times faster than BOX, this means that the silane oxide which covers the ring, the waveguides and the couplers is completely etched before having a complete cantilever release (see fig. 5.15c and 5.15g). The absence of the silane oxide layer modifies the performance of the grating couplers: the coupling angle is slightly modified and the efficiency is probably compromised by the presence of residuals due to HF etching process.
The last inconvenience is that the AlSi electrical paths on the oxide float as the SiO_2 is etched during the release step. This compromises the electrical continuity between the pads and the drive electrode or the gauges (fig. 5.17b).

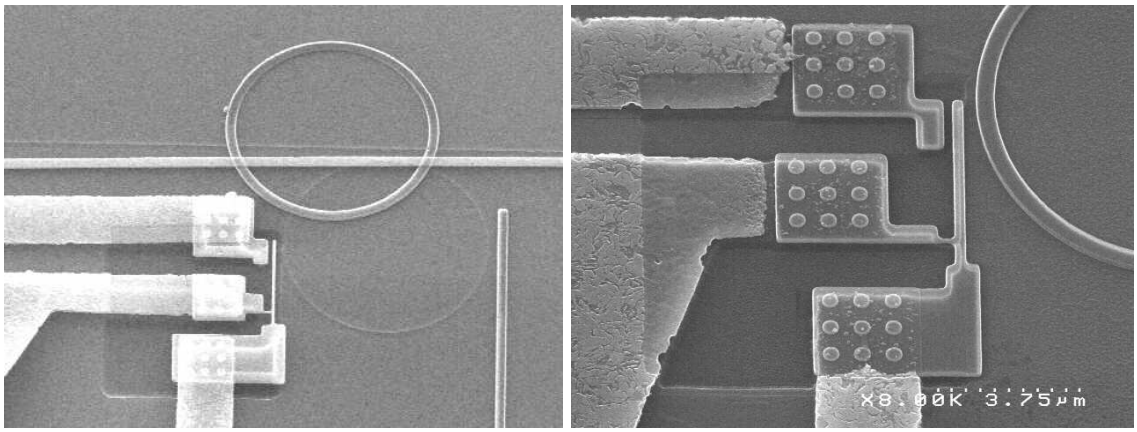

(a) Released photonic elements. (b) Damaged electric path.

Figure 5.17: Typical fabrication problems.

So the existing process has to be improved to be more compatible with HF etching release. A different approach is chosen for the next run: the electrical conductivity from the pads up to the device is assured by a metal layer deposited directly on the crystalline silicon. In the lasts nano-meters, between the end of metal and the

device, the silicon is already highly doped during the step devoted to gauges. This makes the VIA fabrication useless taking out a fragile and floating metal path.

When this technology will be really applied for mass sensing, a protection layer on the ring is recommended. A landing mass on the optical ring resonator modifies the resonance wavelength according to the contact area and to the particle optical index. A shifted optical resonance modifies the responsivity of the optomechanical transduction since the laser would be tuned now in a point where the local slope is different (in the worst case null).
It is true as well that the mass sensing requires only the *NEMS* oscillation frequency and not the amplitude. Even if the signal detection is affected only at second order, the protection layer over the ring would facilitate the operations.

Membrane issues

The fail of the AlSi patterning produced blind holes on the membrane as shown in fig. 5.18a. In this situation, a complete release was impossible since the HF could not etch the oxide below the membrane. Several attempts were done until the etching process released the bus waveguides in fig. 5.18b; as a result, the devices were out of service.

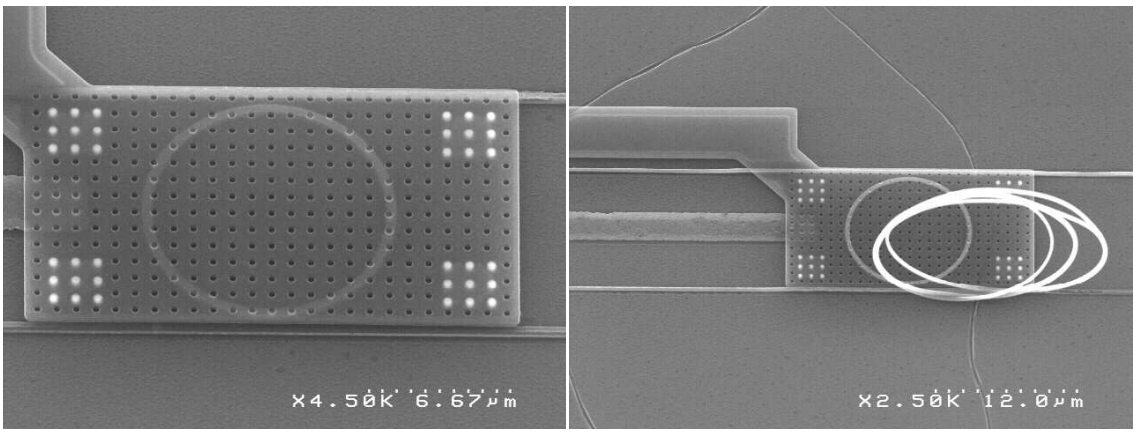

(a) (b)

Figure 5.18: Membrane fabrication error: (a) blind holes avoid the membrane release, the HF etching started only from the edges, (b) multiple HF etchings result in waveguide release.

But all is not lost: since we released only a quarter of the wafer, an additional AlSi patterning could be attempted to solve this problem on the other devices. The mask alignment and the photolithography on a rough surface are anyway tricky op-

erations.

5.8 Conclusions

On the basis of endorsed bricks (such as couplers, waveguides, ring resonators, cantilevers, membranes, and piezo-gauges), we designed and fabricated two electro-optomechanical devices coupling a *NEMS* to an optical ring resonator.
The uniqueness of these devices is the electrical actuation and a parallel piezoresistive detection which assures an independent readout of the cantilever displacement. This device is more than a *NEMS* mass sensor prototype but it is a tool to investigate the optomechanical transduction and the frequency noise in *NEMS* resonator.

Despite the wafer yield is low, we got enough in-plane cantilever devices for this work but, most importantly, we identified the sources of fabrication issues.

Chapter 6

Design and setup of test bench

The amazing phenomena at nanoscale have to be detected from our macroscopic world. For this reason, a big effort was done to build a dedicated experimental bench around the optomechanical samples above described in chapter 5.
Once the design of the masks was complete and the fabrication of devices was in progress, we started to design a custom optomechanical test bench. As it often happens, the characterization of an innovative technology needs an innovative experimental setup, this obliges physicists to a further effort in terms of creativity with the reward of obtaining results from scratch.
We anticipated possible upgrades in order to bequeath to the laboratory a flexible setup for future experiments.
The last step before measurements on the devices was to characterize the instrumentation around the chamber to evaluate the limits of the equipment and accuracy of the transduction.

6.1 Specifications and solutions

The starting point of the test bench design is the experimental setup currently used at the optics department of *CEA-Grenoble*, it enables to test photonic devices in air according to the standards of this laboratory. Two optical fibers are placed close to the wafer in order to inject and collect the light from the device. Although I draw inspiration by different test benches, the basic concept is an optical fiber fixed in the extremity of an arm which is displaced with 3-axis stage. The coupling angle is set by the geometry of the notch that hosts the fiber. Differently from previous systems, the optomechanical sample is placed in a vacuum chamber and linked electrically and optically to the equipments via sealed feedthroughs.

We fixed some ambitious targets for the optomechanical test bench:

- maximum sample size $3.5\,cm \times 3.5\,cm$
- alignment of two fibers ($1\,\mu m$ accuracy, tilt of $11.5°$)
- test of devices in a area of $13\,mm \times 13\,mm$ (without venting the chamber)
- from 1 to 3 electrical contacts for each device
- chamber pressure around $10^{-6}\,mbar$ ($< 10^{-4}\,mbar$)
- easy cryostat upgrade

Since the devices are hybrid (they have optical, electrical and mechanical elements), we need electrical connections between the device and the external equipments in order to perform the electric actuation and the piezoresistive detection. However the real challenge occurs when we combine these requirements with the need to work under vacuum. As a matter of fact, the cantilever has an improved mechanical quality factor at low pressure (at least $10^{-5}\,mbar$).

We designed two solutions:

- Vacuum chamber with internal motorized stages driven from outside (fig. 6.1)
- Vacuum chamber with external manual stages moving a travelling flange on a bellow (fig. 6.2)

The first solution has a relatively big chamber which hosts inside two 3-axis stages with related motors (fig. 6.1). Since the sample, the fibers and the stages are under vacuum, the alignment between the fiber and the coupler is very accurate and stable. We can say that this solution is the vacuum compatible version of the setup already built at the optical department, with the difference that, for obvious reasons, the positioners are driven electrically from outside.
The second solution has a smaller chamber (fig. 6.2), ideally, of the same size of the sample holder. The two fiber arms are welded to travelling flanges displaced by XYZ micrometer manipulators; the vacuum bellow is necessary to compensate the relative movement between the chamber and the flange. The alignment now is quite user-friendly (just screwing stage with hand) but the huge force on the flange demands strong micrometric screws with a not so accurate pitch. This means probably difficulties or long time spent for the alignment. The travelling flange is subject to two forces, the force due to pressure difference between outside and inside the chamber and the spring force of the mechanical deformation of the bellow. Since the minimum length of a bellow is fixed for mechanical stroke reasons, the length of the arms is significant; the thermal drift between sample and optical fiber arms could be an experimental setup problem.

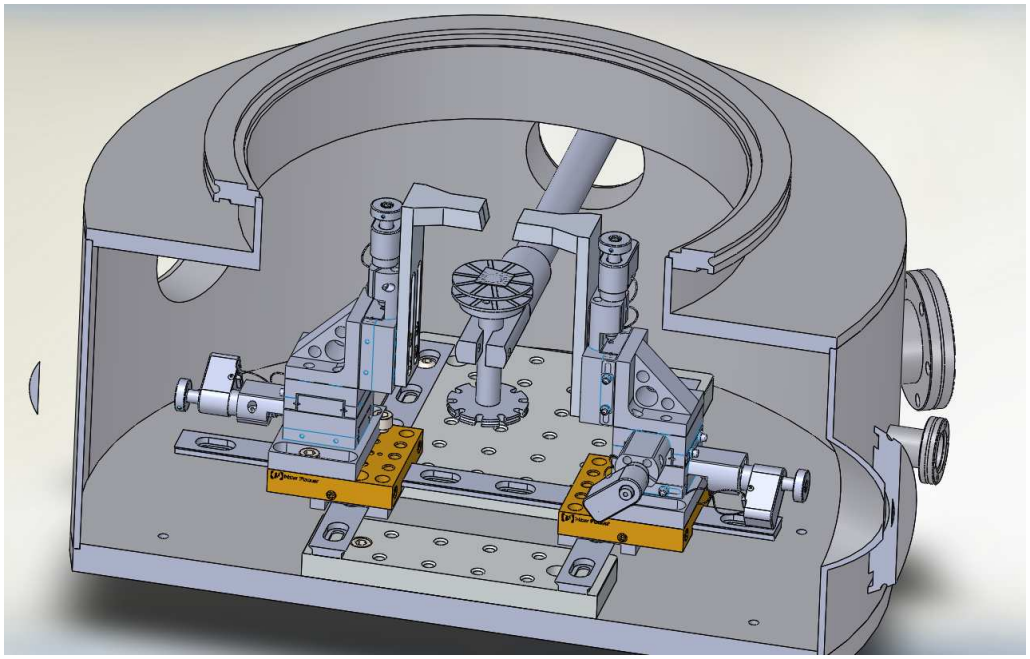

Figure 6.1: First solution scheme: the stages are vacuum compatible and driven from outside.

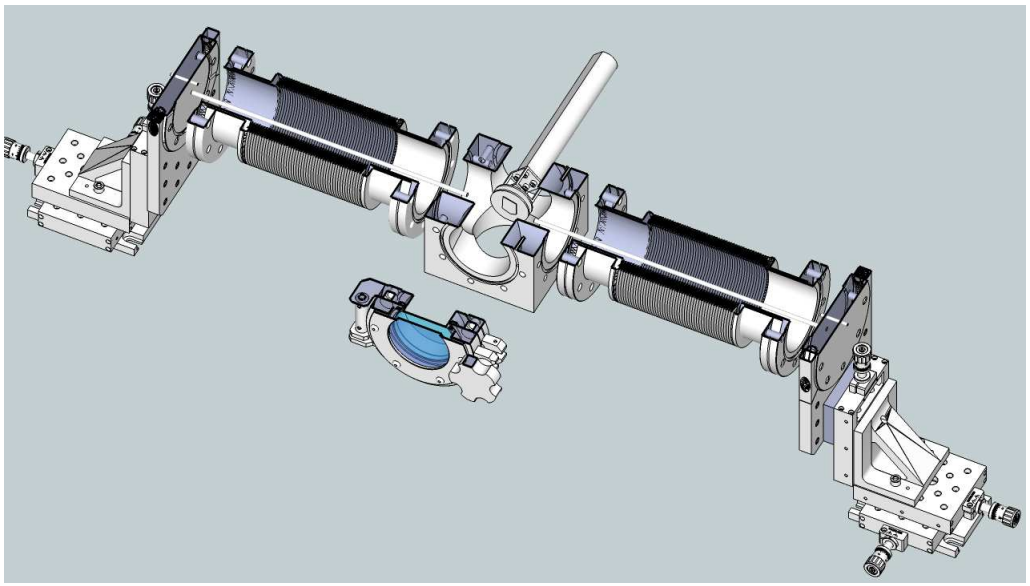

Figure 6.2: Second solution scheme: the external stages are under stress and probe arms are very long.

Finally, we chose the first solution: the risk of a low quality alignment due to thermal drift and poor accuracy of the manual stages was too big with respect to the difference in term of price between the two solutions. In addition, motorized stages allow automatic alignment so it would be possible to perform from now automatic tests over several devices.

6.2 Vacuum chamber, stages and fiber alignment

High vacuum is achieved in a semi-custom cylindrical chamber ($400\,mm$ diameter, $220\,mm$ height). On the lateral side, seven ports of different sizes are present for hosting the pump, the flanges with feedthroughs, the sample holder and the venting. On the top, the big port ($250\,mm$ of diameter) is for the sample charging and it is closed by a flanged viewport for the camera-assisted alignment. Whenever possible we used *ISO* flanges respect to *CF* type: they are less expensive, the fixation is performed quickly and the gasket are reusable.

At the bottom, ten tapped holes are in place to clench two breadboards and offer a versatile stand where the alignment system will operate. The alignment is performed by different steps: thanks to a system of rails, the two stages are displaced manually on the XY plane until the fiber holder is close to the sample holder, then the micrometric screws move narrowly the fibers toward the grating couplers. Then the fiber approaches the substrate until the contact and then it is retracted of 5-$6\,\mu m$. Now Z-axis is locked and we move the fiber exactly on top of the coupler. This operation is done with the help of the camera which provides a top view of the sample. Finally, the ultimate alignment is achieved injecting light into the device and maximizing the outcoming light signal. In this phase, the fibers are moved with an accuracy of $1\,\mu m$. The vacuum modifies slightly the geometry of the chamber and the relative fiber-sample distance. If the experiment requires vacuum, the pump must be switched on between the coarse and fine alignment.

Many sealed feedtroughs are necessary: we need to bias the motors and connect one or more devices to the external equipment.
The $6 \times 2 = 12$ wires for the motors go through a flanged *SubD* connector and are linked directly to control electronics. The electric contacts are made via wire bonding from device pads to the *PCB* card where sample is glued. This card fits into the sample holder which linked to the electric feedthroughs via 5 *SMA* cables. The optical fibers enter or exit from the chamber thanks to two flanged *FC-APC* feedthroughs.

The sample holder is put at the end of a cylindrical bar which is screwed on a

flange. This solution could look strange but this simplifies the upgrade when we want to add a cryostat to the test bench. In fact, the cold finger of the cryostat will replace the bar and cool down the sample holder. Temperature control avoids a thermal drift of the optical resonance and it is crucial for experiment concerning noise investigation and mass deposition in *MEMS*. The upgrade with the cryostat is currently under running.

6.3 Measurement equipments

Once the device is aligned and bonded, we plugged some equipments to the feedthroughs around the chamber: the injected light is provided by a laser and the output light is collected on a photodetector. A Lock-In Amplifier processes in parallel the signals from the photodetector and from piezoresistive gauge.

6.3.1 Laser

For all experiments, we used tunable laser from Yenista (T100S-HP CL). The main characteristics are resumed in the table 6.1:

Wavelength range	1500-1620 nm
Wavelength stability	$\pm 5\,pm/h$ ($\pm 3\,pm/h$; $\pm 5\,pm/24h$ *typical*)
Output power	$\leqslant 10\,dBm$
Output power stability	$\pm 0.01\,dB/h$ ($\pm 0.025\,dB/24h$ *typical*)
Relative intensity noise (RIN)	$-145\,dB/Hz$ ($\geq 0\,dBm$ / $100\,MHz$)
Spectral width (FWHM)	$400\,kHz$ *typical*
Absolute wavelenght stability	$\pm 20\,pm$
Wavelength setting repeatability	$5\,pm$ *typical*
Wavelength setting resolution	$1\,pm$
Continuous sweep speed	1-100 nm/s
High frequency modulation	30 kHz-200 MHz
Auxiliary λ output	0-5 V TLL

Table 6.1: Laser characteristics.

This laser is driven from remote via a GPIB/Python protocol. We can set, change and save any parameter value (λ, power, sweep speed, etc etc) in any moment of the experiment.
As we will see in section 7.2.1, the λ auxiliary output is fundamental for the continuous optical characterisation: the signal passes from 0 to 5 V when the laser cavity is sweeping. This gives us the start and stop instant of the wavelength sweep.

For the step-by-step characterisation (section 7.2.2), the ultimate resolution is limited to $1\,pm$.

6.3.2 Photodetectors

The photodetector is the element which converts the light signal into an electrical signal compatible with the LIA input. For this work, we used models built from a photodiode *p-i-n* and equipped with an integrated transimpedance amplifier.
The signal coming out from an integrated photodetector is:

$$V_{out} = G \cdot \mathcal{R}(\lambda) \cdot P_{in} \tag{6.1}$$

where P_{in} is the incident light power, $\mathcal{R}(\lambda)$ responsivity in $[A/W]$ and G is the transimpedance gain in $[V/A]$.

During the experiments, we used two photodetectors depending on the situation: the model 1881-FC-AC from *Newport* and the model OE-200-IN2 from *Femto*.
We chose the 1811-FC-AC for reasons of workability: the DC output signal is acquired during the fiber alignment and during the optical characterisation. Once the setup is tuned, we use the AC output for the optomechanical detection. The high-pass filter cuts the DC component coming from the laser avoiding the saturation of the LIA input (see section 7.3).
The model OE-200-IN2 fits well for the optomechanical downmixing (see section 7.4). The interesting noise performance at low frequencies assures a detection limited only by the laser shot noise.

The main characteristics for both photodetectors are summed up in table 6.2:

	Newport 1881-FC (DC output)	**Newport 1881-FC** (AC output)	**Femto OE-200-IN2**
Gain $[V/W]$	10^4	$4 \cdot 10^4$	10^4
Bandwidth	DC-$50\,kHz$	$25\,kHz$-$125\,MHz$	DC-$500\,kHz$
NEP $[pW/\sqrt{Hz}]$	x	$22.5\ at\ 17\,MHz$	$2.5\ at\ 10\,kHz$
Saturation power	$> 0.5\,mW$	$55\,\mu W$	$1\,mW$
Wavelength range	$900 - 1700\,nm$	$900 - 1700\,nm$	$900 - 1700\,nm$

Table 6.2: Photodetectors characteristics.

6.3.3 Lock-In Amplifier

For all the experiments we used a Lock-In Amplifier (LIA) from Zurich Instruments. The UHFLI model is a completely digital lock-in amplifier for signals up to

600 MHZ. The two independent inputs ($\pm 1.5\,V$) suit well for the double detection whereas the two outputs ($\pm 1.5\,V$) are used for the cantilever actuation, the gauge biasing or the light modulation. The signals are generated from the internal oscillators of the LIA.
The auxiliary inputs ($\pm 10\,V$) are useful for the optical characterisation of the ring resonator.
All the results were obtained driving the LIA from remote thanks to libraries and scripts in Python.

6.4 The complete setup

From sections 6.2 and 6.3, all the setup elements are chosen. The complete test bench is shown in fig. 6.3:

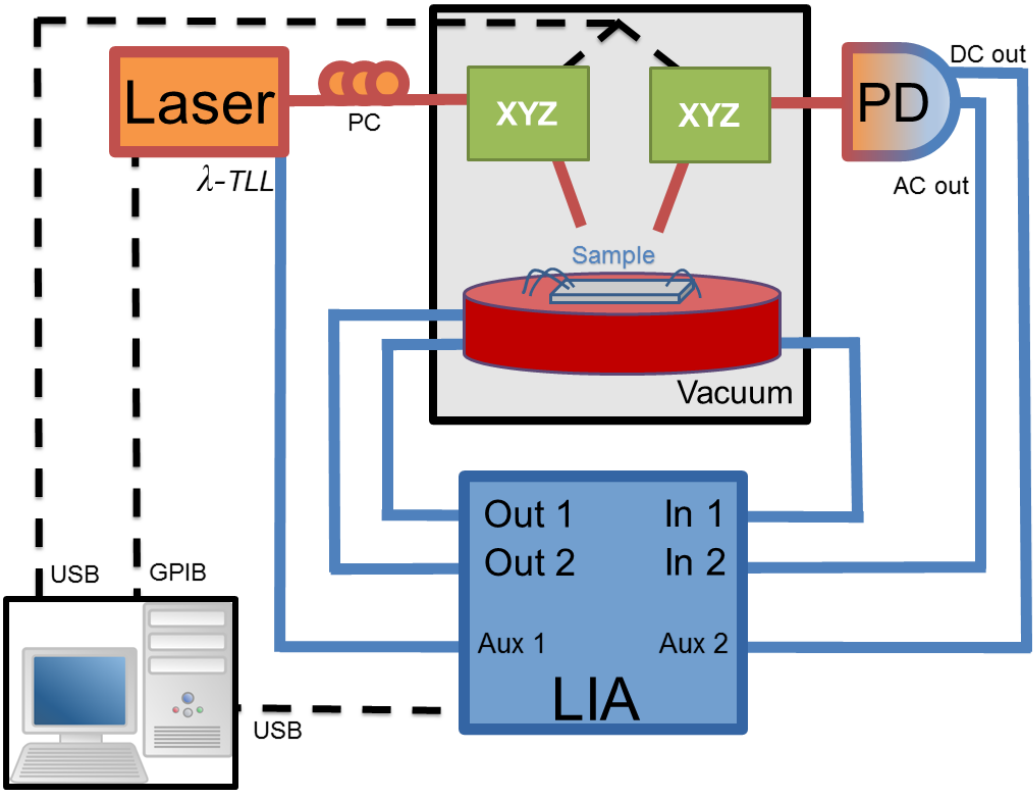

Figure 6.3: Complete scheme setup: the LIA, the stages and the laser are driven from the computer. The two optical fibers are aligned by the stages whereas the wire bonding assures the electric contacts. The electrical components are in blue, the optical components are in orange and the mechanical components are in green. The dashed lines indicate the remote control cables.

the sample inside the vacuum chamber is linked to the the external equipments via wire bonding and the aligned optical fibers. The laser, the LIA and the stages are remote controlled via the computer.
During his stage, Sébastien Dos Santos developed the Python code to drive the stages and designed a graphic user interface. His contribution simplifies the stages displacement operations and makes possible a semi-automatic alignment of the fibers with a view to automatic characterisation of several devices.
The LIA and the laser are driven via Python libraries and home-made scripts because most of the measurement would have been impossible only via LIA software or with manual set of the laser. The initial time spent in coding paid back in terms of versatility, measurement reproducibility and user comfort.

Last details of this setup are a polarisation maintaining fiber (PMF) and polarisation controller (PC) between the laser and the device. Between the laser and the optic table, we used a polarisation maintaining fiber since it avoids polarisation fluctuations due to fiber deformations caused by air currents or user movements (See sections 6.5.4 and 6.6.2). The polarisation controller, instead, provides a correct light polarisation at the input of the grating coupler (see section 5.3).

6.5 Test bench noise evaluation

Once the setup was complete, we calibrated the test bench and we evaluated its performances in terms of noise.
We classify here the noise sources which we expect along the transduction chain:

- Laser
  - Intensity noise
  - Wavelength fluctuation
- Mechanical resonator
  - Thermomechanical noise
  - Johnson noise of gauges
- Instrumentation
  - Lock-In Amplifier
  - Photodetector
- Light injection
  - Light polarisation fluctuation
  - Coupling misalignment

Only the thermomechanical noise and LIA noise are both present for optomechanical and piezoresistive transduction methods.

6.5.1 Laser noise

Since the *NEMS* displacement is measured by the means of a light signal, the laser noise power and its wavelength stability fix the resolution for the optomechanical transduction.

Out of resonance

Far away from the resonance, the power at the *drop* port is zero whereas at the *through* port is $P_0 = \alpha_c P_{laser}$ independently from the wavelength of the laser. (α_c are the coupling losses described in section 5.3).
The power noise density at the *through* port is:

$$S_{\mathcal{R}} = P_0^2 \cdot \frac{S_{\mathcal{R}}}{P_0^2} = P_0^2 \cdot 10^{RIN/10} \qquad [W^2/Hz] \tag{6.2}$$

where RIN is the *relative intensity noise* expressed in dB/Hz.
From data sheet of the laser, the RIN is equal to $-145\ dB/Hz$ at $100MHz$ for $P \geq 1\,mW$ but at *through* port, the light power is usually lower than $50\,\mu W$.
For a laser power of $50\,\mu W$, the RIN is limited by the shot noise:

$$\frac{S_\gamma}{P_0^2} = \frac{2h\nu P_0}{P_0^2} = \frac{2hc}{\lambda P_0} = \frac{2 \cdot 6.626 \cdot 10^{-34} \cdot 3 \cdot 10^8}{1550 \cdot 10^{-9} \cdot 50 \cdot 10^{-6}} = 5.13 \cdot 10^{-15}\, Hz^{-1}$$
$$\Rightarrow RIN_\gamma = -143\, dB/Hz > -145\, dB/Hz \quad (6.3)$$

Attenuating a laser beam, we attenuate at the same time the noise coming from the laser until the shot noise dominates:

$$S_\gamma = 2h\nu P_0 = \frac{2hcP_0}{\lambda} = \frac{2 \cdot 6.626 \cdot 10^{-34} \cdot 3 \cdot 10^8 \cdot 50 \cdot 10^{-6}}{1550 \cdot 10^{-9}} = 1.28 \cdot 10^{-23}\, W^2/Hz \quad (6.4)$$

Let us notice that $\sqrt{S_\gamma} = 3.578\, pW/\sqrt{Hz}$ could be higher or lower than the noise equivalent power of the photodetector (see eq. (6.19) in section 6.5.3).

On resonance

When the laser is tuned on the optical peak, any wavelength fluctuation is turned into a intensity fluctuation by virtue of the local peak slope. (See chapter 4)
In the best configuration, during an optomechanical transduction, the laser is set at the maximum slope of the *Lorentzian* response of the optical resonator as in fig. 6.4.

Assuming that the laser has a power noise density and a wavelength fluctuation completely independent, we add up the two contributions and estimate the power noise density at the *drop* or *through* port.

At the *through* output of the optical resonator we obtain a light power of

$$P_\mathcal{R}(\lambda, P_0) = P_0 \left(1 - \frac{C_\mathcal{R}\ \gamma_{opt}^2}{(\lambda - \lambda_r)^2 + \gamma_{opt}^2}\right) \quad (6.5)$$

where $C_\mathcal{R}$ is the contrast for the *through* port, λ_r is the resonance wavelength and $Q_{opt} = \lambda_r/2\gamma_{opt}$ is the optical quality factor. Q_{opt} and λ_r are fixed since are parameters of optical resonator and the laser power is attenuated by the couplers losses as follows $P_0 = \alpha_c \cdot P_{laser}$ (see section 5.3).
During the experiment, $\lambda_{laser} = \lambda_r - \frac{\sqrt{3}}{3}\gamma_{opt}$, so $P_\mathcal{R}(\lambda_{laser}) = P_0 - \frac{3}{4}P_0 C_\mathcal{R}$.
The total noise at the *through* port has two components, one from the intensity noise (in this case, the shot noise) and another due to the wavelength fluctuation.

$$S_\mathcal{R} = \left(\left.\frac{\partial P_\mathcal{R}}{\partial \lambda}\right|_{\lambda_{laser}} \cdot \delta\lambda\right)^2 + \frac{2hcP_\mathcal{R}}{\lambda_{laser}} \quad (6.6)$$

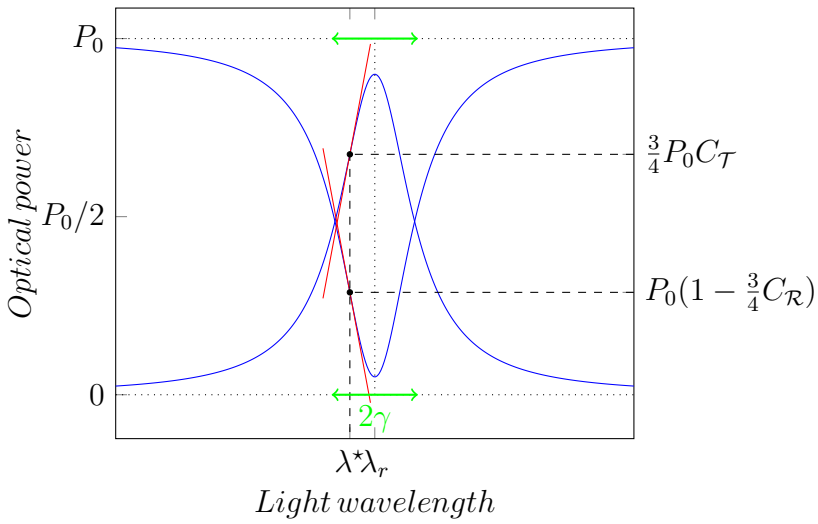

Figure 6.4: Lorentzian peak of the optical resonator with linear approximation around $\lambda^\star = \lambda_r - \frac{\sqrt{3}}{3}\gamma$. For simplicity, the plotted peaks have unitary contrast.

$$S_{\mathcal{R}} = \left(-\frac{3\sqrt{3}Q_{opt}P_0C_{\mathcal{R}}}{4\lambda_r}\cdot\delta\lambda\right)^2 + \frac{2hcP_0}{\lambda_{laser}}\left(1-\frac{3}{4}C_{\mathcal{R}}\right) \tag{6.7}$$

The laser noise transmitted through the ring resonator now depends also on the laser wavelength stability $\delta\lambda$.
Unfortunately, we do not have values for $\delta\lambda$ and the laboratory is not equipped for a direct measurement. We just observe an increased noise density at the photodetector output when the laser is tuned on the optical resonance peak. (Figure 6.10 in section 6.6.1)

6.5.2 Mechanical resonator noise

Thermomechanical Noise

Thermomechanical (or *Brownian*) noise is due to the *Brownian* motion of the particles which impact the cantilever and to internal processes like the phonon-phonon interaction. It could be explained as stochastic force acting in every direction but we observe it only in the direction of the beam deflection. This noise is a real mechanical displacement which is transduced by the piezoresistive and optomechanical detections. $S_f(\omega)$ is defined as a thermomechanical force spectral density with a white spectrum being equal to

$$S_f(\omega) = \frac{4M_n\omega_r k_B T}{Q_m} \qquad [N^2/Hz] \tag{6.8}$$

where M_n is modal mass of the cantilever mode, ω_r the resonance frequency, k_B the Boltzmann constant, T the temperature and Q_m the mechanical quality factor of the beam.
The mechanical resonator acts as a filter, so the spectral density of the cantilever displacement is obtained from the transfer function of a harmonic oscillator [71].
By limiting to the first mode, the cantilever displacement at the position x will result as

$$S_{th}(\omega) = \frac{\psi_1^2(x)}{M_1 Q_m} \frac{4\omega_r k_B T}{(\omega^2 - \omega_r^2)^2 + \left(\frac{\omega\omega_r}{Q_m}\right)^2} \qquad [m^2/Hz] \tag{6.9}$$

where $\psi_1(x)$ is the shape of the fundamental cantilever mode.
On resonance ($\omega = \omega_r$), the *thermomechanical noise* at the cantilever end ($\psi_1(L) = 1$) has an amplitude equal to

$$S_{th}(\omega) = \frac{4k_B T Q_m}{M_1 \omega_r^3} \qquad [m^2/Hz] \tag{6.10}$$

Johnson-Nyquist noise

It arises from the thermal agitation of electrical carriers in electrical conductors and it depends on resistance R and temperature T. It is a white noise whose power spectral density (PSD) is written as

$$S_J(\omega) = 4k_B T R \qquad [V^2/Hz] \tag{6.11}$$

Being a resistor, the piezoresistive gauge is affected by the *Johnson* noise whereas this noise is not present for the optomechanical detection. From a direct measure, the resistance of the gauges plus the wire bonding is around $50k\Omega$. It gives rise a noise of:

$$S_J(\omega) = 4 \cdot 1.3806488 \cdot 10^{-23} \cdot 298 \cdot 50 \cdot 10^3 \simeq 8.23 \cdot 10^{-16}\ V^2/Hz$$

6.5.3 Instrumentation noise

The equipments which read the signal coming from the devices (i.e. Lock-In or photodetector) are responsible for the instrumentation noise. A good experimenter works to minimize this noise until it becomes negligible respect to intrinsic noises like the *shot* noise, the *thermomechanical* noise or the *Johnson* noise which are due respectively to the laser, to the cantilever and to the gauges.

Lock-In Amplifier noise

The digital Lock-In Amplifier has an analog-to-digital converter for each *high frequency input*. From the datasheet, the best noise level is 4 $nV/\sqrt{Hz}$ but it depends on the frequency, on the input range and on the input impedance, as we can see from fig. 6.5.

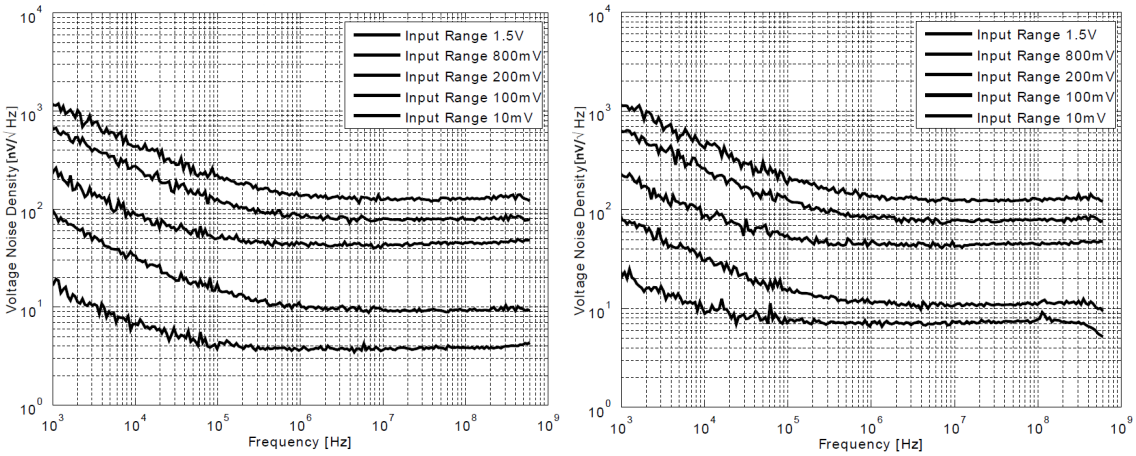

(a) 50 Ω input impedance (b) 1 $M\Omega$ input impedance

Figure 6.5: Voltage noise density at the LIA input

For piezoresistive and optomechanical detections, the instrumentation noise coming from the LIA is always negligible compared to the other noise sources.
For the optical characterisation of the ring instead, we use the *auxiliary inputs* as describe in section 7.2. We did not have noise information from the manufacturer but we will measure it experimentally in section 6.6.2.

Photodetector noise

The light collected from the device contains the signal of the *NEMS* displacement readout. The light signal has to be converted into an electrical signal before being processed by the LIA. That is why the photodetector noise is a key parameter which fixes the resolution of the optomechanical transduction. Most of the time, the photodetector is the limiting element of the transduction chain because its noise contribution is dominant compared to the light shot noise and to the LIA input noise. However, the optomechanical downmixing technique enables a transduction using photodetectors with interesting noise level (see section 7.4).
The noise sources in a photodetector are mainly three:

- Noise from internal resistance

- Noise from biasing
- I/V amplifier noise

A photodiode in the dark without biasing exhibits *Johnson* noise due to finite resistance of the depletion layer of the p-i-n junction. This current noise spectral density is

$$S_{SH}(f) = \frac{4k_BT}{R_{SH}} \qquad [A^2/Hz] \tag{6.12}$$

In presence of biasing, the dark current I_d generates shot noise, so the current noise density results

$$S_i(f) = \frac{4k_BT}{R_{SH}} + 2eI_d \qquad [A^2/Hz] \tag{6.13}$$

Finally, the current signal is converted to a voltage signal thanks to the I/V amplifier, so the voltage noise density at the photodetector output results

$$S_V(f) = |G(f)|^2 \cdot \left(\frac{4k_BT}{R_{SH}} + 2eI_d + S_a(f)\right) \qquad [V^2/Hz] \tag{6.14}$$

being $S_a(f)$ the noise spectral density at the input of the I/V amplifier and $G(f)$ the transfer function of the I/V amplifier. Since the I/V amplifier is integrated in our photoreceivers, we have an experimental access only to $S_V(f)$ and not to single noise terms.
If we bring back $S_V(f)$ to the photodetector input, we obtain the *noise equivalent power* (NEP):

$$\mathrm{NEP}(f) = \frac{\sqrt{S_V(f)}}{|G(f)| \cdot \mathcal{R}(\lambda)} = \frac{\sqrt{\frac{4k_BT}{R_{SH}} + 2eI_d + S_a(f)}}{\mathcal{R}(\lambda)} \qquad [W/\sqrt{Hz}] \tag{6.15}$$

Often happens that the limiting noise comes from the I/V amplifier term $S_a(f)$. In our case, we will find out a measured NEP which is not flat (see 6.6.1). This means that the *shot* or the *Johnson* noise cannot be the dominant noises since their spectra are flat by definition.

Now, if we light the diode with a light beam, the current photogenerated will add an extra shot noise

$$S_i(f) = \frac{4k_BT}{R_{SH}} + 2e(I_d + I_L) \qquad [A^2/Hz] \tag{6.16}$$

$$S_V(f) = |G(f)|^2 \cdot \left(\frac{4k_BT}{R_{SH}} + 2e(I_d + I_L) + S_a(f)\right) \qquad [V^2/Hz] \tag{6.17}$$

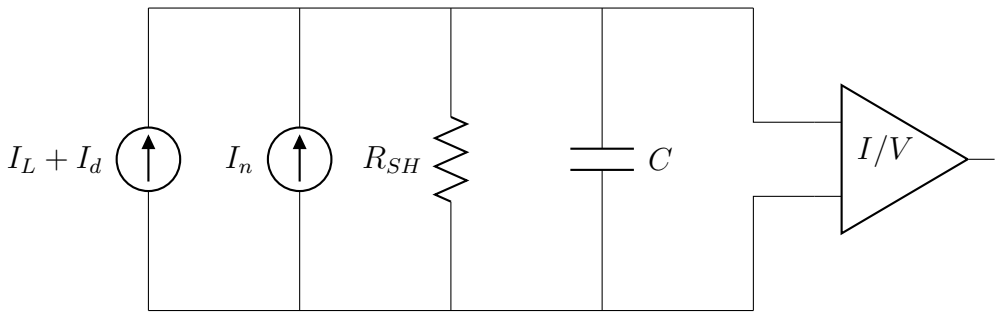

Figure 6.6: The equivalent circuit for a photoreceiver: I_L is photogenerated signal, I_d the dark current, I_n the source of noise calculated integrating eq. (6.16) over the measurement bandwidth. R and C are the resistance and the capacitance of the depletion layer of the diode, they act as a low-pass filter reducing the photodetector bandwidth. Actually the photodetector bandwidth is limited by the I/V amplifier.

The signal-to-noise ratio for a noise equivalent bandwidth $NEBW$ will result:

$$\frac{S}{N} = \frac{V_{out}^2}{\int_{BW} S_V(f)\, df} = \frac{\mathcal{R}^2 \cdot P_{in}^2}{\left[\frac{4k_BT}{R_{SH}} + 2e(I_d + \mathcal{R} \cdot P_{in}) + S_a(f)\right] \cdot NEBW} \tag{6.18}$$

Increasing the incident light power P_{in}, the shot noise coming from incident light will be the dominant noise and the signal-to-noise ratio scales linearly with the power. The upper limit for incident power comes from non linearities (or saturation) of the transimpendance amplifier. In practice, the beam power is limited by thermal effects occurring in the optical ring which lead to a non-linear optomechanical transduction as we will see in section 7.2.

From the datasheet, the noise equivalent power (NEP) of the 1811-FC-AC photodetector is

$$NEP(f) = \begin{cases} 2.5\ pW/\sqrt{Hz} & \text{for } 0 < f < 10\ MHz \\ 22.5\ pW/\sqrt{Hz} & \text{for } 10 < f < 200\ MHz \end{cases} \tag{6.19}$$

If we multiply these values for the transimpedance gain $G = 40\,000\ V/W$, we obtain a voltage noise density at the output of the detector equal to

$$\sqrt{S_V(f)} = \begin{cases} 100\ nV/\sqrt{Hz} & \text{for } 0 < f < 10\ MHz \\ 900\ nV/\sqrt{Hz} & \text{for } 10 < f < 200\ MHz \end{cases} \tag{6.20}$$

For a light beam of $50\,\mu W$, the shot noise is around $3.6\,pW/\sqrt{Hz}$. The noise contribution coming from the photodetector (i.e. the NEP) is expected higher than the shot noise around the mechanical resonance frequency ($\sim 17\,MHz$).

6.5.4 Light injection

Other noises arise from the light coupling mechanism and by the mechanical instability of the setup. To be precise, they turn up when light passes through the two couplers even if the optical or mechanical resonators are not present. A packaging of the device with optical bonding removes this sources of noise but obliges a single device preparation. This solution is suitable only for a small number of devices made with a mature process where the yield is high.

Light polarisation fluctuation

The grating couplers on the wafer are sensible to light polarization since they are optimised for TE mode (see section 5.3). Every bending of the fibers changes the light polarization inside the fiber core, and since the coupler acts like a polarisation filter, the result is an attenuation of the light signal injected into the device.
The fiber bending is due to the pump vibrations, to air currents and to user movements and it causes a light modulation detected from the photodetector.
The solution is to use a polarization-maintaining fiber (PMF) between the laser and the polarization controller (PC) and to fix mechanically the fiber between the polarisation controller and the input coupler.
The output fiber is not affected because the photodetector is not sensible to light polarization.

Coupling misalignment

The fiber and the light coupler are aligned with the help of micrometric stages which move a fiber holder. During an experiment, a thermal drift modifies the relative position between fiber and coupler. This gives rise to an attenuation of the power light injected or collected into and from the device. Thermal drift effect is significant at the scale of hours. (See fig. 6.7)

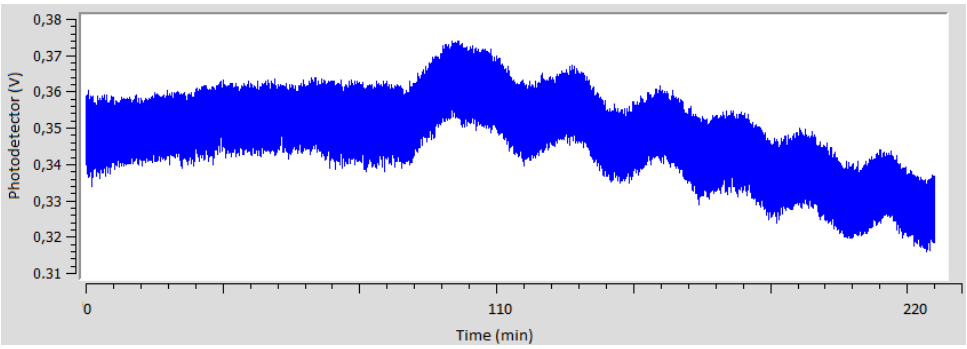

Figure 6.7: Fiber-coupler misalignment due to thermal drift over 220 minutes.

A similar misalignment occurs at higher frequency: especially under vacuum, the end of the fiber vibrates like a single clamped cantilever. This induces a light modulation at the mechanical resonance frequencies of the system formed by the fiber holder plus the fiber. (See fig. 6.8). The magnitude of this noise could be evaluated performing two different measures: a normal alignment and a special one having the fiber in full contact with the substrate.

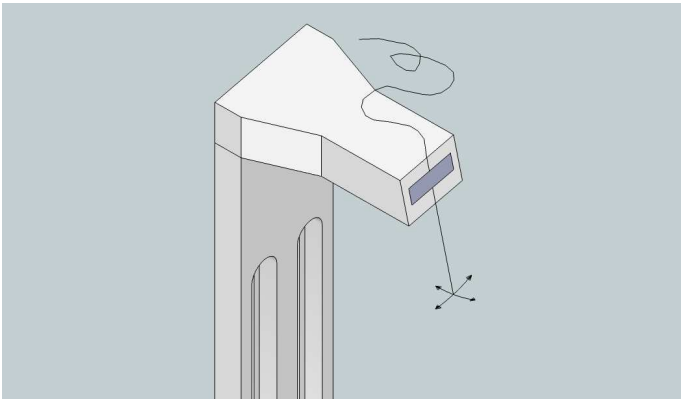

Figure 6.8: Oscillations of the fiber clamped into the fiber holder.

In presence of a damper which isolates the pump vibration from the vacuum chamber, this noise is partially reduced but further optimisations on the fiber aligning system are advisable.

6.6 Test bench noise measurements

In the following pages we will characterize experimentally the noise contributions in the optomechanical setup. Whenever possible, we compared the experimental values to the expected noises described in the previous section 6.5.
In the next subsection 6.6.1, we test the AC output of the photodetector *NewPort* plugged to the *high frequency input* of the Lock-In Amplifier. This test is performed to evaluate the noise level during the optomechanical transduction (section 7.3).
The subsection 6.6.2 tests the DC output of the photodetector *NewPort* plugged to the *auxiliary input* of the Lock-In Amplifier. It aims to evaluate the noise level during the acquisition of the optical spectrum on a ring resonator (section 7.2).

6.6.1 Noise investigation for the optomechanical detection

First of all, we evaluate the noise level of the *analog to digital converter* of the LIA: performing a power spectral density with a 50 Ω plug, we find out a noise level around 6.5 $nV/\sqrt{Hz}$ (black curve in fig. 6.9), in agreement with specification in fig. 6.5a.

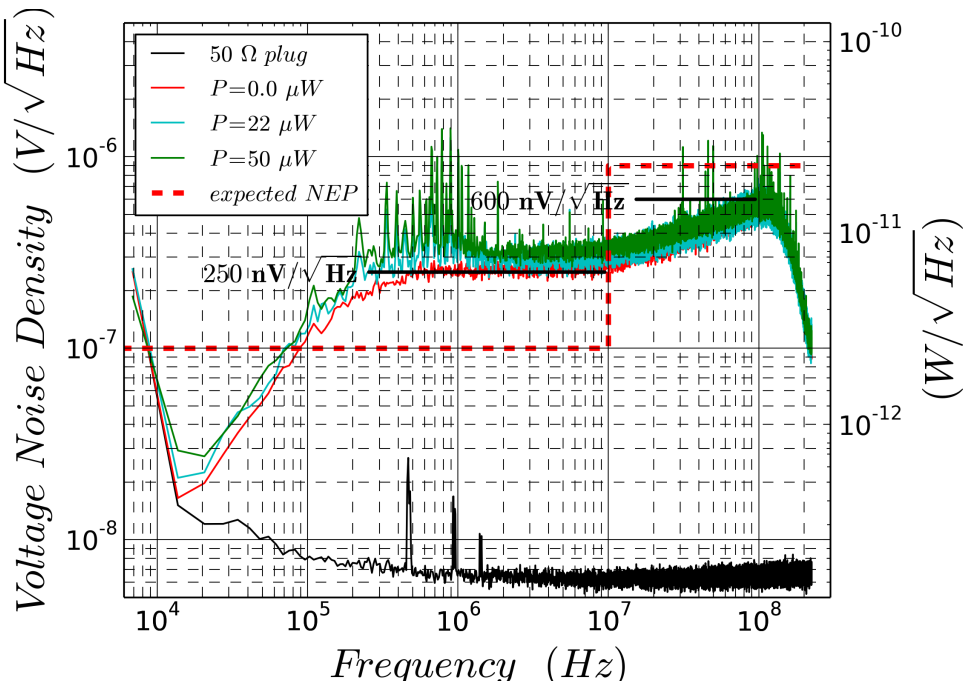

Figure 6.9: Voltage noise density of the system made up of LIA, PD, attenuator and laser: LIA noise is order of magnitudes smaller than the NEP. The laser shot noise shows up in particular for frequencies where the NEP is smaller.

Then we plug the AC output of photodetector *NewPort*, first in the dark to measure the NEP and then with an increasing DC light power. Between the laser and the photodetector, there is a passive 16dB-attenuator to avoid saturation simulating the coupling losses of the device.
From the figure 6.9, we notice that the *analog to digital converter* at the LIA input has a noise which is orders of magnitude lower than the photodetector and the laser. The measured NEP (red curve) shows clearly the bandwidth of the photodetector limited at $125MHz$. Between 0 and 10 MHz we observe a noise of 250 $nV/\sqrt{Hz}$, then it grows up to 600 $nV/\sqrt{Hz}$ for higher frequencies. The photodetector noise is in partial agreement with the nominal NEP in eq. (6.20) which is shown by the dashed red line.
From red, cyan and green curves, we can discern the shot noise of the light beam from the photodetector noise. It is evident only for frequencies in between 0.7 and 10 MHz, where the NEP contribution to the total noise is smaller. For $50\mu W$ on the photodetector, the total noise density will be:

$$\sqrt{S_{tot}} = \sqrt{S_\gamma + NEP^2} = \sqrt{143^2 + 250^2} = 288\, nV/\sqrt{Hz} \tag{6.21}$$

a value compatible with the green curve in fig. 6.9.
The laser adds to the noise spectrum also a series of harmonics in the ranges of 0.2-2 MHz and 30-125 MHz.

We replace now the light attenuator with the device placed into the vacuum chamber in a pressure around of $10^{-5}\, mbar$. The light is coupled into the device thanks to the fiber alignment system shown in fig. 6.1.
From the cyan and blue curves in fig. 6.10, we notice that the presence of the device increases the noise density further in the range 1-20 MHz, where the *NEP* does not dominate. This noise is probably due to oscillations of the fiber ends in proximity of grating coupler.
If now, we tune the laser wavelength on an optical resonance peak (purple curve), we notice two things: the noise density increases again and a peak shows up at 17 MHz. Since the optical cavity is a narrow wavelength filter, any wavelength oscillation is translated in intensity fluctuation, so the additional noise could originate from a wavelength noise of the laser described in section 6.5.1. In any case, further investigation is required.

Figure 6.11 is a zoom on the peak at 17 MHz: as soon the wavelength is correctly tuned, we are able to detect the cantilever displacement via the optomechanical transduction. This peak is the first and involuntary signature of the *thermomechanical noise* of the cantilever described in section 6.5.2. Despite the frequency resolution being rough, the peak position, the amplitude and the noise floor are compatible with a more accurate measurement in fig. 7.16.

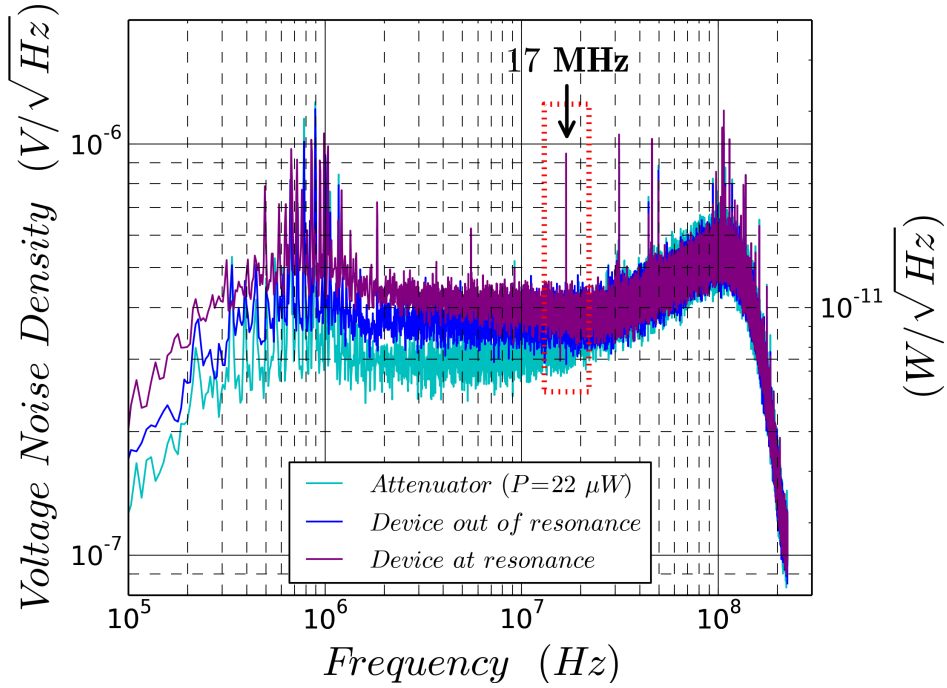

Figure 6.10: Voltage noise density of the system made up of laser, device, PD and LIA: the presence of the device increases the noise density due to the NEP and to the shot noise. A further noise source comes on top if the laser is tuned on the resonance peak.

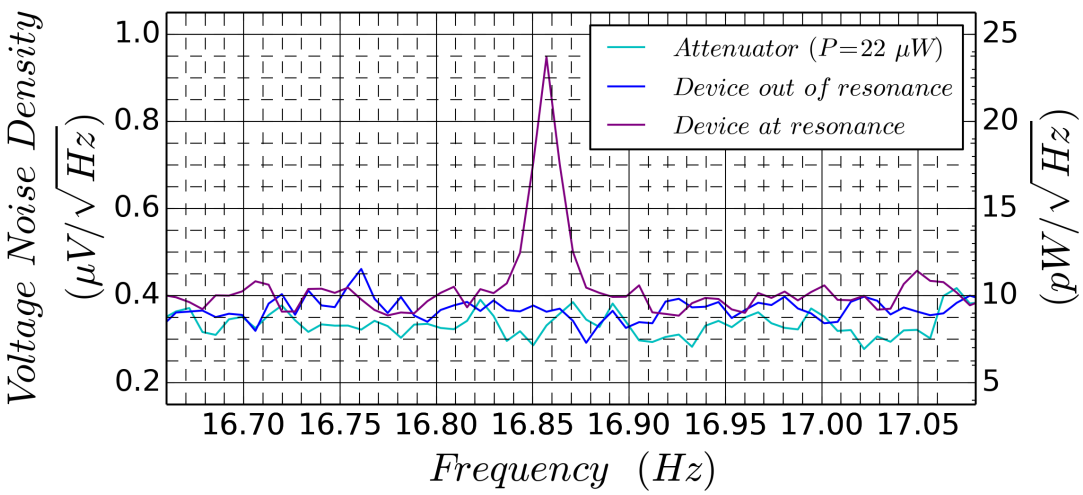

Figure 6.11: First (involuntary) detection of thermomechanical noise.

6.6.2 Noise investigation for the optical characterisation

A noiseless optical characterisation of the device allows a good knowledge of the optical ring and a good choice of the wavelength for the optomechanical transduction. As we will see in section 7.2, the optical characterisation of the device is performed via the DC output of the photodetector *NewPort* plugged to the *auxiliary input* of the Lock-In Amplifier.

As in the previous subsection, we start recording the *voltage noise density* of the *Auxiliary Input* with a 50 Ω plug, then we add, in the order, the photodetector, the laser (attenuated of $16dB$) and finally the device.
From the plot in fig. 6.12, we have the noise density of the auxiliary input (black curve) quite flat around to $10^{-5}\,V/\sqrt{Hz}$. The NEP (in red) is slightly higher than the input noise, especially in between 1 and $10\,kHz$, where a lot of harmonics are added. The 50 kHz-bandwidth of the DC output is consistent with the datasheet.

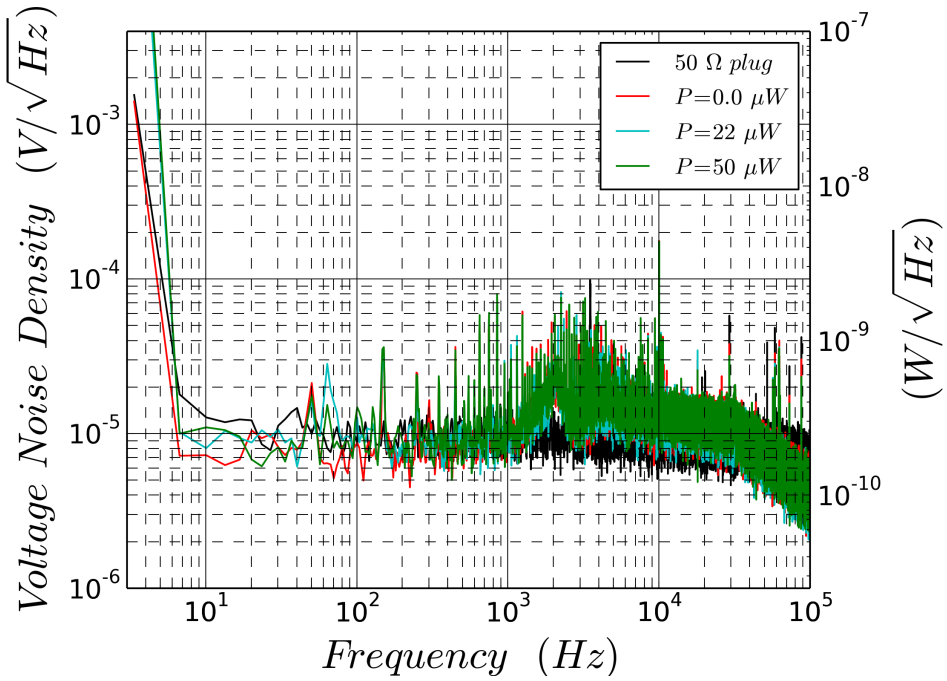

Figure 6.12: Voltage noise density at the *auxiliary input*: the noise level is set by the NEP of the photodetector DC output.

In this case, the shot noise from the laser beam is insignificant for power up to $50\,\mu W$, so cyan and green curves are superimposed to the *NEP* data in red.

We replace now the light attenuator with the device placed into the vacuum

chamber in a pressure around of $10^{-5}\,mbar$. The light is coupled into the device thanks to the fiber alignment system shown in fig. 6.1. When the optical attenuator is replaced by the device and its grating couplers, the situation changes drastically (see fig. 6.13):

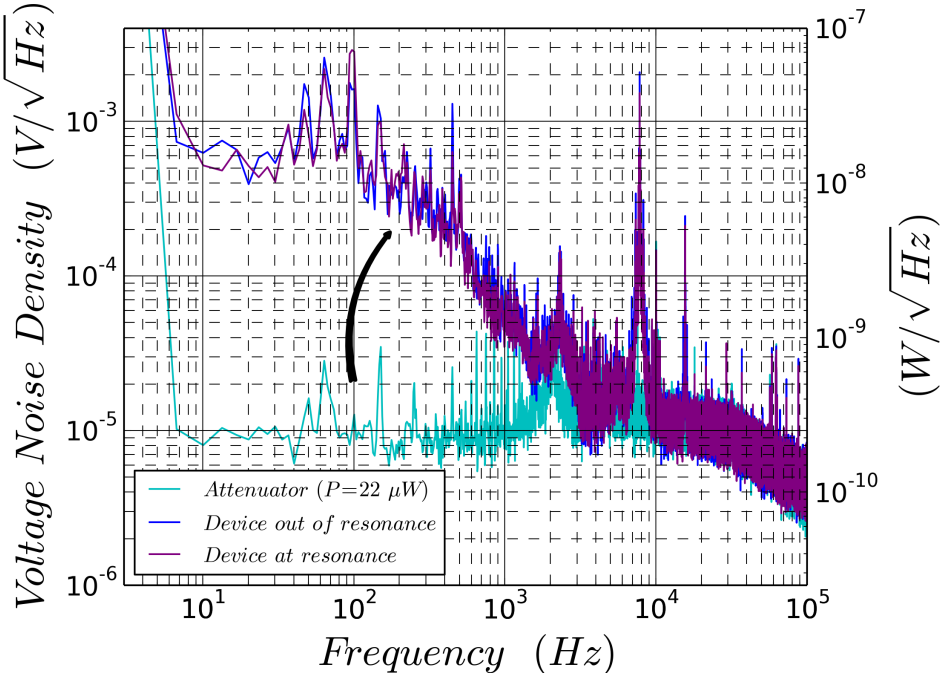

Figure 6.13: Voltage noise density at the *auxiliary input*: the presence of the device and the couplers adds low frequency noise and a peak at $8\,kHz$.

Now the biggest contribution to noise comes from the presence of the device, especially at very low frequency where the optical characterisation is performed. The probable responsible of this noise is the oscillation of the fiber alignment system relative to the grating couplers. Some clear peaks around $100\,Hz$, $500\,Hz$, $8\,kHz$ and $10.5\,kHz$ are detected, the origin is today unexplored but these frequencies should match the in-vacuum resonance frequencies of the fiber clamped into the holder (see fig. 6.8).
The pump seems not to be the cause of these vibrations, because switching off the pump the noise spectrum is not modified.

These last two sections (6.6.1 and 6.6.2) fix the noise level which affects all the optomechanical detections and all ring characterisations in the following chapter.

From fig. 6.11, we expected an optomechanical transduction at $17\,MHz$ having a noise floor of $0.4\,\mu V/\sqrt{Hz}$. The main responsible is the photodetector noise but

smaller contributions come from the laser and the coupling system.

The optical characterisation is affected by low frequency noise ($1\,mV/\sqrt{Hz}$) due to drift and vibration of the fiber holders (see fig. 6.13). The immediate solution is to reduce the measurement bandwidth as much as possible via a low-pass filter or to perform a step-by-step characterisation shown in section 7.2.2.

For future works, a proper packaging of the devices could eliminate the alignment step and cancel the noise introduced by the oscillation of free-end fibers under vacuum.

6.7 Conclusions

We developed a complete test bench for testing the opto-electromechanical devices under vacuum. This setup enables the characterisation of tens of devices injecting and collecting the light by the means of two optical fibers aligned to the wafer. Electrical connections are in place to perform the electrical actuation and the piezoresistive detection of the cantilever.
The hybrid nature of the devices obliged us to reflect long time on fibers alignment, electrical cabling, space constraint and vacuum compatibility of the components. Also a good understanding of the laser and photodetector physics was key. All these aspects make the optomechanical test bench an interesting instrumentation challenge.

Once the system was complete, we evaluated and measured the noise performance of the entire setup: this configuration offers an optomechanical transduction with a noise level of $0.4\,\mu V/\sqrt{Hz}$ within the typical frequency range of these devices ($1-30\,MHz$). This noise level is more than adequate to detect the thermomechanical noise displacement of the cantilever.
However, the alignment system and the free-end fibers suffer from low frequency vibrations which preclude a long-term and stable device coupling. A proper packaging could easily solve this issue.

By having this experimental setup, we are ready for the characterisation of the optomechanical devices.

Chapter 7

Experimental characterization of the device

This chapter reports the experimental characterisation of the in-plane cantilever device described in section 5.4.1. The efforts in device fabrication (chapter 5) and in the test bench setup (chapter 6) are rewarded with the results which are shown in the following pages. Unless otherwise indicated, all the measurements are performed on the device #3 illustrated in fig. 5.9.
The general purpose of this chapter is to demonstrate the performances of our optomechanical system: the ultimate goal is to develop a *NEMS* devices similar to [61] and [2] which benefit from the optomechanics better performances and a simplified multiplexing.

Preliminary measurements are performed to test the mechanical and photonic parts separately. Then, the optomechanical transduction of the cantilever is studied for different drive voltages and for different wavelengths.
The detection of *thermomechanical noise* of the resonator proves the performance of the optomechanical transduction. Moreover, it makes possible a calibration of the transduction and an evaluation of the optomechanical coupling factor.
An *in-situ* comparison between transductions is possible only by having a parallel detection on the same mechanical resonator: this is the innovative aspect of these devices. By the means of the double detection, we investigate not only the linearity of the optomechanicanical detection but the frequency stability of the cantilever: the two completely independent readouts accredit the hypothesis of a mechanical origin for frequency fluctuations in silicon resonators [8].
Since a limiting noise for the readout is the photodetector NEP, the optomechanical downmixing technique is developed to shift the transduction signal to an arbitrary low frequency: now we can detect up to the third resonance mode using low-bandwidth photodetectors which have interesting performances in terms of

noise. The optomechanical downmixing fits for the *NEMS* mass spectrometry which requires the tracking of higher mechanical modes at risen frequencies. (See sections 2.3.2 and 2.4).
We test as well the possibility of an optical actuation of the cantilever via the optical gradient force. Despite the actuation efficiency being weaker with respect to electrostatic actuation, we can measure the cantilever displacement thanks to the piezoresistive detection. At longer term, we aim to obtain a transduction and an actuation which are simultaneously performed by the means of optomechanics.

7.1 Piezoresistive detection

Since the release is the trickiest step of technological fabrication, the first experiment aims to check the status of the devices with a purely electrical characterisation. As described in section 5.5, in-plane cantilevers have a parallel piezoresistive detection and an electrostatic actuation.
The aim is to inspect if the mechanical resonator moves in a proper way and to find its resonance frequency.

As for an usual *M/NEMS* characterisation, we excite the cantilever through the electrode and we measure the displacement thanks to the piezoresistive gauge. In this case, we have a single gauge device where the variation of resistance δR is proportional to the deflection of the cantilever. The downmixing technique [70][69] increases the *signal-to-noise background* (SNB) of the transduction and bypasses the *cut-off frequency* of the cables and the *NEMS* resistor which form a low-pass filter.

7.1.1 Cut-off frequency of the system

The equivalent electrical scheme for the piezoresistive detection setup is shown in figure 7.1. Calculating the transfer function $H(\omega)$ of the voltage divider formed by the device resistance and the setup impedance, we can evaluate the cut-off frequency f_c of the system.

We consider the device impedance as purely resistive: R_g is the resistance of the unstressed gauge and δR is the variation of resistance which is proportional to cantilever displacement. By the means of piezoresistive properties of the nanogauge, δR is always negligible with respect to R_g.
Then we calculate the setup impedance Z_{setup} formed by the LIA impedance plus the cable capacitance. The cable resistance is considered negligible with respect to R_{LIA}.

$$Z_{setup} = \frac{R_{LIA}}{1 + jR_{LIA}C_{setup}\,\omega} \tag{7.1}$$

where $C_{setup} = C_{cable} + C_{LIA}$.
From the formula of a voltage divider,the transfer function of the system results as

$$\boxed{H(\omega) = \frac{V_{out}}{V_{bias}} = \frac{R_{LIA}}{R_{LIA} + R_g}\frac{1}{1 + j\dfrac{R_g R_{LIA} C_{setup}}{R_g + R_{LIA}}\omega}} \tag{7.2}$$

In other words, the setup acts a low-pass filter having a cut-off frequency equal to

$$\boxed{\omega_c = \frac{R_g + R_{LIA}}{R_g R_{LIA} C_{setup}}} \tag{7.3}$$

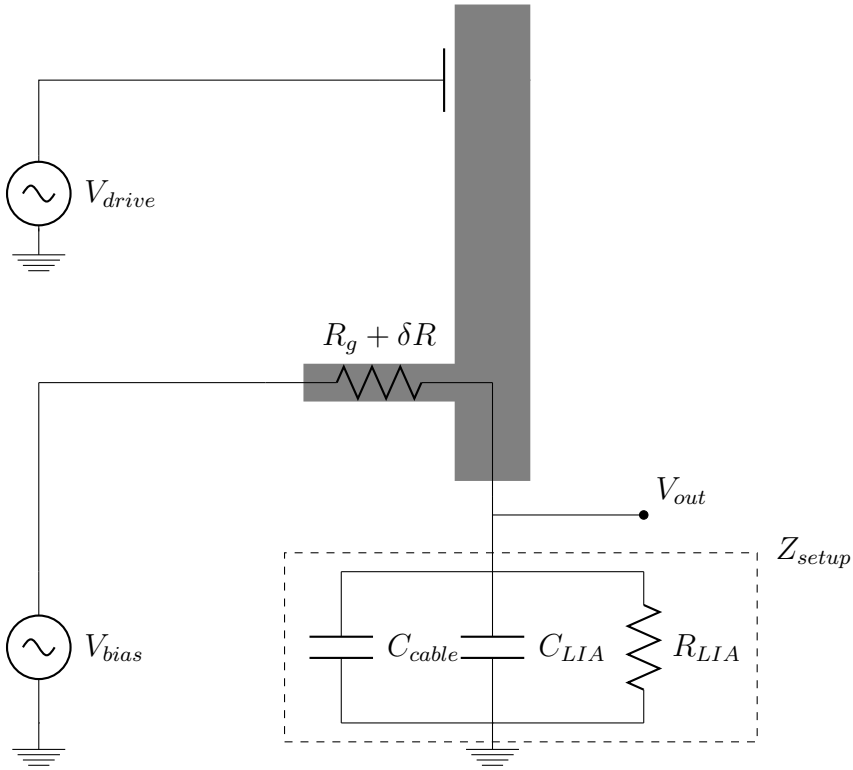

Figure 7.1: The equivalent circuit for the piezoresistive detection: the device resistance $R_g + \delta R$ and the setup impedance Z_{setup} form a voltage divider. δR is the variation of the gauge resistance as a consequence of the cantilever displacement.

From a two-terminal measurement, we obtain $R_g = 74.7\,k\Omega$ and we know $C_{cable} = 100\,pF/m$, $R_{LIA} = 1\,M\Omega$ and $C_{LIA} = 16\,pF$ from the specifications.
Using a cable $1\,m$ long, we estimate the cut-off frequency as follows:

$$\omega_c = \frac{74.7 \cdot 10^3 + 10^6}{74.7 \cdot 10^3 \cdot 10^6 \cdot 116 \cdot 10^{-12}} \simeq 124 \cdot 10^3\,\mathrm{rad}/s \tag{7.4}$$

$$\boxed{f_c = \omega_c/2\pi = 19.74\,kHz} \tag{7.5}$$

It means that the transduction signal components above f_c are attenuated by the low-pass filter built by the parasitic capacitance of the setup. Since our devices oscillate at several MHz (see table 5.3), a direct detection of *NEMS* displacement may be impossible. For the piezoresistive detection, we have to adopt the downmixing approach described in the following section.

7.1.2 The piezoresistive downmixing

To deal with the cut-off frequency of the system in eq. (7.5), we implement the downmixing scheme for the piezoresistive gauge readout [72][70].
We actuate the cantilever at frequency ω or $\omega/2$ applying a sinusoidal drive voltage to the electrode

$$V_{drive}(t) = V_{drive}\cos(\omega t) \text{ or } V_{drive}\cos(\omega t/2) \tag{7.6}$$

with $\omega \gg \omega_c$. The generic drive frequency ω is much higher than the cut-off frequency in eq. (7.4) because the mechanical resonance frequency for such cantilever is in the order of tens of MHz. In both cases, from section 5.6, the applied force has a component at frequency ω and the cantilever oscillates at frequency ω, modifying, as consequence, the gauge resistance

$$\delta R(t) = \delta R\cos\left[\omega t + \phi(\omega)\right] \propto x(\omega)\cos\left[\omega t + \phi(\omega)\right] \tag{7.7}$$

$x(\omega)$ and $\phi(\omega)$ are the magnitude and phase response of the cantilever for an excitation at frequency ω. The resistance variation δR is an image of the cantilever displacement. From eq. (5.3), the cantilever response $x(\omega)$ is proportional to V_{drive} or to V_{drive}^2 depending on the ω or $\omega/2$ excitation.
Applying the basics of the the electrical downmixing, we polarize the gauge with a bias voltage at frequency slightly different from the drive frequency, such as $\omega + \Delta\omega$, where $\Delta\omega \ll \omega_c \ll \omega$

$$V_{bias}(t) = V_{bias}\cos[(\omega + \Delta\omega)t] \tag{7.8}$$

Like the drive frequency, the bias frequency is well above the cut-off ($\omega + \Delta\omega \gg \omega_c$), so V_{out} will be negligible compared to V_{bias} since $H(\omega + \Delta\omega) \ll 1$. The current flowing through the gauge results as

$$I_g = \frac{V_{bias} - V_{out}}{R_g + \delta R} \simeq \frac{V_{bias}}{R_g + \delta R} \simeq \frac{V_{bias}}{R_g}\left(1 - \frac{\delta R}{R_g}\right) \tag{7.9}$$

It means that the output voltage at the first order in δR is

$$V_{out} = V_{bias} - R_g I_g = V_{bias}\frac{\delta R}{R_g} \tag{7.10}$$

The output signal is the result of a mixing between the bias signal and the signal due to the gauge compression. Thanks to eq. (7.7) and (7.8), we write the explicit expression for the output voltage

$$V_{out}(t) = V_{bias}\frac{\delta R(\omega)}{R_g}\cos[(\omega + \Delta\omega)t] \cdot \cos\left[\omega t + \phi(\omega)\right] \tag{7.11}$$

applying the *Werner* formula, we obtain

$$V_{out}(t) = V_{bias}\frac{\delta R(\omega)}{R_g}\frac{\cos[\Delta\omega t - \phi(\omega)] + \cos[(2\omega + \Delta\omega)t + \phi(\omega)]}{2} \tag{7.12}$$

Focusing on the first term of eq. (7.12), we note that the magnitude and phase of the cantilever, which vibrates at frequency ω, are moved to the downmixing frequency $\Delta\omega$. For cantilevers having a resonance frequency in the order of MHz, only the component at $\Delta\omega$ passes through the low-pass filter in eq. (7.2) and it is measured via synchronous detection by the LIA:

$$|V_{LIA,\Delta\omega}(\omega)| = \frac{V_{bias}}{2\sqrt{2}R_g}\delta R(\omega) \propto \frac{V_{bias}}{2\sqrt{2}R_g}x(\omega) \tag{7.13}$$

The factor $\sqrt{2}$ is due to the fact that the LIA measure a RMS value of the signal amplitude.
The electrical downmixing technique is presented by the scheme in fig. 7.2:

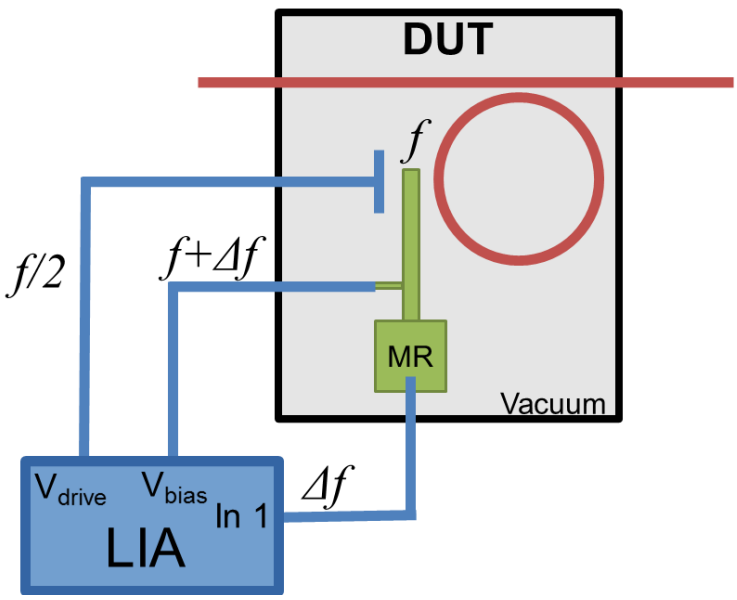

Figure 7.2: Piezoresistive downmixing setup. DUT: device under test, MR: mechanical resonator, LIA: LockIn amplifier. In blue the electric elements, in orange the optics and in green the mechanical domain.

Experimentally, we obtain the mechanical response in magnitude $x(\omega)$ and phase $\phi(\omega)$ scanning the drive frequency around the mechanical resonance. Each point of the mechanical spectrum is the result of the signal demodulation at frequency $\Delta\omega$.

7.1.3 Optimisation of the downmixing frequency

We characterize the piezoresistive downmixing setup varying the downmixing frequency Δf from 4 to 150 kHz (fig. 7.3) and we notice that over 45 kHz the signal amplitude is attenuated by the cable impedance (fig. 7.4).

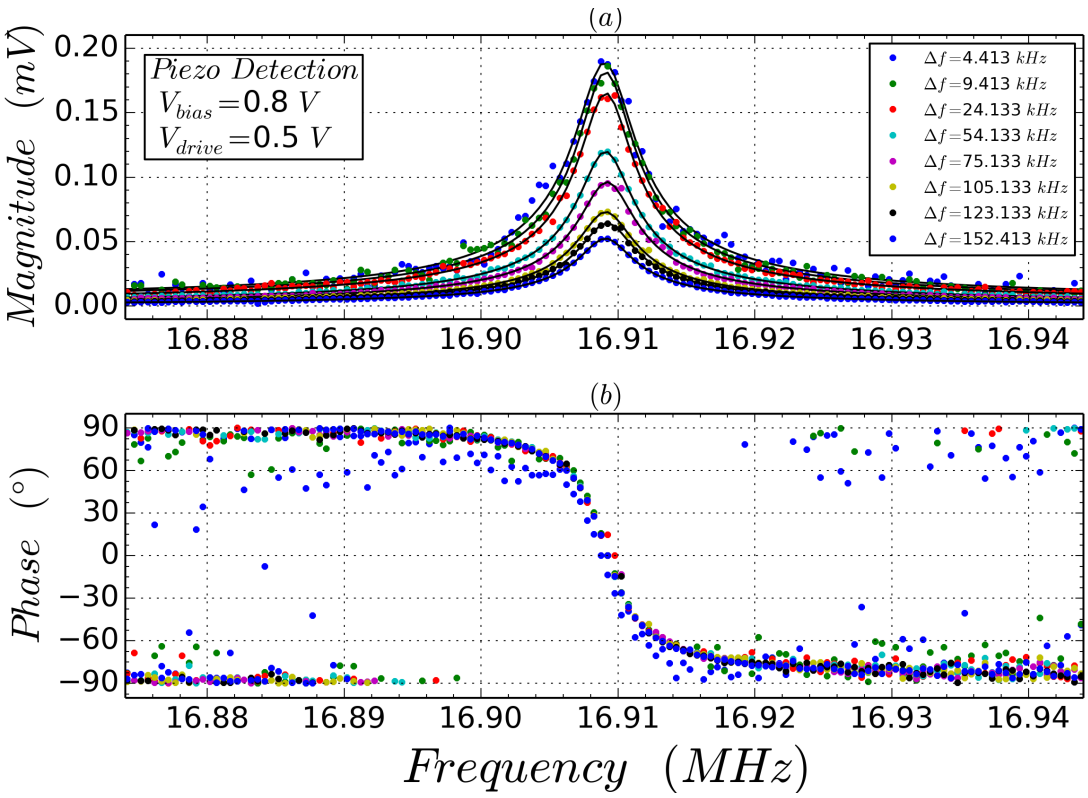

Figure 7.3: Piezoresistive detection for different downmixing frequencies Δf: (a) magnitude and (b) phase response of the cantilever. For values of Δf over 45 kHz, the signal amplitude is attenuated by cable impedance.

Comparing the expression in eq. (7.13) and the fitted parameter A_0 in fig. 7.4, we estimate the relative resistance variation $\delta R/R_g$ at resonance for a $V_{drive} = 0.5\,V$:

$$A_0 \equiv \frac{|V_{LIA}|}{V_{bias}} = \frac{\delta R(\omega_r)}{2\sqrt{2}R_g} \Rightarrow \frac{\delta R(\omega_r)}{R_g} = 2\sqrt{2}A_0 \simeq 6.6 \cdot 10^{-4} \tag{7.14}$$

The fit in fig. 7.4 also provides an experimental cut-off frequency around 45 kHz, a value two times higher than what we expect from eq. (7.5).
Despite the low-pass transfer function in fig. 7.4 could advise a downmixing frequency Δf lower than 45 kHz, we have to remind that the LIA input is affected by $1/f$ noise up to 100 kHz (see fig. 6.5b). This means that choosing a downmixing

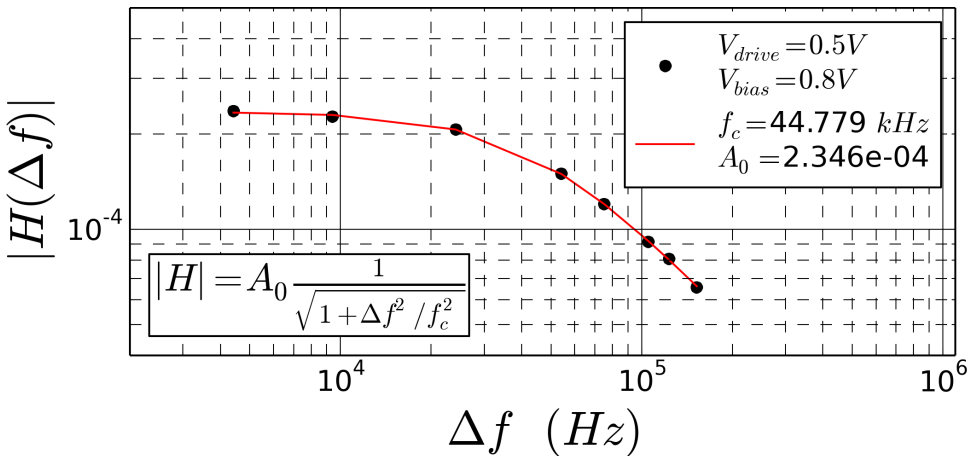

Figure 7.4: Low pass transfer function for different downmixing frequencies Δf: the mechanical peak amplitude in fig. 7.3*a* decreases as Δf goes over $45\,kHz$.

frequency Δf too low could be wrong as well: we are looking for the best signal-to-noise ratio and not for the higher signal amplitude. In order to optimize the signal-to-noise ratio, we have to take into account the total noise of the system, and not only that related to the device. For this reason, we calculate the *Allan deviation* for each Δf and we found that over $75\,kHz$ the signal and noise are attenuated by the same factor. (See fig. 7.5)

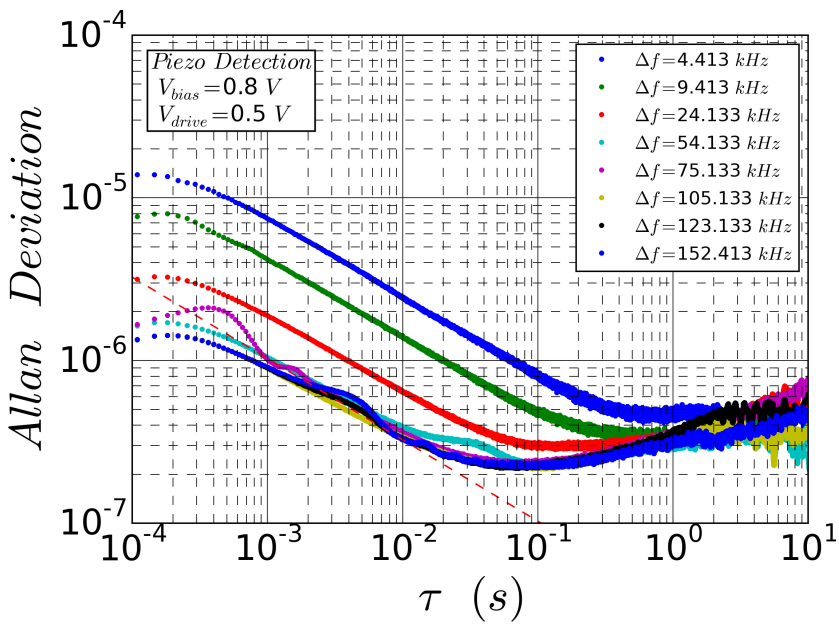

Figure 7.5: *Allan deviation* of the cantilever for different Δf

The dashed red line is a theoretical evaluation of the *Allan deviation* according to the *Robin*'s formula [21][22][23]

$$\frac{\Delta f}{f} = \frac{1}{2Q_m}\frac{N}{S}\sqrt{\frac{1}{2\tau}} \tag{7.15}$$

where Q_m is the mechanical Q-factor, N the noise level at resonance, S is the signal at resonance of the driven cantilever and τ the integration time.
At the light of this result, all the piezoresistive detections in the following chapters are performed with a downmixing frequency of $105.133\,kHz$.

In this section we verify that the release process in fig. 5.15g is done correctly, we identify the first mechanical resonance of the cantilever already predicted in table 5.3 and we optimise a key parameter for the piezoresistive detection such as the downmixing frequency Δf.

7.2 Optical spectrum

Once we are sure of the good state of mechanics, we deal with the photonic parts. To perform the optomechanical transduction, we need a clear measurement of the optical spectrum of the ring resonator in order to find the resonance wavelength and the optical Q-factor. A good knowledge of optical peak shape is a key to correctly tune the laser and evaluate the responsivity of the transduction (for further details, see section 7.3.7). We use two methods to characterize the optical response of the ring: the *continuous* and the *step-by-step* wavelength scanning.

7.2.1 Continuous wavelength scanning

The light is injected into the device after being correctly polarised since the couplers accept only TE polarisation. (See section 5.3). The laser wavelength is shifted linearly from λ_{min} to λ_{max} and, simultaneously, the output power is recorded in the time domain. The setup is shown in fig. 7.6:

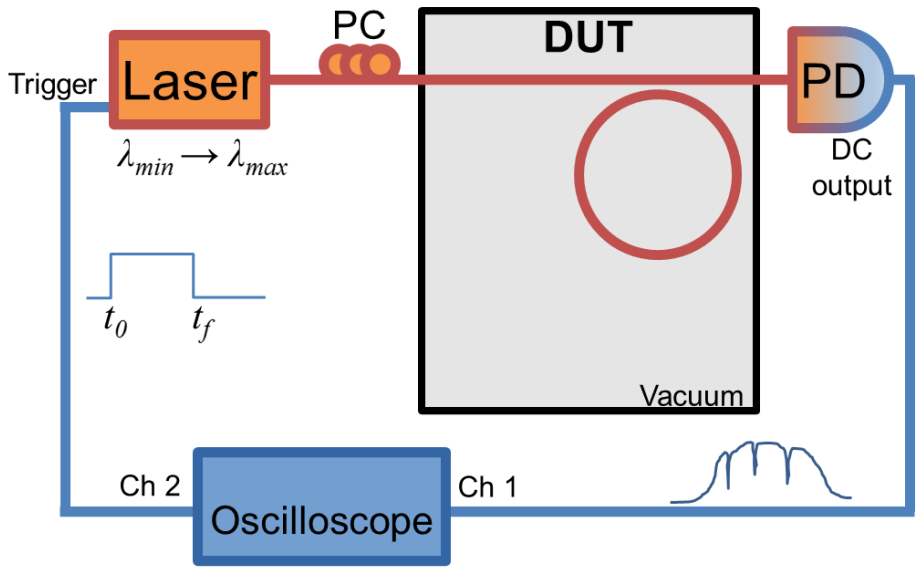

Figure 7.6: Continuous wavelength scanning setup. PC: polarization controller, DUT: device under test, PD: photodetector. In blue the electrical elements and in orange the optics.

Assuming a constant scanning speed v_{sweep}, we can associate each point in the time domain to a precise wavelength by the means of

$$\lambda = \lambda_{min} + (t - t_0) \cdot v_{sweep} \tag{7.16}$$

where t_0 is the starting instant of the scan provided by the trigger.
The higher the sampling rate and the lower the scan speed, better the wavelength resolution.

$$Resolution_\lambda = \frac{v_{sweep}}{Sampling\ Rate} \tag{7.17}$$

A sampling rate acquisition of $1\,kSa/s$ over $100\,s$, it is adequate to target a resolution of $1\,pm$ over a range of $100\,nm$, with a scan speed of $1\,nm/s$.
If we want to improve the resolution in λ, we just decrease the wavelength scanning speed or increase the sampling rate at a cost of an increased noise in the measurement.
Uncertainties originate from an imperfect scan speed which could be non-constant or different from the nominal value. Whereas for the wavelength sweep linearity we have to trust the laser manufacturer, we can recalculate for each measurement a real sweep speed as

$$v_{sweep} = \frac{\lambda_{max} - \lambda_{min}}{t_f - t_0} \tag{7.18}$$

It is possible to detect when the laser cavity starts and stops (t_0 and t_f) thanks to an auxiliary signal from the laser.
Since, in this case, the optical spectrum is a sequence of thin peaks, the bandwidth of the photodetector has to be large enough to follow the signal, especially for high-speed wavelength scanning. But large bandwidth means more noise superimposed to the spectrum, for this reason a scan speed between 1 and $10\,nm/s$ is advisable.

A typical optical spectrum is shown in fig. 7.7: three optical resonances with a FSR of $17\,nm$ are superposed to the response of the grating couplers shown in section 5.3.

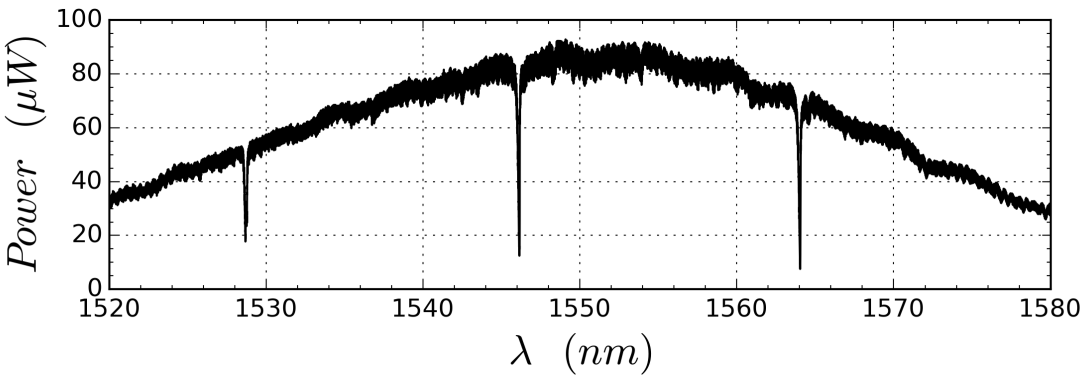

Figure 7.7: An example of optical spectrum obtained with a continuous wavelength scanning: the ring response is superposed to the grating coupler response.

This technique provides in a short time a preliminary ring optical spectrum. Once

the peaks position is detected, a step-by-step scanning is performed to characterize a selected peak with more details.

7.2.2 Step by step wavelength scanning

The step-by-step optical characterisation is performed as follows: the light tuned to a given wavelength is injected into the device and the optical power is measured at the *through* or at the *drop* ports. Then a new wavelength is set and a new power value is recorded, this routine is repeated for the entire wavelength range.

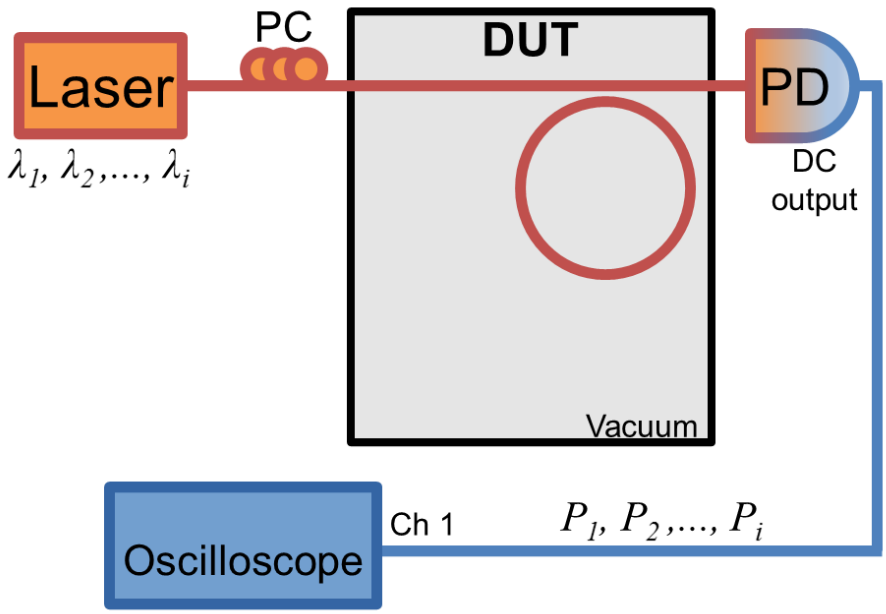

Figure 7.8: Step-by-step scanning setup. PC: polarization controller, DUT: device under test, PD: photodetector. In blue the electric elements and in orange the optics.

This method is quite accurate because it is possible to average the output power in order to decrease noises due to the photodetector and due to the free-end fiber oscillation. On the other hand, the step-by-step routine is really time-consuming and becomes quickly inapplicable for wide wavelength scanning.
Having a $1\,pm$ step, an averaging time of $100\,ms$ and a delay time due to the laser cavity displacement and to the remote control, the scanning speed results around $1.16\,pm/s$. That means a $24h$ scanning for a $100\,nm$ wavelength range. Obviously this delay is unacceptable because the fibers alignment is affected by the thermal drift and because the optical resonance shifts with temperature variations.

The step-by-step scanning is applied only around a single resonance peak, usually in a wavelength range of 300-400 pm. When the photodetector has a dedicated DC output, it is preferable to use it since the high frequencies are automatically filtered out.

Figure 7.9 shows the optical peak for the device #3 (see section 5.4.1) that will be used in the following sections for the optomechanical transduction. The presence of the double peak instead of a single peak is explained by a degeneration of clockwise and anti-clockwise modes of light propagation which arises from roughness and defects of the ring or from the presence of the cantilever [73][74][75][76].

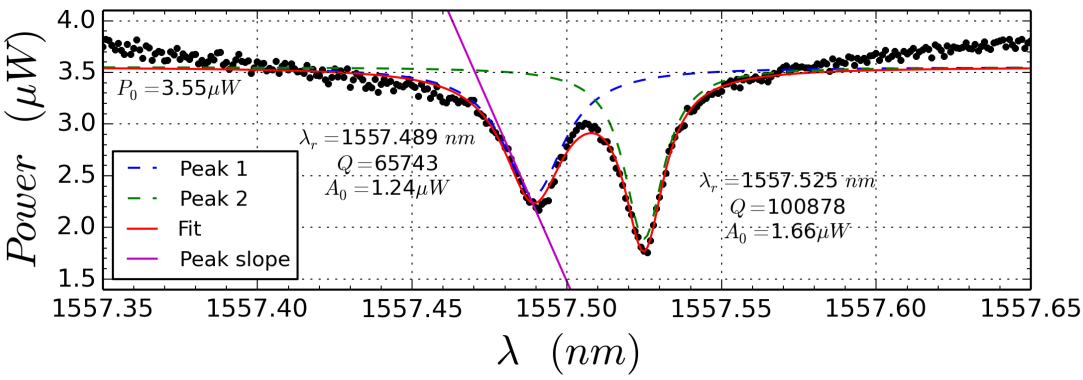

Figure 7.9: Typical optical spectrum of the ring from step by step scan.

Fitting the data with a double *Lorentzian* function, we obtain the resonance wavelength, the optical *Q-factor* and the amplitude for both peaks. Thanks to eq. (3.43) we calculate the *finesse* for the left and the right peak:

$$\mathcal{F} = \frac{FSR_\lambda \cdot Q_{opt}}{\lambda_r} = \begin{cases} \frac{17 \cdot 65743}{1557.489} \simeq 717.6 & \text{for left peak} \\ \frac{17 \cdot 100878}{1557.525} \simeq 1101 & \text{for right peak} \end{cases} \tag{7.19}$$

From the definition in eq. (3.44a), the contrast for the *through* port is

$$C_\mathcal{R} = \frac{\mathcal{R}_{max} - \mathcal{R}_{min}}{\mathcal{R}_{max}} = \begin{cases} \frac{1.24}{3.55} \simeq 0.35 & \text{for left peak} \\ \frac{1.66}{3.55} \simeq 0.48 & \text{for right peak} \end{cases} \tag{7.20}$$

As shown in fig. 7.10, for an input power higher than 6 μW, the peaks show a non-*Lorentzian* shape due to the thermo-optical effect [38] or to the Kerr effect [77]. Differently from [78], we did not observe hysteresis when the scanning is performed on both directions (fig. 7.11).

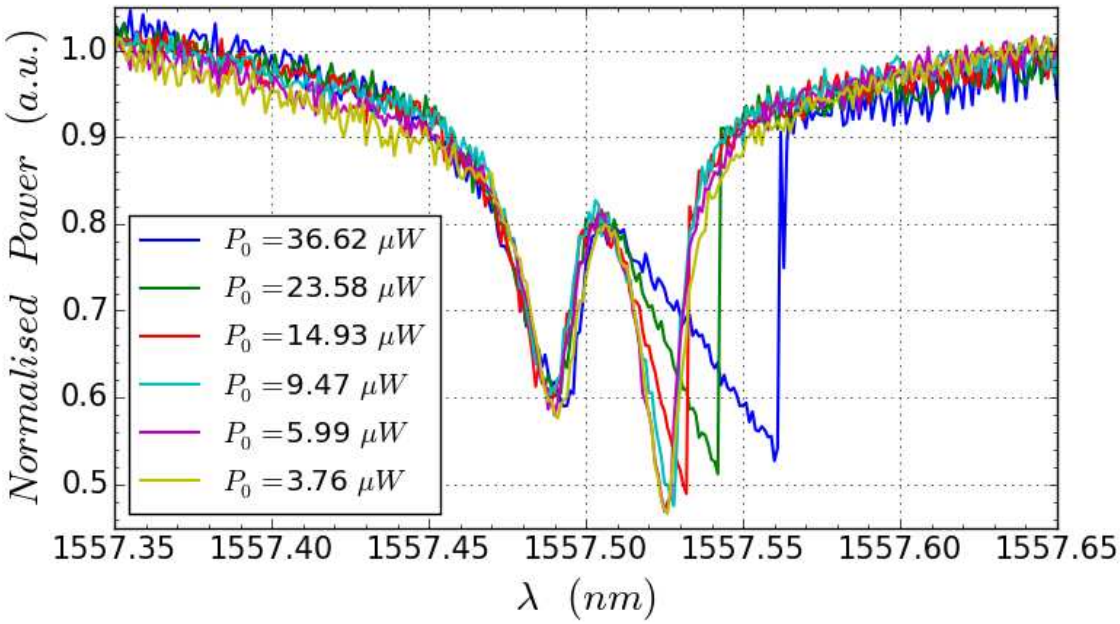

Figure 7.10: Optical spectrum of the ring for different laser power: as the out-of-resonance power is higher than of $6\,\mu W$, the right peak shows a non-linearity due to the thermo-optical effect [38] or to the Kerr effect [77].

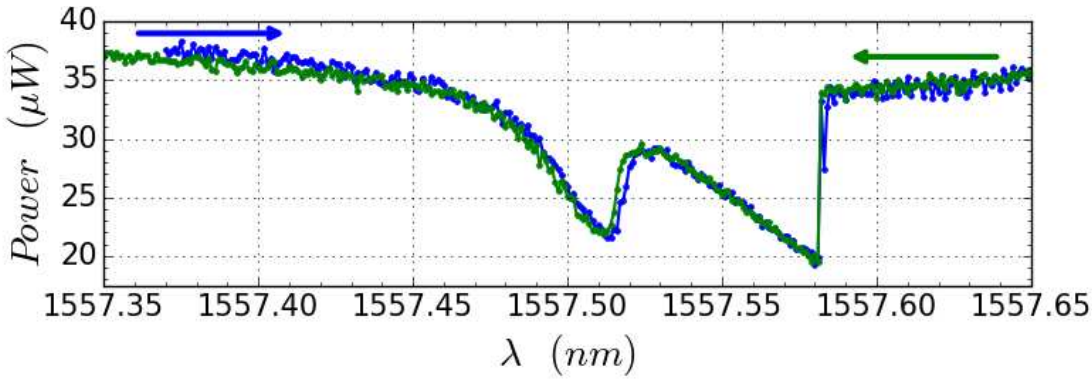

Figure 7.11: Optical spectrum of the ring for direct and inverse wavelength sweep: despite the right peak is in the non-linear regime, no hysteresis is detected for this ring.

Although the degeneration of propagating modes and the thermo-optical effect are very interesting phenomena, we stay focused on the optomechanical detection: we will use the left side of the left peak which never shows a non-linear behaviour up to $45\,\mu W$ of out-of-resonance power. (The power stocked on the left resonance is probably lower because of a lower optical Q-factor).

As predicted in section 4.3 and investigated in section 7.3.7, the optomechanical transduction responsivity strongly depends on the slope of the optical peak. Assuming a *Lorentzian* spectrum of the ring, we estimate the peak slope at the optimal wavelength point by the means of fitted values in fig. 7.9:

$$\left.\frac{dP}{d\lambda}\right|_{\lambda=1557.485\,nm} = \frac{3\sqrt{3}}{4}\frac{P_0 C_{\mathcal{R}} Q_{opt}}{\lambda_r} \simeq 68\,\mu W/nm \tag{7.21}$$

The magenta line in fig. 7.9 shows the linear approximation of the optical peak around a wavelength of $1557.485\,nm$.

At this point, the optical spectrum of the ring is properly characterised and we are ready to perform the optomechanical detection of the cantilever displacement.

7.3 Optomechanical direct detection

From section 4.3, we know that the direct optomechanical detection is performed with the laser wavelength tuned on the side of the optical resonance. A correct wavelength is set thanks to a step-by-step scanning in fig. 7.12: the laser wavelength is swept manually until the output power achieved approximately 3/4 of the peak amplitude. Unfortunately, the choice of the best operating point (good linearity and steepest slope) is subjective. That is why the comparison between different transductions is hard whenever the laser is retuned or the optical spectrum shifts because of thermal drift.

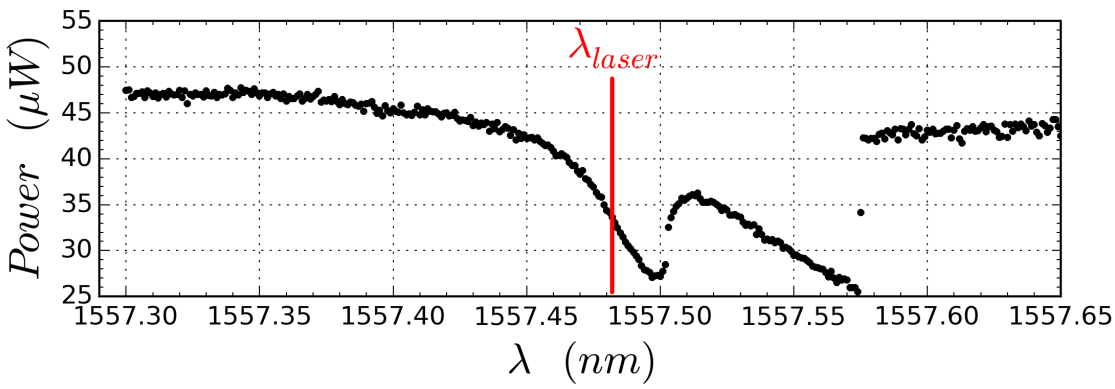

Figure 7.12: Optical resonance spectrum: the laser wavelength is tuned in correspondence of the steepest slope on the left side of the peak. Here $\lambda_{laser} = 1557.482\,nm$.

7.3.1 Transduction scheme

The experimental setup is shown in fig. 7.13: the laser power has only a DC component of magnitude P_{laser} usually between 1 and $3\,mW$ depending on the quality of grating couplers (see section 5.3).
The cantilever, placed into the evanescent field of the ring, modulates the spectrum shift of the optical resonator (details in chapter 4). The photodetector collects the light which is modulated at frequency f, the same frequency of the mechanical oscillation, and provides an electrical signal to the LIA.
The actuation is performed electrically by applying to the electrode a sinusoidal signal of amplitude V_{drive} at frequency $f/2$: as we saw in section 5.6, the cantilever oscillates at frequency f. The LIA uses the same oscillator to generate the actuation at $f/2$ and for the demodulation at f, in this way, we obtain the phase information of the mechanical oscillator.

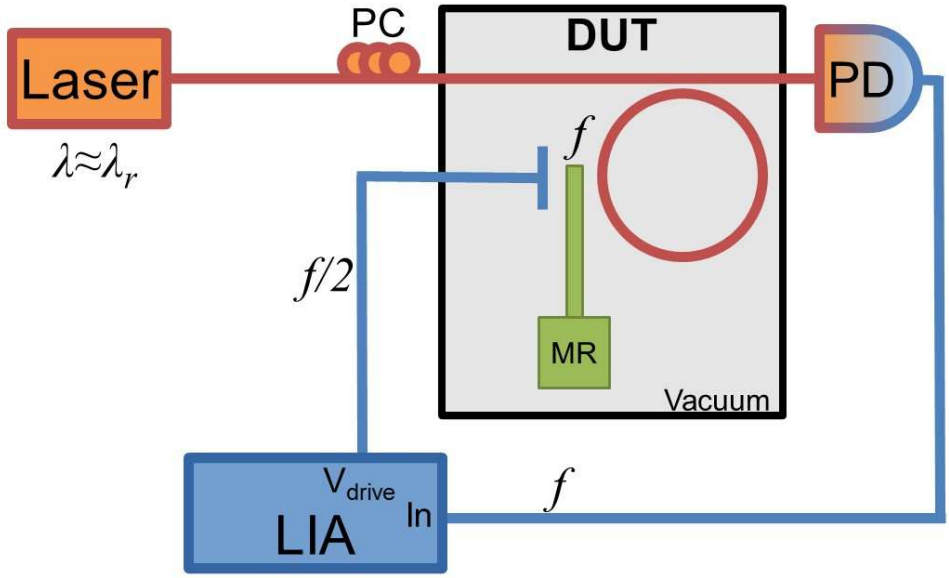

Figure 7.13: Optomechanichal direct setup. PC: polarization controller, DUT: device under test, MR: mechanical resonator, PD: photodetector, LIA: Lock-In Amplifier. In blue the electric elements, in orange the optics and in green the mechanical domain.

If the cantilever does not move, the power coming out from the *through* port and collected on the photodetector will be

$$P_{pd} = T(\lambda_{laser}) \cdot \alpha_c \cdot P_{laser} = T(\lambda_{laser}) \cdot P_0 \tag{7.22}$$

where P_0 is the laser power attenuated by the coupling losses α_c (section 5.3) and $T(\lambda)$ is the optical spectrum of the ring in fig. 7.12.
$T(\lambda)$ is described analytically by the *Airy* function detailed in chapter 3 but it can be approximated locally by a negative *Lorentzian* peak as we did in section 4.3:

$$T(\lambda) = \left(1 - \frac{C_{\mathcal{R}}\ \gamma_{opt}^2}{(\lambda - \lambda_r)^2 + \gamma_{opt}^2}\right) \tag{7.23}$$

$C_{\mathcal{R}}$ is the contrast, λ_r is the resonance wavelength and $\gamma_{opt} = \lambda_r/2Q_{opt}$ is the HWHM of the peak.

Now, any displacement of the cantilever modifies the resonant wavelength via the optomechanical coupling described in section 4.1. The optical spectrum shifts accordingly to the resonance and a variation of light power occurs on the photodetector. As we saw in the section 4.3, this variation is proportional to the slope of the optical peak and proportional to the optomechanical coupling factor g_{om}.

Since the cantilever oscillates at frequency f, the resulting signal on the photodetector is calculated by the means of eq. (4.16):

$$P_{pd}(t) = T(\lambda_{laser}) \cdot P_0 + \frac{3\sqrt{3}}{4} \frac{P_0 C_{\mathcal{R}} Q_{opt} \lambda_r}{c} \cdot \frac{g_{om}}{2\pi} \cdot x(f) \cos[2\pi f t + \phi(f)] \tag{7.24}$$

where $x(f)$ and $\phi(f)$ are the magnitude and phase response of the cantilever.
The continuous background $T(\lambda_{laser})P_0$ is automatically filtered by the photodetector (*NewPort 1811-FC-AC*) and the component at frequency f is measured by the Lock-In Amplifier via synchronous detection.
According to the eq. (7.24), the signal magnitude from the LIA detection is

$$|V_{LIA,f}(f)| = G_{pd} \cdot \frac{3\sqrt{3}}{4} \frac{P_0 C_{\mathcal{R}} Q_{opt} \lambda_r}{c} \cdot \frac{g_{om}}{2\pi} \cdot \frac{x(f)}{\sqrt{2}} \tag{7.25}$$

The factor $\sqrt{2}$ is due to the fact that LIA measures the RMS value of the signal component at frequency f.

The fig. 7.14 shows the optomechanical transduction for different drive voltages on the electrode: each of these 500 points results from the demodulation of the photodetector signal at frequency f with a time constant of $1\,ms$. If we add a time delay between two points to reach the harmonic regime (8-10 times the LIA time constant) and some *USB* communication delay, a mechanical spectrum is recorded in 15-20 seconds.
The mechanical resonance frequency at $16.91\,MHz$ matches that from the preliminary piezoresistive transduction in fig. 7.3 and it is compatible with the theoretical evaluation in table 5.3. A small shift of the mechanical resonance towards low frequencies is observed especially from the phase response of the cantilever: this is due to the negative stiffness effect acting on the resonator as V_{drive} increases (see section 5.6). The Q-factor values in fig. 7.14 decrease for larger actuations because of a deformation in the mechanical response.

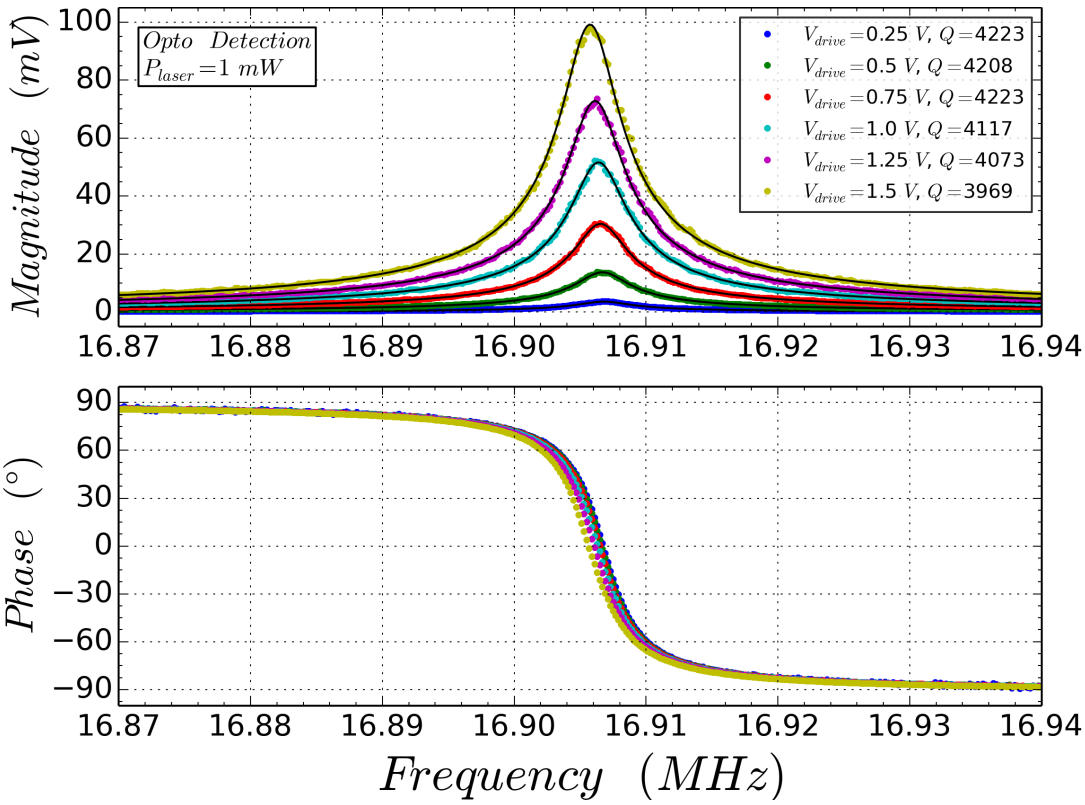

Figure 7.14: Optomechanical detection for different actuations: magnitude and phase response of the mechanical cantilever. For higher V_{drive}, the resonance frequency slightly shifts because of the negative stiffness effect whereas the Q-factor decreasing denotes a peak deformation.

Plotting the peak amplitude versus the power of the drive voltage in fig. 7.15, we can establish that the transduction shows signs of saturation for $V_{drive} > 1.0\,V$. From eq. (5.3), the actuation force is proportional to V_{drive}^2 whilst here the transduction deviates from the expected law for larger actuations. We consider the transduction as non-linear whenever the deviation from the expected value is bigger than the 10%. With the help of fig. 7.15, we fixed here the upper limit of the linearity transduction to an actuation voltage equal to $1.0\,V$.

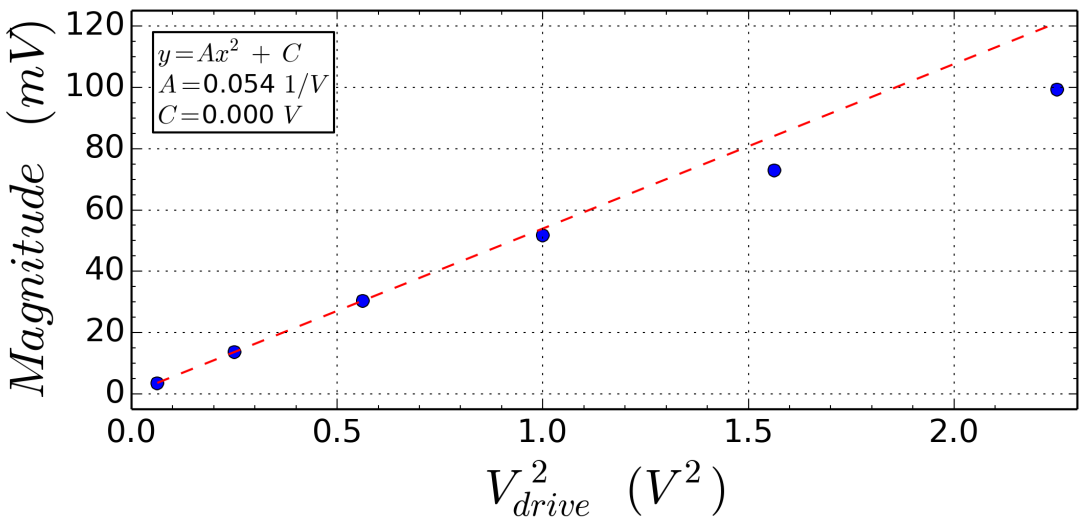

Figure 7.15: Peak amplitudes of fig. 7.14 versus the drive voltage: for V_{drive} higher than $1\,V$ the transduction deviates from the expected law. From eq. (5.3), the actuation force is proportional to V_{drive}^2.

Thanks to the double transduction (section 7.3.6), we will demonstrate that the non-linearity originates from the optomechanical readout and not from the mechanical domain. To properly explain this non-linearity, we have to know the amplitude of oscillation and evaluate the optomechanical coupling factor g_{om}. With these two values, we estimate that the resonance wavelength shift, due to cantilever oscillation, is comparable to the FWHM of the optical peak. (See section 7.3.7).

7.3.2 Thermomechanical noise and dynamic range

As explained in section 6.5.2, the minimum motion of the resonator is limited by thermomechanical noise. A good transduction must be able therefore to readout the thermomechanical motion of the cantilever.
Setting V_{drive} to zero, we demodulate the signal from the photodetector at frequency f as done before. In order to properly estimate the mean value of the noise, each point of the plot is averaged over $1\,s$ before passing to the next point.
To limit the measurement time to 4-5 minutes, the number of points in the plot is reduced to 250. In a 30-minute time frame, the thermal drift of ring resonance could already impact the sensitivity of the measurement. The presence of the cryostat or any sample temperature control system would probably solve this issue. If the measurement session lasts more than 1-2 hours, the thermal drift causes also input/output fibers misalignment. The result is a variation of the injected power P_0 as shown in section 6.5.4.

As we can see from fig. 7.16, the *Brownian* motion of the cantilever is transduced by the means of the optomechanical detection: the thermomechanical peak is centred to the resonance frequency having an amplitude of $2.69\,\mu V/\sqrt{Hz}$.

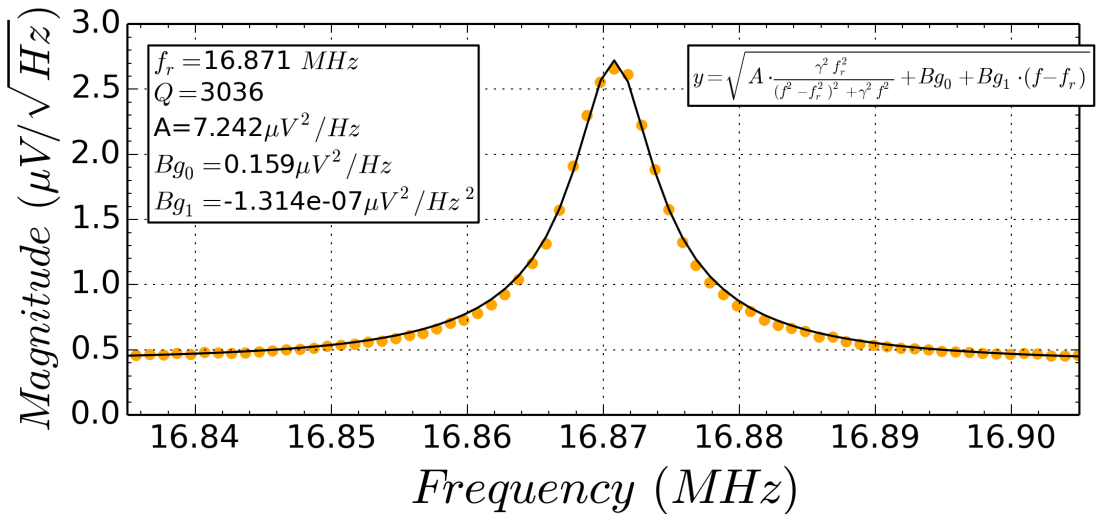

Figure 7.16: Power spectral density of the transduction signal around the resonance frequency. The *Brownian* motion of the resonator exceeds the instrumentation noise. In this plot, the thermomechanical noise has been normalised to $1Hz$-bandwidth.

The detection threshold of $0.4\,\mu V/\sqrt{Hz}$, obtained from the background value, corresponds to the laser shot noise plus the instrumentation noise (i.e. NEP and LIA input noise). The expected value is slightly lower than the measured one:

$$\sqrt{G_{pd}^2(S_{shot}+NEP^2)+S_{LIA}} \simeq 0.27 < 0.4\,\mu V/\sqrt{Hz} \tag{7.26}$$

where S_{shot} is $8.6788 \cdot 10^{-24}\,W^2/Hz$ from eq. (6.4), the measured NEP at $17\,MHz$ is $6.25 \cdot 10^{-12}\,W/\sqrt{Hz}$ from fig. 6.9 and $\sqrt{S_{LIA}(20MHz)}$ is $10\,nV/\sqrt{Hz}$ from the specification in fig. 6.5a.
The value for the background noise in fig. 7.16 is also coherent with the power noise density measured during the setup characterisation in section 6.6.1. (See fig. 6.11).

To find the dynamic range of the transduction, we plot in fig. 7.17 the thermomechanical noise together with the mechanical spectra of the driven cantilever. We define the dynamic range of the transduction as the ratio between the largest and the smallest detectable signal in the linear regime. In this case, at resonance, the largest signal in the linear regime is the mechanical peak amplitude for the actuation voltage of $0.86\,V$. Always at resonance, the smallest detectable signal is limited by the thermomechanical noise over the instrumentation noise, here $2.72\,\mu V/Hz$.
As illustrated by the arrow in fig. 7.17, we obtain a dynamic range of $86\,dB$.

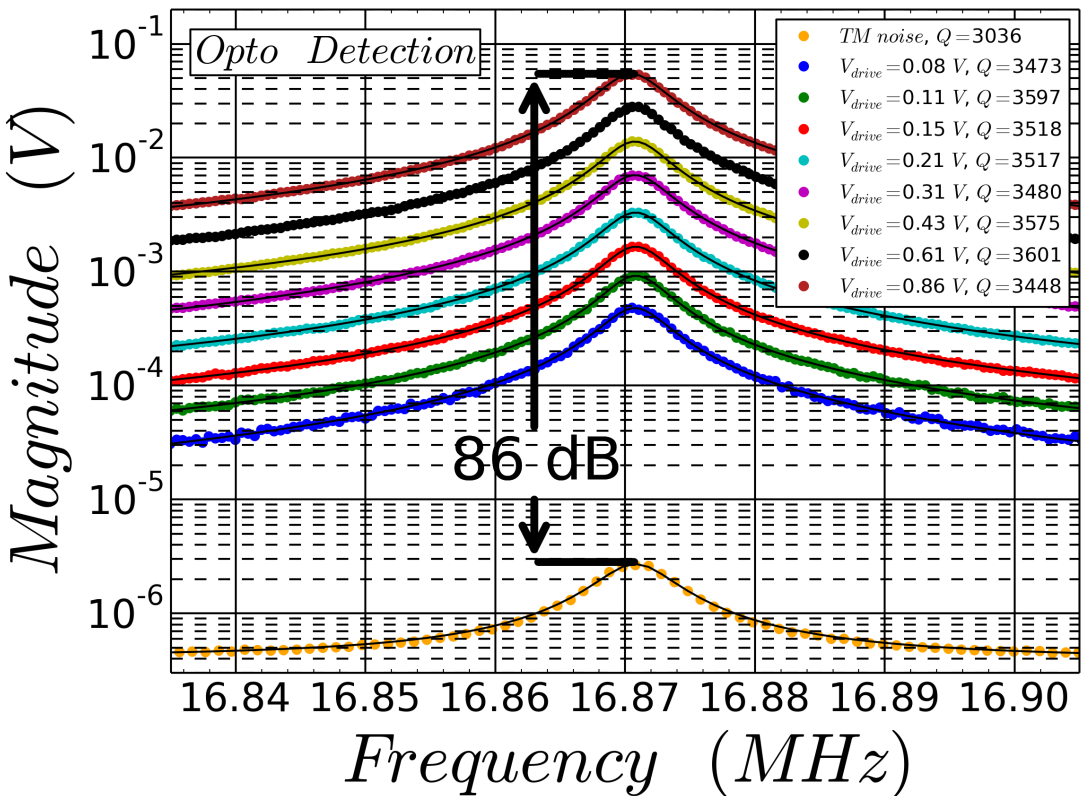

Figure 7.17: Dynamic range of the optomechanical detection: fixing the non-linear threshold at $V_{drive} = 0.86\,V$, the dynamic range is $86\,dB$. The thermomechanical noise from fig. 7.16 is always normalised to $1Hz$-bandwidth.

7.3.3 Allan deviation

Since the mainframe of this work is the neutral mass sensing (see section 2.3), we evaluated the cantilever frequency stability by the means of optomechanical transduction.
We drive the cantilever at its resonance and we track the resonance frequency over 100 s by monitoring the phase signal in open-loop. The resonance frequency fluctuation is obtained from the phase fluctuation using the phase response of the resonator, or better, its linear approximation close to resonance frequency

$$\Delta f \simeq -\Delta\phi \frac{f_r}{2Q_m} \tag{7.27}$$

Once we have the frequency fluctuation signal, we can calculate and plot the *Allan deviation* in fig. 7.18.

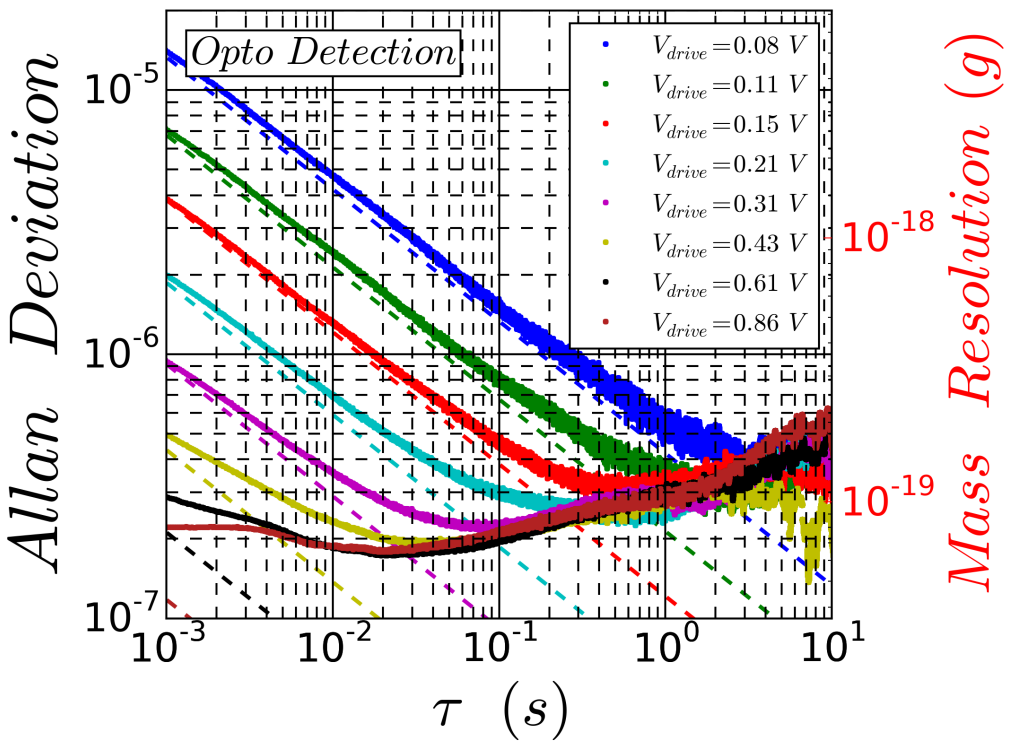

Figure 7.18: *Allan deviation* of the cantilever with optomechanical detection: for low drive voltages and short integration times, the data follows the dynamic range formula in eq. (7.28) (dashed lines). For higher drive voltages and longer integration times, the curves meet a lower bound.

The curves in fig. 7.18 show the *Allan deviation* of the cantilever for different drive voltages: we observe a plateau due to resonance frequency fluctuations, similarly to

the one in [8].
As we will see better in section 7.3.6, this measurement endorses the hypothesis of a mechanical origin of cantilever frequency fluctuation.
The dashed lines are theoretical evaluations of the *Allan deviation* according to the *Robin*'s formula [21][22][23]

$$\frac{\Delta f}{f} = \frac{1}{2Q_m}\frac{N}{S}\sqrt{\frac{1}{2\tau}} \tag{7.28}$$

where Q_m is the mechanical Q-factor, N is the noise voltage, S is the signal at resonance of the driven cantilever and τ the integration time. The values for S, N and Q_m are obtained directly from fig. 7.17.

From fig. 7.18, using this system as mass sensor, we would achieve a mass resolution lower than $100\,zg$ for an integration time between 10 and $100\,ms$. The drive voltage is a key parameter for the cantilever stability but an actuation larger than $0.61\,V$ does not improve the *Allan deviation* because of anomalous frequency fluctuations [8].

7.3.4 Readout calibration

The detection of the *thermomechanical noise* (section 7.3.2) is not only a proof of a good sensitivity but provides a way to calibrate the detection chain. Thanks to the calibration, it is possible to know how many (micro)volts the *LIA* reads out for one (pico)meters of cantilever displacement, quantifying in this way the optomechanical transduction responsivity.
First we calculate theoretically the amplitude of the mechanical oscillation due to the *Brownian motion*, then we compare this value to the peak amplitude of a thermomechanical spectrum obtained experimentally.

From theory (see section 6.5.2), the motion of the free end of the cantilever under thermal excitation has the following spectrum

$$S_{th}(\omega) = \frac{1}{M_1 Q_m} \frac{4\omega_r k_B T}{(\omega^2 - \omega_r^2)^2 + \left(\frac{\omega\omega_r}{Q_m}\right)^2} \qquad [m^2/Hz] \tag{7.29}$$

on resonance ($\omega = \omega_r$), the thermomechanical noise reaches an amplitude equal to

$$S_{th}(\omega_r) = \frac{4k_B T Q_m}{M_1 \omega_r^3} \qquad [m^2/Hz] \tag{7.30}$$

In this condition, the amplitude of the motion is well known and we use it as reference value to calibrate the detection chain. From eq. (7.25), the thermomechanical peak amplitude A_{th} which is expected results

$$\sqrt{A_{th}} = G_{pd} \cdot \frac{3\sqrt{3}}{4} \frac{P_0 C_{\mathcal{R}} Q_{opt} \lambda_r}{c} \cdot \frac{g_{om}}{2\pi} \cdot \sqrt{S_{th}} \qquad [V/\sqrt{Hz}] \tag{7.31}$$

Since the thermal noise is already expressed in terms of RMS value, the factor $\sqrt{2}$ does not appear in the above equation.
Finally the global responsivity for the optomechanical transduction $\mathfrak{R}_{opto}$ is written as follows

$$\mathfrak{R}_{opto} = \sqrt{\frac{A_{th}}{S_{th}}} \qquad [V/m] \tag{7.32}$$

Experimentally, we measure the thermomechanical noise spectrum of the device via the optomechanical transduction, exactly like we already done in section 7.3.2. As always, the measurement is performed with the cantilever under vacuum.
After tuning the laser according to the optical characterisation in fig. 7.19, we acquire the thermomechanical motion of the cantilever illustrated in fig. 7.20: we obtain a mechanical peak at 16.951 MHz with a Q-$factor$ around 4429 and an amplitude A_{th} of $4.784\,\mu V^2/Hz$.

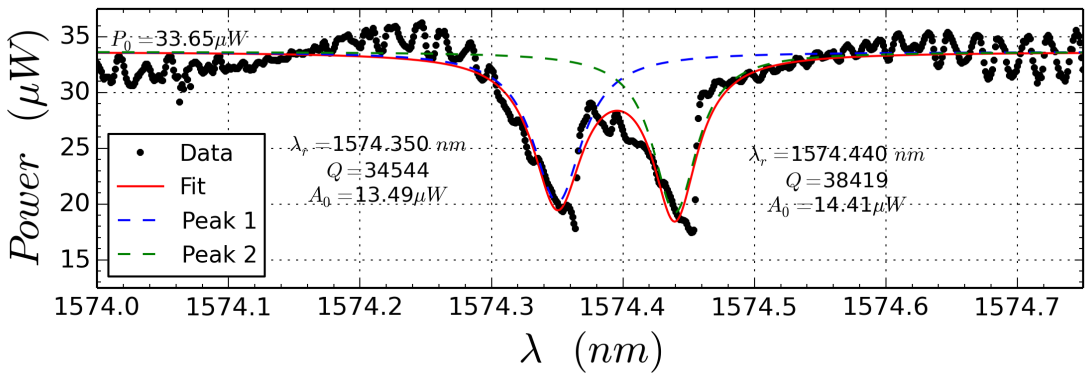

Figure 7.19: Double *Lorentzian* fit on the optical ring spectrum.

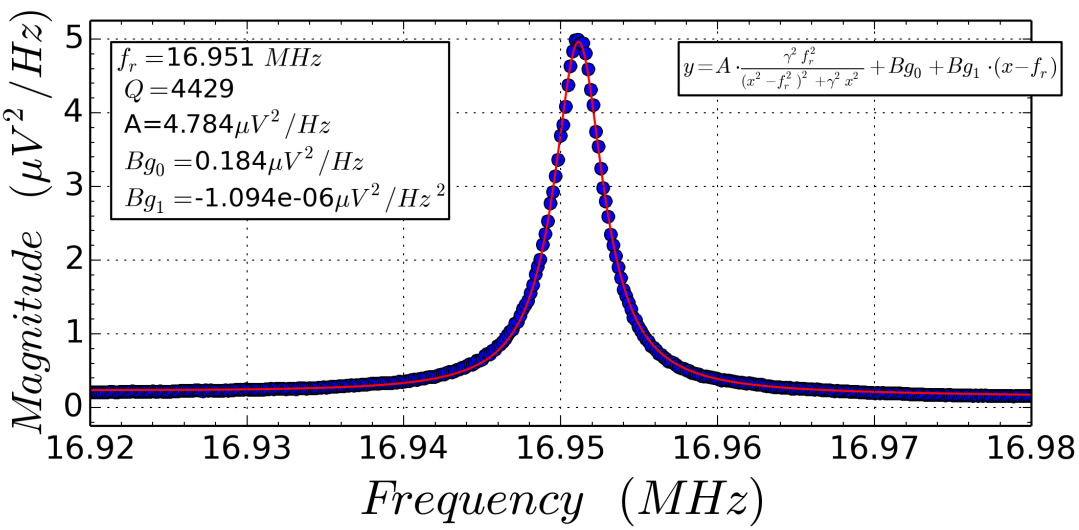

Figure 7.20: *Brownian motion* of the cantilever under vacuum. In this plot, the *thermomechanical noise* is normalised to $1Hz$-bandwidth.

From eq. (7.30), the *Brownian motion* of the cantilever at resonance is estimated as follows

$$S_{th}(\omega_r) = \frac{4 \cdot 1.3806488 \cdot 10^{-23} \cdot 298 \cdot 4429}{0.25 \cdot 0.8 \cdot 10^{-15} \cdot (2\pi \cdot 16.951 \cdot 10^6)^3} \simeq 0.301\, pm^2/Hz \tag{7.33}$$

so that we can calculate the transduction responsivity

$$\boxed{\mathfrak{R}_{opto} = \sqrt{\frac{A_{th}}{S_{th}}} = \frac{\sqrt{4.784\,\mu V^2/Hz}}{\sqrt{0.301\,pm^2/Hz}} \simeq 4\,\mu V/pm} \tag{7.34}$$

To confirm this result, we perform the thermomechanical detection of the cantilever at ambient pressure and we obtain a similar transduction responsivity. Differently from before, we perform the *thermomechanical noise* spectrum of the cantilever in air (see fig. 7.21): obviously, at ambient pressure the mechanical Q-factor drops to 27 and the peak amplitude A_{th} is reduced to $0.04\,\mu V^2/Hz$.

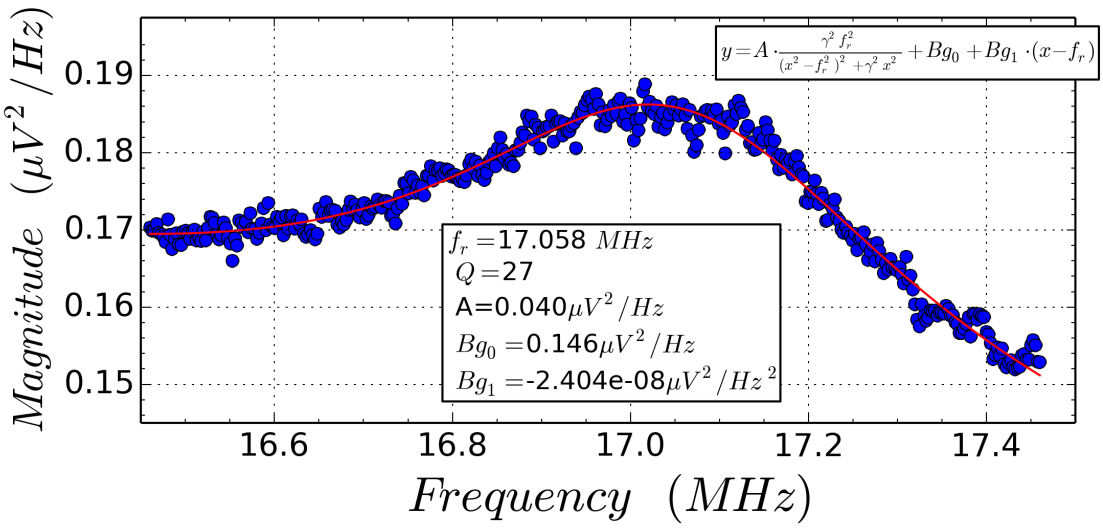

Figure 7.21: *Brownian motion* of the cantilever at ambient pressure. In this plot, the *thermomechanical noise* is normalised to $1Hz$-bandwidth.

Following the same procedure, the theoretical *Brownian motion* at atmospheric pressure has an amplitude (at resonance) of

$$S_{th}(\omega_r) = \frac{4 \cdot 1.3806488 \cdot 10^{-23} \cdot 298 \cdot 27}{0.25 \cdot 0.8 \cdot 10^{-15} \cdot (2\pi \cdot 17.058 \cdot 10^6)^3} \simeq 1.804 \cdot 10^{-3}\, pm^2/Hz \tag{7.35}$$

and the transduction responsivity in air is equal to

$$\boxed{\mathfrak{R}_{opto}^{air} = \sqrt{\frac{A_{th}}{S_{th}}} = \frac{\sqrt{0.04\,\mu V^2/Hz}}{\sqrt{1.804 \cdot 10^{-3}\, pm^2/Hz}} \simeq 4.7\,\mu V/pm} \tag{7.36}$$

The responsivity of the optomechanical transduction is similar for a cantilever in air and under vacuum. The difference around the 18% can be explained as follows: a new fiber alignment and a new optical characterisation were done between the two experiments, this means that the laser wavelength could be in a zone where the slope is slightly different. Another cause of mismatch comes from the fit incertitude on the mechanical peak data.

7.3.5 Optomechanical factor evaluation

The calibration of the readout chain is useful for defining a total responsivity of our device but it does not investigate what happens at each transduction step.
We already have all the elements to estimate the *optomechanical coupling factor* of the system (see section 4.1). From equation 7.31, let us focus now on g_{om}

$$g_{om} = \frac{8\pi}{3\sqrt{3}} \frac{c}{G_{pd} P_0 C_{\mathcal{R}} Q_{opt} \lambda_r} \cdot \sqrt{\frac{A_{th}}{S_{th}}} \tag{7.37}$$

we know the amplitude of the mechanical peak A_{th} from fig. 7.20 and we know the cantilever oscillation from the eq. (7.33). The wavelength resonance, the optical Q-$factor$ and the optical peak amplitude $P_0 C_{\mathcal{R}}$ are obtained from the fit of optical characterisation in fig. 7.19.
Consequently we evaluate the *optomechanical coupling factor* g_{om} as follows

$$g_{om} = \frac{8\pi}{3\sqrt{3}} \frac{2.99792 \cdot 10^8}{40\,000 \cdot 13.5 \cdot 10^{-6} \cdot 34547 \cdot 1574.350 \cdot 10^{-9}} \sqrt{\frac{4.784 \cdot 10^{-12}}{3.01 \cdot 10^{-25}}} \tag{7.38}$$

$$\Rightarrow \boxed{g_{om} \simeq 1.968 \cdot 10^{17} \, \frac{\text{rad}}{s \cdot m} = 0.1968 \, \frac{G\text{rad}}{s \cdot nm}} \tag{7.39}$$

This value is coherent with the simulation shown in section 4.2. However, similar optomechanical systems (i.e. a cantilever coupled to a waveguide) shows g_{om} values which are 3-4 orders of magnitude larger [35][7]. Besides, the tested device has a larger optomechanical gap compared to the above-cited articles (200 nm vs 70-160 nm, see device #3 in table 5.3). Just remember that the optomechanical coupling strongly depends on the optomechanical gap because the evanescent wave decreases exponentially outside the waveguide. Furthermore, our optomechanical device has a minimal coupling zone since the optical ring has no straight waveguide part. This fact also contributes to the discrepancy in the g_{om} values.

Dries Van Thourhout and Joris Roels reviewed other optomechanical systems which show a range of coupling factor values from 0.13 to 773 GHz/nm [45]. A similar g_{om} measurement is shown in [79].

7.3.6 Comparison with piezoresistive detection

The originality of these devices is the presence of a parallel piezoresistive transduction of the cantilever displacement. *In-situ* comparison is now possible between piezoresistive and optomechanical readout (see sections 5.5 and 7.1).
This configuration is very useful for studying the intrinsic properties of the nanocantilever independently from the transduction method.
The setup, shown in fig. 7.22, is the result of a combination of the two previous setups in figures 7.2 and 7.13. In response to the electrical excitation (V_{drive}), the cantilever oscillates stressing the gauge and perturbing the optical ring simultaneously. Both readout methods are already described in the sections 7.1 and 7.3.

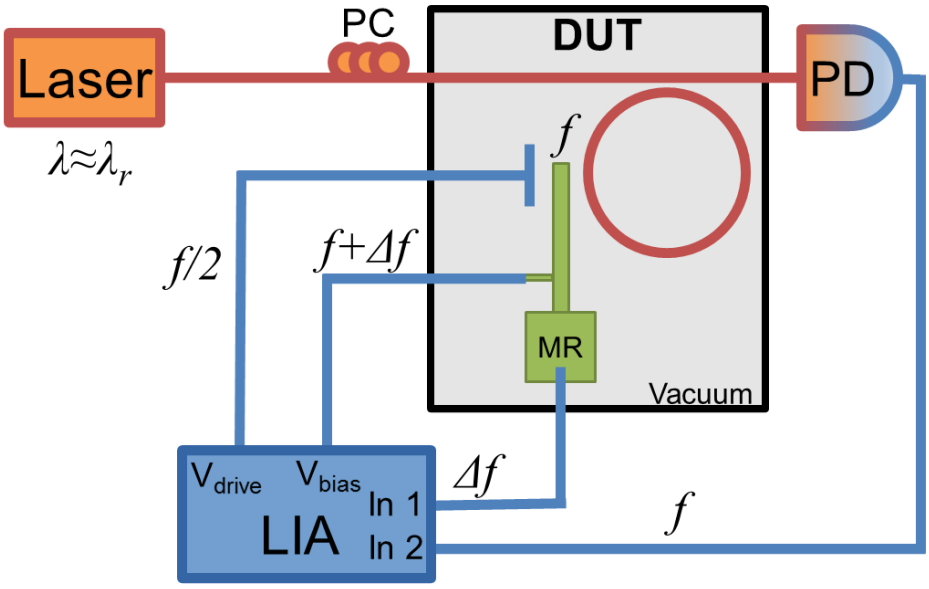

Figure 7.22: Parallel transduction setup. PC: polarization controller, DUT: device under test, MR: mechanical resonator, PD: photodetector, LIA: Lock-In Amplifier. In blue the electric elements, in orange the optics and in green the mechanical domain.

Similarly to previous sections, we performed the transduction for different drive voltages, the results are gathered in fig. 7.23.
At first sight, for equal cantilever displacement, we observe that the optomechanical readout provides a considerable signal, around 50 times higher than the piezoresistive one. To be fair, the large optical signal is due to the transimpedance gain of the photodetector and it is not an intrinsic quality of the optomechanical transduction. By adding a voltage amplifier between the nanogauge and the LIA, the two

transductions would provide equivalent signals.
However, the optomechanical transduction has already some advantages: the optical signal can travel over long distances with negligible attenuation and it is immune to electromagnetic interferences or parasitic capacitances.

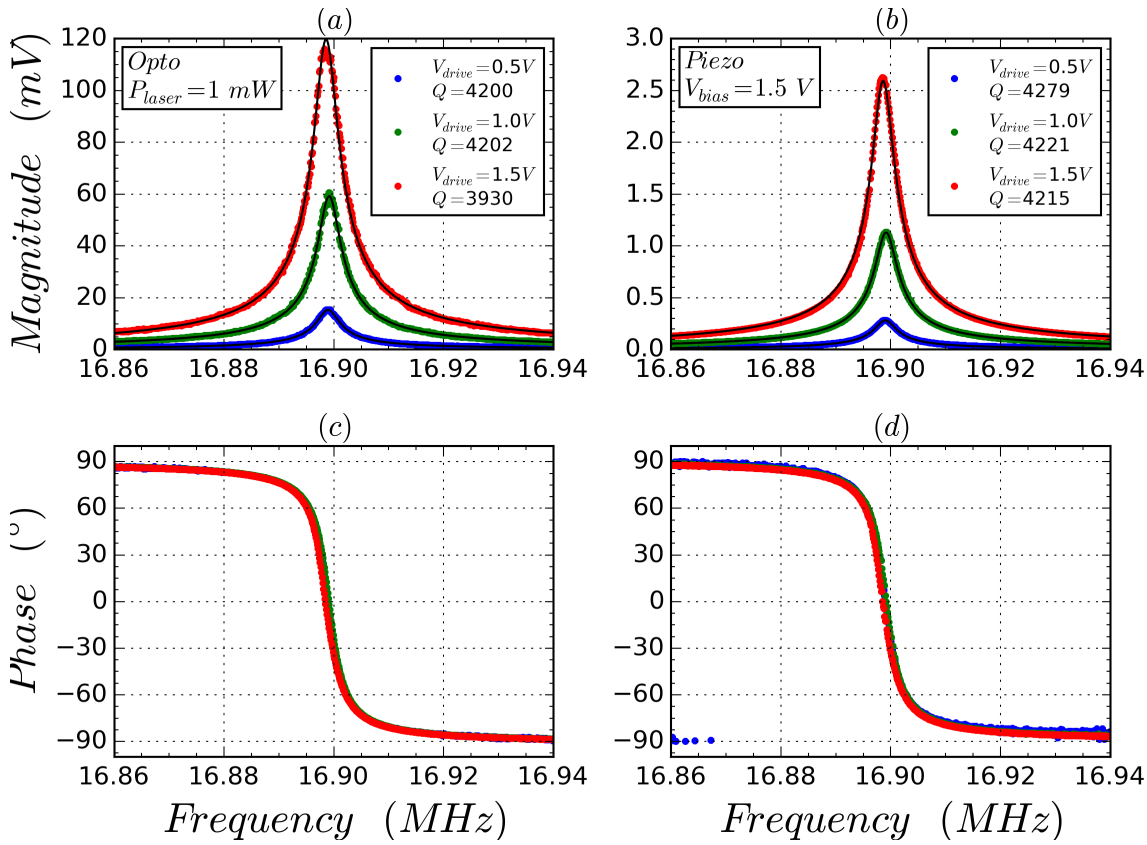

Figure 7.23: Comparison of two transductions: (*a*) magnitude and (*c*) phase of the cantilever by means of optomechanical transduction and (*b*) magnitude and (*d*) phase of the cantilever by means of piezoresistive transduction.

In the following pages, we will compare the linearity and the dynamic range of the two transduction techniques.

Optomechanical non-linearity

Paying attention to the Q-factor values in fig. 7.23, we can already predict a non-linear transduction only for the optomechanical readout technique: from fig. 7.23(a), the mechanical Q-factor decreases considerably for larger actuation voltages due to a peak deformation. The same thing does not happen for the piezoresistive transduction in fig. 7.23(b).

The fig. 7.24 is obtained plotting the peaks amplitudes in figures 7.23(a) and 7.23(b) versus the drive voltage:

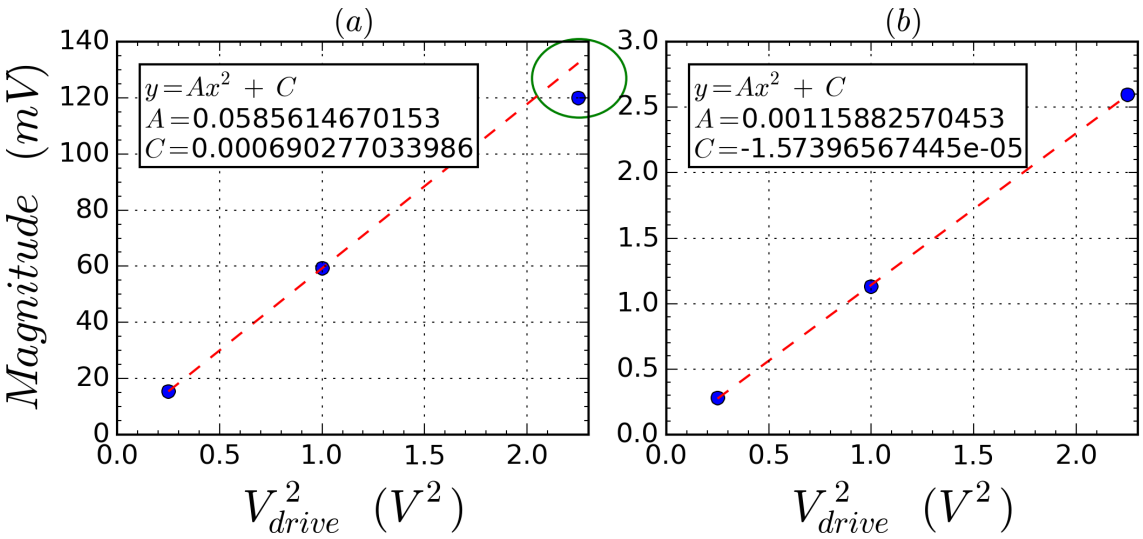

Figure 7.24: Peak amplitude versus the drive voltage for (a) optomechanical detection and (b) piezoresistive detection.

The green circle highlights the saturation of the optomechanical signal for larger cantilever displacement ($V_{drive} = 1.5V$). Conversely, the piezoresistive detection follows the expected trend given in section 5.6 for $f/2$ excitation.
If the cantilever had been in the non-linear regime, we would have detect an identical non-linear trend for both detection. This proves that the non-linearity arises from the optomechanical transduction and not from the cantilever mechanics.
This parallel detection excludes a mechanical origin of the non-linearity already observed in fig. 7.14 and 7.15. An explanation of this phenomenon will be provided in section 7.3.7.

Dynamic range and responsivity

Using the same setup (fig. 7.22), we detect now the thermomechanical movement of the cantilever by the means of the double detection.
Figure 7.25 shows, on the same plot, the thermomechanical noise (red points) and the mechanical response of the driven cantilever (blue points) for both transductions. From fig. 7.24, we consider that the optomechanical readout is linear up to a drive voltage of $1\,V$: we obtain in this way a dynamic range of $89.8\,dB$. For the same drive voltage, the piezoresistive readout shows a dynamic range of $85\,dB$ but since it does not suffer from non-linearity, it could be higher.

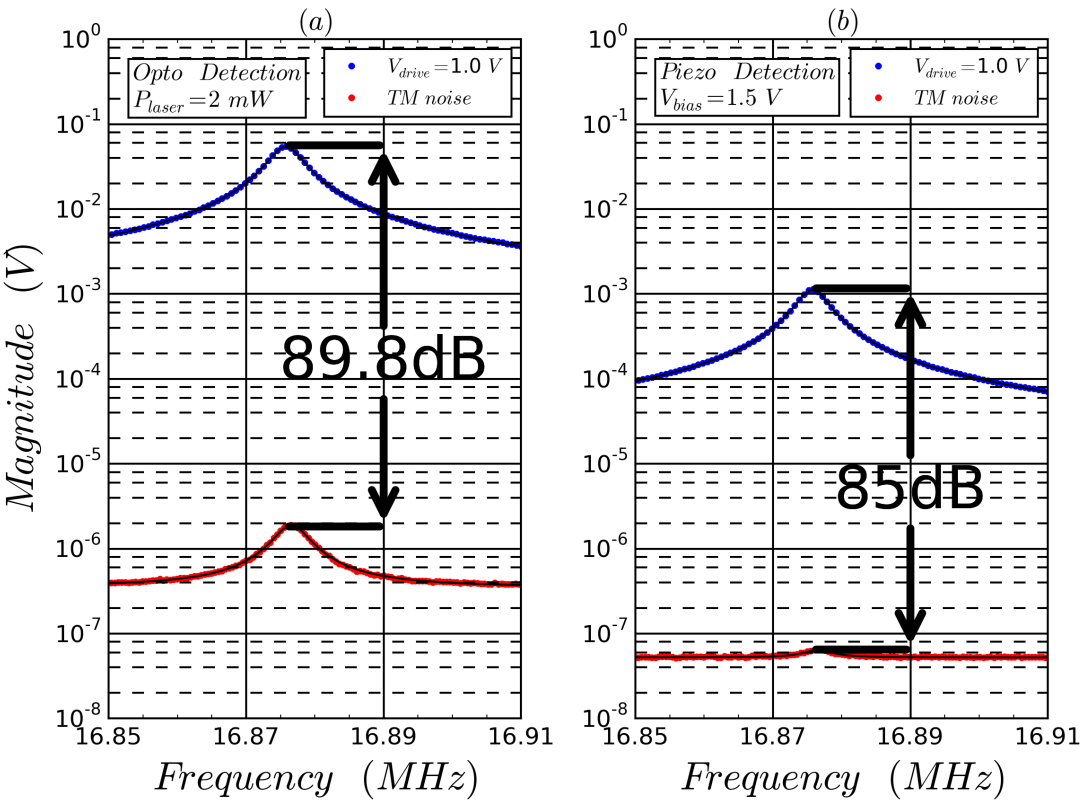

Figure 7.25: Dynamic range comparison between the two detections: (a) optomechanical and (b) piezoresistive. For a thermomechanical noise normalised to $1Hz$-bandwidth, the dynamic range is respectively $89.8\,dB$ and $85\,dB$.

The piezoresistive detection in fig. 7.25(b) suffers from a higher detection threshold compared to the optomechanical transduction: the *Brownian* motion of the cantilever is less solved with respect to the optomechanical detection in fig. 7.25(a). The background noise for the piezoresistive detection is due to the *Johnson* noise of the nanogauge plus the instrumentation noise of the LIA; the measured value for the detection threshold of $5.3 \cdot 10^{-8}\,V/\sqrt{Hz}$ is slightly higher than expected:

$$\sqrt{S_J + S_{LIA}} \simeq 4 \cdot 10^{-8} < 5.3 \cdot 10^{-8}\,V/\sqrt{Hz} \tag{7.40}$$

where S_J is $1.2291 \cdot 10^{-15}\,V^2/Hz$ from eq. (6.11) and $\sqrt{S_{LIA}(105kHz)}$ is $20\,nV/\sqrt{Hz}$ from fig. 6.5b.

As done in section 7.3.4, we calculate the responsivity of the transductions by knowing the amplitude of thermal motion.
From the fits on experimental thermomechanical spectra (red curves in fig. 7.25),

we obtain the peak amplitudes:

$$A_{th}^{opto} = 3.48142776\,\mu V^2/Hz \tag{7.41a}$$

$$A_{th}^{piezo} = 0.001429771\,\mu V^2/Hz \tag{7.41b}$$

and by the means of eq. (7.30), we calculate the theoretical noise spectrum amplitude:

$$S_{th} = \frac{4k_B T Q_m}{M_1 \omega_r^3} \simeq 0.295\,pm^2/Hz \tag{7.42}$$

Let remind that the thermomechanical noise does not depend on the transduction. According to eq. (7.32), the responsivity for both methods will result as

$$\mathfrak{R}_{opto} = \sqrt{\frac{A_{th}^{opto}}{S_{th}}} \simeq 3.44\,\mu V/pm \tag{7.43a}$$

$$\mathfrak{R}_{piezo} = \sqrt{\frac{A_{th}^{piezo}}{S_{th}}} \simeq 0.07\,\mu V/pm \tag{7.43b}$$

As already noted, for equal cantilever displacement, the optomechanics provides a larger readout signal. For this particular setup configuration, the optomechanical transduction responsivity is evaluated 50 times higher compared to piezoresistive detection. Furthermore, we get a more interesting result: with respect to the piezoresistive detection, the optomechanical detection has a lower threshold detection which is well below the thermomechanical noise of the cantilever. The weak point of the optomechanical detection is a limited linearity, its cause is investigated in the section 7.3.7.

Allan deviation in parallel

Following the same procedure described in section 7.3.3, we record the *Allan variance* simultaneously for both transductions and we plot them in fig. 7.26: because the piezoresistive transduction presents a non-negligible detection noise threshold produced by instrumentation, the optomechanical transduction shows a lower *Allan variance* for short integration times, where the *Robin*'s formula in eq. (7.28) is well respected.
For higher drive voltages and longer integration times, all the curves meet again a lower bound as in fig. 7.18. This rigid wall is exactly the same for both transductions: this means that the *anomalous frequency noise* investigated in [8] does not depend on the readout technique.

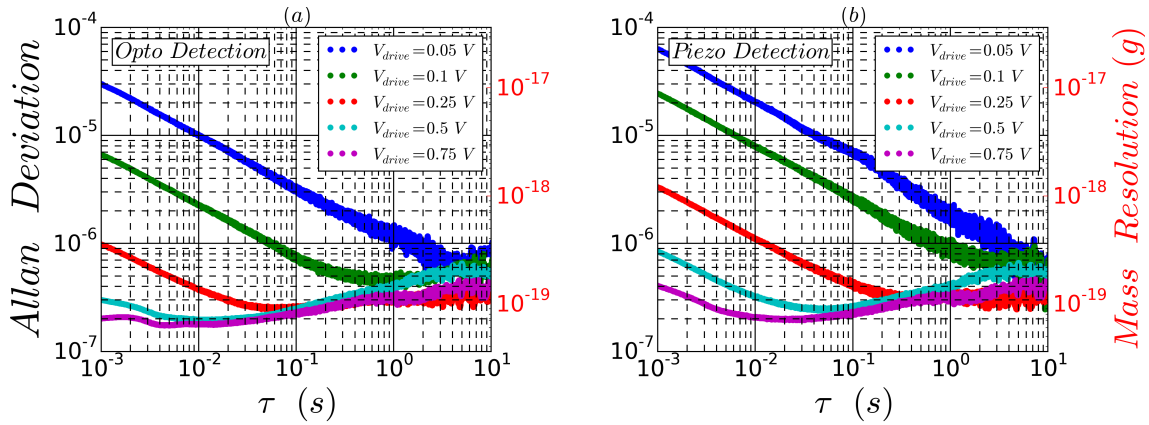

Figure 7.26: Comparison between *Allan variances* performed with (*a*) optomechanical detection and with (*b*) piezoresistive detection. For higher drive voltages, both methods show an identical lower bound caused by the anomalous phase noise.

As above discussed in section 2.3.2 and 2.4, with the introduction of the optomechanics, the transduction benefits already from a larger bandwidth and a simplified multiplexing. Furthermore, in comparison with the piezoresistive readout, we obtain also an improved responsivity and a lower detection threshold which leads to a smaller *Allan variance*. On the other hand, the transduction linearity is limited for the optomechanical readout.

7.3.7 Transduction for different wavelengths

To test the dependence of optomechanical transduction on the measurement wavelength, we perform it for different wavelengths. We check here if the transduction responsivity $\mathfrak{R}$ depends on the local slope of the optical peak around the measurement wavelength as predicted in section 4.3.
Using the calibrations done in section 7.3.4 and 7.3.5, we formulate also a hypothesis about the non-linearity of the optomechanical transduction which is highlighted in fig. 7.15 and 7.24.

We perform four different optomechanical transductions tuning the laser at four different wavelengths: out of resonance (λ_1), at the base of the optical peak (λ_2), at the best slope (λ_3) and on resonance (λ_4). (See fig. 7.27).

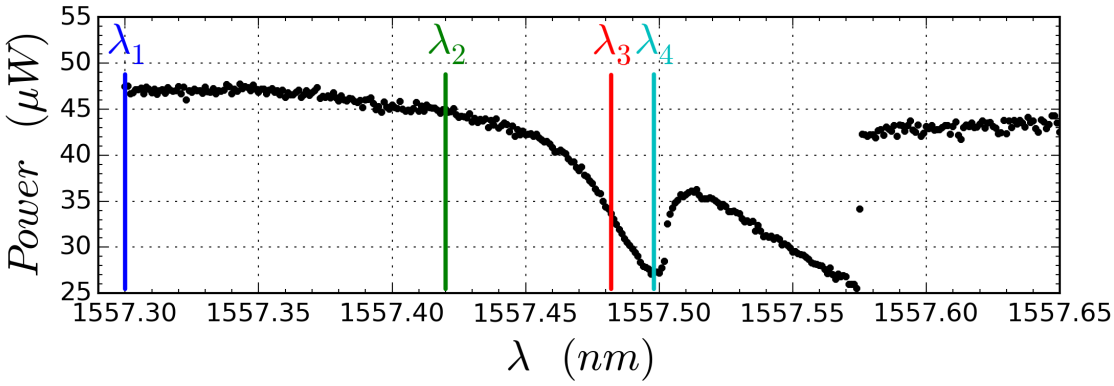

Figure 7.27: The transduction is performed tuning the laser at four different wavelengths: out of resonance, at the base of the peak, at the best slope and on resonance.

The setup configuration does not change from fig. 7.13 in section 7.3. An identical drive voltage of $1.5\,V$ is applied each time to the actuation electrode in order to compare the transduction signals for equal cantilever displacement.
The four different transductions are plotted in fig. 7.28(a): the transduction signal is almost null for the laser in λ_1, weak for λ_2 and maximum for the laser tuned at λ_3. It proves that the readout responsivity is linked to the slope of optical peak, as stated in section 4.3.
The mechanical response for λ_4 is quite unexpected: theoretically, the slope on optical resonance is null but, in practice, we observe a mechanical peak having an amplitude of $50\,mV$. A dissipative coupling could explain this trend; if the optomechanical coupling is not completely dispersive as found in section 4.2, the ring spectrum is not simply shifted but deformed too. The data points are quite noisy probably due to the non-linearity of the right side of the optical peak.

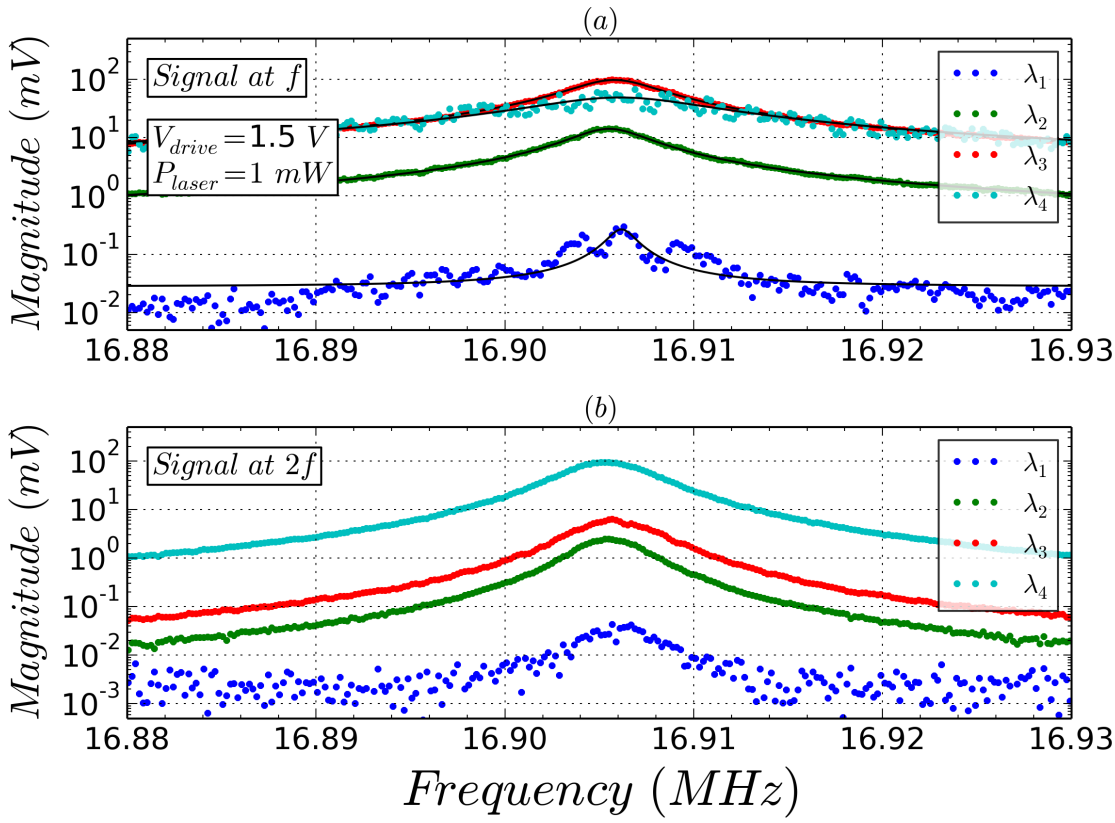

Figure 7.28: Mechanical response for different wavelengths: (a) the transduction responsivity depends on the laser wavelength tuning, (b) the signal component at $2f$ is a signature of the non-linearity of the transduction.

Thanks to the UHF-LIA, we demodulated the signal from the photodetector also at frequency $2f$ in order to check the non-linearity of the transduction (fig. 7.28(b)): the highest cyan peak comes from the measurement with the laser tuned at resonance (λ_4).
The cantilever displacement shifts the cavity at frequency f but the light is modulated at frequency $2f$ since the laser is tuned exactly at resonance. Although not linear at all, it could be considered a new type of transduction which provides a good signal level for applications demanding the laser on resonance. We can imagine a setup configuration where the optical actuation (see section 7.5) and the optical detection are performed by the means of a single laser which is tuned on the optical resonance.
The transduction performed at λ_3 shows as well a non-linearity which is coherent with the non-linearities already shown in the previous sections. The ratio between the amplitudes of the red peaks in fig. 7.28(a) and 7.28(b) states a non-linearity

around the 10% which has been already found in fig. 7.15. Calibrating the transduction via the detection of the thermomechanical spectrum, we are able to show in the following pages the source of this non-linearity.

For each wavelength, we acquired the thermomechanical spectrum of the cantilever (fig. 7.29) with the same procedure described in section 7.3.2. Having enough sensitivity only for λ_3 and λ_4, we obtain respectively a thermomechanical peak amplitude of $7.4690\,\mu V^2/Hz$ and $0.6295\,\mu V^2/Hz$ and the Q-factors of 3901 and 3551.

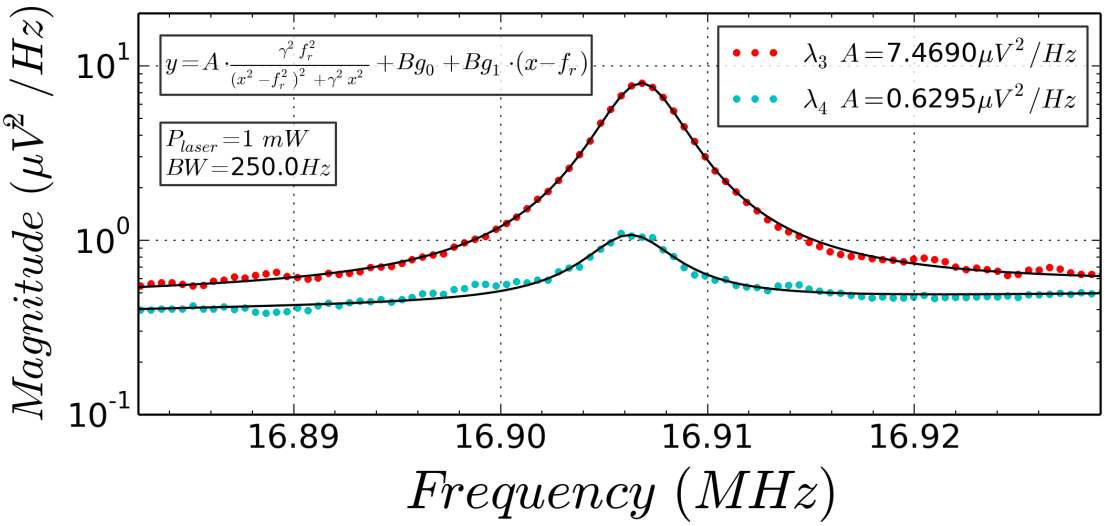

Figure 7.29: Thermomechanical noise spectra for different laser wavelengths. In this plot, the thermomechanical noise is normalised to $1Hz$-bandwidth.

As already done in section 7.3.4, we use the *thermomechanical noise* to calibrate the transduction chain obtaining the cantilever displacement in nm.
According to eq. (7.32), the responsivity for the transduction performed at λ_3 is

$$\mathfrak{R}_3 = \sqrt{\frac{A_{th}}{S_{th}}} = 5.172\,\mu V/pm \tag{7.44}$$

and similarly, the responsivity for λ_4 results as

$$\mathfrak{R}_4 = \sqrt{\frac{A_{th}}{S_{th}}} = 1.574\,\mu V/pm \tag{7.45}$$

Once the transduction is calibrated, we can plot again red curve from fig. 7.28(a) which describes the mechanical response performed at λ_3 for the driven cantilever.

As you can see from fig. 7.30, now the scale on the y-axis is nm.
For an actuation of $1.5V$ at the mechanical resonance frequency, the cantilever has an RMS oscillation amplitude of $18.983\,nm$. From the simulation in section 4.2, we estimated that for a cantilever oscillation of only $5\,nm$, the optical spectrum is already slightly deformed by a (partially) dissipative coupling. The optomechanical transduction has non-linear components because we are already out of the approximation of small cantilever displacement.

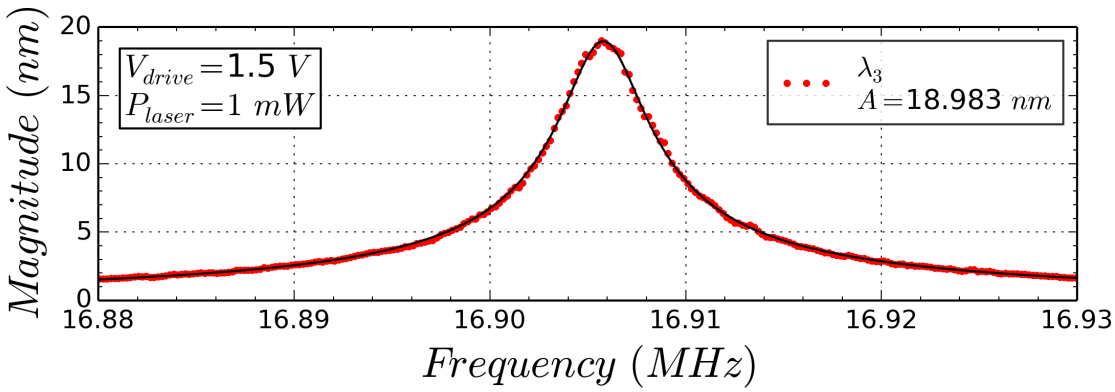

Figure 7.30: Calibrated transduction for λ_3: at resonance, the cantilever oscillates with an RMS amplitude of $18.983\,nm$.

However, neglecting for a moment the optical spectrum deformation, a second source of non-linearity arises from the linear approximation of the optical peak slope around the laser wavelength. (See section 4.3).
Knowing the optomechanical coupling factor from section 7.3.5, we calculate the optical spectrum shift in frequency and then convert it to wavelength. In the hypothesis that the g_{om} is constant over the displacement range, we have

$$\Delta\nu = \frac{g_{om}\cdot\Delta x}{2\pi} = \frac{g_{om}\cdot 2\sqrt{2}A}{2\pi} = \frac{0.1968\,\frac{\text{Grad}}{s\cdot nm}\cdot 2\sqrt{2}\cdot 18.983\,nm}{2\pi} = 1.682\,GHz \tag{7.46}$$

The $\sqrt{2}$ factor converts the RMS amplitude, measured by the LIA, in the absolute oscillation amplitude. Converting the light frequency shift in a wavelength shift, we obtain a optical spectrum shift equal to

$$|\Delta\lambda| \simeq \frac{\lambda^2}{c}\Delta\nu = \frac{(1557.481\cdot 10^{-9})^2}{2.99792\cdot 10^8}\cdot 1.682\cdot 10^9 \simeq 14\,pm \tag{7.47}$$

A wavelength shift of the ring spectrum around $14\,pm$ is comparable with the optical peak width. This means that, during the transduction, an important portion of the peak is scanned; we can see it graphically from fig. 7.31.

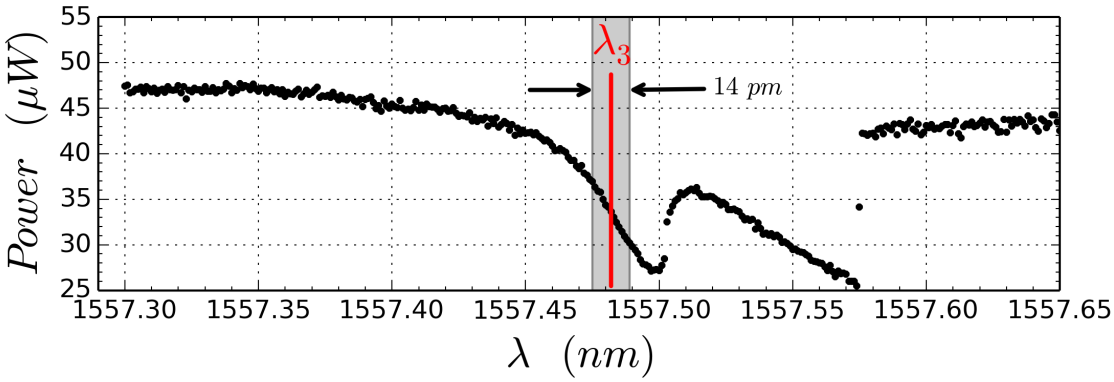

Figure 7.31: The wavelength shift covers almost completely the peak side. For this cantilever oscillation the transduction results affected by non-linearity.

For a 14 pm spectrum shift around λ_3, the linear approximation for the optical peak slope is not completely adequate any more.
Designing an optical ring having a lower Q-factor results in a wider peak upon which the linear approximation remains valid for wider ranges. As it often happens, we have to partially sacrifice the responsivity performances to improve the transduction linearity.

These simple evaluations find two possible sources of the non-linearity which affects the optomechanical transduction. For large oscillation amplitudes, the cantilever couples the optical ring too much modifying the shape of the optical spectrum. In this way, the optomechanical coupling factor results partially dissipative over the oscillation range. Furthermore, for thin optical peaks, the linear approximation around the laser wavelength becomes quickly inaccurate as soon as the optical ring is detuned of an amount comparable with the FWHM of the peak.
Playing on the device design parameters, a weaker coupling between the cantilever and the optical ring together with a lowered optical Q-factor are two possible solutions for the transduction non-linearities. On the other hand, according to eq. (4.16), the transduction responsivity is affected because of the reduction of g_{om} and Q_{opt}.

7.4 Optomechanical downmixing

In this section, we report a measurement method for nanomechanical resonators which enables the readout of mechanical resonance frequencies beyond the photodetector bandwidth.
The proposed technique, called *optomechanical downmixing*, represents an experimental solution to transport the measurement signal at arbitrary low frequencies. We show that this method can easily readout the *Brownian noise* of the device, without degrading the performance of the system with respect to direct measurement shown in the previous section 7.3. In the case that the transduction performance is limited by the photodetector, this technique allows employing low-bandwidth/low-noise photodetectors, leading to higher resolution for sensing applications.
This is a key in particular for mass spectrometry applications where both high displacement sensitivity and multi-mode operation are required. (See sections 2.4 and 2.3.2).

We present a solution to bring the interested optical signal at lower frequency in order to detect it with a low NEP/low BW photodetector. At the same time, the signal-to-noise ratio is preserved with respect to direct optomechanical detection. We detect *NEMS* displacements which occur at frequencies higher than the photodetector bandwidth and, at the same time, we take advantage of low NEP typical of low bandwidth photodetectors. In other words, the transduction bandwidth is not limited by the photodetector bandwidth any more. Removing this limit, the higher mechanical modes are easily accessible, even if they occur at frequencies higher than photodetector bandwidth.

7.4.1 Transduction scheme

In the downmixing scheme (fig. 7.32), the laser optical power P_{laser} is modulated at a frequency close to f, the mechanical actuation frequency

$$P_{laser}(t) = P_{laser} + P_{laser} \cdot M \cos[2\pi(f + \Delta f)t] \tag{7.48}$$

where M is the modulation index between 0 and 1.
As long as the cantilever does not move, the power coming out from the *through* port and collected on the photodetector will be

$$P_{pd}(t) = T(\lambda_{laser}) \cdot P_0 + T(\lambda_{laser}) \cdot P_0 \cdot M \cos[2\pi(f + \Delta f)t] \tag{7.49}$$

where $P_0 = \alpha_c P_{laser}$ is the laser power attenuated by the coupling losses α_c (section 5.3) and $T(\lambda)$ is the optical spectrum of the ring from eq. (7.23).

When the cantilever oscillates at frequency f, the optical power on the photodetector is the result of the mixing of the laser intensity with the resonator motion.

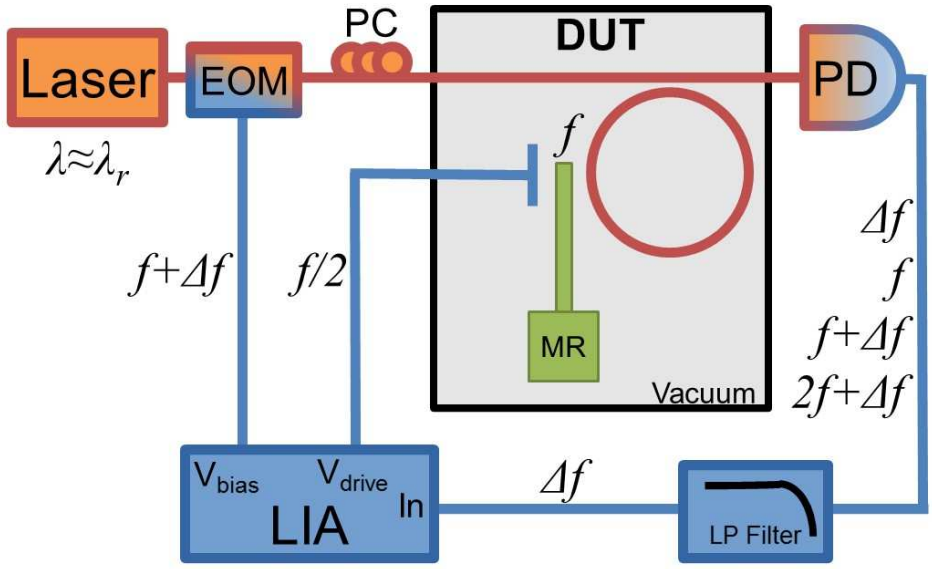

Figure 7.32: Optomechanical downmixing setup. EOM: electro-optic modulator, PC: polarization controller, DUT: device under test, MR: mechanical resonator, PD: photodetector, LP Filter: low-pass filter, LIA: Lock-In Amplifier. In blue the electric elements, in orange the optics and in green the mechanical domain.

In some steps, we can isolate the DC component, the components at Δf, f, $f+\Delta f$ and $2f+\Delta f$:

$$\begin{aligned} P_{pd}(t) = T(\lambda_{laser}) \cdot P_0 + T(\lambda_{laser}) \cdot P_0 \cdot \cos[2\pi(f+\Delta f)t] \\ + \frac{3\sqrt{3}}{4}\frac{P_0 Q_{opt}\lambda_r}{c} \cdot \frac{g_{om}}{2\pi} \cdot x(f)\cos[2\pi f t + \phi(f)] \\ + \frac{3\sqrt{3}}{4}\frac{P_0 Q_{opt}\lambda_r}{c} \cdot \frac{g_{om}}{2\pi} \cdot x(f) \cdot \frac{M}{2} \cdot \cos[2\pi(2f+\Delta f)t + \phi(f)] \\ + \frac{3\sqrt{3}}{4}\frac{P_0 Q_{opt}\lambda_r}{c} \cdot \frac{g_{om}}{2\pi} \cdot x(f) \cdot \frac{M}{2} \cdot \cos[2\pi\Delta f t - \phi(f)] \end{aligned} \quad (7.50)$$

where $x(f)$ and $\phi(f)$ are respectively the magnitude and phase response of the cantilever.
The DC component is automatically filtered by the photodetector (*NewPort 1811-FC-AC* section 6.3.2) and the component at frequency Δf is measured by the Lock-In Amplifier via a synchronous detection.
The low-pass filter in fig. 7.32 eliminates all the frequencies above Δf. This avoids the saturation of the ADC of the input of the LIA, in this way we can use the best input range benefiting from the best LIA sensitivity. All the other components would have been filtered anyway by the Lock-In detection.

The mechanical response (amplitude and phase) is thus transduced at an arbitrary modulation frequency Δf (here typically $100\,kHz$). Focusing on the component at Δf of eq. (7.50), the transduction signal on the photodetector is

$$P_{pd}^{\Delta f}(t) = \frac{3\sqrt{3}}{4}\frac{P_0 Q_{opt}\lambda_r}{c} \cdot \frac{g_{om}}{2\pi} \cdot x(f) \cdot \frac{M}{2} \cdot \cos[2\pi\Delta f t - \phi(f)] \tag{7.51}$$

consequently, the magnitude of the cantilever oscillation from the LIA detection results as

$$|V_{LIA,\,\Delta f}(f)| = G_{pd} \cdot \frac{3\sqrt{3}}{4}\frac{P_0 Q_{opt}\lambda_r}{c} \cdot \frac{g_{om}}{2\pi} \cdot \frac{M}{2} \cdot \frac{x(f)}{\sqrt{2}} \tag{7.52}$$

The factor $\sqrt{2}$ is due to the fact that LIA measures the RMS value of the signal component at frequency Δf.
Compared to direct detection in eq. (7.25), the signal is decreased by a factor $M/2$ but the same happens for the the *thermomechanical noise*. For this reasons the dynamic range of the measurement is preserved when the dominating noise in downmixing is the *thermomechanical* noise.
M is maximised until the non-linearities appear in the electro-optic modulator and the modulation can not be considered harmonic any more.

7.4.2 Comparison with direct transduction

Driving the cantilever with a voltage V_{drive}, we perform both methods concurrently in order to compare the transduction efficiency. We remove the low-pass filter at the LIA input and we measure simultaneously the third and the fifth terms of eq. (7.50) demodulating the photodetector signal at frequencies f and Δf. For a preliminary validation, the photodetector *Newport* is used for both techniques but in the next section we will use the photodetector *Femto* to benefit from the downmixing.
Fig. 7.33 demonstrates that the downmixing technique successfully transduces the mechanical motion of the resonator and, like the direct technique, provides a large signal level. The latter is decreased by a factor of roughly 3, due to the fact that $M \simeq 0.66$. For sensing applications, the dynamic range is a key to obtain a good frequency stability and hence a good limit of detection (see section 7.3.3). Although someone might be concerned by the signal decreasing, data in fig. 7.33 shows that the dynamic range obtained with the downmixing technique is very similar to that one obtained with the direct method. This happens because the *thermomechanical noise* of the mechanical resonator is easily resolved with both techniques. For the downmixing, the dynamic range on resonance is slightly degraded because the thermomechanical noise is closer to the detection threshold. However, choosing a low bandwidth/low NEP photodetector, the downmixing technique should offer a lower detection threshold.

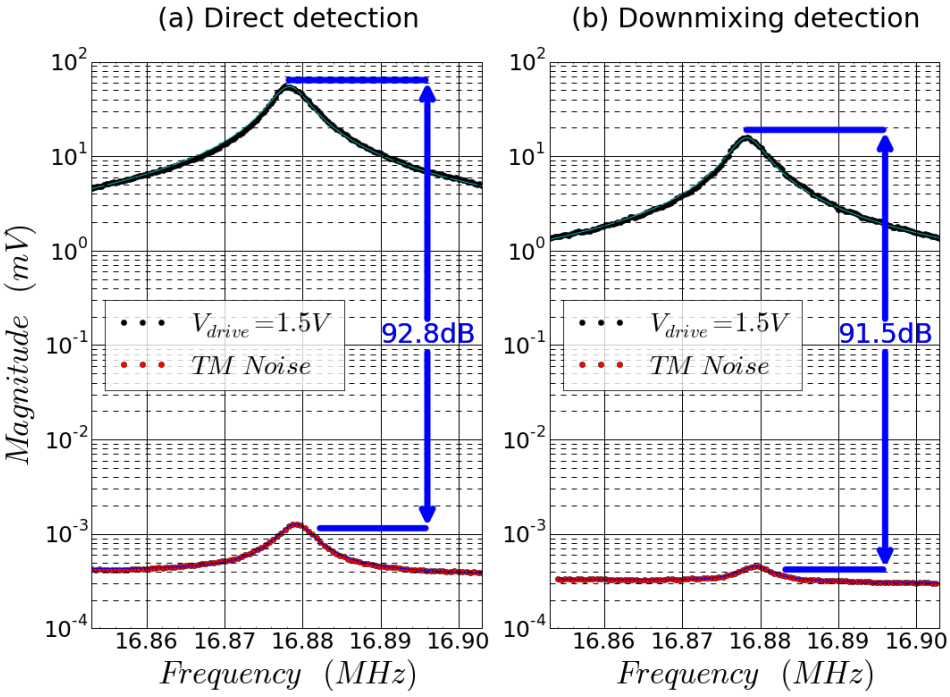

Figure 7.33: Mechanical peak of the 1st resonance obtained from (a) direct and (b) downmixing technique. TM stands for thermomechanical noise, which is normalized to 1 Hz. The dynamic range is very similar for the two techniques.

For mass sensing application, the mass resolution is proportional to the frequency stability of the resonator. We measured the *Allan deviation* (as done in section 7.3.3) with both techniques obtaining comparable values shown in fig. 7.34. Everything is coherent since, at the mechanical resonance, we are limited by the *thermomechanical noise* which is the dominating noise in both technique. As always, we observe the lower bound which does not depend on the transduction, as discussed in section 7.3.6. Just to give an idea of performances, using this system as mass sensor, we would achieve a mass resolution of 100 zg.

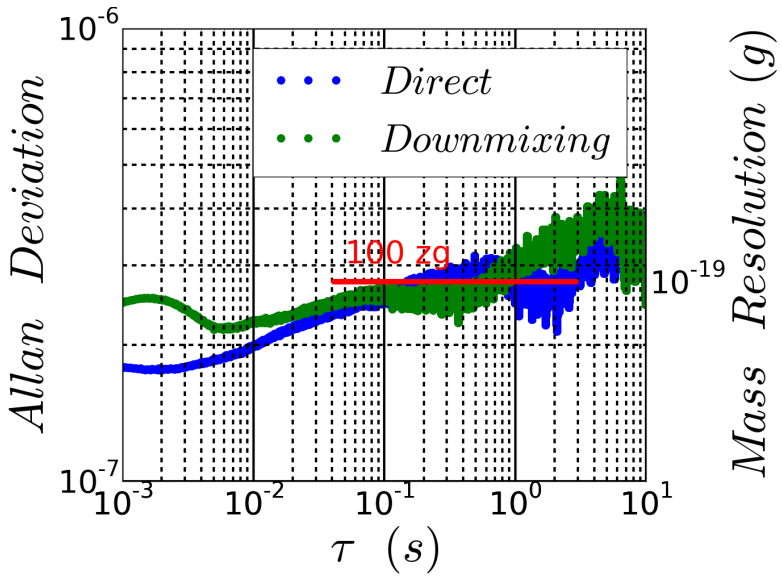

Figure 7.34: *Allan deviation* of the cantilever at resonance frequency: comparison between direct and downmixing technique.

7.4.3 Higher-order modes

Up to now, the two techniques are comparable in terms of dynamic range and frequency stability. Differently from direct detection, the optomechanical downmixing has an advantage: the frequency at which the transduction occurs is independent from the mechanical frequency of the cantilever. Increasing the actuation frequency, we now investigate higher mechanical modes having always a component of the transduction signal at frequency Δf.

We are able now to substitute the current photodetector from *NewPort* with a dedicated one from *Femto*. (Specifications in section 6.3.2).
We show in fig. 7.35 the cantilever readout up to the third resonance mode: we are detecting the first, the second and the third mechanical mode, respectively at 16.9, 104 and 278 MHz, using a photodetector which has only a 500 kHz bandwidth. For this particular case, the photodetector *Femto OE-200-IN2* has a NEP of $2.5\,pW/\sqrt{Hz}$, ten times smaller than the previous photodetector used for the direct detection. Thanks to the downmixing, the transduction is largely limited by the shot noise of the light, in contrast to previous measurement shown in section 6.6.1. Just remember that for a light power of $P = 50\,\mu W$, the shot noise which affects the beam is $\sqrt{S_{shot}} = \sqrt{2hcP/\lambda} = 3.58\,pW/\sqrt{Hz}$ >NEP.

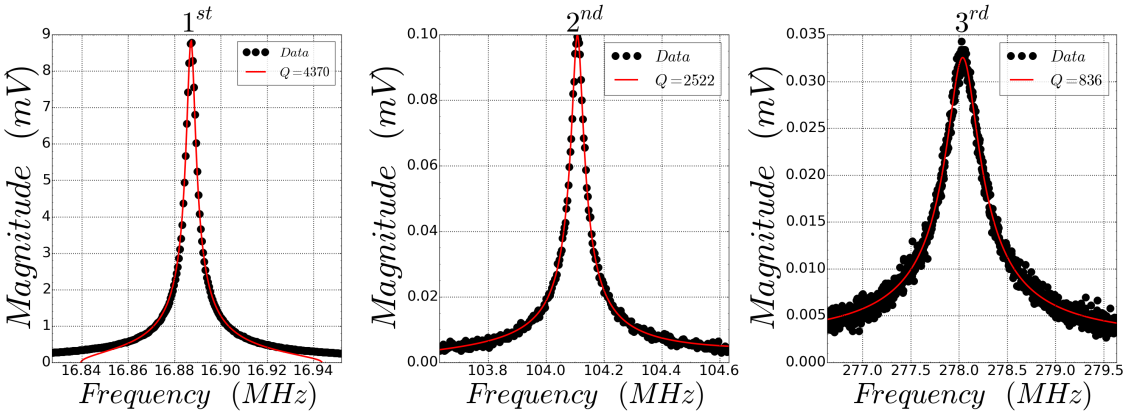

Figure 7.35: Mechanical response of the cantilever up to the third resonance: we are detecting resonance frequencies up to 278 MHz with a photodetector having a bandwidth of 500 kHz.

As further benefits, the photodetector provides an electrical signal at the demodulation frequency Δf which is handily processed by standard low frequency electronics. Moreover, this electrical signal does not suffer from the parasitic capacitances of transmission line cables.

We found a good solution to detect higher order resonances without being limited by the photodetector or by the electronics bandwidth anymore. The performance in terms of transduction is preserved or, in some cases, improved since, in general, the low-bandwidth photodetectors show better NEP values. The downmixing technique fits very well for the mass sensing application which demands the detection of higher mechanical modes at high frequencies further increased by the *NEMS* downscaling.

While the downmixing technique solves the issues associated with the high-frequency transduction of the resonator, the electrical actuation of the device presents the same issues: cantilever actuation still remains at very high frequencies because of *NEMS* downscaling trend. For this reason, the optical actuation is investigated and performed in the following section.

7.5 Optical actuation

From section 4.4, we know that the light travelling into a waveguide applies a force to elements in the evanescent field. Here we use this force to excite the cantilever and we detect its mechanical response via the piezoresistive transduction from section 7.1.

The response time of the ring resonator has an order of magnitude 6 times smaller than the response time of the mechanical resonator. Knowing the typical values of the characterised devices, the following relation is always valid

$$\frac{Q_m}{f_m} \simeq 0.2\,ms \gg \frac{Q_{opt}}{\nu_{opt}} \simeq 0.3\,ns \tag{7.53}$$

In this regime, it is impossible to meet *back-action* effects [14]. So we always consider the action of the light as instantaneous compared to any mechanical response.

The setup for the optical actuation is shown in fig. 7.36: the light injected into the ring is modulated at frequency f while the cantilever readout is performed with the standard piezoresistive technique from section 7.1. The frequency f is swept around the mechanical resonance frequency of the cantilever in order to obtain its mechanical response.

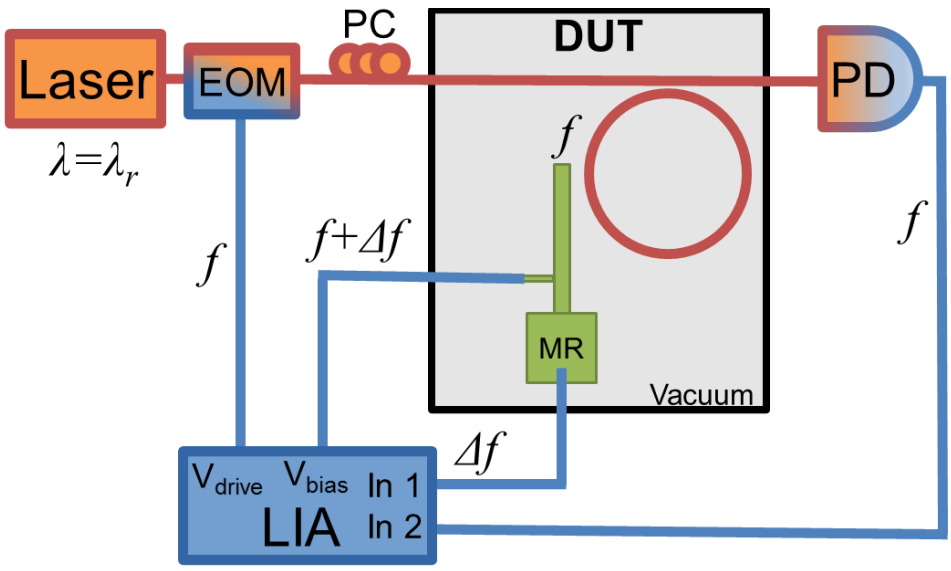

Figure 7.36: Optical actuation setup. EOM: electro-optic modulator, PC: polarization controller, DUT: device under test, MR: mechanical resonator, LIA: Lock-In Amplifier. In blue the electric elements, in orange the optics and in green the mechanical domain.

Differently from the transduction in sections 7.3 and 7.4, the laser wavelength is tuned exactly at the optical resonance as illustrated in fig. 7.37. In this way, we inject the maximum amount of power into the ring improving the force applied to the cantilever.

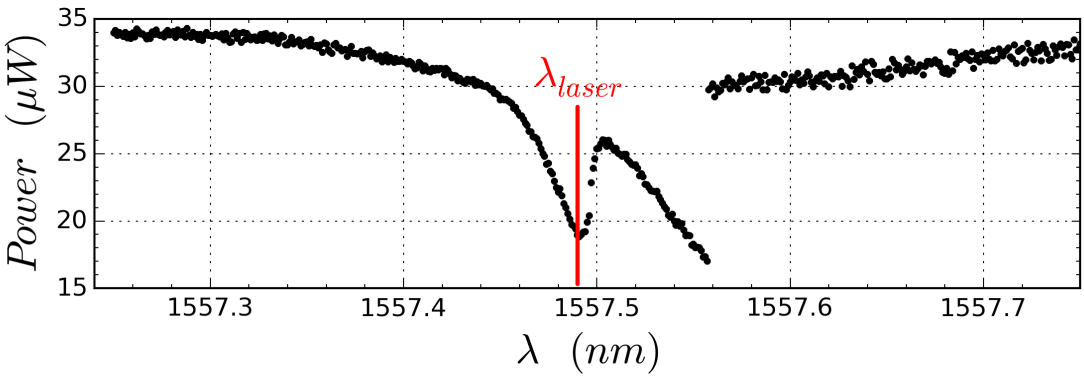

Figure 7.37: Optical spectrum of the ring: to improve the actuation the laser is tuned exactly on resonance. Neglecting other losses, the coupling losses are around $14.7\,dB$ for two grating couplers (see section 5.3). $C_{\mathcal{R}}$ is around 0.34, $\mathcal{F} = 716.6$ and $\lambda_r = 1557.488\,nm$

Differently from the optomechanical downmixing in section 7.4, the drive voltage, provided by the LIA output, tunes the modulation factor M of the injected light:

$$P_{laser}(t) = P_{laser} + M(V_{drive}) \cdot P_{laser} \cdot \cos(2\pi f t) \tag{7.54}$$

From the plot in fig. 7.38, we observe the mechanical spectrum for different V_{drive}: the modest optomechanical coupling factor [7][45] and the relatively low power in the ring are responsible for the weak cantilever actuation (see fig. 4.8). The value for the optomechanical coupling factor is fixed by the small coupling zone (no racetrack) and the optomechanical gap of $200\,nm$. Anyway, the usual mechanical resonance peak at $16.9\,MHz$ is clearly detected by the means of the piezoresistive detection. For this particular device, the efficiency of the optical actuation is about 30 times smaller than the electrostatic actuation. This is evaluated from the comparison between the purple peak in fig. 7.38 and the blue peak in fig. 7.23(*b*) in which both transductions are performed with a gauge polarisation V_{bias} of $1.5\,V$ and a V_{drive} of $0.5\,V$.
It is not completely correct to compare in absolute the two actuations for an equal V_{drive}: the optical actuation depends on external factors (e.g electro-optic modulator) and on device parameters (e.g. coupling losses, g_{om} and optical ring finesse),

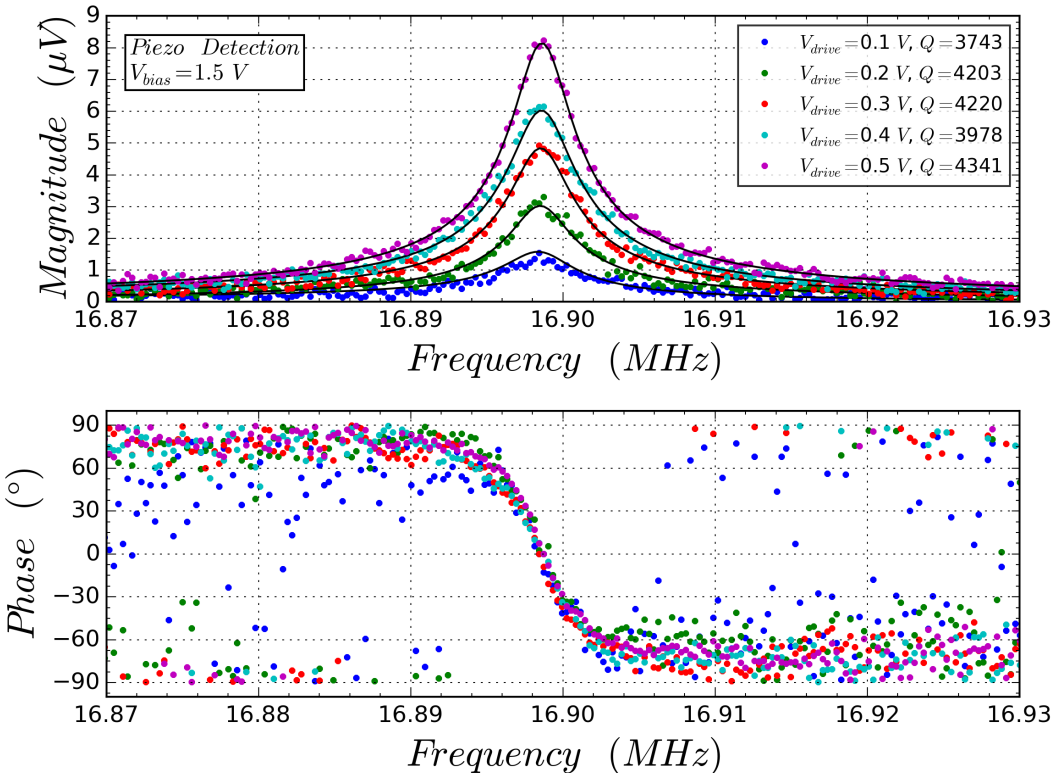

Figure 7.38: Cantilever mechanical response for different optical actuations. The detection is performed via the piezoresistive gauge. Solid lines correspond to the fits done on the experimental data points.

whereas the electrostatic actuation depends on the electrode shape. They have completely different natures and trends, but the factor 30 gives us an idea, at least for this device and for the specific drive voltage of $0.5\,V$.

The specification for the electro-optical modulator does not provide an accurate value for the modulation factor M. For a given V_{drive}, it is difficult to know exactly the amplitude of the laser beam modulation: that is why we prefer to measure it. The *through* port is monitored and the signal from the photodetector is demodulated at f (see fig. 7.36). We evaluate directly the amplitude of the light modulation in the following way:

$$M(V_{drive})P_{laser} = \frac{|V_{LIA,f}| \cdot \sqrt{2} \cdot \alpha_c}{G_{pd} \cdot (1 - C_{\mathcal{R}})} \tag{7.55}$$

where $\alpha_c \simeq 30$ are the coupling losses for both couplers, $C_{\mathcal{R}}$ is the contrast for the *through* port and G_{pd} is the photodetector gain. The factor $\sqrt{2}$ comes from the demodulation process since a LIA measures the RMS value of the amplitude.
With the help of eq. (3.52), we estimate the power inside the ring on resonance.

We have to attenuate the laser power by the first coupler and then multiply it by *contrast* and the *finesse*:

$$P_{ring}(t) = P_{laser}(t) \cdot \frac{C_{\mathcal{R}}}{\sqrt{\alpha_c}} \cdot \frac{\mathcal{F}}{\pi} \tag{7.56}$$

By the means of equations (7.54), (7.55) and (7.56), we find the explicit expression for the light power circulating in the ring resonator:

$$P_{ring}(t) = \frac{P_{laser}}{\sqrt{\alpha_c}} \cdot C_{\mathcal{R}} \cdot \frac{\mathcal{F}}{\pi} + \frac{|V_{LIA,f}| \cdot \sqrt{2} \cdot \sqrt{\alpha_c}}{G_{pd} \cdot (1 - C_{\mathcal{R}})} \cdot C_{\mathcal{R}} \cdot \frac{\mathcal{F}}{\pi} \cdot \cos(2\pi f t) \tag{7.57}$$

During the experiment, we get $|V_{LIA,f}|$ from the LIA for each V_{drive}, then we calculate the amplitude of the laser power modulation thanks to eq. (7.55). Similarly, the modulation of the light power inside the ring is obtained by the means of second term in eq. (7.57).
In table 7.1, we listed the amplitude of the modulations for the laser (3rd column) and the amplitude of the modulation for the light into the ring (4th column):

Drive voltage	***Through* signal at f**	**Amplitude of laser light modulation**	**Amplitude of ring light modulation**
V_{drive}	$\lvert V_{LIA,f}\rvert$	$M(V_{drive})P_{laser}$	$M(V_{drive})P_{laser} \cdot \frac{C_{\mathcal{R}}}{\sqrt{\alpha_c}} \frac{\mathcal{F}}{\pi}$
$[V]$	$[mV]$	$[\mu W]$	$[mW]$
0.1	45	85.23	1.56
0.2	90	170.5	3.13
0.3	135	255.7	4.69
0.4	175	311.5	6.08
0.5	220	416.7	7.64

Table 7.1: Estimation of the optical power modulations for each drive voltage V_{drive}.

Let us recall that, for this device, $\mathcal{F} = 716.6$ and $C_{\mathcal{R}} = 0.34$. As already shown in eq. (7.19) and (7.20), these values are obtained from the fitted spectrum in fig. 7.9. In this way, not only do we estimate the amplitude of light modulation inside the ring but we also verify that the opto-electrical modulator is (almost) linear for V_{drive} up to $0.5\,V$.

The last step for a quantitative analysis of the optical gradient force is the calibration of the cantilever displacement in *pm* units. Fortunately, the piezoresistive readout is really repeatable since it does not require any discretionary preparation such as the laser tuning or the fiber alignment. The electrical bonding assures stable

device contacts and the demodulation frequency Δf is always equal to $105\,kHz$, from section 7.1. We can reuse the calibration made in section 7.3.6, considering it as reliable. Conversely, it is difficult to compare the optomechanical detections from different experiments since every measurement session requires a new fiber alignment and a new laser tuning.
From the eq. (7.43b), we know the responsivity for the piezoresistive transduction ($\mathfrak{R}_{piezo} = 0.07\,\mu V/pm$) and we use it to calibrate the y-axis of plot in fig. 7.38. We can now plot in fig. 7.39 the mechanical peak amplitudes (at resonance) versus the amplitude of the light modulation into the ring:

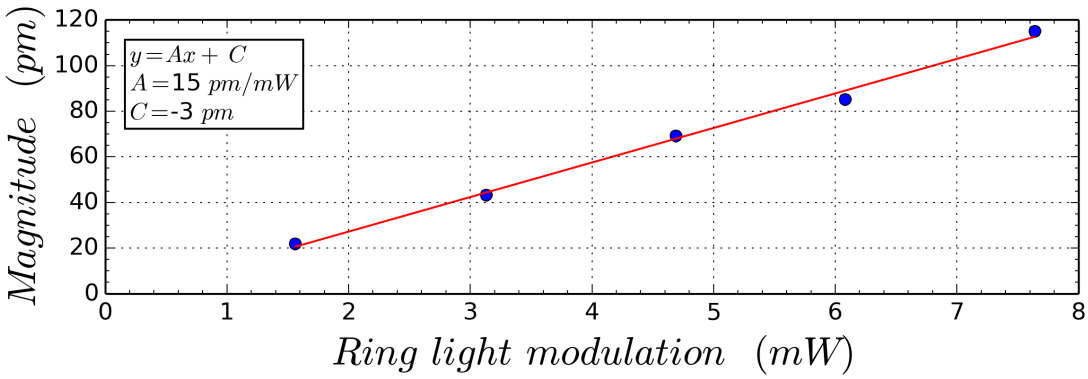

Figure 7.39: Cantilever oscillation amplitude (at resonance) for different optical actuations: on the x-axis, the values of the modulated light power inside the ring (4th column of table 7.1) and on the y-axis, the mechanical peak amplitude from fig. 7.38 after being converted in pm.

We demonstrated that the cantilever oscillation amplitude is proportional to the light modulation power. The optical gradient force increases linearly with the light power which is coherent with the theoretical description made in section 4.4.
Beyond this result, the parallel opto/piezo transduction shows once more its usefulness: since the piezoresistive detection is a repeatable and well established technique, this device is a unique tool to investigate quantitatively the optical gradient force.

7.6 Conclusions

In this chapter, we performed the optomechanical detection of an in-plane cantilever investigating the dynamic range and the linearity of the transduction. Through the detection of the *Brownian motion*, we calibrate the responsivity of the transduction in air and under vacuum. Furthermore, we evaluate experimentally the optomechanical coupling factor between ring and cantilever.
The parallel piezoresistive transduction is more than a practical debugging tool: it enables a simultaneous comparison between transduction techniques *in-situ*. It contributes to the investigation of non-linearity and frequency stability. For equal displacement, the optomechanical transduction has better performances but it becomes non-linear before the cantilever mechanical response enters in the non-linear regime.
We endorse as well the mechanical origin of frequency fluctuations for *NEMS* resonators. Since the *Allan variances* for both techniques have the same absolute value, the anomalous noise for long integration time does not originate from the cantilever transduction.

In the frame of mass sensing, we developed the optomechanical downmixing to track higher resonance modes which occur at very high frequencies because of *NEMS* downscaling. Thanks to this technique, the displacement signal is transferred at arbitrary low frequency and it can be detected by low-NEP photodetectors and processed by low-bandwidth electronics. In other words, we are not limited anymore by the transduction bandwidth but only by the actuation.

To close the loop of the optomechanics applied to *NEMS*, we explore the optical actuation in order to remove a further obstacle for neutral mass sensing. Since optical signals are not limited by parasitic capacitances, the optical actuation has a bandwidth which is limited only by the time response of the optical cavity. We excite the cantilever by the means of the optical gradient force and we detect the displacement via the piezoresistive detection. Taking advantage of multiplexing offered by the photonics, the next step is a optical actuation combined with the optomechanical detection. This is known in literature as the *pump/probe* setup.

Chapter 8

Conclusion

Optomechanical detection improves the *NEMS* transduction in terms of *responsivity*, *bandwidth* and *multiplexing* with regards to most electrical methods. A readout having these performances opens the way for a boosted *NEMS downscaling*: the next generation of devices will take advantage of downscale benefits preserving at the same time the transduction efficiency.

From a technological point of view, the challenge of the project was merging *photonics*, *piezoresistive gauges*, *electrical actuation* and *released mechanics*. The efforts led to a sufficient number of in-plane cantilever devices whereas the membrane devices are still waiting for a successful release.
Despite the first fabrication process being unreliable, we identified the technological issues and we solved them: the next run has been simplified removing the via metal path, the piezoresistive detection and adopting an *all pass* ring geometry. The electrical actuation is maintained by virtue of its simple implementation and efficacy.
A further optimisation of the ring resonator could improve the responsivity and the dynamic range of the transduction via a correct tuning of the optical quality factor and the contrast.

We developed here a *test bench* for the optomechanical devices *under vacuum*: the light is injected and collected by the means of two *optical fibers* aligned with the sample inside a vacuum chamber. The laser beam travels through the device and it is measured by a *photodetector*, then the signal processing is performed by a *Lock-In Amplifier*. Additional electrical contacts enable the piezoresistive detection and the electrostatic actuation. The instrumentation which forms the setup is coordinated by the means of a dedicated software.
A deeper investigation of the test bench is required especially about light injecting noise: the optical characterisation presents higher than expected noise levels and *Allan deviation* is affected by harmonics which still have a unknown origin. When

the wafer yield is improved, a correct packaging will tackle the fiber alignment issue at its source.
Anyway, all the below listed results are obtained thanks to this setup which is today a solid reference for electro-optomechanical experiments under vacuum. Moreover, the experimental system is open to easy upgrades which are already under way. A cryostat would enable low-temperature experiments which investigate further the *NEMS* mass sensing and the cantilever frequency fluctuation.

The test bench enables the characterisation of the fabricated devices delivering interesting results. In the first instance, the piezoresistive transduction is a practical tool to debug the fabrication technology. After that, it excludes the hypothesis of a *mechanical non-linearity* of the cantilever. Finally, the parallel transduction proves to be useful for a more fundamental investigation concerning the *NEMS frequency stability*: the *Allan deviation* shows a lower bound which is identical for both transduction method; it endorses the hypothesis that the *anomalous frequency noise* has a mechanical origin.
We developed the *optomechanical downmixing* which extends the *NEMS* detection at very high frequencies: since the displacement is transduced at arbitrary low frequency, the photodetector bandwidth ceases being a limiting factor and the obtained signal is processed by standard electronics. Considering the favourable noise level of low-bandwidth photodetectors, the transduction resolution is therefore limited only by the laser *shot noise*.
Once the *NEMS* resonance frequencies will achieve the GHz domain, the *electrical actuation* will be a further limiting factor. For this reason, the optical actuation has been explored with encouraging results: the cantilever moves under the action of the *optical gradient force* and the displacement is proportional to laser power modulation.

This work introduced the *optomechanics* at *LCMC* laboratory making the *Leti* a new scientific actor in the optomechanical *NEMS* domain.

Appendix A

Ring Resonators

In this appendix are collected the details of calculation for the ring resonator properties shown in chapter 3.

A.1 All pass resonator

From eq. (3.6a), the normalised power $\mathcal{R}$ in the *through* waveguide is

$$\mathcal{R} = |E_{t1}|^2 = E_{t1} \cdot E_{t1}^* = \frac{-\alpha + te^{-i\theta}}{-\alpha t^* + e^{-i\theta}} \cdot \frac{-\alpha + t^* e^{i\theta}}{-\alpha t + e^{i\theta}} = \frac{\alpha^2 + |t|^2 - \alpha(t^* e^{i\theta} + te^{-i\theta})}{1 + \alpha^2|t|^2 - \alpha(t^* e^{i\theta} + te^{-i\theta})} =$$
$$= \frac{\alpha^2 + |t|^2 - \alpha|t|[e^{i(\theta-\phi_t)} + e^{-i(\theta-\phi_t)}]}{1 + \alpha^2|t|^2 - \alpha|t|[e^{i(\theta-\phi_t)} + e^{-i(\theta-\phi_t)}]} = \frac{\alpha^2 + |t|^2 - 2\alpha|t|\cos(\theta - \phi_t)}{1 + \alpha^2|t|^2 - 2\alpha|t|\cos(\theta - \phi_t)} \quad \text{(A.1)}$$

where $t = |t|e^{i\phi_t}$.
t represents the portion of light which is not coupled into the ring and ϕ_t the phase shift of the coupler. ($t^* = |t|e^{-i\phi_t}$)

The circulating power $\mathcal{P}$ in the ring is calculated from eq. (3.6b)

$$\mathcal{P} = |E_{i2}|^2 = E_{i2} \cdot E_{i2}^* = \frac{-\alpha\kappa^*}{-\alpha t^* + e^{-i\theta}} \cdot \frac{-\alpha\kappa}{-\alpha t + e^{i\theta}} = \frac{\alpha^2|k|^2}{1 + \alpha^2|t|^2 - \alpha(t^* e^{i\theta} + te^{-i\theta})} =$$
$$= \frac{\alpha^2(1 - |t|^2)}{1 + \alpha^2|t|^2 - \alpha|t|[e^{i(\theta-\phi_t)} + e^{-i(\theta-\phi_t)}]} = \frac{\alpha^2(1 - |t|^2)}{1 + \alpha^2|t|^2 - 2\alpha|t|\cos(\theta - \phi_t)} \quad \text{(A.2)}$$

Concerning the phase shift between input and output, from the equation (3.6a)

we can also calculate the effective phase shift Φ induced by the ring resonator:

$$\begin{aligned}
\Phi = \arg(E_{t1}) = \arg\left(e^{i\pi}e^{i\theta}\cdot\frac{\alpha - te^{-i\theta}}{1-\alpha t^* e^{i\theta}}\right) = \\
= \arg(e^{i(\pi+\theta)}) + \arg(\alpha - te^{-i\theta}) - \arg(1-\alpha t^* e^{i\theta}) = \\
= \pi + \theta + \arctan\left(\frac{\mathrm{Im}\,(\alpha - te^{-i\theta})}{\mathrm{Re}\,(\alpha - te^{-i\theta})}\right) - \arctan\left(\frac{\mathrm{Im}\,(1-\alpha t^* e^{i\theta})}{\mathrm{Re}\,(1-\alpha t^* e^{i\theta})}\right) = \\
= \pi + \theta + \arctan\left(\frac{|t|\sin(\theta-\phi_t)}{\alpha - |t|\cos(\theta-\phi_t)}\right) - \arctan\left(\frac{-\alpha|t|\sin(\theta-\phi_t)}{1-\alpha|t|\cos(\theta-\phi_t)}\right) \\
= \pi + \theta + \arctan\left(\frac{|t|\sin(\theta-\phi_t)}{\alpha - |t|\cos(\theta-\phi_t)}\right) + \arctan\left(\frac{\alpha|t|\sin(\theta-\phi_t)}{1-\alpha|t|\cos(\theta-\phi_t)}\right) \quad \text{(A.3)}
\end{aligned}$$

The phase response for a ring with no intrinsic losses ($\alpha = 1$) is plotted in figure (A.1a) for different values of the coupling coefficient $|t|$. In figure (A.1b), we see that for critical coupling ($\alpha = |t|$) the phase jumps of π on resonance, for over and undercoupling, the phase shift is continuous near the resonance.

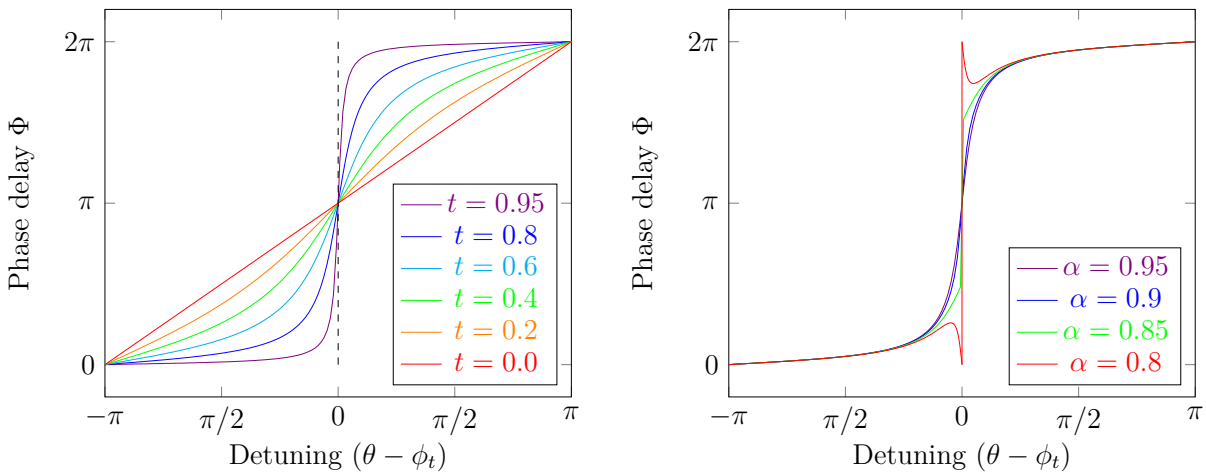

(a) Phase delay Φ for different values of $|t|$ and with $\alpha = 1$

(b) Phase delay Φ for different values of α and with $|t| = 0.85$

Figure A.1: Phase delay of a all pass resonator.

A.2 Add-Drop resonator

Applying the conditions (3.13a) and (3.13b), the system in (3.14) evolves in:

$$\begin{cases} E_{t1} = t_1 + \kappa_1 \alpha_2 e^{i\theta_2} E_{r3} & \text{(A.4a)} \\ E_{r1} = -\kappa_1^* + t_1^* \alpha_2 e^{i\theta_2} E_{r3} & \text{(A.4b)} \\ E_{t2} = \kappa_2 \alpha_1 e^{i\theta_1} E_{r1} & \text{(A.4c)} \\ E_{r3} = t_2^* \alpha_1 e^{i\theta_1} E_{r1} & \text{(A.4d)} \end{cases}$$

if we substitute (A.4b) in (A.4c) and (A.4d),

$$\begin{cases} E_{t1} = t_1 + \kappa_1 \alpha_2 e^{i\theta_2} E_{r3} & \text{(A.5a)} \\ E_{r1} = -\kappa_1^* + t_1^* \alpha_2 e^{i\theta_2} E_{r3} & \text{(A.5b)} \\ E_{t2} = \kappa_2 \alpha_1 e^{i\theta_1} (-\kappa_1^* + t_1^* \alpha_2 e^{i\theta_2} E_{r3}) & \text{(A.5c)} \\ E_{r3} = t_2^* \alpha_1 e^{i\theta_1} (-\kappa_1^* + t_1^* \alpha_2 e^{i\theta_2} E_{r3}) & \text{(A.5d)} \end{cases}$$

then we solve (A.5d) for E_{r3},

$$\begin{cases} E_{t1} = t_1 + \kappa_1 \alpha_2 e^{i\theta_2} E_{r3} & \text{(A.6a)} \\ E_{r1} = -\kappa_1^* + t_1^* \alpha_2 e^{i\theta_2} E_{r3} & \text{(A.6b)} \\ E_{t2} = -\kappa_1^* \kappa_2 \alpha_1 e^{i\theta_1} + \kappa_2 t_1^* \alpha_1 \alpha_2 e^{i(\theta_1+\theta_2)} E_{r3} & \text{(A.6c)} \\ E_{r3} = \dfrac{-\kappa_1^* t_2^* \alpha_1 e^{i\theta_1}}{1 - t_1^* t_2^* \alpha_1 \alpha_2 e^{i(\theta_1+\theta_2)}} = \dfrac{-\kappa_1^* t_2^* \alpha_1 e^{i\theta_1}}{1 - t_1^* t_2^* \alpha e^{i\theta}} & \text{(A.6d)} \end{cases}$$

and then we substitute it in the other equations

$$\begin{cases} E_{t1} = t_1 + \kappa_1 \alpha_2 e^{i\theta_2} \dfrac{-\kappa_1^* t_2^* \alpha_1 e^{i\theta_1}}{1 - t_1^* t_2^* \alpha e^{i\theta}} & \text{(A.7a)} \\ E_{r1} = -\kappa_1^* + t_1^* \alpha_2 e^{i\theta_2} \dfrac{-\kappa_1^* t_2^* \alpha_1 e^{i\theta_1}}{1 - t_1^* t_2^* \alpha e^{i\theta}} & \text{(A.7b)} \\ E_{t2} = -\kappa_1^* \kappa_2 \alpha_1 e^{i\theta_1} + \kappa_2 t_1^* \alpha e^{i\theta} \dfrac{-\kappa_1^* t_2^* \alpha_1 e^{i\theta_1}}{1 - t_1^* t_2^* \alpha e^{i\theta}} & \text{(A.7c)} \\ E_{r3} = \dfrac{-\kappa_1^* t_2^* \alpha_1 e^{i\theta_1}}{1 - t_1^* t_2^* \alpha e^{i\theta}} & \text{(A.7d)} \end{cases}$$

$$\begin{cases} E_{t1} = t_1 + \dfrac{-\kappa_1 \kappa_1^* t_2^* \alpha e^{i\theta}}{1 - t_1^* t_2^* \alpha e^{i\theta}} = \dfrac{t_1 - t_1 t_1^* t_2^* \alpha e^{i\theta} - \kappa_1 \kappa_1^* t_2^* \alpha e^{i\theta}}{1 - t_1^* t_2^* \alpha e^{i\theta}} & \text{(A.8a)} \\ E_{r1} = -\kappa_1^* + \dfrac{-\kappa_1^* t_1^* t_2^* \alpha e^{i\theta}}{1 - t_1^* t_2^* \alpha e^{i\theta}} & \text{(A.8b)} \\ E_{t2} = -\kappa_1^* \kappa_2 \alpha_1 e^{i\theta_1} + \dfrac{-\kappa_1^* \kappa_2 t_1^* t_2^* \alpha \alpha_1 e^{i\theta} e^{i\theta_1}}{1 - t_1^* t_2^* \alpha e^{i\theta}} & \text{(A.8c)} \\ E_{r3} = \dfrac{-\kappa_1^* t_2^* \alpha_1 e^{i\theta_1}}{1 - t_1^* t_2^* \alpha e^{i\theta}} & \text{(A.8d)} \end{cases}$$

$$\begin{cases} E_{t1} = \dfrac{t_1 - t_2^* \alpha e^{i\theta}(|t_1|^2 + |\kappa_1|^2)}{1 - t_1^* t_2^* \alpha e^{i\theta}} & \text{(A.9a)} \\ E_{r1} = \dfrac{-\kappa_1^* + \kappa_1^* t_1^* t_2^* \alpha e^{i\theta} - \kappa_1^* t_1^* t_2^* \alpha e^{i\theta}}{1 - t_1^* t_2^* \alpha e^{i\theta}} & \text{(A.9b)} \\ E_{t2} = \dfrac{-\kappa_1^* \kappa_2 \alpha_1 e^{i\theta_1} + \kappa_1^* \kappa_2 t_1^* t_2^* \alpha \alpha_1 e^{i\theta} e^{i\theta_1} - \kappa_1^* \kappa_2 t_1^* t_2^* \alpha \alpha_1 e^{i\theta} e^{i\theta_1}}{1 - t_1^* t_2^* \alpha e^{i\theta}} & \text{(A.9c)} \\ E_{r3} = \dfrac{-\kappa_1^* t_2^* \alpha_1 e^{i\theta_1}}{1 - t_1^* t_2^* \alpha e^{i\theta}} & \text{(A.9d)} \end{cases}$$

$$\begin{cases} E_{t1} = \dfrac{t_1 - t_2^* \alpha e^{i\theta}}{1 - t_1^* t_2^* \alpha e^{i\theta}} & \text{(A.10a)} \\ E_{r1} = \dfrac{-\kappa_1^*}{1 - t_1^* t_2^* \alpha e^{i\theta}} & \text{(A.10b)} \\ E_{t2} = \dfrac{-\kappa_1^* \kappa_2 \alpha_1 e^{i\theta_1}}{1 - t_1^* t_2^* \alpha e^{i\theta}} & \text{(A.10c)} \\ E_{r3} = \dfrac{-\kappa_1^* t_2^* \alpha_1 e^{i\theta_1}}{1 - t_1^* t_2^* \alpha e^{i\theta}} & \text{(A.10d)} \end{cases}$$

We obtain the mode amplitude at the *through* and *drop* ports respectively from equations (A.10a) and (A.10c).

Let's now calculate the output power in *through* $\mathcal{R}$

$$\begin{aligned} \mathcal{R} = |E_{t1}|^2 = \frac{t_1 - t_2^* \alpha e^{i\theta}}{1 - t_1^* t_2^* \alpha e^{i\theta}} \cdot \frac{t_1^* - t_2 \alpha e^{-i\theta}}{1 - t_1 t_2 \alpha e^{-i\theta}} = \\ = \frac{|t_1|^2 + \alpha^2 |t_2|^2 - \alpha(t_1^* t_2^* e^{i\theta} + t_1 t_2 e^{-i\theta})}{1 + \alpha^2 |t_1|^2 |t_2|^2 - \alpha(t_1^* t_2^* e^{i\theta} + t_1 t_2 e^{-i\theta})} = \\ = \frac{|t_1|^2 + \alpha^2 |t_2|^2 - \alpha |t_1||t_2|(e^{i(\theta - \phi_{t_1} - \phi_{t_2})} + e^{-i(\theta - \phi_{t_1} - \phi_{t_2})})}{1 + \alpha^2 |t_1|^2 |t_2|^2 - \alpha |t_1||t_2|(e^{i(\theta - \phi_{t_1} - \phi_{t_2})} + e^{-i(\theta - \phi_{t_1} - \phi_{t_2})})} = \\ = \frac{|t_1|^2 + \alpha^2 |t_2|^2 - 2\alpha |t_1||t_2| \cos(\theta - \phi_{t_1} - \phi_{t_2})}{1 + \alpha^2 |t_1|^2 |t_2|^2 - 2\alpha |t_1||t_2| \cos(\theta - \phi_{t_1} - \phi_{t_2})} = \\ = 1 - \frac{(1 - |t_1|^2)(1 - \alpha^2 |t_2|^2)}{1 + \alpha^2 |t_1|^2 |t_2|^2 - 2\alpha |t_1||t_2| \cos(\theta - \phi_{t_1} - \phi_{t_2})} \end{aligned} \quad \text{(A.11)}$$

where $t_1 = |t_1| e^{i\phi_{t_1}}$ and $t_2 = |t_2| e^{i\phi_{t_2}}$.

Similar steps for the *drop* power $\mathcal{T}$:

$$\begin{aligned}
\mathcal{T} = |E_{t2}|^2 = \frac{-\kappa_1^* \kappa_2 \alpha_1 e^{i\theta_1}}{1 - t_1^* t_2^* \alpha e^{i\theta}} \cdot \frac{-\kappa_1 \kappa_2^* \alpha_1 e^{-i\theta_1}}{1 - t_1 t_2 \alpha e^{-i\theta}} = \\
= \frac{\alpha_1^2 |\kappa_1|^2 |\kappa_2|^2}{1 + \alpha^2 |t_1|^2 |t_2|^2 - \alpha(t_1^* t_2^* e^{i\theta} + t_1 t_2 e^{-i\theta})} = \\
= \frac{\alpha_1^2 (1 - |t_1|^2)(1 - |t_2|^2)}{1 + \alpha^2 |t_1|^2 |t_2|^2 - \alpha |t_1||t_2| (e^{i(\theta - \phi_{t_1} - \phi_{t_2})} + e^{-i(\theta - \phi_{t_1} - \phi_{t_2})})} = \\
= \frac{\alpha_1^2 (1 - |t_1|^2)(1 - |t_2|^2)}{1 + \alpha^2 |t_1|^2 |t_2|^2 - 2\alpha |t_1||t_2| \cos(\theta - \phi_{t_1} - \phi_{t_2})}
\end{aligned} \tag{A.12}$$

And from eq. (A.10), we get the internal ring power $\mathcal{P}$:

$$\begin{aligned}
\mathcal{P} = |E_{r1}|^2 = \frac{-\kappa_1^*}{1 - t_1^* t_2^* \alpha e^{i\theta}} \cdot \frac{-\kappa_1}{1 - t_1 t_2 \alpha e^{-i\theta}} = \\
= \frac{|\kappa_1|^2}{1 + \alpha^2 |t_1|^2 |t_2|^2 - \alpha(t_1^* t_2^* e^{i\theta} + t_1 t_2 e^{-i\theta})} = \\
= \frac{|\kappa_1|^2}{1 + \alpha^2 |t_1|^2 |t_2|^2 - \alpha |t_1||t_2| (e^{i(\theta - \phi_{t_1} - \phi_{t_2})} + e^{-i(\theta - \phi_{t_1} - \phi_{t_2})})} = \\
= \frac{|\kappa_1|^2}{1 + \alpha^2 |t_1|^2 |t_2|^2 - 2\alpha |t_1||t_2| \cos(\theta - \phi_{t_1} - \phi_{t_2})}
\end{aligned} \tag{A.13}$$

Bibliography

[1] J. Chaste, A. Eichler, J. Moser, G. Ceballos, R. Rurali, and A. Bachtold, "A nanomechanical mass sensor with yoctogram resolution," *Nature Nanotechnology*, vol. 7, pp. 301–304, Apr. 2012.

[2] E. Sage, A. Brenac, T. Alava, R. Morel, C. Dupré, M. S. Hanay, M. L. Roukes, L. Duraffourg, C. Masselon, and S. Hentz, "Neutral particle mass spectrometry with nanomechanical systems," *Nature Communications*, vol. 6, p. 6482, Mar. 2015.

[3] M. S. Hanay, S. I. Kelber, C. D. O'Connell, P. Mulvaney, J. E. Sader, and M. L. Roukes, "Inertial imaging with nanomechanical systems," *Nature Nanotechnology*, vol. 10, pp. 339–344, Mar. 2015.

[4] M. Aspelmeyer, T. J. Kippenberg, and F. Marquardt, "Cavity optomechanics," *Reviews of Modern Physics*, vol. 86, pp. 1391–1452, Dec. 2014.

[5] C. Baker, C. Belacel, A. Andronico, P. Senellart, A. Lemaitre, E. Galopin, S. Ducci, G. Leo, and I. Favero, "Critical optical coupling between a GaAs disk and a nanowaveguide suspended on the chip," *Applied Physics Letters*, vol. 99, no. 15, p. 151117, 2011.

[6] E. Gavartin, P. Verlot, and T. J. Kippenberg, "A hybrid on-chip optomechanical transducer for ultrasensitive force measurements," *Nature Nanotechnology*, vol. 7, pp. 509–514, June 2012.

[7] V. T. K. Sauer, Z. Diao, M. R. Freeman, and W. K. Hiebert, "Optical racetrack resonator transduction of nanomechanical cantilevers," *Nanotechnology*, vol. 25, p. 055202, Feb. 2014.

[8] M. Sansa, E. Sage, E. C. Bullard, M. Gély, T. Alava, E. Colinet, A. K. Naik, L. G. Villanueva, L. Duraffourg, M. L. Roukes, G. Jourdan, and S. Hentz, "Frequency fluctuations in silicon nanoresonators," *Nature Nanotechnology*, Feb. 2016.

[9] M. Fernandez-Regulez, M. Sansa, M. Serra-Garcia, E. Gil-Santos, J. Tamayo, F. Perez-Murano, and A. San Paulo, "Horizontally patterned Si nanowire growth for nanomechanical devices," *Nanotechnology*, vol. 24, p. 095303, Mar. 2013.

[10] S. Fanget, S. Hentz, P. Puget, J. Arcamone, M. Matheron, E. Colinet, P. Andreucci, L. Duraffourg, E. Myers, and M. Roukes, "Gas sensors based on gravimetric detection—A review," *Sensors and Actuators B: Chemical*, vol. 160, pp. 804–821, Dec. 2011.

[11] David Thomson et al., Aaron Zilkie, John E Bowers, Tin Komljenovic, M Nedeljkovic, and J.M. Fedeli, "Roadmap on silicon photonics," *Journal of Optics*, vol. 18, no. 7, p. 073003, 2016.

[12] W.-C. Chiu, C.-C. Chang, J.-M. Wu, M.-C. M. Lee, and J.-M. Shieh, "Optical phase modulators using deformable waveguides actuated by micro-electromechanical systems," *Optics Letters*, vol. 36, p. 1089, Apr. 2011.

[13] K. J. Vahala, "Optical microcavities," *Nature*, vol. 424, pp. 839–846, Aug. 2003.

[14] T. J. Kippenberg and K. J. Vahala, "Cavity Optomechanics: Back-Action at the Mesoscale," *Science*, vol. 321, no. 5893, pp. 1172–1176, 2008.

[15] C. Metzger, I. Favero, A. Ortlieb, and K. Karrai, "Optical self cooling of a deformable Fabry-Perot cavity in the classical limit," *Physical Review B*, vol. 78, July 2008.

[16] P. H. Kim, C. Doolin, B. D. Hauer, A. J. R. MacDonald, M. R. Freeman, P. E. Barclay, and J. P. Davis, "Nanoscale torsional optomechanics," *Applied Physics Letters*, vol. 102, no. 5, p. 053102, 2013.

[17] G. S. Wiederhecker, L. Chen, A. Gondarenko, and M. Lipson, "Controlling photonic structures using optical forces," *Nature*, vol. 462, pp. 633–636, Dec. 2009.

[18] M. Eichenfield, R. Camacho, J. Chan, K. J. Vahala, and O. Painter, "A picogram- and nanometre-scale photonic-crystal optomechanical cavity," *Nature*, vol. 459, pp. 550–555, May 2009.

[19] W. Weaver, S. Timoshenko, and D. H. Young, *Vibration problems in engineering.* New York: Wiley, 5th ed ed., 1990.

[20] M. S. Hanay, *Towards single-molecule nanomechanical mass spectrometry.* PhD thesis, California Institute of Technology, 2011.

[21] E. Rubiola, "On the measurement of frequency and of its sample variance with high-resolution counters," *Review of Scientific Instruments*, vol. 76, no. 5, p. 054703, 2005.

[22] D. W. Allan, "Time and frequency (time-domain) characterization, estimation, and prediction of precision clocks and oscillators," *IEEE Trans Ultrason Ferroelectr Freq Control*, vol. 34, no. 6, pp. 647–654, 1987.

[23] W. P. Robins, *Phase Noise in Signal Sources.* The Institution of Engineering and Technology, Michael Faraday House, Six Hills Way, Stevenage SG1 2AY, UK: IET, Jan. 1984.

[24] Y. T. Yang, C. Callegari, X. L. Feng, K. L. Ekinci, and M. L. Roukes, "Zeptogram-Scale Nanomechanical Mass Sensing," *Nano Letters*, vol. 6, pp. 583–586, Apr. 2006.

[25] W. Hiebert, "Mass sensing: Devices reach single-proton limit," *Nature Nanotechnology*, vol. 7, pp. 278–280, May 2012.

[26] D. H. Russell and R. D. Edmondson, "High-resolution Mass Spectrometry and Accurate Mass Measurements with Emphasis on the Characterization of Peptides and Proteins by Matrix-assisted Laser Desorption/Ionization Time-of-flight Mass Spectrometry," *Journal of Mass Spectrometry*, vol. 32, pp. 263–276, Mar. 1997.

[27] M. S. Hanay, S. Kelber, A. K. Naik, D. Chi, S. Hentz, E. C. Bullard, E. Colinet, L. Duraffourg, and M. L. Roukes, "Single-protein nanomechanical mass spectrometry in real time," *Nature Nanotechnology*, vol. 7, pp. 602–608, Aug. 2012.

[28] A. K. Naik, M. S. Hanay, W. K. Hiebert, X. L. Feng, and M. L. Roukes, "Towards single-molecule nanomechanical mass spectrometry," *Nature Nanotechnology*, vol. 4, pp. 445–450, July 2009.

[29] M. V. Salapaka, H. S. Bergh, J. Lai, A. Majumdar, and E. McFarland, "Multimode noise analysis of cantilevers for scanning probe microscopy," *Journal of Applied Physics*, vol. 81, no. 6, p. 2480, 1997.

[30] S. Dohn, W. Svendsen, A. Boisen, and O. Hansen, "Mass and position determination of attached particles on cantilever based mass sensors," *Review of Scientific Instruments*, vol. 78, p. 103303, Oct. 2007.

[31] E. Sage, O. Martin, C. Dupre, T. Ernst, G. Billiot, L. Duraffourg, E. Colinet, and S. Hentz, "Frequency-addressed NEMS arrays for mass and gas sensing applications," pp. 665–668, IEEE, June 2013.

[32] V. T. K. Sauer, Z. Diao, M. R. Freeman, and W. K. Hiebert, "Wavelength-division multiplexing of nano-optomechanical doubly clamped beam systems," *Optics Letters*, vol. 40, p. 1948, May 2015.

[33] I. De Vlaminck, J. Roels, D. Taillaert, D. Van Thourhout, R. Baets, L. Lagae, and G. Borghs, "Detection of nanomechanical motion by evanescent light wave coupling," *Applied Physics Letters*, vol. 90, no. 23, p. 233116, 2007.

[34] O. Basarir, S. Bramhavar, and K. L. Ekinci, "Motion Transduction in Nano-electromechanical Systems (NEMS) Arrays Using Near-field Optomechanical Coupling," *Nano Letters*, vol. 12, pp. 534–539, Feb. 2012.

[35] V. T. K. Sauer, Z. Diao, M. R. Freeman, and W. K. Hiebert, "Nanophotonic detection of side-coupled nanomechanical cantilevers," *Applied Physics Letters*, vol. 100, p. 261102, June 2012.

[36] W. Bogaerts, P. De Heyn, T. Van Vaerenbergh, K. De Vos, S. Kumar Selvaraja, T. Claes, P. Dumon, P. Bienstman, D. Van Thourhout, and R. Baets, "Silicon microring resonators," *Laser & Photonics Reviews*, vol. 6, pp. 47–73, Jan. 2012.

[37] D. G. Rabus, *Integrated ring resonators: the compendium.* No. 127 in Springer series in optical sciences, Berlin: Springer, 2007.

[38] M. Borselli, T. J. Johnson, and O. Painter, "Beyond the Rayleigh scattering limit in high-Q silicon microdisks: theory and experiment," *Optics Express*, vol. 13, no. 5, p. 1515, 2005.

[39] L. Ding, C. Baker, P. Senellart, A. Lemaitre, S. Ducci, G. Leo, and I. Favero, "High Frequency GaAs Nano-Optomechanical Disk Resonator," *Physical Review Letters*, vol. 105, Dec. 2010.

[40] C. Chauveau, P. Labeye, J.-M. Fedeli, J. Hazart, S. Blaize, and G. Lerondel, "Validation of an analytical model of Si-ring resonators for designing a 1 x 8 multiplexer in SCISSOR configuration," *Optical and Quantum Electronics*, vol. 44, pp. 541–547, Oct. 2012.

[41] R. Soref and B. Bennett, "Electrooptical effects in silicon," *IEEE Journal of Quantum Electronics*, vol. 23, pp. 123–129, Jan. 1987.

[42] F. Vollmer and S. Arnold, "Whispering-gallery-mode biosensing: label-free detection down to single molecules," *Nature Methods*, vol. 5, pp. 591–596, July 2008.

[43] F. Vollmer, D. Braun, A. Libchaber, M. Khoshsima, I. Teraoka, and S. Arnold, "Protein detection by optical shift of a resonant microcavity," *Applied Physics Letters*, vol. 80, no. 21, p. 4057, 2002.

[44] B. Taurel, "Étude théorique et expérimental du couplage optique dans les systèmes optomécaniques," *Rapport de projet de fin d'études, École nationale supérieure de physique, électronique, matériaux*, 2016.

[45] D. Van Thourhout and J. Roels, "Optomechanical device actuation through the optical gradient force," *Nature Photonics*, vol. 4, pp. 211–217, Apr. 2010.

[46] A. Ashkin, "Acceleration and Trapping of Particles by Radiation Pressure," *Physical Review Letters*, vol. 24, pp. 156–159, Jan. 1970.

[47] C. Pin, B. Cluzel, C. Renaut, E. Picard, D. Peyrade, E. Hadji, and F. de Fornel, "Optofluidic Near-Field Optical Microscopy: Near-Field Mapping of a Silicon Nanocavity Using Trapped Microbeads," *ACS Photonics*, vol. 2, pp. 1410–1415, Oct. 2015.

[48] W. H. P. Pernice, M. Li, and H. X. Tang, "Theoretical investigation of the transverse optical force between a silicon nanowire waveguide and a substrate," *Opt. Express*, vol. 17, no. 3, pp. 1806–1816, 2009.

[49] M. L. Povinelli, M. Loncar, M. Ibanescu, E. J. Smythe, S. G. Johnson, F. Capasso, and J. D. Joannopoulos, "Evanescent-wave bonding between optical waveguides," *Opt. Lett.*, vol. 30, pp. 3042–3044, Nov. 2005.

[50] F. Riboli, A. Recati, M. Antezza, and I. Carusotto, "Radiation induced force between two planar waveguides," *The European Physical Journal D*, vol. 46, no. 1, pp. 157–164, 2008.

[51] A. Mizrahi and L. Schächter, "Two-slab all-optical spring," *Optics Letters*, vol. 32, no. 6, p. 692, 2007.

[52] W. H. P. Pernice, M. Li, D. Garcia-Sanchez, and H. X. Tang, "Analysis of short range forces in opto-mechanical devices with a nanogap," *Opt. Express*, vol. 18, no. 12, pp. 12615–12621, 2010.

[53] M. Li, W. H. P. Pernice, C. Xiong, T. Baehr-Jones, M. Hochberg, and H. X. Tang, "Harnessing optical forces in integrated photonic circuits," *Nature*, vol. 456, pp. 480–484, Nov. 2008.

[54] M. Eichenfield, C. P. Michael, R. Perahia, and O. Painter, "Actuation of micro-optomechanical systems via cavity-enhanced optical dipole forces," *Nature Photonics*, vol. 1, pp. 416–422, July 2007.

[55] J. Roels, I. De Vlaminck, L. Lagae, B. Maes, D. Van Thourhout, and R. Baets, "Tunable optical forces between nanophotonic waveguides," *Nat Nano*, vol. 4, no. 8, pp. 510–513, 2009.

[56] M. Li, W. H. P. Pernice, and H. X. Tang, "Tunable bipolar optical interactions between guided lightwaves," *Nature Photonics*, vol. 3, pp. 464–468, Aug. 2009.

[57] C. Kopp, S. Bernabé, B. B. Bakir, J. Fedeli, R. Orobtchouk, F. Schrank, H. Porte, L. Zimmermann, and T. Tekin, "Silicon Photonic Circuits: On-CMOS Integration, Fiber Optical Coupling, and Packaging," *IEEE Journal of Selected Topics in Quantum Electronics*, vol. 17, pp. 498–509, May 2011.

[58] J.-M. Fedeli, F. Schrank, E. Augendre, S. Bernabe, J. Kraft, P. Grosse, and T. Enot, "Photonic-Electronic Integration With Bonding," *IEEE Journal of Selected Topics in Quantum Electronics*, vol. 20, pp. 350–358, July 2014.

[59] C. Chauveau, *Réseaux de résonateurs pour la photonique sur silicium, applications au multiplexage en longueur d'onde.* PhD thesis, 2012.

[60] E. Sage, *Nouveau concept de spectrométre de masse à base de réseaux de nanostructures résonantes.* PhD thesis, 2013.

[61] E. Mile, G. Jourdan, I. Bargatin, S. Labarthe, C. Marcoux, P. Andreucci, S. Hentz, C. Kharrat, E. Colinet, and L. Duraffourg, "In-plane nanoelectromechanical resonators based on silicon nanowire piezoresistive detection," *Nanotechnology*, vol. 21, no. 16, p. 165504, 2010.

[62] Y. Wang, X. Wang, J. Flueckiger, H. Yun, W. Shi, R. Bojko, N. A. F. Jaeger, and L. Chrostowski, "Focusing sub-wavelength grating couplers with low back reflections for rapid prototyping of silicon photonic circuits," *Optics Express*, vol. 22, p. 20652, Aug. 2014.

[63] D. Taillaert, F. Van Laere, M. Ayre, W. Bogaerts, D. Van Thourhout, P. Bienstman, and R. Baets, "Grating Couplers for Coupling between Optical Fibers and Nanophotonic Waveguides," *Japanese Journal of Applied Physics*, vol. 45, pp. 6071–6077, Aug. 2006.

[64] C. Li, H. Zhang, M. Yu, and G. Q. Lo, "CMOS-compatible high efficiency double-etched apodized waveguide grating coupler," *Optics Express*, vol. 21, p. 7868, Apr. 2013.

[65] E. Mile, *Nanowire and carbon nanotube based NEMS resonators.* PhD thesis, Ecole Polytechnique X, June 2010.

[66] R. D. Blevins, *Formulas for natural frequency and mode shape.* Malabar, Florida: Krieger Publishing, reprint ed ed., 2001. OCLC: 636275536.

[67] Y. Kanda, "Piezoresistance effect of silicon," *Sensors and Actuators A: Physical*, vol. 28, pp. 83–91, July 1991.

[68] S. Labarthe, *Design and modelisation of a mass nanosensor using piezoresistive detection.* PhD thesis, Université Joseph-Fourier - Grenoble I, Oct. 2010.

[69] G. Jourdan, E. Colinet, J. Arcamone, A. Niel, C. Marcoux, and L. Duraffourg, "NEMS-based heterodyne self-oscillator," *Sensors and Actuators A: Physical*, vol. 189, no. 0, pp. 512 – 518, 2013.

[70] I. Bargatin, E. B. Myers, J. Arlett, B. Gudlewski, and M. L. Roukes, "Sensitive detection of nanomechanical motion using piezoresistive signal downmixing," *Applied Physics Letters*, vol. 86, no. 13, p. 133109, 2005.

[71] K. L. Ekinci, "Ultimate limits to inertial mass sensing based upon nanoelectromechanical systems," *Journal of Applied Physics*, vol. 95, no. 5, p. 2682, 2004.

[72] L. Duraffourg and J. Arcamone, *Nanoelectromechanical Systems.* Hoboken, NJ, USA: John Wiley & Sons, Inc., Sept. 2015.

[73] B. E. Little, J.-P. Laine, and S. T. Chu, "Surface-roughness-induced contradirectional coupling in ring and disk resonators," *Optics Letters*, vol. 22, p. 4, Jan. 1997.

[74] J. Ctyroky, I. Richter, and M. Sinor, "Dual resonance in a waveguide-coupled ring microresonator," *Optical and Quantum Electronics*, vol. 38, pp. 781–797, Mar. 2007.

[75] S. Blaize, F. Gesuele, I. Stefanon, A. Bruyant, G. Lérondel, P. Royer, B. Martin, A. Morand, P. Benech, and J.-M. Fedeli, "Real-space observation of spectral degeneracy breaking in a waveguide-coupled disk microresonator," *Optics Letters*, vol. 35, p. 3168, Oct. 2010.

[76] K. R. Hiremath and V. N. Astratov, "Perturbations of whispering gallery modes by nanoparticles embedded in microcavities," *Optics Express*, vol. 16, p. 5421, Apr. 2008.

[77] R. Dekker, A. Driessen, T. Wahlbrink, C. Moormann, J. Niehusmann, and M. Först, "Ultrafast Kerr-induced all-optical wavelength conversion in silicon waveguides using 1.55 um femtosecond pulses," *Optics Express*, vol. 14, no. 18, p. 8336, 2006.

[78] C. Baker, S. Stapfner, D. Parrain, S. Ducci, G. Leo, E. M. Weig, and I. Favero, "Optical instability and self-pulsing in silicon nitride whispering gallery resonators," *Optics Express*, vol. 20, p. 29076, Dec. 2012.

[79] M. L. Gorodetsky, A. Schliesser, G. Anetsberger, S. Deleglise, and T. J. Kippenberg, "Determination of the vacuum optomechanical coupling rate using frequency noise calibration," *Optics Express*, vol. 18, p. 23236, Oct. 2010.

Remerciement

J'aimerais tout d'abord remercier les membres de l'équipe de travail: Guillaume, Sébastien et Laurent pour la confiance qu'ils m'ont accordé tout au long de mes recherches. Un grand merci à Marc Sansa, Marc Gely, Jean Marc, Geoffroy, Thomas et Henry pour avoir partagé leurs compétences et leur savoir-faire. Nous avons accompli un travail pour lequel nous pouvons être fiers!
Merci également à Philippe, Karen, Daivid et Boris pour avoir mis à disposition les moyens du laboratoire.
A table, une discussion n'est jamais décevante en compagnie d'Ibraima, Jarek, Romain, Eric, Rémy, Gabrielle, Maxime, Federico, Adrien et Olivier. La pause repas avec vous peut tout arranger, merci pour votre camaraderie.

Grazie a Leandro, perché parto da Grenoble diverso da come sono arrivato. Pur vivendo lontani, credo proprio che manterremo viva la nostra intesa avendo noi *100km per gamba*.
Ringrazio Federica, la mia consigliera personale con pareri onesti e spassionati. Ogni questione si dipana quando puoi presentarti da lei con tanto di autoinvito.
Je souhaite remercier tout particulièrement Sophie, Laurie et Séb pour m'avoir choisi comme colocataire puis comme ami: quoi de mieux que de démarrer et terminer la journée avec vous.
Merci à Audrey pour avoir dédié son temps à la correction du manuscrit.
Grazie a Castellani, Pasini e Flavia per la vostra presenza durante gli ultimi mesi, sarebbe stata decisamente più dura senza di voi. Avete fatto di tutto per convincermi a restare e, vi confesso, che ci siete anche quasi riusciti.
Rendo un merito sportivo agli *arrampicaTori*: Caminale, Carlà e Ilaria. Posso tallonare solamente se siete voi a farmi sicura.
I wish to thank Stefan, Katharina, Costa and Aryan. Thanks for the hiking and skiing days, for the dancing nights and for the open discussions around a table. You all are my open window to Europe.

Ringrazio Enrico, un tipo all'antica. Mi ha mostrato quanto l'eleganza e il buon gusto siano importanti; anche per gli scienziati.

Merci à Jérémie, Mayra, Elisa, Hicham, Tiago, Rodrigo, Antoine, Pierre, Adriana et Benoît me rappellent toujours qu'il faut être motivés, sinon tu as perdu une soirée. Je remercie Louis et les autres rameurs, vous avez su m'initier à l'esprit du club. Une séance d'aviron renforce le corps mais elle vaut surtout mille séances chez le thérapeute.

A Genova mi aspettano i miei amici di sempre: Muscella, Bozzo, Perelli, Mariapaola, Zena, Ilaria, Dani, ma anche un nuovo piccolo amico, Pietro. Che dire, mi siete mancati!
Un grazie ad Anna per avermi stupito. Sarà un fatto prodigioso ma sei l'unica persona con cui mi piace ragionare a lungo termine.

Ringrazio Valentina, la sorella maggiore che da sempre è un riferimento negli eventi della vita.
Rendo grazie a Mamma Rosa e a papà Cino: sono contenti che io sia tornato ma, in qualche modo, lo erano anche quando mi hanno visto partire. A loro dedico un abbraccio più forte degli altri.